
Nano Antennas for Enhancement of Nonclassical Light Emission



Author:

Sebastian K.H. Andersen

Supervisor:

Dr. Sergey I. Bozhevolnyi

*A thesis submitted in partial fulfillment of the requirements
for the degree of Doctor of Philosophy*

at

Center for Nano Optics

Mads Clausen Institute

© 2018 - *SEBASTIAN K. H. ANDERSEN*

ALL RIGHTS RESERVED.

NO PART OF THIS PUBLICATION MAY BE REPRODUCED, TRANSMITTED OR TRANSLATED IN ANY FORM OR BY ANY MEANS, ELECTRONIC OR MECHANICAL, INCLUDING PHOTOCOPY, RECORDING, OR ANY INFORMATION STORAGE AND RETRIEVAL SYSTEM, WITHOUT PRIOR PERMISSION IN WRITING FROM THE AUTHOR.

Summary

This PhD thesis presents an experimental investigation of plasmonic nano antennas for improving the spontaneous emission properties of quantum emitters coupled to an antenna. The experimental results are significant for the generation of non-classical light, as appropriately designed antennas may significantly improve the generation of single photons from individual quantum emitters, in terms of among others photon rate, polarization and directionality. Experimental studies consider the viability of both gold and silver for nano antenna fabrication, while utilizing the nitrogen vacancy center (NV-center) for the generation of non-classical light. Nano antennas are fabricated either by electron beam lithography or nano-manipulation of monocrystalline metal particles, using an atomic force microscope (AFM). Nano diamonds containing NV-centers are introduced into the antenna during antenna assembly, or subsequently picked up with the AFM and placed in the antenna. The antenna response is characterized by dark-field and fluorescence spectroscopy. Single photon generation from an isolated NV-center is confirmed by measuring the 2. order correlation function, while improvements in photon rate are investigated in terms of lifetime and saturation curve measurements of the bare nano diamond, or when inserted into the antenna. The polarization dependent system response is characterized by rotation of respectively the pump polarization or an analyzer in the detection plane, while the antenna emission pattern is obtained by Fourier microscopy. The experimental results are supplemented by finite element modelling for consistent physical explanations of the results.

Resume

Denne PhD-afhandling omhandler et eksperimentelt studie af metalliske nanoantennner, med det formål at forbedre de spontane emissionsegenskaber af kvanteemittere koblet til antennen. De eksperimentelle resultater er signifikante for målsætningen om at realisere ikke klassiske lyskilder, da nanoantennner markant kan forbedre emissionen af fotoner fra en enkelt kvanteemitter, i form af emissionsraten, polarisationen og emissionsmønsteret. Det eksperimentielle studie undersøger både guld og sølv som mulige antennematerialer og anvender "nitrogen vacancy centeret" (NV-center) til at generere ikke-klassisk lys. Nanoantennnerne er fremstillet ved brug af elektronstrålelitografi eller manipulation af monokrystalline metalpartikler ved hjælp af et atomkraft mikroskop (AFM). Nanodiamanter som indeholder NV-centre indsættes i antennen under dennes konstruktion, eller samles op efterfølgende med AFM'en og placeres i antennen. Responset fra antennen er karakteriseret med dark-field og fluorescensspektroskopi. Emissionen af enkelte fotoner fra et enkelt NV-center bekræftes ved at måle 2. ordens korrelationsfunktionen, mens forbedringer i fotonraten undersøges i form af livstidsmålinger og måtningskurver af enten den isolerede nanodiamant, eller når denne er indsat i antennen. Polarisationafhængighed undersøges ved måling af fotonraten under rotation af excitations-laserpolarisationen eller ved rotation af en analysator i detektionsplanet. Antennens emissionsmønster karakteriseres ved Fourier mikroskopi. De eksperimentelle resultater understøttes af numeriske modeller for at opnå konsistente konklusioner for de eksperimentelle målinger.

Preface

This PhD thesis presents the results obtained during my PhD study at the Center for Nano Optics, University of Southern Denmark, from September 2014 to February 2018, under the supervision of Dr. Scient. Sergey I. Bozhevolnyi. The project included a 5-month stay at Birck Nanotechnology Center, University of Purdue in Indiana, USA, at which I was collaborated with researchers from the groups of Professor Alexandra Boltasseva and Professor Vladimir Shalaev. The accumulated work consistutes six peer-reviewed publications: Two co-authorships and four articles written by myself. This thesis is based on five of these publications, appearing in appendix A-E, as they pertain to the subject of this thesis, namely improving the spontaneous emission properties of quantum emitters by coupling to plasmonic nano antennas. A complete list of my publications can be found in the section "Publications and presentations".

Acknowledgements

Foremost I would like to thank my supervisor Dr. Sergey I. Bozhevolnyi for putting faith in me and my ideas. Owing to his critique and sober judgement the PhD project never veered too far off course. Further, I am grateful to my unofficial co-supervisor Shailesh Kumar who built the majority of the experimental setup and introduced me to the experimental techniques. He always kept an open door and a clear head, whenever I was in need of sound advice or an idea needed to be tested. I give thanks to Alexander Roberts for many instructive and pleasant conversations. Many pitfalls in this PhD was avoided because of his experience and help. Michael G. Nielsen and Anders Pors should be acknowledged for their guidance and friendly advice in smoothing the upstart of my PhD. Overall, I would like to thank my colleagues at the center for Nano Optics group, University of Southern Denmark, for creating a helpful and inspiring environment, in which I have enjoyed working.

Further, I am grateful to Prof. Vladimir Shalaev for giving me the opportunity to work at Birck Nanotechnology Center at Purdue University, and the Nano Photonics group at Birck for taking me in. Particularly I would like to thank Sam Peana for giving me a home in the US, and Simeon Bogdanov, Mikhail Shalaginov and Oksana Makarova for their positive attitude and hard work in making the bullseye antenna project happen. Also, I am grateful to Yi Xuan for fabricating the bullseye antenna.

Finally, I would like to thank my family and friends for making my time as a PhD about a lot more than nano antennas. I am thankful to my mother Ingrid Andersen for caring too much and my father Erik Jorgensen for testing my knowledge and making me see things from a new perspective. I am grateful to my brother Teis Davidsen for his enthusiasm and good nature. Last but not least, I am thankful to my girlfriend Emma Holm, for keeping me grounded and always supporting me on the winding road through this project.

List of acronyms

AFM	Atomic force microscope
APD	Avalanche photodiode
CCD	Charge coupled device
CGD	Conductor-gap-dielectric
FWHM	Full width at half-maximum
GSP	Gap surface plasmon
GSPR	Gap surface plasmon resonance
HSQ	Hydrogen silsesquioxane
IRF	Instrument response function
LSP	Localized surface plasmon
NA	Numerical aperture
NV-center	Nitrogen vacancy center
PMMA	Polymethyl methacrylate
SPP	Surface plasmon polariton
TM/TE	Tranverse magnetic/ transverse electric

Contents

1	INTRODUCTION	1
2	OPTICAL MODES AT METALLIC INTERFACES	5
2.1	The wave equation	5
2.2	Free propagating light	7
2.3	Surface plasmon polariton	8
2.4	Two interface plasmonic modes	10
2.5	Localized surface plasmon modes	11
3	SPONTANEOUS EMISSION IN A HOMOGENEOUS ENVIRONMENT	13
4	SPONTANEOUS EMISSION IN AN INHOMOGENEOUS ENVIRONMENT	17
4.1	Dipole emission near a metallic interface	18
4.2	Spontaneous emission near metallic nano antennas	20
5	THE NITROGEN VACANCY COLOR CENTER IN DIAMOND	23
5.1	The nitrogen vacancy center in bulk diamond	23
5.2	The nitrogen vacancy center in nanodiamond	27
6	RATE MODEL OF A 3-LEVEL SYSTEM	29
6.1	Lifetime decay curve	30
6.2	Saturation curve	30
6.3	2. order correlation function	32
6.4	Rotation of laser polarization	34
7	EXPERIMENTAL SETUP AND TECHNIQUES	37
8	NANO ANTENNAS FOR ENHANCEMENT OF NONCLASSICAL LIGHT EMISSION	43
8.1	Metal photoluminescence from gold nano antennas	43
8.2	Spontaneous emission from multiple NV-centers coupled to a silver cube	45
8.3	Non-classical light emission from an NV-center in a silver cube dimer antenna	46
8.4	Efficient emission from multiple NV-centers in a hybrid bullseye antenna	48
8.5	Fabrication of Bragg mirrors for plasmonic cavities	50

9	CONCLUSION AND OUTLOOK	53
	Collection of Papers	
A	GOLD PHOTOLUMINESCENCE WAVELENGTH AND POLARIZATION ENGINEERING	55
B	COUPLING OF NITROGEN-VACANCY CENTERS IN A NANODIAMOND TO A SILVER NANOCUBE	67
C	ULTRABRIGHT LINEARLY POLARIZED PHOTON GENERATION FROM A NITROGEN VACANCY CENTER IN A NANOCUBE DIMER ANTENNA	81
D	HYBRID PLASMONIC BULLSEYE ANTENNAS FOR EFFICIENT PHOTON COLLECTION	101
E	EXCITATION OF SURFACE PLASMON POLARITONS MODES WITH MULTIPLE NITROGEN VACANCY CENTERS IN SINGLE NANODIAMONDS	123
	PUBLICATIONS AND PRESENTATIONS	135
	AUTHORSHIP AGREEMENTS	137
	REFERENCES	143

1

Introduction

With the turn of the twentieth century, scientist and engineers have started to look beyond classical physics and into the expanded rule book of quantum mechanics, in the pursuit of pushing the boundaries of technology within computing [1–3], sensing [4, 5] and communication[6, 7]. A fundamental building block in this endeavour is the controlled generation of a single quantum of light, namely the photon. Single photons can in principle be generated by the attenuation of laser pulses[8] or parametric down conversion[9]. However, photon generation by these approaches is inherently probabilistic. In contrast, the generation of single photons by spontaneous emission from a 2-level system or quantum emitter can in principle allow for deterministic single photon generation. Spontaneous photon emission from a single quantum emitter was first observed from a trapped ion in 1987 [10], while the subsequent and ongoing pursuit of the ideal quantum emitter has lead to a zoo of potential candidates, such as molecules, quantum dots, defects in diamond and the more recent entries of defects in carbon nanotubes or 2-D materials [11–13]. The rate of photon emission from these emitters is limited by the time delay of the excited state lifetime, typically on the order of nanoseconds. Further, the inherent omnidirectional emission pattern of typical electronic dipole transitions makes efficient photon collection a challenge. However, as noted by Purcell in 1946[14], the spontaneous emission properties are a function of both the emitter and the surrounding photonic environment. The emission rate, quantum yield, emission pattern and spectrum all being aspects affected by the environment. Complementary to the study of quantum emitters, the design and realization of suitable photonics environments is thus being studied in order to achieve the best photon source properties. The conventional design relies on efficiently coupling quantum emitter emission to the photonic mode of an engineered resonator or waveguide, which subsequently relays the photons in a desirable fashion. The coupling to the particular photonic mode may be improved either by increasing interaction time or increasing interaction strength by confining the mode to a small volume. Maximizing light-matter interaction by either of

these parameters branches the resonator design into two categories[15]. High-quality factor dielectric cavities allow for a long interaction time between the cavity mode and the quantum emitter, while the mode volume in this case is diffraction limited. In contrast, plasmonic modes supported by resonant metallic nano antennas may be confined to nanometer-sized volumes, while ohmic loss limits the lifetime of the plasmon to the femto-second regime. Either design branch carries distinct advantageous and disadvantages. Exceptional performance has been achieved by the all-dielectric approach at liquid helium temperatures[16]. However, the narrow linewidth of high quality factor dielectric cavities requires precise continuous tuning of the cavity to the emission for stable performance over time, while the high quality factor implies a slowness potentially limiting emission rate[17] or ultrafast switching. On the other hand, the broadband nature of plasmonic resonances makes for a robust system applicable for room temperature operation, while emission may be quite fast[18]. The ohmic loss inherent to plasmonic systems, does however compromise the efficiency at which photons can be generated. Nevertheless, both approaches are, at this point, worth exploring for their various strengths and potentially different impacts on future technologies.

In order to clarify the goal of this thesis, it is instructive to define the performance parameters of the ideal photon source, listed in left-hand box of figure 1.1. The ideal photon source generates a pure stream of indistinguishable single polarized photons at high rate with unity efficiency. The subset of performance parameters required for a specific technological application varies with the application [19]. Real quantum emitters may have many issues leaving them less than ideal photon sources, some of which are listed in the right-hand box in figure 1.1. These issues may to some degree be alleviated by appropriate choice of quantum emitter. The main work of this thesis is focused on the center box, namely the study of nano antennas for pushing the spontaneous emission properties of real quantum emitters towards that of the ideal photon source. The current study makes progress on improving the photon rate, single photon purity, polarization and the efficiency of photon generation.

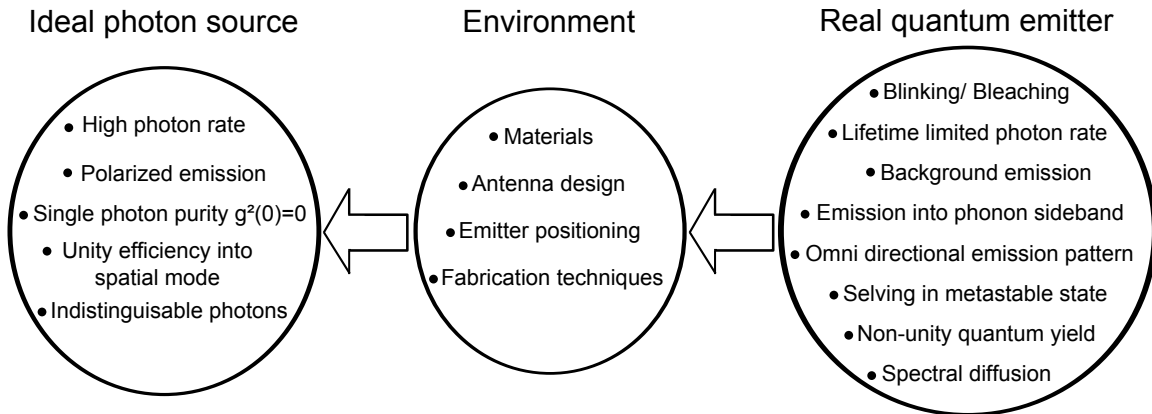


Figure 1.1: Schematic of the thesis problem. By positioning a quantum emitters near metallic nano antennas it is goal to move performance parameters of real quantum emitters closer to the ideal photon source.

In this work we study emission from the Nitrogen vacancy color center (NV-center) contained in nanodiamond crystals. The NV-center is well suited as a quantum emitter, as the emission is photostable at room temperature, while photons may be generated indefinitely without blinking or photobleaching of the emitter. The nanodiamond is introduced into the plasmonic antennas using an atomic force mi-

croscopy (AFM), either by pushing metal particles with the AFM tip or by picking up the nanodiamond and placing it in the antenna. Subsequently, the emission properties are experimentally characterized in order to evaluate performance of the antenna. Chapter 2-7 provides the relevant background for the thesis. Theory is provided by an introduction to the concept of plasmonic modes (chapter 2) and a brief description of spontaneous emission in respectively a homogeneous (chapter 3) and inhomogeneous environment (chapter 4). The photo-physical properties of the NV-center are then reviewed in chapter 5. The introductory chapters close with an analytical model of the experimental measurements relevant for characterizing NV-center emission (chapter 6), along with a description of the experimental setup used to carry out the measurements (chapter 7).

In chapter 8 we review the results of this thesis, while the detailed presentation of the results appear in appendix A-E. The realization of a good single photon source ultimately requires background emission from the environment to be managed as it may corrupt the single photon character of the source. In this context, a better understanding of how background emission arises in plasmonic antennas is desirable. In section 8.1 we review the experimental study of such background emission in the form of gold photoluminescence from gap plasmon resonator arrays. The experimental findings inform our choice of antenna, as we in section 8.2 study the spontaneous emission of multiple NV-centers when coupled to a monocrystalline silver nanocube. In section 8.3, we expand the experiment to the single photon regime, as we consider the case of a single NV-center, situated in the gap of a silver cube dimer antenna. Section 8.4 considers the alternative antenna configuration consisting of a hybrid bullseye antenna containing an ensemble of NV-centers in a nanodiamond. Finally in section 8.5 we review our efforts of fabricating Bragg mirrors on plasmonic waveguide systems and end with a conclusion and outlook in chapter 9.

2

Optical modes at metallic interfaces

Spontaneous emission is the process at which matter spontaneously excites electromagnetic modes by the decay from a higher lying energy state. The process is strongly dependent on the modes supported by the particular environment, which are available for emission. It is therefore instructive to initially review the electromagnetic modes supported by respectively a homogeneous and inhomogeneous environment. Particularly we focus on plasmonic modes supported by dielectric-metal interfaces.

2.1 THE WAVE EQUATION

The relation of electromagnetic field components is described by the macroscopic Maxwell's equations, here given in differential form for SI units,

$$\nabla \cdot \mathbf{D}(\mathbf{r}, t) = \rho(\mathbf{r}, t), \quad (2.1)$$

$$\nabla \cdot \mathbf{B}(\mathbf{r}, t) = 0, \quad (2.2)$$

$$\nabla \times \mathbf{E}(\mathbf{r}, t) = -\frac{\partial \mathbf{B}(\mathbf{r}, t)}{\partial t}, \quad (2.3)$$

$$\nabla \times \mathbf{H}(\mathbf{r}, t) = \frac{\partial \mathbf{D}(\mathbf{r}, t)}{\partial t} + \mathbf{j}(\mathbf{r}, t), \quad (2.4)$$

\mathbf{E} being the electric field, \mathbf{D} the electric displacement field, \mathbf{H} the magnetic field and \mathbf{B} magnetic induction, each being a function of the position \mathbf{r} and time t . The charge density ρ and current density \mathbf{j} constitute source terms for generating the electromagnetic fields. In order to describe field relations in a particular optical material, Maxwell's equations are supplemented by the constitutive relations.

$$\mathbf{D}(\mathbf{r}, t) = \varepsilon_0 \varepsilon(\omega) \mathbf{E}(\mathbf{r}, t), \quad (2.5)$$

$$\mathbf{B}(\mathbf{r}, t) = \mu_0 \mu(\omega) \mathbf{H}(\mathbf{r}, t), \quad (2.6)$$

$$\mathbf{j}_c(\mathbf{r}, t) = \sigma(\omega) \mathbf{E}(\mathbf{r}, t), \quad (2.7)$$

ε_0 and μ_0 being the vacuum permittivity and permeability respectively, while the current density has been separated into the terms $\mathbf{j} = \mathbf{j}_s + \mathbf{j}_c$. \mathbf{j}_s being the source current, responsible for field generation, while \mathbf{j}_c is the induced current density, arising from electric fields in conductive media. The optical response of the material is described by the materials permittivity ε , permeability μ and the conductivity σ . For the present work, materials are assumed to be linear, isotropic, non-magnetic and homogeneous ε , μ and σ thus represent scalar values independent of the position \mathbf{r} in the medium, for which $\mu=1$. For a linear medium the temporal field dependence may be spectrally decomposed into a sum of monochromatic terms

$$\mathbf{E}(\mathbf{r}, t) = \int_{-\infty}^{\infty} \mathbf{E}(\mathbf{r}, \omega) e^{-i\omega t} d\omega, \quad (2.8)$$

$$\mathbf{H}(\mathbf{r}, t) = \int_{-\infty}^{\infty} \mathbf{H}(\mathbf{r}, \omega) e^{-i\omega t} d\omega. \quad (2.9)$$

Without loss of generality, we consider a single monochromatic term, in the spectral summation, with the harmonic time dependence $e^{-i\omega t}$. Time derivatives in equation 2.3 and 2.4 thereby undergo the conversion $\frac{\partial}{\partial t} \rightarrow -i\omega$. Inserting the constitutive relations (equation 2.5-2.7) into Maxwells curls equations 2.3, 2.4 and performing an additional curl operation, we arrive at the wave equation for $\mathbf{E}(\mathbf{r}, \omega)$ and $\mathbf{H}(\mathbf{r}, \omega)$,

$$\nabla \times \nabla \times \mathbf{E}(\mathbf{r}, \omega) - \frac{\omega^2}{c^2} \left(\varepsilon + \frac{i\sigma}{\omega\varepsilon_0} \right) \mathbf{E}(\mathbf{r}, \omega) = i\omega\mu_0 \mathbf{j}_s(\mathbf{r}), \quad (2.10)$$

$$\nabla \times \nabla \times \mathbf{H}(\mathbf{r}, \omega) - \frac{\omega^2}{c^2} \left(\varepsilon + \frac{i\sigma}{\omega\varepsilon_0} \right) \mathbf{H}(\mathbf{r}, \omega) = \nabla \times \mathbf{j}_s(\mathbf{r}). \quad (2.11)$$

The frequency dependence of material parameters being suppressed for simplicity, while $c = 1/\sqrt{\varepsilon_0\mu_0}$ is the speed of light in vacuum. The expression is simplified by incorporating ε and σ into a complex permittivity $\tilde{\varepsilon} = (\varepsilon + i\sigma/\omega\varepsilon_0)$, accounting for material polarization and induced conduction currents, along with associated ohmic loss. The general mode solutions, supported by a particular environment exist without external excitation, the wave equation is therefore solved in the absence of source terms $\mathbf{j}_s = 0, \rho = 0$. Applying the vector identity $\nabla \times \nabla \times \mathbf{F} = \nabla(\nabla \cdot \mathbf{F}) - \nabla^2 \mathbf{F}$ and noting for a homogeneous material in the absence of external charge $\nabla \cdot \mathbf{E} = 0, \nabla \cdot \mathbf{H} = 0$, equation 2.10 and 2.11 can be written in the form of the homogeneous Helmholtz equations

$$\left[\nabla^2 + k_0^2 \tilde{\epsilon} \right] \mathbf{E}(\mathbf{r}, \omega) = 0, \quad (2.12)$$

$$\left[\nabla^2 + k_0^2 \tilde{\epsilon} \right] \mathbf{H}(\mathbf{r}, \omega) = 0, \quad (2.13)$$

$k_0 = \frac{\omega}{c}$ being the vacuum wavenumber. Solutions of equation 2.12 and 2.13 define the electromagnetic waves supported by a linear, isotropic, non-magnetic, homogeneous and source-free environment. In a piece-wise continuous environment, these solutions may be defined for the individual media and boundaries conditions applied to obtain mode solutions for the particular environment. In the present work, we consider a stratified media with a layer-dependent permittivity varying along the z-axis of a cartesian coordinate system. Wave propagation is assumed to occur in the x-z plane, while the field is invariant along y. In this case wave solutions exist in the form of TE- and TM-polarized solutions, having respectively the \mathbf{E} or \mathbf{H} -field component normal to the x-z plane of propagation. As plasmonic mode solutions only exist in the TM-polarized form, we proceed by considering a TM-polarized wave. Determining \mathbf{H} from the now scalar form of equation 2.13 and extracting the electric field components from 2.4, the TM-wave solution for a particular layer may be written in the form[20]

$$\mathbf{E}_j(x, z, \omega) = \begin{pmatrix} E_{xj} \\ 0 \\ E_{zj} \end{pmatrix} e^{ik_x x \pm \kappa_j z}, \quad (2.14)$$

$$\mathbf{H}_j(x, z, \omega) = \begin{pmatrix} 0 \\ H_{yj} \\ 0 \end{pmatrix} e^{ik_x x \pm \kappa_j z}. \quad (2.15)$$

Solutions existing for both $\pm \kappa_j$, while the field components is related by

$$E_{xj} = \frac{\pm i \kappa_j}{\omega \epsilon_0 \tilde{\epsilon}_j} H_{yj}, \quad (2.16)$$

$$E_{zj} = \frac{-k_x}{\omega \epsilon_0 \tilde{\epsilon}_j} H_{yj}. \quad (2.17)$$

The subscript j indexing the particular layer, while k_x is the in-plane propagation constant, conserved across the interfaces, and κ_j is the out-of-plane propagation constant given by

$$\kappa_j = \sqrt{k_x^2 - k_0^2 \tilde{\epsilon}_j}. \quad (2.18)$$

2.2 FREE PROPAGATING LIGHT

Consider initially the wave solution, given by equation 2.14-2.18, for a purely dielectric environment, described by the permittivity ϵ_d (figure 2.1a). Achieving a non-divergent solution imposes the condition

$k_x < k_0\sqrt{\epsilon_d}$, such that $\kappa_d = ik_z$ is complex. The wave thereby exhibits oscillatory behavior along z , propagating in the direction of the wave vector $\mathbf{k} = (k_x, 0, k_z)$, as phase is accumulated along both the x and z -axis. The field distribution of such a plane electromagnetic wave, propagating in free space, is sketched in figure 2.1a, for which the dispersion relation is given by

$$\frac{\omega}{c}\sqrt{\epsilon_d} = |\mathbf{k}| = \sqrt{k_x^2 + k_z^2}. \quad (2.19)$$

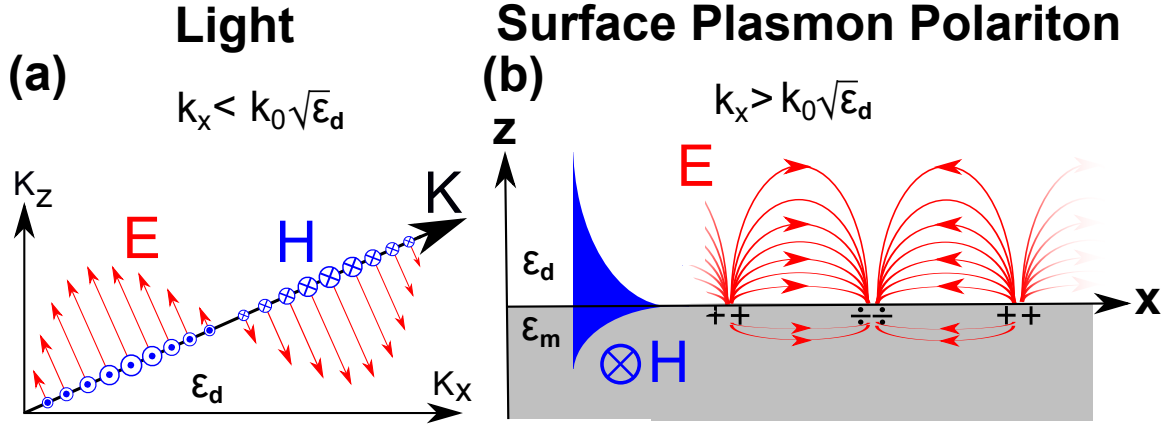


Figure 2.1: Sketch of optical modes (a) Light propagating in a dielectric environment. (b) Surface plasmon polariton propagating along a dielectric-metal interface.

2.3 SURFACE PLASMON POLARITON

Now consider the wave solution confined to a metal-dielectric interface situated at $z=0$ (figure 2.1b). Subscript $j = d, m$ now indexing the dielectric- and metallic half space respectively. For exponential confinement to the interface κ_d, κ_m must be real, thereby imposing the condition $k_x > k_0\sqrt{\epsilon_d}$ on equation 2.18. The condition of a non-divergent solution sets the sign of equation 2.14-2.16, such that $-\kappa_d$ is retained for the dielectric half-space and $+\kappa_m$ for the metallic. Finally, the mode solution must satisfy boundary conditions across the interface, that is continuity of the in-plane electric- and magnetic fields, $E_{xd} = E_{xm}, H_{yd} = H_{ym}$. Applying these boundary conditions to equation 2.16, lead to the interface condition for supporting an exponentially confined electromagnetic mode, known as the surface plasmon polariton (SPP)

$$-\frac{\kappa_d}{\epsilon_d} = \frac{\kappa_m}{\epsilon_m}. \quad (2.20)$$

SPP modes are thus supported by interfaces at which the sign of permittivity changes across the interface, which is the case for a dielectric-metal interface. Noble metals, such as gold and silver, having a negative permittivity in the visible and infrared region. Substituting equation 2.18 into 2.20, we write the single interface SPP dispersion relation in the typical form

$$k_{SPP} = \frac{\omega}{c} \sqrt{\frac{\epsilon_d \epsilon_m}{\epsilon_d + \epsilon_m}}, \quad (2.21)$$

$k_{SPP} = k_x$ being the propagation constant of the SPP. Figure 2.1b illustrates the field distribution of the SPP propagating along a dielectric-metal interface. The SPP wave behavior consists of free electron density oscillations in the metal coupled to the electromagnetic field. From an energy point-of-view, the plasmonic wave results from the oscillatory exchange of energy between the kinetic energy of the electrons and the electromagnetic field, allowing for confinement of the plasmonic mode[21]. In contrast, for free propagating light, oscillatory energy exchange purely occur between the electric and magnetic field, leaving the confinement of such a mode diffraction limited to dimensions of $\sim \lambda_0 / (2\sqrt{\epsilon_d})$. Thus, while plasmonic modes may be confined below the diffraction limit, inherent to the confinement is the ohmic loss associated with free electron density oscillations. The SPP dispersion relation given in equation 2.21 is plotted in figure 2.2 for a SiO₂-Au or SiO₂-Ag interface, together with the dispersion for light given in equation 2.19. The surface confinement of the SPP mode condition the wave vector to always be larger than that of light $\text{Re}(k_{spp}) > k_0\sqrt{\epsilon_d}$. In the case of a lossless metal k_{spp} would go to infinity at the surface plasmon frequency ω_{sp} , indicated with a dashed line, for which the denominator in equation 2.21 is zero, $\epsilon_m(\omega_{sp}) + \epsilon_d = 0$. However for real metals ohmic damping restrict k_{spp} to a finite value. For the respective metals SPP modes are only supported in the frequency region $\omega < \omega_{sp}$.

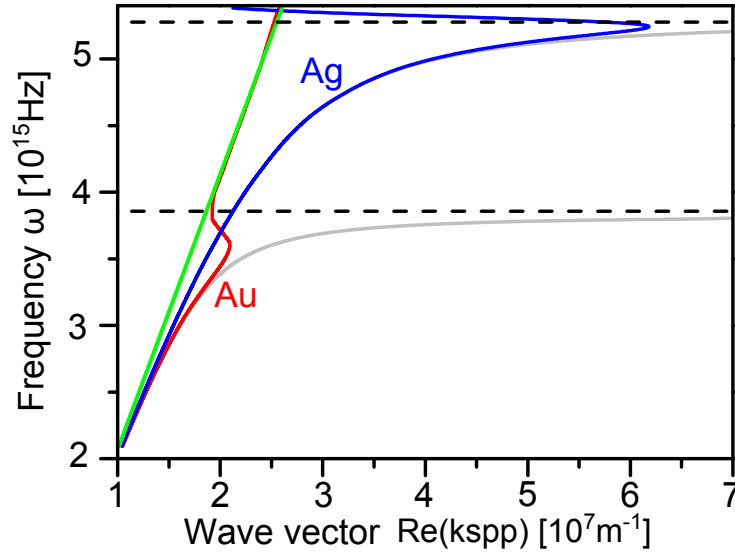


Figure 2.2: Dispersion relation for light propagating in SiO₂ (green) and SPP plotted for a SiO₂-Au interface (red) and SiO₂-Ag interface (blue) using Johnson-Christy data[22]. Grey curves give the corresponding lossless case for which the imaginary part of the permittivity have been set to zero, $\text{Im}(\epsilon_m) = 0$. The surface plasmon frequency is indicated with a black dashed line.

In the interest of quantifying confinement and loss of plasmonic modes it is convenient to introduce the effective index and propagation length of the particular mode, in terms of the real and imaginary part of the propagation constant

$$N_{eff} = \frac{Re(k_{SPP})}{k_0} = \frac{\lambda_0}{\lambda_{SPP}}, \quad (2.22)$$

$$L_p = \frac{1}{2Im(k_{SPP})}. \quad (2.23)$$

Effective index (N_{eff}) being the factor by which the SPP wavelength (λ_{SPP}) is reduced relative to light in vacuum, analogue to the refractive index for free propagating light. L_p being the propagation length over which the energy of the plasmonic mode is decreased to a factor $1/e$, by ohmic loss.

2.4 TWO INTERFACE PLASMONIC MODES

Several plasmonic modes relevant for this thesis is supported by a dual interface configuration, consisting of 3 layers. The plasmonic dispersion relation for such a configuration may be derived by applying boundary conditions to wave solutions of the individual layers, given by equation 2.14-2.17[20]. For brevity, we merely provide the final result in terms of the dispersion relation for the 3-layer system

$$e^{-2\kappa_1 w} \left(\frac{\kappa_1}{\varepsilon_1} - \frac{\kappa_2}{\varepsilon_2} \right) \left(\frac{\kappa_1}{\varepsilon_1} - \frac{\kappa_3}{\varepsilon_3} \right) - \left(\frac{\kappa_1}{\varepsilon_1} + \frac{\kappa_2}{\varepsilon_2} \right) \left(\frac{\kappa_1}{\varepsilon_1} + \frac{\kappa_3}{\varepsilon_3} \right) = 0, \quad (2.24)$$

w being the thickness of the intermediate spacer layer, for $j=1,2,3$ indexing the particular layer as indicated in figure 2.3a. For large spacer layer thickness $w \rightarrow \infty$, equation 2.24 reduces to the single interface SPP dispersion relation for the top and bottom interface, given by equation 2.20. In the case of two metal-dielectric interfaces, the supported SPP modes couple for small w , forming new plasmonic modes. However, the 3 layer dispersion relation (equation 2.24), places no constraint on the material composition and so confined modes may be found for any 3-layer material composition[23]. We here consider two confined plasmonic modes, relevant for this thesis (figure 2.3). The gap surface plasmon (GSP) mode supported by a metal-dielectric-metal layer composition, is illustrated in figure 2.3c. The configuration allow inprinciple for infinite mode confinement with decreasing w [24], while the electric field is preferentially confined to the dielectric layer oriented almost entirely out-of-plane in a capacitor-like fashion. Figure 2.3e illustrate the increasing mode confinement interms of the increasing effective index, with decreasing w . Increased confinement of plasmonic modes is commonly complemented by increasing ohmic losses as illustrated in figure 2.3f, by a decreasing propagation length. The confinement-to-loss trade-off is skewed towards lower losses for the 2nd mode supported by a metal-low index-high index dielectric layer composition, as illustrated in figure 2.3d. The mode coined conductor-gap-dielectric (CGD) mode [23], exhibits increasing confinement with decreasing w (figure 2.3e), with a cut-off at larger w for $N_{eff} \leq n_{tio2}$ as the mode starts leaking into the high index dielectric of refractive index n_{tio2} . In section 8.1 we study the photoluminescence of gold from resonant GSP antenna structures. In section 8.4 we exploit the low losses of CGD mode to realize an efficient antenna for directive spontaneous emission from NV-centers.

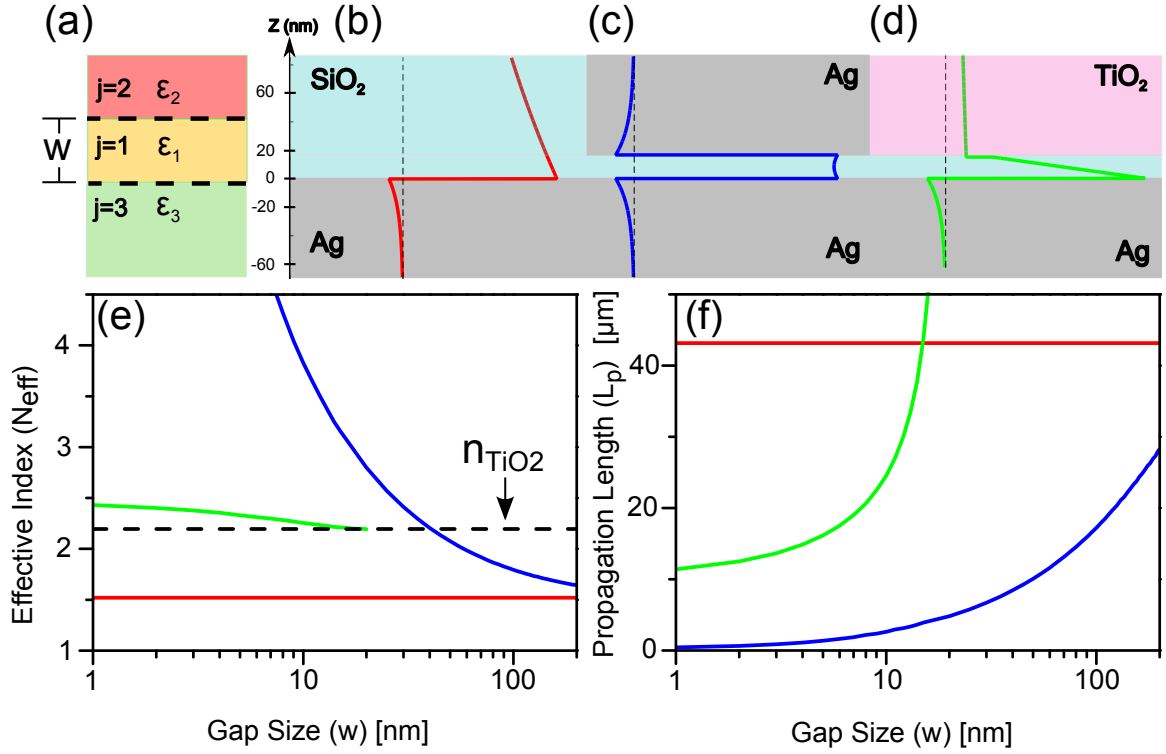


Figure 2.3: Plasmonic modes supported by a 3-layer structure. (a) subscript convention of 3-layer structure, w being the spacer thickness of the intermediate layer. Electric field z -component of plasmonic modes: (b) SPP (red) at SiO₂-Ag interface, (c) GSP mode (blue) supported by Ag-SiO₂-Ag configuration and (d) CGD mode (green) supported by a TiO₂-SiO₂-Ag film configuration. Modes are calculated for a 15 nm gap and 700 nm vacuum wavelength, using linear interpolation of Johnson-Christy data [22], SiO₂ refractive index of $n_{\text{SiO}_2} = 1.45$ and $n_{\text{TiO}_2} = 2.19$ for TiO₂. Color-coded (e) effective index and (f) propagation length of respective modes, given in b-d, as function of gap size.

2.5 LOCALIZED SURFACE PLASMON MODES

The illumination of a metal nanoparticle may lead to free electron density oscillations, known as a localized surface plasmon (LSP). The spectral position (ω_{LSP}) of the LSP mode depend on particle shape [25] and dielectric response of the metal and dielectric environment. For subwavelength spherical particles ω_{LSP} is given by the Frölich condition $\text{Re}(\epsilon_m) = -2\epsilon_d$. The excitation of the LSP mode, by particle illumination, lead to resonant polarization of the particle and correspondingly enhancement of the local electric field around the particle. Figure 2.4 illustrate the local field enhancement for a gold sphere illuminated on resonance by a plane wave. For metal particles much smaller than the wavelength of light, the driving light field may be approximated to be quasi-static. The charge distribution of the excited LSP mode in this case takes a dipolar form (figure 2.4b). The damped harmonic oscillations of LSP mode, is intuitively understood by the analogy to a mass-spring-damper system, an analogy also extending to the coupled response of two particles, examined in section 8.3 [26, 27]. The mass of the free electron cloud oscillate as it experiences a restoring force, from the coulomb attraction to the bared ion cores. Oscillations of the electron "mass" is damped by ohmic loss and scattering of light to free space. Such a linearly damped harmonically oscillating system is well known to have a Lorentzian frequency response, as illustrated in figure 2.4c for the scattering cross section of the gold sphere, at various driving frequencies of the incident light.

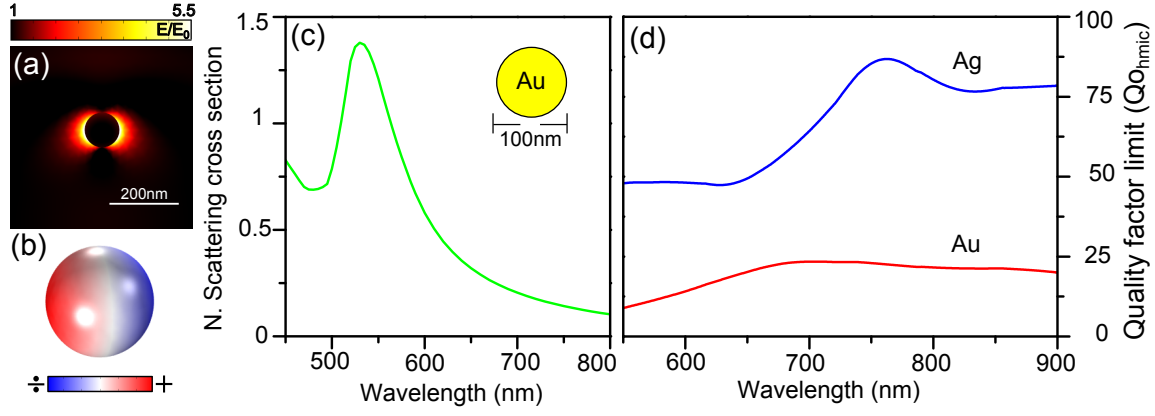


Figure 2.4: Modelling example of LSP mode supported by a 100 nm gold sphere in air. (a) Field enhancement for gold sphere excited by plane wave at the LSP resonance of 530 nm. (b) Corresponding dipolar surface charge distribution of the LSP mode. (c) Scattering cross section of sphere, normalized to the geometrical cross section, illustrating the resonant LSP response. (d) Loss quality factor term Q_{ohmic} , calculated from a linear interpolation Johnson-Christy data [22] for gold (red) and silver (blue). The data was smoothed by a 100 nm moving average filter, to avoid discontinuities related to linear data interpolation.

The width of the spectral response is set by the LSP damping rate γ^{LSP} or may be characterized by the quality factor (Q) defined as 2π times the energy stored in the system wrt. energy dissipated pr. oscillation cycle [28]

$$\Delta\omega_{FWHM} = \gamma^{LSP} = \frac{\omega_{LSP}}{Q}. \quad (2.25)$$

Here $\Delta\omega_{FWHM}$ is the full width half maximum. To quantify the influence of non-radiative and radiative LSP damping, quality factor and damping rate is split into ohmic loss and scattering contributions indexed ohmic or sc respectively

$$\gamma^{LSP} = \gamma_{Ohmic}^{LSP} + \gamma_{SC}^{LSP} = \omega_{LSP} \left(\frac{1}{Q_{ohmic}} + \frac{1}{Q_{SC}} \right). \quad (2.26)$$

The radiation efficiency (η_{LSP}) by which LSP energy is radiated to free space is than given by

$$\eta_{LSP} = \frac{\gamma_{sc}^{LSP}}{\gamma^{LSP}} = \frac{Q_{Ohmic}}{Q_{ohmic} + Q_{sc}}. \quad (2.27)$$

The quality factor and radiation efficiency of the LSP mode is ultimately limited by ohmic losses. In the quasistatic limit the ohmic damping is determined purely by dielectric response of the metal, with the quality factor contribution $Q_{ohmic} = \omega \frac{\partial}{\partial \omega} \text{Re}(\epsilon_m) / (2\text{Im}(\epsilon_m))$ [29]. Figure 2.4d illustrate the quality factor limit Q_{ohmic} for gold and silver over the typical quantum emitter emission range. The limit correspond to zero radiation efficiency. High radiation efficiency is possible for low quality factor dominated by radiation loss, $Q_{ohmic} \gg Q_{sc}$.

3

Spontaneous emission in a homogeneous environment

This chapter describes the process of spontaneous emission in a homogeneous environment. Considering spontaneous emission under such conditions is instructive as it is commonly used as a reference when evaluating emission in an inhomogeneous environment. Spontaneous emission is described in terms of a semiclassical treatment. Light is in this case described classically in terms of a continuous electromagnetic vector field, while the quantum emitter is treated quantum mechanically in terms of a 2-level system, characterized by the level energies E_j and associated stationary states $\psi_j(\mathbf{r}, t) = \psi_j(\mathbf{r}) e^{-iE_j t/\hbar}$, $j = g, e$ indexing the ground and excited state respectively. For a homogeneous environment, wave solutions exist in terms of plane waves, as introduced in section 2.2. Initially, we consider the interaction of the 2-level system, with a single plane wave propagating along the x axis of a Cartesian coordinate system. The electric field of the plane wave is given by $\mathbf{E}(\mathbf{r}, t) = \mathbf{E}_{k,\zeta} \cos(kx - \omega t)$, $\zeta = 1, 2$ indexing one of the two polarization states, illustrated in figure 3.1.

The time evolution of the 2-level system is described by the time dependent Schrödinger equation[30]

$$\hat{H}\Psi(\mathbf{r}, t) = i\hbar \frac{\partial \Psi(\mathbf{r}, t)}{\partial t}, \quad (3.1)$$

\hat{H} being the Hamiltonian operator, giving the energy of the system, while the wavefunction Ψ describes the physical state of the 2-level system. In the presence of a dependent electromagnetic field, \hat{H} is time dependent, and so equation 3.1 no longer has stationary state solutions. Rather, the probability of find-

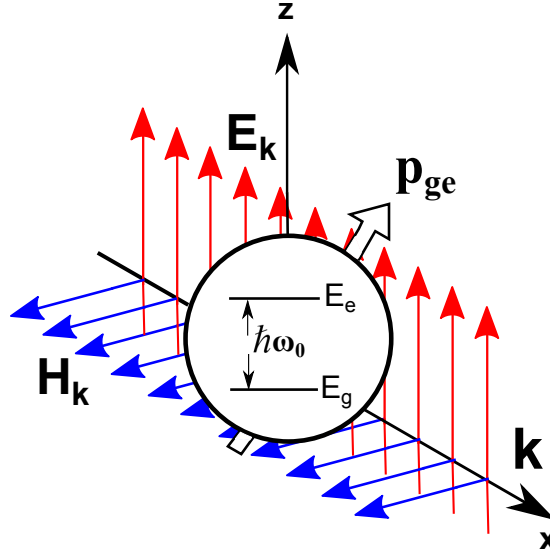


Figure 3.1: Sketch of the interaction of a 2-level system with a plane electromagnetic wave. Optical transitions in the system result from the interaction of the transition dipole moment \mathbf{p}_{ge} with the electric field \mathbf{E}_k (red arrows). \mathbf{H}_k being the magnetic field of the plane wave.

ing the quantum emitter in a particular state varies in time. We here assume that the system is initially in state g or e and the frequency of the incident light is nearly resonant with the transition frequency $\omega_0 = (E_e - E_g) / \hbar$, such that $\omega \approx \omega_0$. The time evolution of Ψ is in this case given by a linear superposition of the stationary states ψ_g and ψ_e ,

$$\Psi(\mathbf{r}, t) = C_g(t) \psi_g(\mathbf{r}) e^{-iE_g t / \hbar} + C_e(t) \psi_e(\mathbf{r}) e^{-iE_e t / \hbar}. \quad (3.2)$$

The probability of finding the system in the ground or excited state is given by $\rho_j = |C_j|^2$, also known as the state population. As the wavelength of the incident light is typically much longer than the dimensions of emitter ($d_{emitter}$), the electric field can be approximated to be constant across the emitter. Neglecting the spatial dependence of the electric field is known as the dipole approximation, relying on the assumption $1 \gg kd_{emitter}$. In the presence of a constant electric field with harmonic time dependence, the Hamiltonian acquires an additional term corresponding to the potential energy of an electric dipole in a static electric field. The electric dipole moment $\mathbf{p} = -e \sum_{electrons} \mathbf{r}_e$, resulting from the distribution of electrons, located at positions \mathbf{r}_e in the quantum emitter system. \hat{H} is in this case given by

$$\hat{H} = \hat{H}_{emitter} + \mathbf{p} \cdot \mathbf{E}_{k,\zeta} \cos(\omega t), \quad (3.3)$$

$\hat{H}_{emitter}$ describing the kinetic and potential energy of the system constituents, in the absence of light. In the interest of examining the transition rate between state g and e , we look for solutions of $C_j(t)$, by inserting equation 3.2 and 3.3 in 3.1 and projecting onto the stationary states by applying $\langle \psi_g |$ or $\langle \psi_e |$, given in the Dirac notation,

$$\frac{\partial C_g(t)}{\partial t} = -i \left(\frac{\mathbf{p}_{ge} \cdot \mathbf{E}_{k,\zeta}}{\hbar} \right) e^{-i\omega_0 t} \cos(\omega t) C_e(t), \quad (3.4)$$

$$\frac{\partial C_e(t)}{\partial t} = -i \left(\frac{\mathbf{p}_{ge} \cdot \mathbf{E}_{k,\zeta}}{\hbar} \right) e^{i\omega_0 t} \cos(\omega t) C_g(t). \quad (3.5)$$

For which $\mathbf{p}_{ge} = \langle \psi_g | \mathbf{p} | \psi_e \rangle$ is the transition dipole moment, characterising the optical transition strength in terms of internal system parameters. Equation 3.4 and 3.5 are difficult to solve in general, however, for a linear optical process it is sufficient to estimate the response around $t = 0$ by substituting initial conditions to the right-hand side. We here consider an emission process by initializing the system in the excited state at $t = 0$, by applying the initial conditions $C_e(0) = 1$; $C_g(0) = 0$. Using the assumption of near resonance incident light $\omega \approx \omega_0$, the probability of finding the system in the ground state after a time t , is determined by a time integration of equation 3.4,

$$\rho_g(t) = |C_g(t)|^2 = \left| \frac{\mathbf{p}_{ge} \cdot \mathbf{E}_{k,\zeta}}{\hbar} \right|^2 \left(\frac{\sin\left(\frac{1}{2}(\omega - \omega_0)t\right)}{\omega - \omega_0} \right)^2. \quad (3.6)$$

Typically, the light-matter interaction occurs over many optical cycles, that is $\omega_0 t \gg 1$. Further, assuming a long enough interaction time such that $(\omega - \omega_0)t \gg 1$, it is appropriate to apply the identity $\frac{2}{\pi} \lim_{t \rightarrow \infty} \sin^2\left(\frac{1}{2}(\omega - \omega_0)t\right) / ((\omega - \omega_0)^2 t) = \delta(\omega - \omega_0)$ to simplify equation 3.6. The transition rate may in this case be written as the probability of finding the system in the ground state pr. unit time

$$\gamma_{k,\zeta} = \frac{\rho_g(t)}{t} = \frac{\pi}{2\hbar^2} |\mathbf{p}_{ge} \cdot \mathbf{E}_{k,\zeta}|^2 \delta(\omega - \omega_0). \quad (3.7)$$

Equation 3.7 gives the transition rate for a stimulated emission process. In this process, the 2-level system decays by coherent transfer of energy into the incident plane wave mode k , the transition rate scaling with the square of the electric field. Consider now the transition rate in the absence of incident light. Based on a quantum mechanical treatment of the electromagnetic field, it can be shown in vacuum that each plane wave mode carries a zero-point energy of $\hbar\omega/2$ [31]. That is $\hbar\omega/2 = \frac{1}{2} \int \epsilon_0 \epsilon_d |\mathbf{E}_{k,\zeta}^{vac}|^2 + \mu_0 |H_{k,\zeta}^{vac}|^2 dV_q$, V_q being the quantization volume, while the superscript index the vacuum field. As magnetic and electric field energy are equal for a plane wave, the vacuum field strength is given by

$$|\mathbf{E}_{k,\zeta}^{vac}| = \sqrt{\frac{\hbar\omega}{2\epsilon_0 \epsilon_d V_q}}. \quad (3.8)$$

In the absence of an incident light beam, a decay rate into mode k thereby still exists, resulting from the non-zero field strength of the vacuum mode. This transition from the excited- to the ground state upon by excitation of mode k , is known as spontaneous emission and may be thought of as stimulated emission by the vacuum field, as given by equation 3.7. The total spontaneous decay rate is obtained by

summing the transition rate into all plane wave modes,

$$\gamma = \frac{\pi}{2\hbar^2} \sum_{k,\zeta} |\mathbf{p}_{ge} \cdot \mathbf{E}_{k,\zeta}^{vac}|^2 \delta(\omega - \omega_0). \quad (3.9)$$

Equation 3.9 is Fermi's golden rule for the special case of spontaneous emission, stating that the spontaneous emission rate of a 2-level is the summed transition rate into all available optical modes, satisfying energy conservation. The transition rate into the individual optical modes scaling with the square of the electric field projection on the dipole axis. The resulting emission pattern follows the transition rate into the various plane wave modes, scaling with $|\mathbf{p}_{ge} \cdot \mathbf{E}_{k,\zeta}|^2 \propto \sin^2(\theta)$, θ being the angle of the \mathbf{k} -vector wrt. the dipole axis. Figure 3.2 shows the well known dipole emission pattern following the $\sin^2(\theta)$ dependence.

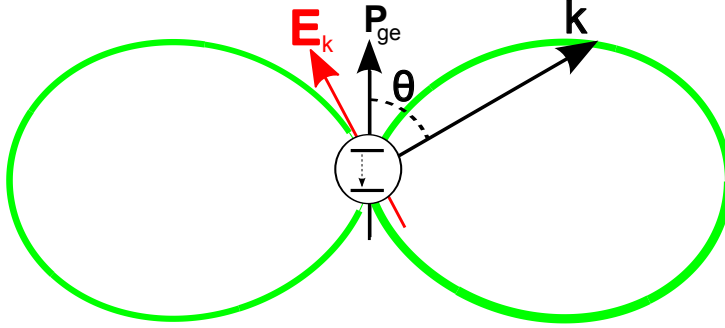


Figure 3.2: Emission pattern of a dipole in a homogeneous environment (green) for \mathbf{p}_{ge} defining the dipole axis. The emission pattern may be understood as emission into the various plane wave \mathbf{k} -modes, with the transition rate scaling as $|\mathbf{p}_{ge} \cdot \mathbf{E}_k|^2 \propto \sin^2(\theta)$.

The total spontaneous decay rate in a homogeneous environment with a permittivity ε_d is given by the summed decay rate into all plane wave \mathbf{k} -modes and is given by [32]

$$\gamma_0 n_d = \frac{|\mathbf{p}_{ge}|^2 \omega_0^3}{3\pi \varepsilon_0 \hbar c^3} n_d. \quad (3.10)$$

γ_0 being the spontaneous decay rate in vacuum, defined by the transition dipole moment and energy of the particular transition, while the spontaneous decay rate scales linearly with the refractive index of the environment $n_d = \sqrt{\varepsilon_d}$. Equation 3.10 sets the photon rate limit, experimentally detectable from a single quantum emitter typically on the order of ~ 100 MHz. However, for realistic experiments the photon rate is compromised by a non-unity quantum yield and shelving in a meta-stable state. Further, the non-directional emission pattern inherent to dipole emission in a homogeneous environment is highly problematic for photon collection with an objective. In the preceding chapter, we consider how these emission parameters may be improved in an inhomogeneous environment.

4

Spontaneous emission in an inhomogeneous environment

In this chapter we consider the process of spontaneous emission in an inhomogeneous environment. It is in this case convenient to consider spontaneous emission in a classical picture. The quantum emitter is in this case described in terms of a harmonically oscillating electric point dipole or current source.

In a linear medium on the assumption of harmonic time dependence, the power dissipated in a volume V is given by [33]

$$P = \oint_V \langle \mathbf{S} \rangle \cdot \mathbf{n} da = -\frac{1}{2} \int \text{Re} (\mathbf{j}^* \cdot \mathbf{E}) dV. \quad (4.1)$$

For which $\langle \mathbf{S} \rangle$ is the time average Poyntings vector, while \mathbf{n} is the unit vector normal to the surface enclosing the volume V . The volume may contain both loss and driving terms and so \mathbf{j} represents both source and conduction currents. Considering a volume containing only the quantum emitter described by dipole source $\mathbf{j}_s(\mathbf{r}) = -i\omega \mathbf{p} \delta(\mathbf{r} - \mathbf{r}_0)$, located at \mathbf{r}_0 , the power radiated by the electric dipole is given by

$$P = \frac{\omega}{2} \text{Im} (\mathbf{p}^* \cdot \mathbf{E}(\mathbf{r}_0)). \quad (4.2)$$

$\mathbf{E}(\mathbf{r}_0)$ being the electric field generated by the dipole at the dipole position ¹. In the classical picture

¹For analytical purposes the electric field, setup by the dipole, is typically expressed in terms of the dyadic Green function, $\vec{\mathbf{G}}$ in terms of $\mathbf{E}(\mathbf{r}) = \omega^2 \mu_0 \vec{\mathbf{G}} \mathbf{p}$. However for the present purpose of finite element modelling $\vec{\mathbf{G}}$ is not necessary.

the electric field acts as a driving force on the oscillating dipole. The out-of-phase driving field dampens dipole oscillation by radiation of dipole power. Scattering in an inhomogeneous environment, gives rise to an additional driving term (\mathbf{E}_{sc}) for radiation returning to the emitter, upon interaction with the environment. The altered driving field, $\mathbf{E} = \mathbf{E}_0 + \mathbf{E}_{sc}$, thereby changes the rate at which power is radiated by the dipole. \mathbf{E}_0 being the driving field, giving rise to a power P_0 radiated in vacuum. Equation 4.1 and 4.2 may easily be implemented into finite element solvers, to evaluate the power radiated by an electric dipole in an inhomogeneous environment or the power dissipated in nearby metal nano particles, by defining appropriate integrating surfaces. The changed dipole power is most conveniently evaluated with respect to the power radiated in vacuum, yielding a parameter independent of the dipole moment. Noting that the spontaneous decay rate is obtained by dividing with the energy of a photon ² $\gamma = P/\hbar\omega$ the spontaneous decay rate enhancement, relative to vacuum, may be evaluated by

$$\frac{\gamma}{\gamma_0} = \frac{P}{P_0}. \quad (4.3)$$

Equation 4.1-4.3 sets the foundation for evaluating the spontaneous decay rate enhancement in an inhomogeneous environment, by finite element modelling.

4.1 DIPOLE EMISSION NEAR A METALLIC INTERFACE

For a more intuitive understanding of spontaneous emission near metal, we consider the simple case of dipole emission in close proximity to a metal-dielectric interface. The situation was experimentally examined by Drexhage in 1970[34], while the experimental results were later analytically reproduced by the work of among others Chance et. al. [35] and Ford & Weber[36]. We here consider the model derived by Ford & Weber³. With a strong analogy to the k-mode sum, as it appears in Fermi's golden rule in equation 3.9, the model is based on a Fourier decomposition $\mathbf{E}(\mathbf{r}) = \int \mathbf{E}_{\mathbf{k}} e^{i\mathbf{k} \cdot \mathbf{r}} d\mathbf{k}$ of the dipole field in equation 4.2. The dipole power with respect to vacuum is given in equation 4.4 as a sum over the in-plane wave-vector component k_x of the respective k-modes,

$$\frac{P}{P_0} = \frac{\omega}{2\varepsilon_d P_0} \int_0^\infty \text{Re} \left\{ p_\perp^2 \left(\frac{k_x^3}{i\kappa_d} (1 + r_p e^{i\phi}) \right) + p_\parallel^2 \left(\frac{k_x^3 - \kappa_d^2}{2i\kappa_d} (1 + r_s e^{i\phi}) - \frac{k_x \kappa_d}{2i} (1 - r_p e^{i\phi}) \right) \right\} dk_x, \quad (4.4)$$

$$\phi = 2i\kappa_d z_p, \quad (4.5)$$

$$r_p = \frac{\kappa_d \varepsilon_m - \kappa_m \varepsilon_d}{\kappa_d \varepsilon_m + \kappa_m \varepsilon_d}, \quad (4.6)$$

$$r_s = \frac{\kappa_d - \kappa_m}{\kappa_d + \kappa_m}. \quad (4.7)$$

Here r_p and r_s are the Fresnel reflection coefficients for p- and s-polarized light respectively, z_p being

²Note the classical dipole moment \mathbf{p} is not equal to the quantum mechanical transition dipole moment \mathbf{p}_{ge} . The classical expression for P_0 equates to γ_0 upon the conversion $2|\mathbf{p}_{ge}| \rightarrow |\mathbf{p}|$

³Note that the model appears in Gauss units, while the remainder of the thesis is in SI units

the dipole separation from the air-silver interface and ϕ the round trip phase accumulated by radiation reflected at the interface and returning to the emitter. p_{\parallel}, p_{\perp} being the in-plane and out-of-plane dipole component respectively.

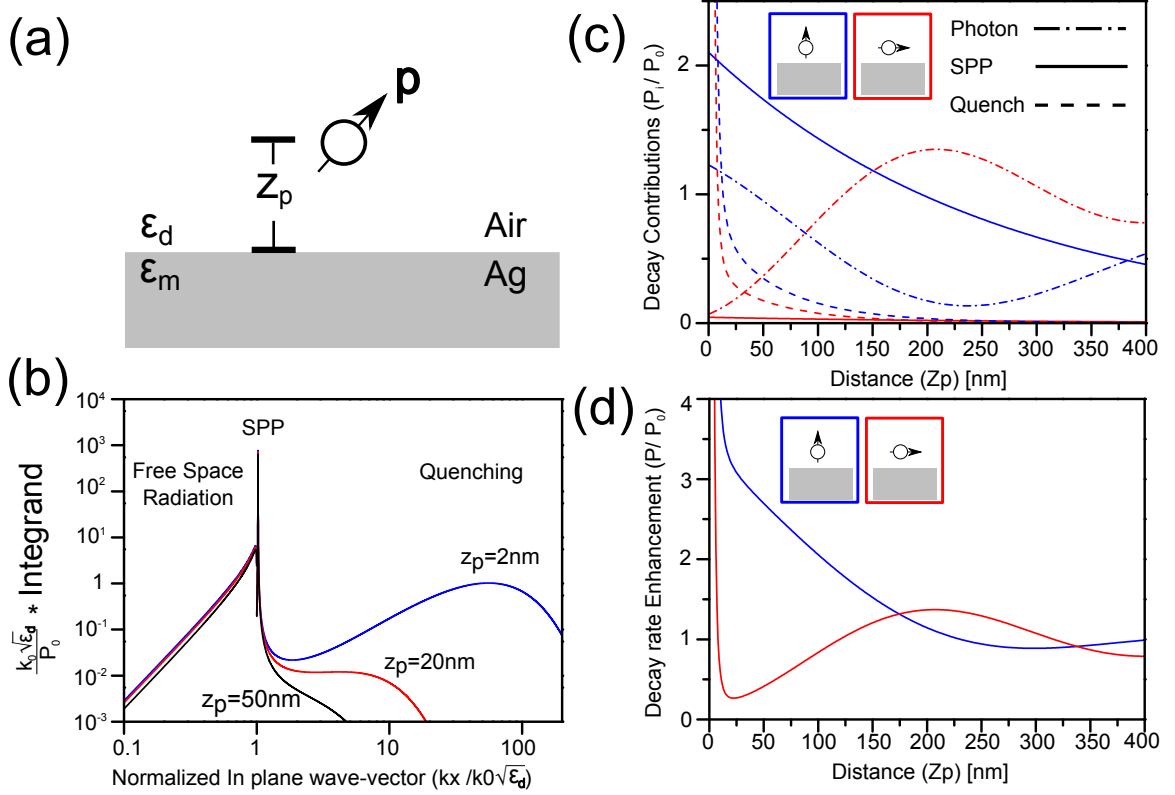


Figure 4.1: Dipole emission above an air-ag interface, analytically modelled at a vacuum wavelength of 700 nm using Johnson-Christy data [22]. (a) Sketch of system, z_p gives the dipole-interface separation. (b) Power radiated by vertical dipole decomposed into contributions of the respective k -vector modes for $z_p = 50$ nm (black), $z_p = 20$ nm (red), $z_p = 2$ nm (blue). (c) Normalized power radiated by vertical (blue) or horizontal (red) dipole, decomposed into free space radiation (dash-dot), SPP (solid) or quenching (dashed). (d) Power radiated by vertical (blue) or horizontal (red) dipole with respect to vacuum.

Initially we consider the power radiated into the respective k -modes by plotting the integrand of equation 4.4 as function of k_x (figure 4.1b). As the dipole approaches the metal interface, dipole radiation accesses modes of increasingly larger k . It is instructive to split the dipole radiation into three regions. The region $k_x \leq k_0 \sqrt{\epsilon_d}$ may be assigned to free space radiation as introduced in section 2.2. The pole in r_p (equation 4.6) gives rise to a peaked region corresponding to radiation into SPP that is $k_x = k_{SPP}$ (see equation 2.20), while the region of large k_x is assigned to non-radiative quenching. The power radiated by a dipole near a metallic interface thus contains contributions from three decay paths, radiation to free space (P_{Photon}), SPP (P_{SPP}) and quenching (P_{Quench}), each term dependent on the dipole position and orientation. The total power dissipated by the dipole is thereby given by

$$P(z_p, \mathbf{p}) = P_{Photon}(z_p, \mathbf{p}) + P_{SPP}(z_p, \mathbf{p}) + P_{Quench}(z_p, \mathbf{p}). \quad (4.8)$$

Figure 4.1c illustrates the position dependent decay path contributions for a vertical or horizontal dipole

respectfully. At small metal-dipole separations ($z_p < 10 \text{ nm}$) quenching is the dominating decay path, as emission into large k-modes dominates. At intermediate separation ($10 \text{ nm} < z_p < 200 \text{ nm}$) SPP is the dominating decay path for a vertical dipole having purely p-polarized radiation, while a horizontal dipole radiates poorly into SPP as the SPP electric field is preferentially out-of-plane, orthogonal to the dipole orientation. Dipole radiation to free space exhibits oscillatory behavior with z_p due to interference, tending to the power P_0 radiated in a homogeneous environment for large z_p . The suppression of free space radiation for a horizontal dipole at small z_p is intuitively understood as a mirrored dipole charge distribution induced in the metal. The anti-phase oscillations of the dipole and mirror charges effectively cancel radiation to free space by destructive interference. Figure 4.1d gives the total power radiated by the dipole, relative to vacuum. As the dipole accesses the additional decay paths of SPP and quenching, related to the metallic interface, the radiation of dipole power is accelerated relative to vacuum $P > P_0$. However, in an inhomogeneous environment, dipole radiation may also be suppressed $P < P_0$, as illustrated here for a horizontal dipole close to the metal interface. The distance dependent trend of decay into photons at large separation, SPP at intermediate and quenching at small, has also been demonstrated for a metal particle attached to an AFM tip [37, 38]. While Ford and Weber attribute quenching to electron scattering and electron-hole excitation, quenching near nano metal particles further arises from emission into higher order ('dark') localized surface plasmon modes [39].

4.2 SPONTANEOUS EMISSION NEAR METALLIC NANO ANTENNAS

Having established the distance dependent decay rate channels available to a quantum emitter in close proximity to a metal interface, we move on to consider spontaneous emission from a quantum emitter in close proximity to a metallic nano antenna. The nano antenna may be considered as a metallic nano particle supporting a LSP mode, introduced in section 2.5. As previously described in section 2.5, the antenna may concentrate power in the near-field, when the LSP mode is excited by an external light source such as a pump laser. Further the antenna will radiate energy stored in the LSP mode to the far-field with an antenna efficiency given by equation 2.27. The particular antenna radiation pattern depends on the particular antenna geometry [40, 41]. In the following we consider how the antenna influences the process of excitation and subsequent spontaneous emission of a quantum emitter positioned in close proximity to the antenna. In the limit of weak pumping, the rate (γ_{ex}) at which the quantum emitter is excited scales with the square of the pump field (E_{ex}) projected onto the absorption dipole axis, that is $\gamma_{ex} \propto |\mathbf{p}_{abs} \cdot \mathbf{E}_{ex}|^2$, \mathbf{p}_{abs} being the absorption dipole moment of the quantum emitter [33]. Figure 4.2a illustrates the case of a quantum emitter positioned at \mathbf{r}_0 close to the nano antenna, while being excited by a focused laser at a frequency ω_{ex} . The polarization of the antenna by the pump field, results in a local field enhancement, which enhances the excitation rate of the quantum emitter by a factor

$$\frac{\gamma_{ex}}{\gamma_{ex,0}} = \frac{|\mathbf{p}_{abs} \cdot \mathbf{E}_{ex}(\mathbf{r}_0, \omega_{ex})|^2}{|\mathbf{p}_{abs} \cdot \mathbf{E}_{ex,0}(\mathbf{r}_0, \omega_{ex})|^2}. \quad (4.9)$$

The excitation rate $\gamma_{ex,0}$ and pump field $\mathbf{E}_{ex,0}$ referring to case in which the antenna is absent. The excited quantum emitter subsequently decays spontaneously. While previous sections have considered

an emitter with unity quantum yield, we here expand to the more realistic case of quantum emitter with a non-unity quantum yield. The decay may in this case occur radiatively at a rate γ_r or non-radiatively at a rate γ_{nr} . The total spontaneous rate given $\gamma = \gamma_r + \gamma_{nr}$ with the quantum yield $q_e = \gamma_r/\gamma$. The non-radiative decay being an intrinsic parameter of the quantum emitter, independent of the photonic environment, while the radiative decay rate is determined by the available optical decay paths. Figure 4.2b illustrate the radiative decay paths of a quantum emitter in close proximity of the antenna. The radiative decay rate being the summed contribution of the rate into photons ($\gamma_{photons}$), quenching (γ_{Quench}) and the LSP mode of the antenna (γ_{LSP}). The total decay rate of the quantum emitter is thereby given by

$$\gamma(r_0, \mathbf{p}) = \gamma_{nr} + \gamma_{photon}(r_0, \mathbf{p}) + \gamma_{LSP}(r_0, \mathbf{p}) + \gamma_{Quench}(r_0, \mathbf{p}). \quad (4.10)$$

The radiative decay rate terms depending on the quantum emitter position and dipole orientation, as exemplified in section 4.1. The quantum yield and photon rate of the emission process may be improved by maximizing the decay rate γ_{LSP} to the antenna, thereby increasing the radiative decay rate relative to intrinsic non-radiative decay. As illustrated in figure 4.2b the LSP excitations are subsequently converted to photons with an antenna efficiency given by equation 2.27. Photons radiated by the antenna conform to the antenna radiation pattern, which may be optimized for efficient collection with an objective by appropriate antenna design [42]. Achieving a directional high photon rate, facilitated by the antenna thereby relies on optimizing the decay rate to the antenna, γ_{LSP} . In the interest of sketching out general design principles for optimizing γ_{LSP} , we consider the expression given by Colas de Frances *et. al.* [32] for the decay rate into a single resonant mode, normalized to the decay rate in a homogeneous environment, while assumming unity intrinsic quantum efficiency,

$$\frac{\gamma_{LSP}}{\gamma_0 n_d} = \Gamma_p \frac{|\hat{\mathbf{p}} \cdot \hat{\mathbf{E}}_{LSP}^{vac}(r_0)|^2}{1 + 4Q^2 \left(\frac{\omega_0 - \omega_{LSP}}{\omega_{LSP}} \right)^2}, \quad (4.11)$$

$$\Gamma_p = \frac{3}{4\pi^2} \left(\frac{\lambda_0}{n_d} \right)^3 \frac{Q}{V_q}. \quad (4.12)$$

Where $\hat{\mathbf{p}} = \mathbf{p}/|\mathbf{p}|$ is the dipole moment unity vector associated with emission at the vacuum wavelength $\lambda_0 = 2\pi c/\omega_0$. $\hat{\mathbf{E}}_{LSP}^{vac}(\mathbf{r})$ being the LSP mode distribution of the antenna, normalized to $|\hat{\mathbf{E}}_{LSP}^{vac}(\mathbf{r})| = 1$ at the antinode. Q and V_q represent the quality factor and mode volume associated with the LSP antenna mode⁴. Equation 4.11 consist of two terms. Γ_p is typically known as the Purcell factor associated with the LSP antenna mode and represent the maximal decay rate that may be achieved into the particular antenna mode, normalized to a homogeneous environment. Evidently the Purcell factor may be improved by increased confinement of the particular antenna mode, spectrally (higher Q) and spatially (smaller V_q). While the Q -factor is loss limited in a plasmonic system as illustrated in figure 2.4, the modes may be confined to very small volumes. The second term account for spatial and spectral

⁴The evaluation of V_q for an open, dissipative system such as a metallic nano antenna, require the theory of quasi-normal modes which is beyond the scope of this thesis, while currently being studied by theorists[43, 44]

”mismatch”. The term is maximized by matching the emission wavelength to the antenna resonance $\omega_0 = \omega_{LSP}$. Further the quantum emitter should be positioned at the maximum field amplitude, with the dipole moment aligned to the electric field of the LSP mode. The optimization of Q/V_q is a matter of antenna design. However to experimentally reach the potential of the particular design, techniques for accurate emitter positioning is required. For this purpose a wide range emitter positioning techniques are being explored [45–48]. In the present work, we apply an AFM for emitter positioning, this technique also give us some freedom to align the antenna field with the emitter dipole moment, as demonstrated in section 8.3. It should be noted that beyond optimizing γ_{LSP} , high antenna efficiency and a directive antenna emission pattern is desirable, for achieving a large photon rate at high efficiency. In plasmonic nano antennas maximizing Q may therefore not be desirable as it leads to zero antenna efficiency, see equation 2.27.

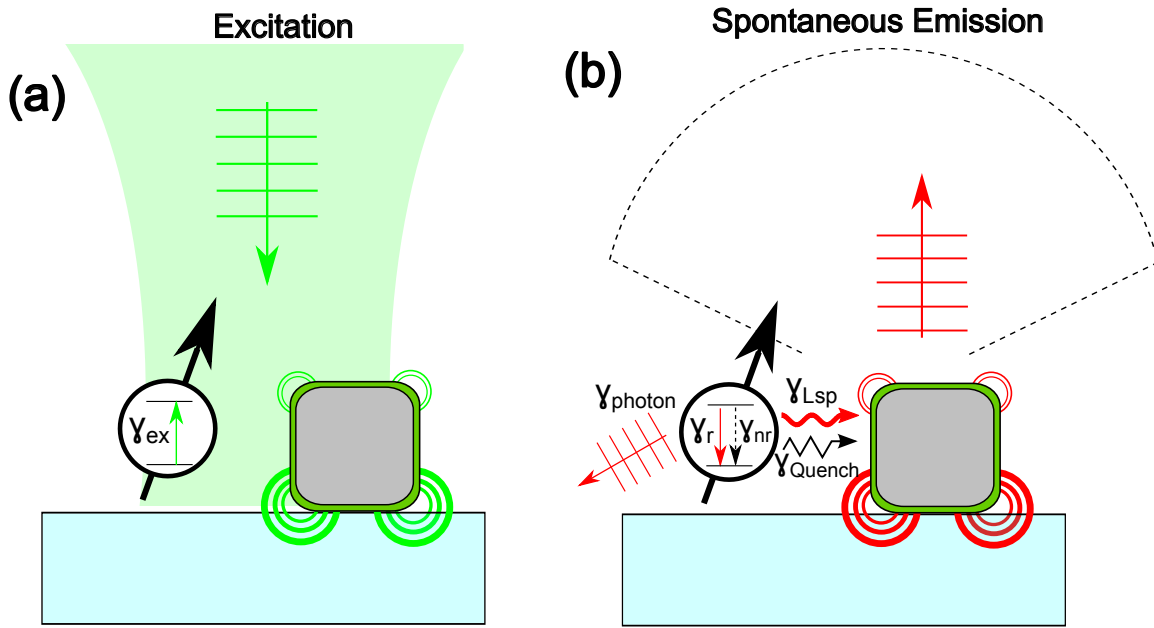


Figure 4.2: Sketch of quantum emitter-antenna interaction in emission process (a) Excitation of quantum emitter, polarization of the metal particle results in local electric field enhancement increasing the excitation rate (b) Spontaneous emission, the radiative decay rate (γ_r) results from the rate contributions into photons (γ_{photon}), the LSP mode (γ_{Lsp}) supported by the metal particle or quenching (γ_{Quench}). The excited LSP mode partially decays by scattering of radiation to free space. Photons directly emitted or scattered into the solid collection angle of the objective (dashed line) is experimentally detected.

5

The nitrogen vacancy color center in diamond

Since its discovery in 1965 the nitrogen-vacancy center (NV-center) has attracted significant attention for its remarkable properties. The exceptionally long electron spin coherence time of the ground spin triplet, at room temperature (up to 1.8 ms Bulk/ $210 \mu\text{s}$ nanodiamond) [49, 50], along with spin dependent inter-system crossing rates for the excited electronic state, has allowed for initialization[51], coherent manipulation[52] and optical read-out [53] of the spin of a single electron in the system with application in quantum information processing. Further the perturbation of ground spin levels in the presence of external electric, magnetic or strain fields has found applications within sensing [5, 54, 55]. Though for the present work, it is the ability of the NV-center to generate single photons at room temperature, in photostable fashion without blinking or bleaching, that is of interest. The following section reviews the process in which single photons are generated from the NV-center at room temperature, with the purpose of providing a footing for an analytic description and interpretation of the experimental results, presented in the preceding chapters. The process becomes increasingly complex once an NV-center is positioned close to a diamond interface, as is the case for an NV-center situated in a nanodiamond. The chapter therefore initially considers, the more wellbehaved situation of a NV-center in bulk diamond, for which most fundamental studies have been performed. The chapter then moves on to consider changes of the emission properties, once the NV-center is positioned in a nanodiamond.

5.1 THE NITROGEN VACANCY CENTER IN BULK DIAMOND

The range of impurities in diamond is as multifaceted as the color palette they give rise to. The most abundant impurity in natural diamond is nitrogen, causing a yellow hue for $\sim 97\%$ of all natural diamonds classified as type I diamond, with nitrogen contents of 0.3-0.05%. Much more rare in nature is type II diamond with a very low nitrogen content ($< 0.05\%$), deriving its color from more exotic impu-

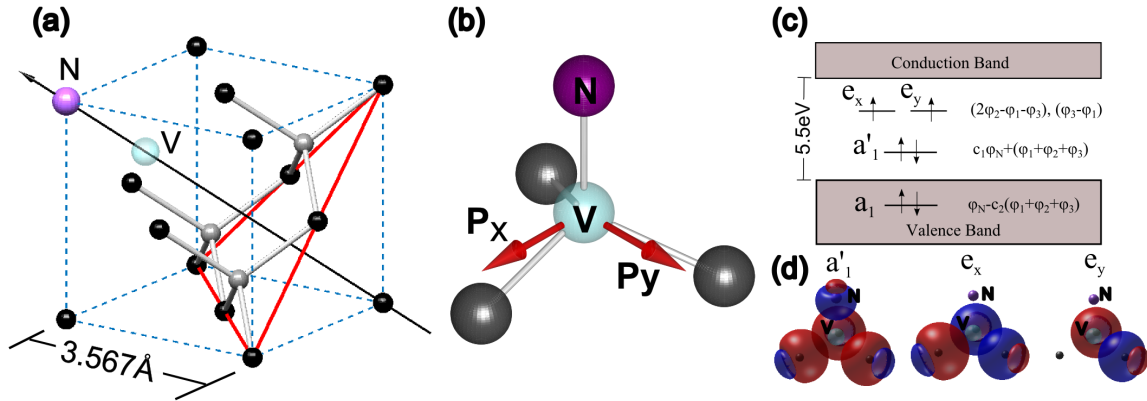


Figure 5.1: (a) Unit cell of the diamond lattice, with substitutional nitrogen-vacancy pair forming the NV-center located along the $[111]$ crystal axis. (b) The NV-center, red arrows indicate the orientation of the transition dipole moments, facilitating absorption and spontaneous emission of light by electron transition between molecular orbitals $p_x : a'_1 \leftrightarrow e_x$; $p_y : a'_1 \leftrightarrow e_y$. (c) Energy hierarchy of molecular orbitals of the NV-center wrt. the diamond band gap. Arrows indicate a possible electron spin configuration of the negatively charged NV-center in the ground state. (d) Isosurface sketch of the NV-center molecular orbitals in diamond bandgap constructed from sp^3 dangling bond orbitals.

urities such as boron. Stable impurities in the diamond matrix may form discrete electronic energy levels in the diamond band gap. Optical transitions between these energy levels in the form of spontaneous emission and the absorption of light, give color to the otherwise transparent diamond material, earning such defects the name of color centers. The exceptionally large diamond band gap of 5.5 eV hosts more than 500 color centers, while ~ 10 is bright enough to be detected on a single defect level and stably operated as single photon emitters [56–58]. Among these, the NV-center is the most common and most intensely studied [59].

The nitrogen-vacancy center consists of a substitutional nitrogen atom (N) and vacancy (V) pair situated along the $[111]$ crystal direction in diamond with C_{3v} symmetry (figure 5.1). Four possible orientations of the N-V axis are hence possible within the diamond lattice. The strongly localized electronic states of system [60], warrant a molecular model description of the electron system [61], described in terms of molecular orbitals (MO), given by a linear combination of the four sp^3 dangling bonds of the nitrogen- and three nearest carbon atoms (figure 5.1d). The NV-center exists in a neutral- (NV^0) or negative charge state (NV^-) [62] for which the molecular orbitals are occupied by respectively five or six electrons [63]: Three electrons supplied by the nearby carbon atoms, two from the nitrogen atom and one potentially trapped electron (figure 5.1c). The optical transitions from the ground to the excited states occur by promoting an electron between the a'_1 MO and the energetically degenerate e_x, e_y MO's, situated deep in the diamond band gap. Figure 5.2 illustrates the energy levels of the total electron system for the NV^0 and NV^- charge states, along with optical transitions and experimentally determined lifetimes and transition rates based on references [64–68]. The ground state (symmetry A_2) of the NV^- charge state is a spin triplet state existing in configurations of integer spin projections $m_s = -1, 0, 1$. A spin conserving optical transition ($\Delta m_s = 0$) connects the ground state to the degenerate excited triplet states E_x, E_y . Transitions into respectively E_x and E_y is facilitated by two orthogonal transition dipole

moments $\mathbf{p}_x, \mathbf{p}_y$ lying in the plane normal to the N-V axis (figure 5.1 b) [69, 70]. The orthogonal configuration of $\mathbf{p}_x, \mathbf{p}_y$ typically makes excitation of the NV^- center weakly dependent on laser polarization. Once excited, phonon-promoted population averaging of the E_x, E_y states occur on the ps time scale [71, 72]. The subsequent spontaneous emission ($E_x \rightarrow A_2; E_y \rightarrow A_2$) is hence polarized along either dipole axis, irregardless of the state initially excited. [73]. The $E_x, E_y \rightarrow A_2$ transition is bright enough to detect the NV-center on a single emitter level [74], and easily recognizable by the 637 nm zero phonon line (ZPL) for the NV^- charge state (figure 5.3c). The NV-center exhibits exceptional photostability, as an indefinitely stable photon rate is achievable by optically cycling the $E_x, E_y \leftrightarrow A_2$ transition under continuous laser illumination [75] (figure 5.3b). Bright optical cycles are only temporarily interrupted during inter-system crossing to the singlet state (A_1), which quickly relaxes to the meta-stable state (E) with a shelving time of ~ 150 ns. The probability of intersystem crossing is strongly dependent on the spin projection of the excited state. Using numbers from figure 5.2, the probability of intersystem crossing is respectively $6.3 \text{ ns} \cdot 90 \text{ MHz} = 57\%$ for $m_s = \pm 1$ and $13 \text{ ns} \cdot 10 \text{ MHz} = 13\%$ for $m_s = 0$, while relaxation from the singlet state preferentially occurs into the $m_s = 0$ spin projection of the ground state. The accumulated effect is after a few excitation cycles, the system is "spin polarized" into the $m_s=0$ state, with a high probability of finding the NV^- in the $m_s=0$ state. The subsequent optical cycles thus mainly occur between the bright $m_s=0$ levels, for which transitions into dark periods in the singlet state, occur least frequently. Further illumination of the NV-center in the six electron NV^- charge state may convert the system into the five electron NV^0 charge state by optically pumping an electron into the conduction band, a process known as photoionization. In a similar fashion, the NV^0 charge state may be optically converted to NV^- by capturing an electron from the valence band. The NV-center in this way continuously flip-flop between charge states, making the ZPL for both NV^0 (575 nm) and NV^- (637 nm) visible in the fluorescence spectrum from a single NV-center (figure 5.3c). The relative strength of the NV^0 and NV^- state in the fluorescence spectrum is determined by the ratio of the ionization and recombination rates at which the NV-center converts between charge states, as indicated in figure 5.2. These conversion rates are strongly dependent on the laser wavelength, as for blue light (440 nm) the NV^0 state is preferentially populated in a one-photon ionization process. For green light (510 nm - 540 nm) the NV^- state is optimally populated up to $\sim 75\%$ of the time, while red light (>575 nm) pumps the NV-center into NV^0 , leaving the system dark as laser photons have insufficient energy for excitation of the NV^0 state. [76].

Having reviewed the dynamical transitions between electronic energy levels in the NV-center, we conclude the section by sketching out the full optical cycle of excitation and spontaneous emission involving the vibrational band of the ground and excited electronic state. (figure 5.3a). In this simplified picture the quasi-continuum of vibrational modes of the diamond lattice is condensed into a single effective vibrational mode for which the summed displacement of nuclei, during the vibrational motion, is described by the normal coordinate. The displacement of nuclei from equilibrium is restricted by the electrons, whose energy acts as a spring potential for the vibrational motion, in the Born-Oppenheimer approximation. In this case, the vibrational states become simple harmonic oscillator states associated with the potential surfaces of the ground and excited electronic energy levels, as indicated (figure 5.3a). According to the Franck-Condon principle the electronic transition moment between various vibra-

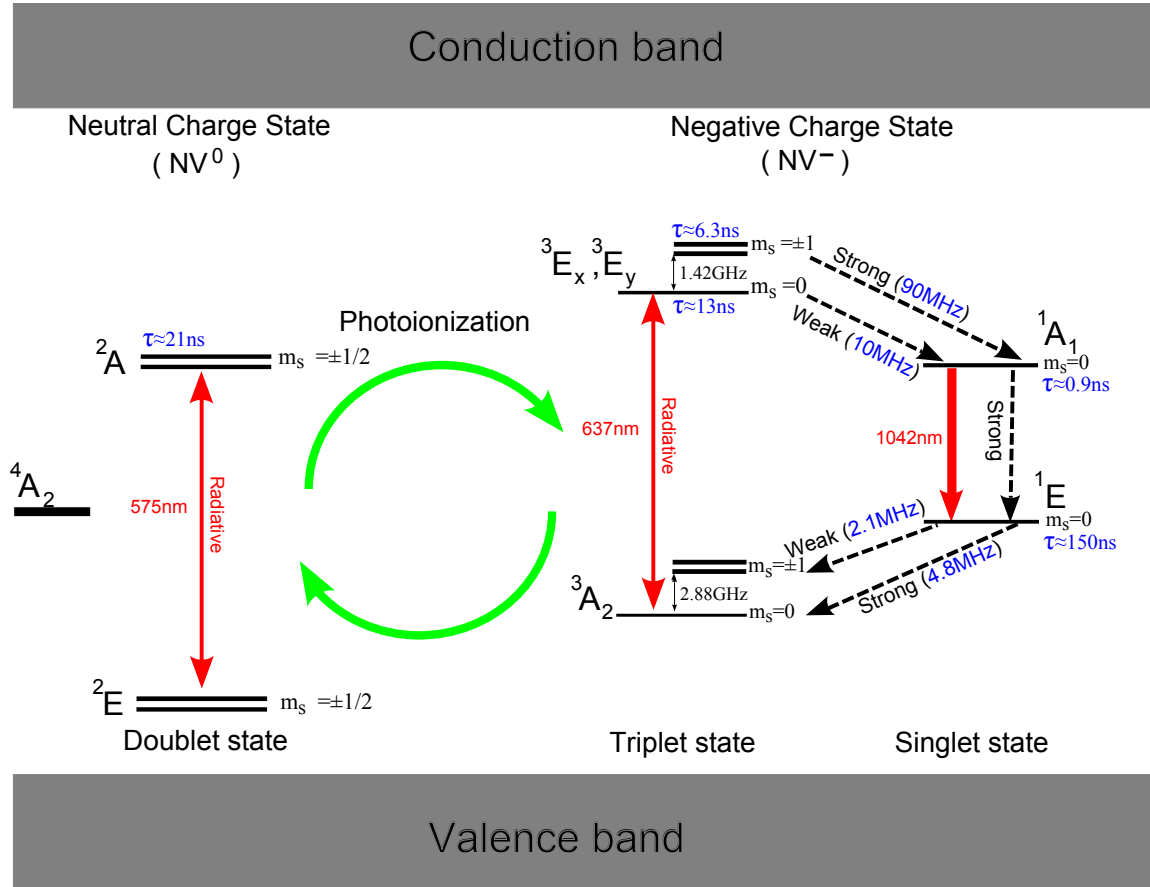


Figure 5.2: Electronic energy levels of the NV-center, situated in the band gap of diamond (horizontal lines). The electronic energy levels are labeled according to symmetry and spin multiplicity (number of spin levels). The experimentally measured lifetime of each level is indicated in blue. Non-radiative decay out of each level is indicated by a dashed line and the rate is given in blue. Optically observable transitions are indicated by vertical red lines and labeled by the transition wavelength, emission or absorption.

tional levels in the ground and excited state is proportional to the overlap of the vibrational wave functions. The shift of the excited state potential surface may be understood as a new nuclei equilibrium, giving the redistribution of electronic charge. The shift removes the orthogonality between the ground and excited state vibrational levels. Excitation may thus occur into the stair-case of vibrational levels, setting up the absorption band. A subsequent relaxation in the excited state-vibrational band, occurring on the ps timescale, puts the system in the zero-vibrational level of the excited electronic state. Spontaneous photon emission occurs by the different decay paths into the ground state vibrational levels, setting up the fluorescence spectrum by a linear progression of Lorentzian contributions for the respective vibrational levels. Remembering that the transition probability into the respective levels is proportional to the overlap of the vibrational wavefunctions, one may qualitatively understand the shape of the NV-center fluorescence spectrum in figure 5.3b. The zero phonon line for the NV⁻ charge state is observed at the largest energy as no lattice vibrations in this case is excited, while the shifting of the excited state potential surface results in the largest spectral intensity being observed in the vibrational side band.

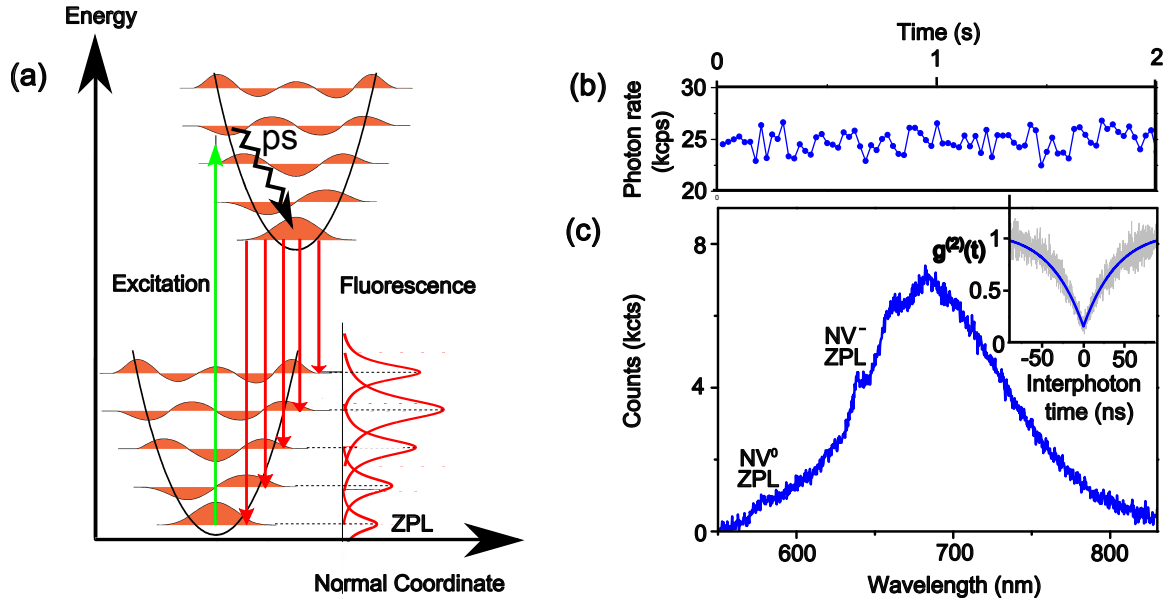


Figure 5.3: (a) Sketch of excitation and emission cycle, involving vibrational levels of the electronic ground and excited state. (b) Time trace of detected photon rate from a single NV-center in a nanodiamond, demonstrating photostable emission, $25 \mu\text{s}$ time binning. (c) Corresponding fluorescence spectrum of the NV-center obtained with 532 nm laser excitation. The presence of photoinitiation is visible as the ZPL of both NV^0 and NV^- is observable. Inset confirm signal originate from a single NV-center as $g^{(2)}(0) < 0.5$

5.2 THE NITROGEN VACANCY CENTER IN NANODIAMOND

This section, reviews the changed emission properties of the NV-center when contained in a nanodiamond, relative to the properties in bulk diamond. NV-centers in nanodiamonds typically exhibit an increased lifetime, relative to that of bulk. Considering equation 3.10, the increased lifetime is expected as the lifetime is inversely proportional to the refractive index of the embedding media, typical lifetimes of the NV^- charge state in a 25 nm nanodiamond being $\sim 30 \text{ ns}$. However, while experimental reports of the NV^- lifetime are consistent in bulk diamond, the lifetime varies significantly between individual NV-centers in nanodiamonds [77, 78]. The lifetime spread may partly be attributed to the irregular shape of the nanodiamond and random NV-center position [78], however, experimental observations cannot purely be explained by variations of the photonic environment [77, 79]. Studies indicate the onset of a non-radiative decay rate for nanodiamonds $\leq 150 \text{ nm}$, resulting in decreasing quantum yield with the decreasing size of the nanodiamond [79]. Indeed, a decreasing quantum yield has been confirmed as the NV-center approaches a diamond interface [80]. A quantum yield of 10-90% have been measured for $\sim 100 \text{ nm}$ nanodiamonds and 0-20% for $\sim 25 \text{ nm}$ nanodiamonds [77]. Photostable emission has been confirmed from NV-centers down to a nanodiamond size of 5 nm [81].

Further, the NV-center charge state populations are strongly dependent on the surface terminations of the nanodiamond. A hydrogen terminated diamond surface forms a conductive surface layer, effectively discharging NV-centers in close proximity to the surface, to preferentially be found in the neutral NV^0 charge state [82]. Alternatively, oxygen surface terminations stabilize the NV-center in negative NV^-

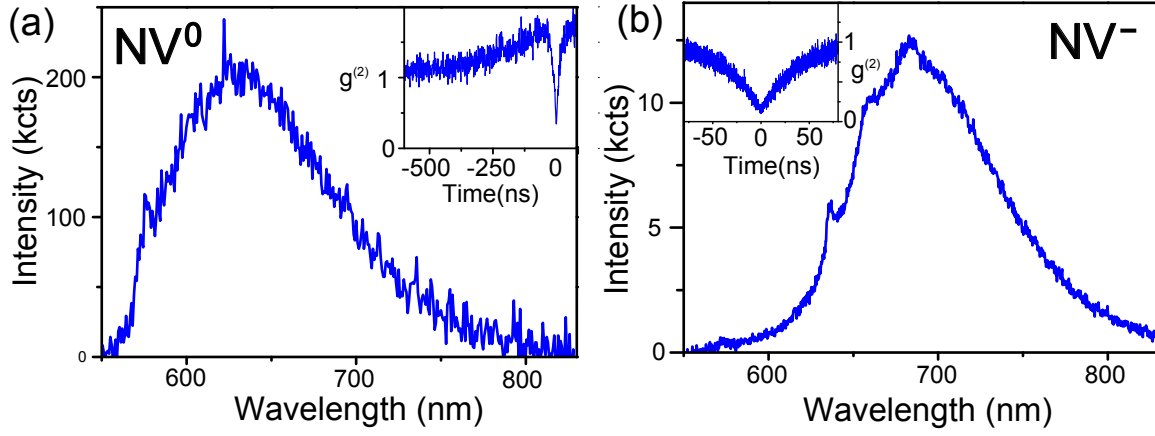


Figure 5.4: Fluorescence spectrum of a single NV-center situated in two different nanodiamonds, measured in the lab, both excited by a continuous wave 532 nm wavelength pump laser. NV-center spectrums are strongly dominated by respectively (a) the neutral- (NV^0) and (b) negative charge state. The $g^{(2)}$ measurements in inset indicate detected signal preferentially originates from a single NV-center.

charge state [83]. Figure 5.4a, b illustrates the effect for two NV-centers in different nanodiamonds, exhibiting the fluorescence spectrum of the NV^0 and NV^- charge state respectfully. Given the large variation in the emission properties of the NV-center in nanodiamonds, it is preferable to precharacterize the particular nanodiamond before incorporating the NV-center into an antenna configuration, for a reliable emitter reference.

6

Rate model of a 3-level system

This chapter provides an analytical model for the experimental conditions under which a NV-center spontaneously emits photons. The overarching purpose is to quantify parameters in the emission process by later fitting the analytical model to experimental measurements. The NV-center is modelled as a 3-level system (figure 6.1), representing the ground-, excited- and meta-stable state of the negative charge state. The probability of finding the system in the respective states is given by the corresponding populations ρ_g , ρ_e and ρ_m . System excitation, by illumination from a pump laser, is represented by an excitation rate γ_{ex} , while the decay out of the excited state is given by respectively a radiative- (γ_r), a non-radiative decay rate (γ_{nr}) and an inter-system crossing rate (γ_{ISC}). Transition from the meta-stable to the ground state occurs at a rate γ_g . The rate model assumes no coherent exchange of energy between the system and excitation or emission fields [30], valid in the present work as the pump laser is not resonant with emission but excites the system through the absorption band, while emission occurs in the weak-coupling regime. The rate model may be represented by a set of 1. order differential equations for the state populations (eq. 6.1) and a condition for conservation of the total population (eq. 6.2), stating that the system must be found in one of the three states [33].

$$\frac{d}{dt} \begin{pmatrix} \rho_g \\ \rho_e \\ \rho_m \end{pmatrix} = \begin{pmatrix} -\gamma_{ex} & \gamma_r + \gamma_{nr} & \gamma_g \\ \gamma_{ex} & -\gamma_r - \gamma_{nr} - \gamma_{ISC} & 0 \\ 0 & \gamma_{ISC} & -\gamma_g \end{pmatrix} \begin{pmatrix} \rho_g \\ \rho_e \\ \rho_m \end{pmatrix} \quad (6.1)$$

$$\rho_g + \rho_e + \rho_m = 1 \quad (6.2)$$

In the following equation 6.1 and 6.2 are solved for a series of initial conditions corresponding to measurement situations realized in the laboratory.

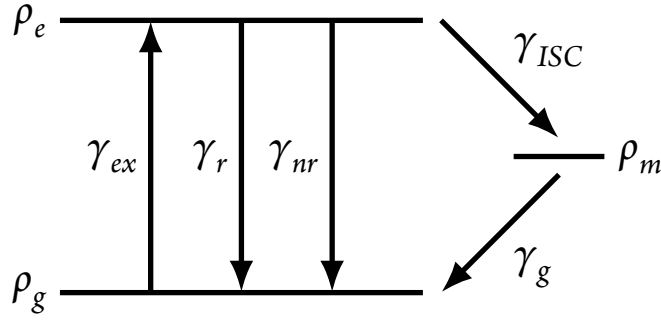


Figure 6.1: Schematic of rate model for a 3-level system, consisting of a ground-, an excited- and a meta-stable state, with corresponding populations, ρ_g , ρ_e and ρ_m respectively. The ground and excited state are connected by an excitation rate (γ_{ex}) and radiative- (γ_r) and nonradiative (γ_{nr}) decay rate. The inter-system crossing rate (γ_{ISC}) connects the excited state to the meta-stable state, while the meta-stable state subsequently decays to the ground state at a rate γ_g .

6.1 LIFETIME DECAY CURVE

Consider the situation for which the emitter is initialized in the excited state by a sharp laser pulse at $t=0$. The situation corresponds to the initial condition $\rho_e = 1$, while $\gamma_{ex} = 0$ for $t > 0$. The probability of detecting a photon at a later time interval $t; t + dt$ is in this case proportional to $d\rho_e(t)/dt = -\gamma\rho_e(t)$, for which the total decay rate of the excited state is given by

$$\gamma = \frac{1}{\tau} = \gamma_r + \gamma_{nr} + \gamma_{ISC}, \quad (6.3)$$

τ being the lifetime of the excited state. Solving equation 6.1 under these initial conditions, the time dependence of the excited is given by

$$\rho_e(t) = e^{-\gamma t}. \quad (6.4)$$

The excited state population is proportional to the probability of detecting a photon at a particular time interval $t; t + dt$. Therefore the total decay rate of the excited state may be obtained by fitting equation 6.4 to the experimentally measured lifetime decay curve, consisting of a time-binned histogram of photon detection events, relative to the excitation pulse as illustrated in figure 6.2

6.2 SATURATION CURVE

Consider the emitter, excited from a continuous wave laser at constant power, corresponding to a time-independent excitation rate. The system is in this case operating in steady-state and so the populations are independent of time, imposing the steady-state condition $\frac{d\rho_e}{dt} = \frac{d\rho_g}{dt} = \frac{d\rho_m}{dt} = 0$. The detected photon R may in this case be written as

$$R = \eta\gamma_r\rho_e, \quad (6.5)$$

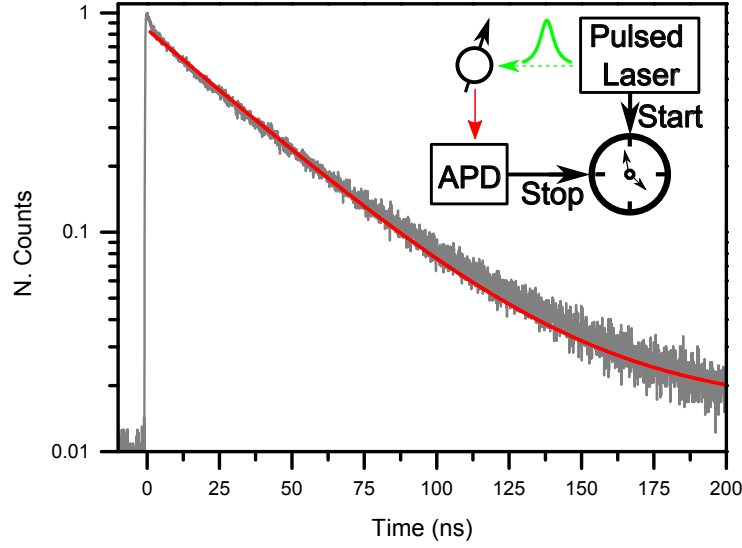


Figure 6.2: Experimental lifetime decay curve (grey) obtained by histogramming the time of photon detection events from a single NV-center, relative to the excitation pulse (inset) for a pulse period of 400 ns, 30 μW laser power and histogram time binning of 64 ps. Single exponential fit (red) of lifetime data finding an excited state lifetime of 37.7 ns.

η being the collection efficiency of the objective, that is the probability of collecting an emitted photon with the objective.¹ Solving equation 6.1 for ρ_e under steady-state conditions, the detected photon rate from a 3-level system is given by

$$R = \left(\frac{\eta\gamma_r}{1 + \gamma_{ISC}/\gamma_g} \right) \left(\frac{\gamma_{ex}}{\gamma_{ex} + \gamma/(1 + \gamma_{ISC}/\gamma_g)} \right). \quad (6.6)$$

For an examination of the power dependent response, we simplify the system and consider the response of a 2-level system, obtained by setting $\gamma_{ISC} = 0$,

$$R = \eta\gamma_r \left(\frac{\gamma_{ex}}{\gamma_{ex} + \gamma} \right). \quad (6.7)$$

Consider initially the non-saturated regime for which the emitter is excited at low laser power, such that $\gamma \gg \gamma_{ex}$. R is in case limited by the excitation rate, increasing linearly with laser power. Defining the emitter quantum efficiency by $q_e = \gamma_r/\gamma$, the photon rate in the non-saturated regime is given by

$$R = \eta q_e \gamma_{ex}. \quad (6.8)$$

Operating the emitter at saturation such that $\gamma \ll \gamma_{ex}$, R is limited by the radiative decay rate, for which R approaches the asymptotic photon rate limit of

$$R_{\infty} = \eta\gamma_r. \quad (6.9)$$

For experimental purposes, γ_{ex} is commonly not known directly and so it is convenient to rewrite equation 6.7 in terms of laser power (P), using the relation $P \propto \gamma_{ex}$,

¹Further, to calculate the experimentally detected photon rate, the transmission of the experimental setup and quantum efficiency of detector need to be accounted for.

$$R = R_{\infty} \frac{P}{P + P_{sat}}, \quad (6.10)$$

P_{sat} being the saturation laser power. Figure 6.3 illustrates an exemplary model fit of equation 6.10 to the experimentally measured saturation curve from a single NV-center. Comparing equation 6.6 and 6.10, it is apparent that the saturation curve model also captures the behavior of a 3-level system, while the meaning of the fitted coefficients is slightly different.

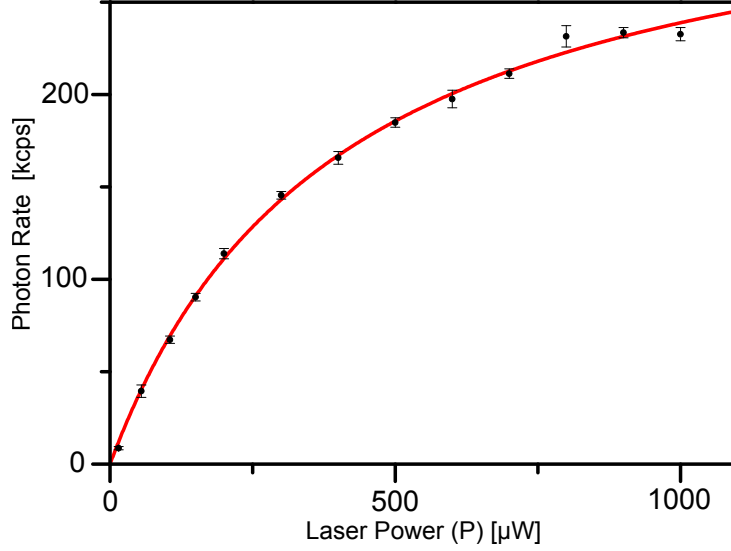


Figure 6.3: Experimental saturation curve measured from single NV-center (black). Data points are obtained as the average photon rate from a 2 s time trace, with background subtracted from a nearby sample surface, while laser polarization is set for maximal counts. Error bars representing 1 standard deviation in photon rate. Model fit (red) given by equation 6.10 finding $R_{\infty} = 335 \text{ kcps}$, $P_{sat} = 402 \mu\text{W}$.

6.3 2. ORDER CORRELATION FUNCTION

The 2. order correlation function $g^{(2)}(\tau)$ is instrumental for the classification of light sources. Classical light, as described by continuous fields, following $g^{(2)}(0) \geq 1$, while for non-classical light $g^{(2)}(0) \geq 0$. $g^{(2)}(\tau)$ is obtained by measuring the autocorrelation of the light intensity I , according to

$$g^{(2)}(\tau) = \frac{\langle I(t)I(t+\tau) \rangle}{\langle I(t) \rangle^2}. \quad (6.11)$$

In the single photon language, $g^{(2)}(\tau)$ gives the probability of detecting a photon at time $t+\tau$ on the condition of having detected a photon at time t . A single quantum emitter may only emit one photon at a time and so light from a single photon source is characterized by $g^{(2)}(0) = 0$, as the probability of detecting two photons at the same time is zero. A quantum mechanical treatment gives the $g^{(2)}(0)$ -value for n_{qe} quantum emitters[31],

$$g^{(2)}(0) = 1 - \frac{1}{n_{qe}}. \quad (6.12)$$

The detection of a photon at $t = 0$ corresponds to the initial condition $\rho_g(0) = 1$, as the system in this case must have transitioned to the ground state, while the probability for the next photon to be detected at time τ is $\eta\gamma_r\rho_e(\tau)$. The 2. order correlation function can in this case be written

$$g^{(2)}(\tau) = \frac{\eta\gamma_r\rho_e(\tau)}{\eta\gamma_r\rho_e(\infty)} = \frac{\rho_e(\tau)}{\rho_e(\infty)}, \quad (6.13)$$

$\eta\gamma_r\rho_e(\infty)$ being the normalization factor given by the steady-state photon rate reached at a time longer than the transient response. $\rho_e(\tau)$ is solved for by taking the Laplace transform of eq 6.1 and solving the coupled differential equations using the initial condition $\rho_g = 1$. Subsequently transforming to the time domain using the Heavy-side theorem yield[33]

$$a = -\gamma_{ex} - \gamma_g; \quad b = \gamma_r + \gamma_{nr} - \gamma_g; \quad c = \gamma_g; \quad d = -\gamma_r - \gamma_{nr} - \gamma_{ISC}; \quad f = \gamma_g \quad (6.14)$$

$$s_{\pm} = -\frac{a+d}{2} \pm \sqrt{\left(\frac{a-d}{2}\right)^2 + bc}; \quad A_1 = \frac{c(1+f/s_-)}{s_- - s_+}; \quad A_2 = -\frac{c(1+f/s_+)}{s_- - s_+}; \quad A_3 = \frac{cf}{s_- s_+} \quad (6.15)$$

$$\rho_e(\tau) = A_1 e^{s_- \tau} + A_2 e^{s_+ \tau} + A_3. \quad (6.16)$$

The coefficient A_3 gives the steady-state population of the excited state $\rho_e(\infty) = A_3$. Inserting equation 6.16 in equation 6.13, the 2. order correlation function is given by

$$g^{(2)}(\tau) = 1 + \frac{A_1}{A_3} e^{s_- \tau} + \frac{A_2}{A_3} e^{s_+ \tau}. \quad (6.17)$$

Figure 6.4 gives an experimental $g^{(2)}(\tau)$ measurement from a single NV-center, using the Hanbury Brown-Twiss configuration [84], consisting of a 50:50 beam splitter and two avalanche photodiodes connected to an electronic timing box in a start-stop configuration. The measurement is obtained by histogramming the inter photon time (τ) between photon detection events in a start-stop configuration. For normalization, equation 6.16 is fitted to the histogram and the coefficient A_3 is used for data normalization, to obtain the $g^{(2)}(0)$ -value. The non-zero $g^{(2)}(0)$ -value results from sample background and detector dark counts, which for the model fit is included in A_3 .

A physical insight into equation 6.17 may be gained using the relation $-A_1/A_3 = 1 + A_2/A_3$, while assuming that the emitter is operated in the non-saturated regime and transition into the meta-stable

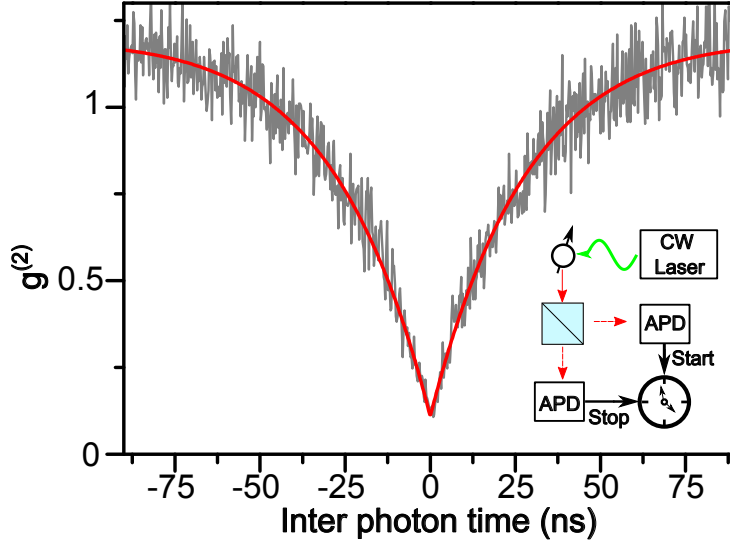


Figure 6.4: $g^{(2)}$ measurement of single NV-center, excited by a 532 nm continuous wave laser at 300 μ W, using 256 ps time binning (grey). Model fitted (red) finding a $g^{(2)}(0)$ -value of 0.11.

state is slow. That is assuming $\gamma_r + \gamma_{nr} \geq \gamma_{ex} \gg \gamma_{ISC} \geq \gamma_g$, equation 6.17 may be written

$$g^{(2)}(\tau) = 1 - \left(1 + \frac{A_2}{A_3}\right)e^{-(\gamma_{ex} + \gamma_r + \gamma_{nr})\tau} + \frac{A_2}{A_3}e^{-\left(\frac{\gamma_{ex}\gamma_{ISC}}{\gamma_g(\gamma_{ex} + \gamma_r + \gamma_{nr})} + \gamma_g\right)\tau}. \quad (6.18)$$

The first exponential term in equation 6.18 is responsible for the initial slope of the $g^{(2)}(\tau)$, including both excitation- and decay rate terms, as the emitter must be excited and spontaneously decay before a second photon can be detected. The second exponential term is related to shelving in the meta-stable state, causing $g^{(2)}$ bouncing or increased probability of detecting a photon, at a delayed time. The presence of γ_{ex} in both terms causes curve narrowing at short times and increased bouncing at longer times, with increased laser power.

6.4 ROTATION OF LASER POLARIZATION

Consider now the detected photon rate upon rotation of the pump laser polarization, linearly polarized along the sample plane. The excitation rate in this case varies with the projection of the pump field on the NV-centers dipole axis, according to

$$\gamma_{ex}(\phi) \propto \sum_{j=x,y} |\mathbf{E}_{ex}(\phi) \cdot \mathbf{p}_j|^2. \quad (6.19)$$

Summing over the orthogonally oriented dipole axis \mathbf{p}_x and \mathbf{p}_y of the NV^- charge state (figure 5.1b), the geometrical orientation of $\mathbf{p}_x, \mathbf{p}_y$ may be defined in terms of the normal vector to the dipole plane \mathbf{V}_{NV} , described by the azimuthal angle θ_{NV} and polar angle ϕ_{NV} and the angular position (Θ) in the dipole plane, as indicated in figure 6.5a. Assuming that the emitter is operated in the non-saturated regime, such that photon rate scales linearly with excitation rate (see equation 6.8), the photon rate can be shown to follow [85]

$$R \propto |\mathbf{E}_{ex}|^2 |\mathbf{p}|^2 \left(1 - \cos(\varphi - \varphi_{NV})^2 \sin(\theta_{NV})^2 \right), \quad (6.20)$$

φ being the polar angle, defining the orientation of the pump field (\mathbf{E}_{ex}) polarized along the sample plane, while equal dipole moment is assumed $|\mathbf{p}| = |\mathbf{p}_x| = |\mathbf{p}_y|$. As equation 6.20 is independent of Θ the measurement contains no information about the dipole orientation in the dipole plane. The orientation of the dipole plane may however be determined by fitting equation 6.20 to experimental data, with some ambiguity, as φ_{NV} , $\varphi_{NV} + \pi$ and $\pm\theta_{NV}$ yield equally good model fits. Figure 6.5a, b illustrate such a least-square-fit to experimental data from an NV-center. The measurement provides the dipolar response of the NV-center and allows for the maximum in-plane dipole projection to be determined.

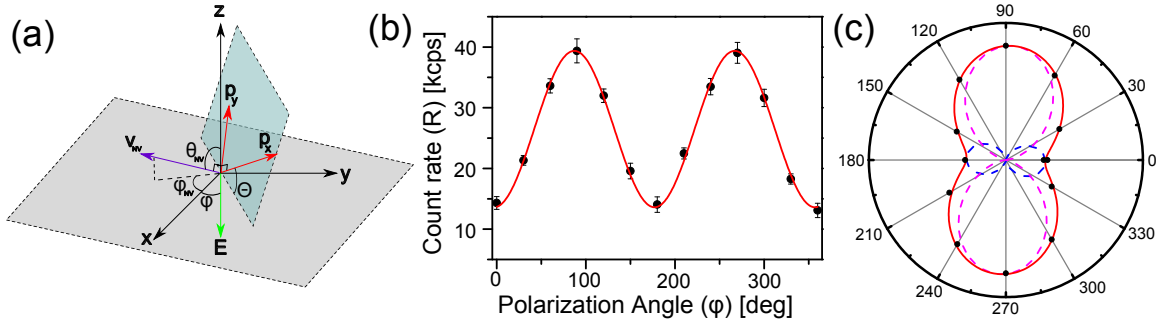


Figure 6.5: (a) Sketch of the dipole axis $\mathbf{p}_x, \mathbf{p}_y$ contained in the dipole plane with normal vector \mathbf{V}_{NV} defining the N-V axis, described by the azimuthal angle θ_{NV} and polar angle φ_{NV} . The sample plane is indicated in grey, containing the pump field \mathbf{E}_{ex} oriented along the polar angle φ . (b) Photon rate from a single NV-center, measured as a function of the pump field orientation (black dot), errorbar 1 std and model fit (red) (c) identical data in polar plot, magenta and black dashed lines give possible model contributions from \mathbf{p}_x and \mathbf{p}_y .

7

Experimental setup and techniques

This chapter reviews the experimental setup and describes the techniques for AFM manipulation and characterization of the emission properties of quantum emitters. The analytical model for experimental measurements was described in section 6. The experimental setup has been continuously evolving throughout the work of this thesis, part of the PhD work being contributions to the design, construction and continuous improvement of the setup. We here present the current version of the experimental setup, while prior setup versions appear in the individual publications. A sketch of the current setup is given in figure 7.1.

Quantum emitters are excited at a wavelength of 532 nm by an ultra stable continuous wave laser (CL532-100-O CrystaLaser) or a pulsed laser (LDH-P-FA-530L - Picoquant) with a pulse width of ~ 50 ps operating at a pulse period from 12.5-400 ns. The laser of choice is introduced into the excitation light path (green path figure 7.1) by a flip mirror. A short pass filter (cut-off 750 nm) filters residual light of the fundamental laser harmonic. The laser is subsequently passed through a configuration consisting of a polarizing beam splitter sandwiched between two half-wave plates, for the control of laser power and orientation of pump polarization. The laser power is controlled by manually rotating the first half-wave plate, thereby changing the power passed directly through the polarizing beam splitter. The polarizing beam splitter subsequently defines the polarization axis for both pump lasers. Rotating the second half-wave plate results in a rotation of the linearly polarized pump light. In the interest of achieving a diffraction limited laser spot, the pump light is passed through an asymmetric spatial filter, consisting of a short (6 cm) and long (20 cm) focal length lens and a 100 μm pinhole. The configuration filters and expands the beam to a gaussian beam, wide enough to overfill the backaperture of the objective. Figure 7.2a shows a photograph of the excitation light path in the experimental setup. After spatial filtering, the pump light is passed to the backport of an inverted microscope (IX73 - Olympus), shown in figure 7.2b. The inverted microscope holds two filter cube turrets for introducing various filters in the

light path. Conventionally, pump light is reflected off a dichroic mirror in the top turret, with a cut-off 535 nm (FF535-SDio1 - SEMROCK). The pump light is focused onto the sample with a x100, 0.9 NA air objective (MPlanFLN - Olympus), used in appendix b, or a x100 1.4 NA oil objective (UPlanSAPO - Olympus), used in appendix c.

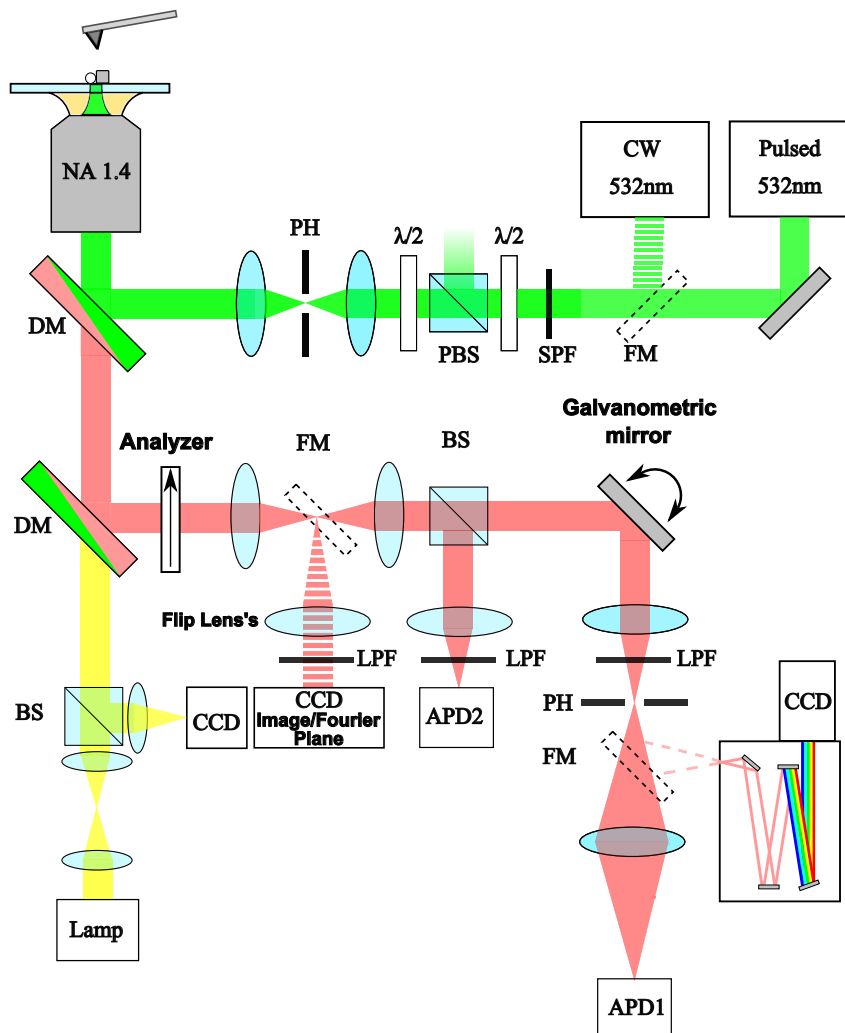


Figure 7.1: Schematic of experimental setup for characterization of emission properties of quantum emitters. Green indicates the excitation path of the pump laser light, red the detection path of quantum emitter fluorescence and yellow the path of lamp light for bright field microscopy. FM: Flip mirror, SPF: Short pass filter (750 nm cut-off), $\lambda/2$: Half-wave plate, PBS: Polarizing beamsplitter, PH: Pin hole, DM: Dichroic mirror (cut-off 550 nm), BS: Non-polarizing beamsplitter, LPF: Long pass filter (550 nm cut-off), APD: Avalanche photodiode.

The position of the sample is indicated in figure 7.2b. When using the oil objective, an AFM (Solver Pro - NT-MDT) is mounted on top of the microscope for manipulation of nanodiamonds or silver cubes spincoated on a quartz coverslip. The AFM and sample are mounted on a micrometer stage, which allows for rough alignment of the AFM cantilever to the laser beam. The procedure for alignment of cantilever to laser beam is described in appendix c. Fine positioning and scanning of the sample wrt. the laser beam is facilitated by a piezo stage mounted on the micrometer stage (figure 7.2). For focusing and sample inspection by bright field microscopy, a halogen lamp, configured for Köhler illumination, illuminates the sample through a bottom port in the microscope (yellow light path, figure 7.1). Sam-

ple inspection is done through the ocular or imaging onto a CCD camera, back through the bottom microscope port.

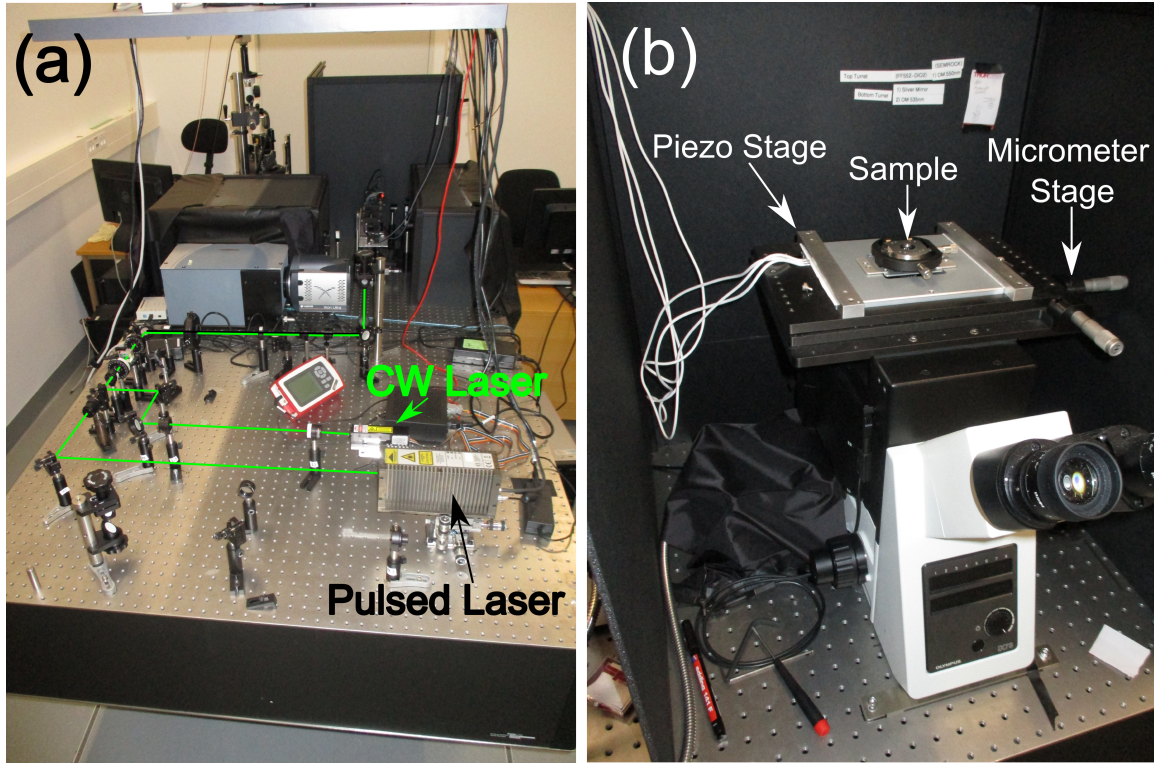


Figure 7.2: Photographs of experimental setup for characterization of NV-center emission properties and AFM assembly of nano particle antennas. (a) Excitation light path, green line indicate the light path of pump light from the contineous wave(CW) and pulsed laser. The pump light is input to the backport of an inverted microscope. (b) Inverted microscope, the sample position along with piezostage and alignment micrometer stage is indicated. For particle manipulation, the AFM may be placed ontop of the inverted microscope.

The emission from the quantum emitter, which is collected by the objective, is reflected off a dichroic mirror (FF552-Dio2 - SEMROCK) in the bottom microscope turret, split by a 50:50 non-polarizing beam splitter and imaged onto two avalanche photo diodes(APD)(τ -SPAD - Picoquant), in the Hanbury-Brown Twiss configuration. In order to limit background counts, arising from ambient light in the laboratory, each APD is placed in a darkbox, resulting in a detector dark count of 200-500 cps with the light off in the room. The fluorescence detected by APD₁ (see figure 7.1) is imaged through a $100\ \mu\text{m}$ pinhole, which allows for confocal scanning of fluorescence by mapping out the photon rate detected by APD₁ as function of piezo-stage position. For histogramming of a lifetime decay curve, described analytically in section 6.1, the pulsed laser is operated at 400 ns pulse period, much longer than the typical NV-center lifetime. The onset of each laser pulse is indicated by an electronic sync pulse sent to an electronic timing box (Picoharp 300 - Picoquant) which starts a clock, the detection of a photon on APD₁ stops the clock, thereby time-tagging the photon event¹. Timing uncertainty in time-tagging of photon detection events is given by the instrument response function(IRF) measured to $\sim 800\ \text{ps}$

¹In pratice, lifetime decay curves is recorded in reverse start-stop mode. Photon detection starting clock and the sync laser pulse stopping clock. The reason being to only run the timing circuit at the rate of photon detection events rather than the laser pulse rate.

FWHM, uncertainty arising from finite pulse laser width (~ 50 ps), uncertainty in the electronic timing circuit (4 ps), analog-to-digital conversion (64 ps time binning typically used), and uncertainty in the timing of photon-to-electronic pulse conversion related to the detector. The IRF was not corrected for in this work, as experimentally measured lifetimes were much longer than the IRF FWHM.

For measuring the 2. order correlation function, analytically described in section 6.3, the start sync signal is obtained upon a detection event on APD₂ and stop signal from APD₁. The $g^{(2)}$ measurement thus consists of histogramming the interphoton time between photon detection events on APD₂ and APD₁. Time-tagging between two APD's results in an increased timing uncertainty, which may limit $g^{(2)}(0)$ -value for a sharp slope around $\tau = 0$.

For saturation curve measurements, analytically described in section 6.2, a 2 s time trace of photon detection events from APD₁ and APD₂ is obtained for a series of the laser powers. The saturation curve is obtained by plotting the time average photon rate from each time trace, against the laser power. For each saturation curve the focus was initial optimized and laser spot aligned to the NV-center by maximizing the detected photon rate, while stepping in 100 nm intervals with the piezo stage. The pump polarization was then optimized for maximum counts. Each saturation curve was corrected for sample background measured from a nearby plane sample surface.

Mapping photon rate as a function of pump polarization, analytically described in section 6.4 is done by recording the 2 s time traces from APD₁ and APD₂, while rotating pump polarization over 360° in 15° steps. Plotting the time average photon rate of each trace against the pump polarization angle, reveals the pump polarization dependence.

The fluorescence spectrum is obtained by introducing a flip mirror in front of APD₁, deflecting the photons onto a grating spectrometer (Shamrock 500i - Andor) which disperses the light onto an electron-multiplying CDD (EMCCD)(iXon Ultra 888 - Andor). At a laser power of $100\mu W$, a good spectrum from a single NV-center could be achieved within an integration time of 5 min.

For probing the polarization of emitted light, an analyzer (LPVIS100-MP2 - Thorlabs, 550-1500 nm), mounted on a rotational motorstage, is introduced in the detection light path and photons reflected off a flip mirror onto a CCD (Orca4LT - Hamamatsu), set to image the emission spot. Integrating camera counts of the emission spot for various analyzer angles maps out the polarization dependence of the emitted light.

Having described the experimental setup and measurement procedures for characterizing the spontaneous emission properties, we proceed by reviewing the procedure for AFM assembly of nanodiamond-silver cube systems, applied in appendix b and c. The AFM assembly procedure is described by reviewing the assembly of a cube dimer antenna around a nanodiamond containing a single NV-center, appearing as experiment d in appendix c. In this experiment a low fluorescence quartz coverslip (SPI supplies) was cleaned by a RCA1 cleaning step which removed biological residue and made the surface hydrophilic for successful spincoating of nanodiamonds(MSY 0-0.05 GAF - Microdiamant) diluted 1:50 in mili-Q, followed by 100 nm silver cubes (nanoComposix) diluted 1:2 in Mili-Q water and finally silver nano wires synteasized in-house. The nano wires act as reference markers for locating the

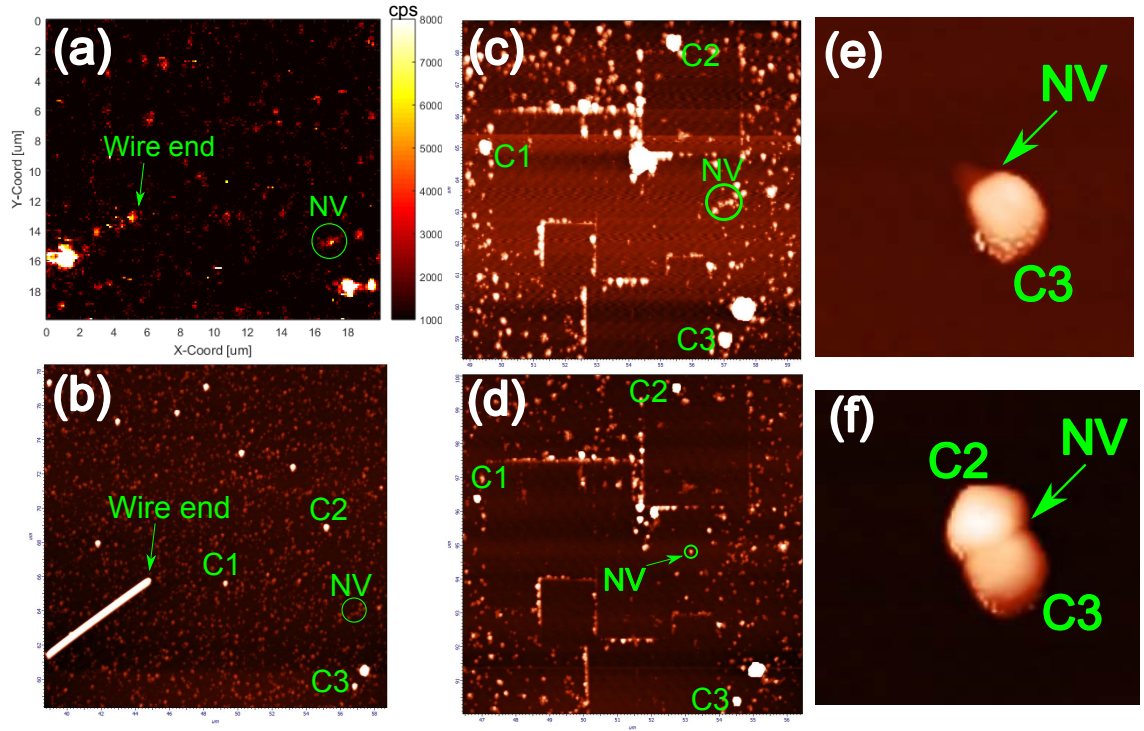


Figure 7.3: Procedure for identifying a nanodiamond containing an NV-center and the AFM assembly of a cube dimer antenna. (a) Fluorescent scan of sample, an identified NV-center is circled in green. (b) AFM scan of the same sample area, the estimated NV-center position is circled and 3 silver cubes identified with labeling C1-C3. (c) Clearing of sample by AFM contact mode scanning. (d) Separation of nanodiamonds potentially containing the NV-center, by AFM manipulation, and identification of correct nanodiamond. AFM assembly of cube dimer antenna around nanodiamond pushing (e) cube C3 and (f) cube C2 to the NV-center.

particular nano diamond containing an NV-center in both the fluorescent scan map and AFM scan². Figure 7.3a show a fluorescence scan of the sample performed at a $100\mu W$ laser power using the oil objective for excitation and photon collection. The end of a silver wire is visible as a reference point. Within the scan a fluorescent spot has been identified to arise from a single NV-center, confirmed by lifetime curve, spectrum and $g^{(2)}$ measurement. Figure 7.3b show the corresponding AFM scan of the same area. Transferring the NV-center coordinate position with respect to the wire end, from the fluorescent scan to the AFM scan, an area can be identified, within which the nanodiamond containing the NV-center is located. In the AFM scan (figure 7.3b) the estimated NV-center position has been circled and labeled NV. The 100 nm silver cubes may easily be identified in the AFM scan by the difference in height to the 25-40 nm nanodiamonds. Three cubes labeled C1-C3 are immediately available in the vicinity of the NV-center setting the ground for AFM assembly of the cube dimer antenna. To allow for isolating the nanodiamond containing the NV-center and pushing cubes to the NV-center, sample area is cleared by scanning in contact mode. Figure 7.3c show the sample after an area has been cleared by contact mode scans. Contact mode scanning blunts the AFM tip (NSG10 - NT-MDT, 10 nm tip radius) and increase the chance of picking up cubes or nanodiamonds during subsequent AFM manipulation. The AFM tip was therefore changed after such scanning in contact mode. The cleared area in figure 7.3c give cube C1-C3 a clear path to the NV-center, while the potential nanodiamonds containing the NV-

²for single cube experiments in appendix b, gold reference marks defined electron beam lithography was used instead of silver nano wires.

center, indicated with a circle, can be separated such that the correct nanodiamond may be identified. In figure 7.3d the nanodiamonds have been dispersed into the cleared area, by pushing the individual nanodiamonds with the AFM tip. For particle manipulation with the AFM, an area is initially scanned in non-contact mode, AFM manipulation is then performed by transitioning to contact-mode and moving the AFM tip over the nanodiamond, along the path of intended particle movement. A subsequent scan in non-contact mode reveals the new position of the particle and a new cycle of AFM manipulation can be performed. For successful particle movement, the tip radius of curvature should be smaller or same size, as the particle radius for maximizing the translational force applied to the particle [86, 87]. After separating the nano diamonds, the nanodiamond containing the NV-center is identified by aligning the laser beam to the NV-center. Moving the AFM tip over the individual nanodiamonds in non-contact mode, while monitoring the laser spot on the CCD camera, increased scattering of laser light was observed when the cantilever was placed over the correct nanodiamond. The nanodiamond identified in this way, is circled in figure 7.3d. With the correct nanodiamond identified, the cube dimer antenna was assembled around the NV-center by AFM manipulation. The optimal approach for AFM manipulation of cubes was to minimize the force applied by the tip to the sample. That is operating at the minimal set point, in which the AFM goes into contact mode. In this setting the successrate of cubes pushes was $\sim 75\%$, while the blunting of the tip was slow, thereby decreasing the chance of picking up the cube during AFM manipulation. Deterministic cube movement was best achieved by pushing normal to a cube facet, with the AFM tip centered on the facet. With this approach cubes would often move in a straight line. For deterministic alignment of the cube facet, normal to the NV-center dipole axis as is done in appendix c, the cube facet would be aligned slightly away from the nanodiamond and pushed in a straight line to cube. Figure 7.3e, f illustrate the assembly of the cube dimer antenna around the selected nanodiamond.

8

Nano antennas for enhancement of nonclassical light emission

This chapter summarises the results achieved throughout this PhD. For an in-depth discussion of the results, the reader is referred to the individual publications appearing in appendix A-E. The aim of this chapter is to put each publication into the context of the thesis, namely developing nano antennas for enhancing the generation of non-classical light. The publications are discussed in the chronological order in which the work was conducted, in the hope of clarifying the logical progression of the work.

8.1 METAL PHOTOLUMINESCENCE FROM GOLD NANO ANTENNAS

Gold and silver are the metals of choice for achieving a strong plasmonic response in the visible and near infrared region, coinciding with the emission wavelength of typical quantum emitters. Silver exhibits the lowest ohmic loss (see figure 2.4d) and largest band-gap energy ($\sim 3.4\text{eV}$) [88], in principle preventing metal luminescence for excitation wavelengths $\geq 400\text{ nm}$. However, under ambient conditions silver steadily corrodes, forming compounds such as silver sulfide (Ag_2S) [89, 90], which ruins the plasmonic properties. Silver corrosion inevitably makes samples difficult to work with in the laboratory, as they are not stable over long time periods. In contrast, gold is chemically inert, making it viable for long-term ambient operation. However, the lower band gap energy ($\sim 2.2\text{eV}$) results in metal photoluminescence [91] for a typical excitation wavelength of 532 nm , potentially degrading the single photon purity of a quantum emitter incorporated into a gold nano antenna. While filtering is an option to limit background emission from gold [92], it is generally desirable to expand the understanding of how metal photoluminescence arises in gold nano antennas, so as to better evaluate the viability of gold for a particular antenna design in combination with a particular quantum emitter.

Appendix A presents a study of metal photoluminescence from arrays of gold nano patch antennas consisting of a top nano particle separated from a plane gold film by a thin dielectric spacer layer (figure 8.1a). The resonant response of the antenna may be understood as a standing wave resonance arising from the propagating GSP mode, introduced in section 2.4, reflecting at the top particle terminations [24]. The antenna design is thus known as a gap plasmon resonator, with the gap surface plasmon resonance (GSPR) defined by the dimension d of the top particle according to

$$\frac{2\pi}{\lambda_0^{res}} N_{eff}^{GSP} d + \phi_r = \pi, \quad (8.1)$$

λ_0^{res} being the resonance vacuum wavelength, N_{eff}^{GSP} the effective index of the GSP mode and ϕ_r the reflection phase. In the presented work, gold nano patch antennas are demonstrated to spectrally enhance the photoluminescence from gold at the GSPR, relative to a plane gold film (figure 8.1b, c). The enhancement is believed to arise from radiative electron hole recombination by excitation of the resonant GSP mode. The subsequent scattering of the GSP mode to free space increases the apparent quantum yield of electron hole recombination process, estimated to be $\sim 10^{-10}$ for a plane gold film [91]. The spectral dependence and polarization of gold photoluminescence from nano antennas is studied as a function of the GSPR spectral position and pump polarization for energetically degenerate GSPR's supported by a cylindrical top particle ($d_1=d_2$), or non-degenerate GSPR's supported by a rod top particle ($d_1 \neq d_2$). The polarization of photoluminescence is tuned from near unpolarized for degenerate GSPR to strongly polarized for non-degenerate GSPR. Photoluminescence from rod arrays being polarized spectrally at the GSPR, with photoluminescence being polarized along the rod-axis associated with the GSPR. Interestingly, photoluminescence from disk antennas is observed to be weakly polarized along the axis of pump polarization. In the case of rods, photoluminescence is enhanced at the GSPR, when the pump polarization is aligned with the associated rod axis. For a physical explanation of experimental observations, we introduce an intuitive analytical model. The model states that the enhancement of photoluminescence, associated with a particular GSP mode, scales with the overlap between the GSP mode and the intensity distribution of the pump field in the metal. The idea that plasmonically enhanced gold photoluminescence scales with the spatial overlap between pump field and radiating GSP mode in the metal was qualitatively suggested by Hailong Hu *et. al.* [93], based on a study of gold disks. The presented study solidifies this proposition, with the development of an analytical description and an experimental demonstration of a photoluminescence spectrum, modulated by the pump polarization for non-degenerate plasmonic resonances.

For single photon generation the resonant enhancement of background metal luminescence is problematic, as it is desirable to tune antenna resonance to the emission wavelength of the quantum emitter. The intuitive picture of photoluminescence scaling with pump and antenna mode overlap in the metal suggests that the effect is most significant for strongly confined plasmonic modes, as the modal energy in the metal increases with confinement. However, the gold photoluminescence is less significant at long wavelengths, partially due to an increasing negative permittivity of the gold, pushing the field to the

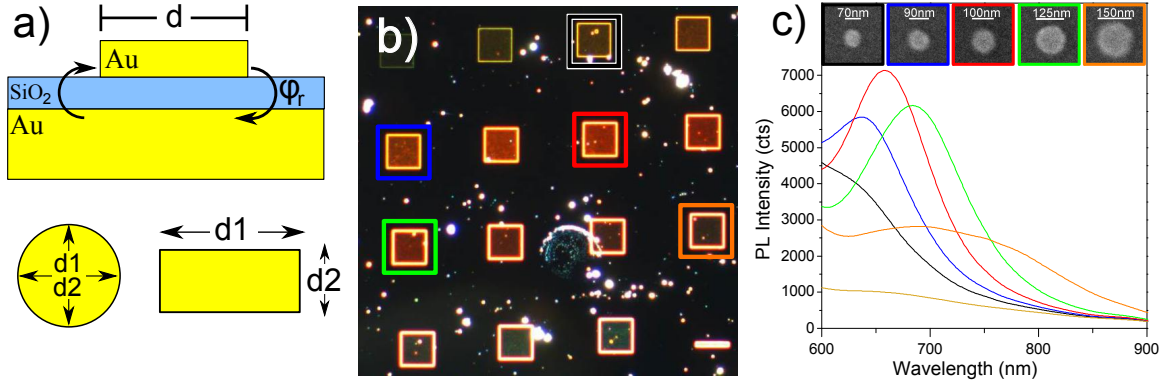


Figure 8.1: (a) Schematic of nano patch antenna, the GSP standing wave resonance is set by the dimension d of the top particle. Top particles defined either as disks ($d_1=d_2$) or rods ($d_1 \neq d_2$). (b) Dark-field image of disk arrays with disk diameter increasing in a conventional reading directing. The array color represents the spectral position of the resonance. Color-coded arrays were used for the experimental study. (c) Corresponding color-coded photoluminescence spectrum from arrays and electron microscopy images (top panel). Yellow color represents the plane gold film.

dielectric side and decreasing electron hole population. Gold may in this sense still be interesting to explore for quantum emitters emitting at long wavelengths such as the silicon vacancy center with a zero phonon line at 737 nm [94]. The utilizing of longer wavelength pump, cross-polarized to antenna emission, may be interesting to explore to reduce the background of gold photoluminescence.

8.2 SPONTANEOUS EMISSION FROM MULTIPLE NV-CENTERS COUPLED TO A SILVER CUBE

In section 8.1, plasmonically enhanced photoluminescence from gold was noted to compromise the single photon purity of a quantum emitter-antenna photon source. In this sense, silver is the natural choice of plasmonic material, having a large enough bandgap energy to avoid metal photoluminescence for a typical pump wavelength of 532 nm. However, in this aspect it is worth noting two additional sources of background emission. For a pump wavelength below the bandgap of silver, background emission has been observed from polycrystalline silver processed by electron beam lithography [95], or a Raman process occurring in small metallic gaps [96]. With the goal of avoiding the reported background from polycrystalline silver, we explore the option of utilizing chemically synthesized monocrystalline silver cubes as nano antennas. Monocrystalline silver further has the benefit of reduced ohmic loss as loss from electron scattering on grain boundaries or lattice defects is absent [97]. The smooth well-defined geometry of chemically synthesized nano particles improves the reproducibility of single particle experiments, while lossy adhesion layers [98, 99] may be avoided by this approach. Lossy adhesion layers are typically necessary for nano antennas fabricated by electron beam lithography.

Appendix B constitutes the initial study into utilizing a monocrystalline nano cube for enhancing the spontaneous emission properties of NV-centers coupled to the cube antenna. The cube supports a dipolar LSP mode, driven either by the pump light or spontaneous emission from the NV-center (figure 8.2a). In order to directly observe the changed emission properties of the multiple NV-centers contained in the nanodiamond, the nanodiamond is precharacterized before assembly of the cube-emitter

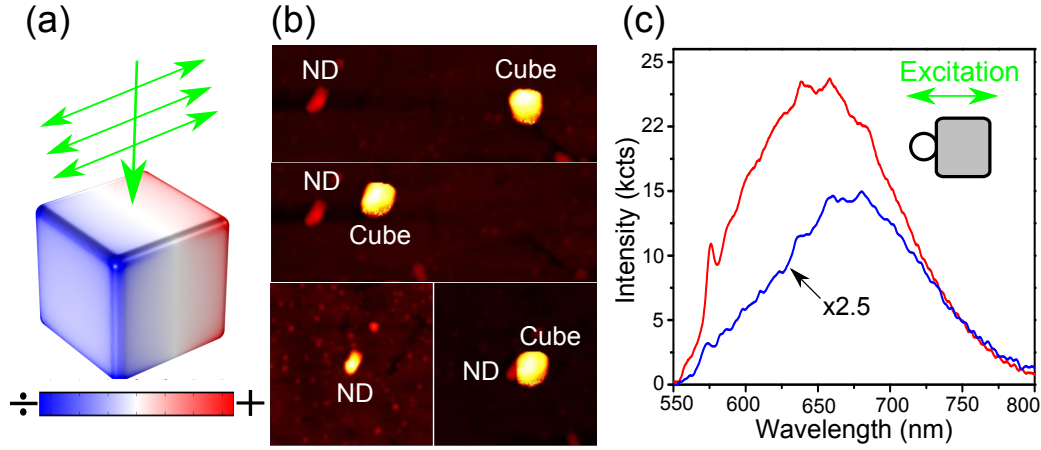


Figure 8.2: (a) Charge distribution of LSP mode supported by 100 nm silver cube, excited by a planewave at normal incidence. (b) AFM assembly of nano diamond-cube system, top and center panel illustrate AFM scans during manipulation of cube toward the nano diamond, lower panel shows the isolated nanodiamond and the final assembled system. (c) fluorescence spectrum of isolated nanodiamond (blue) and nanodiamond-cube system (red) excited for pump polarization along the nanodiamond-cube axis.

system, using an AFM (figure 8.2b). The assembled cube-emitter system exhibited a photon rate enhancement of 4.1 in the non-saturated regime, for pump polarization aligned with the nanodiamond-cube axis (figure 8.2c). For orthogonally aligned pump polarization, the detected photon rate is suppressed by a factor 2 relative to the bare nano diamond. The enhancement and suppression of photon rate is in qualitative agreement with numerically modelled near-field enhancement and suppression of pump light for the respective polarizations. A decay rate enhancement up to 4.1 is observed for the assembled system, accompanied by polarization of the spontaneous emission, as $\sim 90\%$ of the power is detected when the analyzer is aligned with the nanodiamond-cube axis regardless of pump polarization, while emission from the bare nanodiamond was preferentially polarized along the axis of pump polarization. These features constitute two improvements towards the desirable features of an ideal photon source. Further no background was observed from the monocrystalline silver cubes as cubes were not detected in fluorescence mapping, nor did the $g^{(2)}(0)$ -value degrade when a cube was pushed close to a nanodiamond containing 1-2 NV-centers. This is a promising observation for achieving a high purity photon source. The results provide a foundation for incorporating NV-centers into more complex cube-based photon sources.

8.3 NON-CLASSICAL LIGHT EMISSION FROM AN NV-CENTER IN A SILVER CUBE DIMER ANTENNA

In appendix C, we increase the complexity of the cube antenna by demonstrating non-classical light emission from a single NV-center in a cube dimer antenna. At this point it is worth noting that the nano diamond supplier was changed from the one-cube to the two-cube experiment. Over measurements of 20 nanodiamonds with a mean size of 40 nm, reported to contain 1-4 NV-centers, a $g^{(2)}(0) < 0.5$ was never observed. These nano diamonds, supplied by Adamas nanotechnology, was fabricated by Helium-ion bombardment of the nano diamonds followed by annealing [100] and used in the few emitter ex-

periment, appearing in the final part of appendix B. For the two-cube experiment presented in appendix C, MSY 0-0.05 GAF nano diamonds from Microdiamant was used, having a mean size of ~ 25 nm, each nanodiamond having less than a 0.001% chance of containing an NV-center. These nanodiamonds consistently exhibited $g^{(2)}(0) < 0.5$.

The cube dimer antenna may be understood by expanding the picture from section 2.5 of single particle LSP charge oscillations, described as a harmonic oscillator, to the picture of two coupled harmonic oscillators. The interaction of surface charges for cubes in close proximity is analogue to coupling of two spring-mass systems via a spring (figure 8.3a). The spring interaction forms new resonant modes of in-phase and anti-phase motion of the two masses. Correspondingly, cube interaction results in modes of in-phase(bonding mode) and anti-phase(anti-bonding mode) charge oscillations, for which the modal energy is shifted to respectively smaller and larger energy wrt. the isolated cube mode. The bonding cube mode illustrated in figure 8.3b is a promising antenna mode as the electric field is strongly confined to the gap, allowing for efficient coupling of an NV-center to the antenna mode, when placed in the gap. Further, the in-phase cube oscillations result in strong radiative damping, which considering equation 2.27 should result in high antenna efficiency.

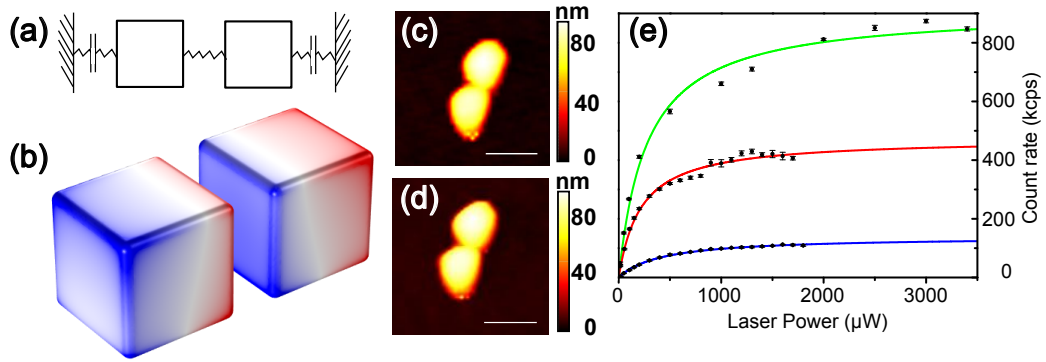


Figure 8.3: (a) analog model for LSP mode of coupled cubes, described by two coupled mass-spring-damper systems. (b) Charge distribution of bonding LSP mode supported by a coupled cube antenna, modelled for two 100 nm cubes illuminated on resonance by a planewave. AFM scan of cube dimer antenna (c) before and (d) after operation at a saturation laser power of 3.4 mW, scalebar 200 nm. (e) Measured saturation curve (point) and model fits (solid) for isolated NV-center(blue), single cube (red) and two-cube configuration (green).

In appendix C, we demonstrate non-classical light emission from a single NV-center positioned in the gap of a dimer antenna, consisting of two 100 nm monocrystalline silver cubes. For optimal coupling of NV-center emission to the antenna mode, the orientation of the in-plane NV-center dipole moment is precharacterized by rotating the pump polarization while monitoring the photon rate. For optimal alignment of antenna mode field to dipole axis, the dimer antenna is subsequently assembled by AFM manipulation with cube facets aligned normal to the dipole axis(figure 8.3c). During antenna assembly, the decay rate, spectrum, polarization, $g^{(2)}$, saturation curve and dependence of pump polarization are tracked from the bare nano diamond to the one-cube and two-cube configuration. Emission parameters are observed to continuously improve throughout antenna assembly. The assembled antenna exhibits good single photon purity, measured to $g^{(2)}(0) = 0.08$. Stable antenna operation at saturation laser powers without antenna damage is demonstrated (figure 8.3d). The experimentally detected photon

rate reaches 850 kcps (figure 8.3e), an improvement of the saturation limited photon rate by a factor 6.6, relative to the isolated nanodiamond. Weakly polarized emission from the isolated nanodiamond was demonstrated to increase from a polarization ratio of 2.1, detected along the minor and major axis, to 9 for the dimer antenna. The experimental results thereby demonstrate improvements of 3 desirable features of the ideal photon source given in figure 1.1: Photon rate, purity and polarization. A comparison of experimental data with finite element modelling indicates that the minor decay rate enhancement of 3.3 results from non-unity quantum yield, the intrinsic quantum yield of the isolated NV-center estimated to 0.35 in the particular experiment. The experimentally observed increase of photon rate is consistent with increased quantum yield of the NV-center when positioned in the antenna, and increased antenna efficiency of the dimer antenna over the single cube configuration. The improved photon rate is thereby attributed to increased quantum yield of the NV-center and high antenna efficiency.

8.4 EFFICIENT EMISSION FROM MULTIPLE NV-CENTERS IN A HYBRID BULLSEYE ANTENNA

In appendix D, we focus on improving the efficiency at which radiation from an NV-center may be collected by an objective or optical fiber. Efficient delivery of photons to a particular optical mode being desirable for technological applications (figure 1.1). For efficient photon collection, highly directional antennas with low antenna losses are required. Further, the efficiency at which photons are emitted from the NV-center may be compromised by non-unity quantum yield of the emitter. It is in this aspect desirable to improve quantum yield by accelerating the radiative decay rate of the emitter, relative to intrinsic non-radiative decay, while also achieving directional emission and low antenna losses.

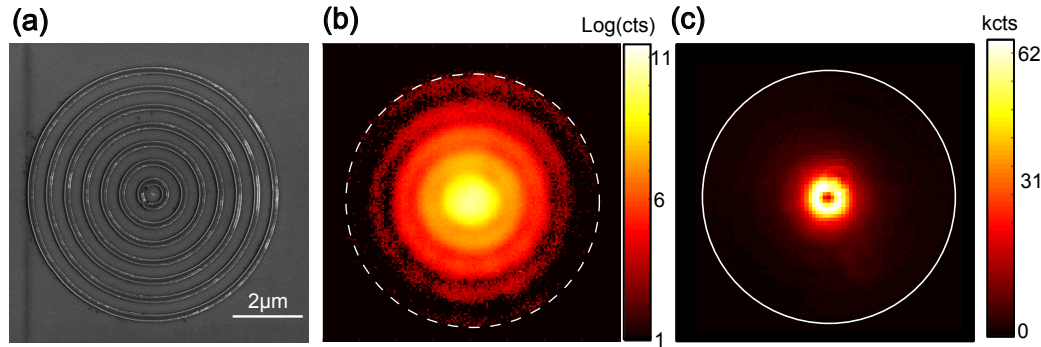


Figure 8.4: (a) Electron micrograph of fabricated bullseye antenna, the nano diamond containing NV-centers appears in the center of the bullseye. (b) log-scale fluorescence image of SPP-coupled emission from the NV-centers, scattering on bullseye grating, obtained for on-resonance filtering (650-740 nm) using 532 nm pump CW pump laser. Dashed line indicates the bullseye antenna boundary. (c) Corresponding back-focal plane image, filtered for on-resonance emission. White boundary indicates the 0.9 NA of the objective.

In appendix D, we propose a hybrid plasmonic bullseye antenna, designed for achieving highly directional emission with low antenna loss, while featuring a moderate decay rate enhancement, desirable for improving quantum yield. As the structuring of silver by electron beam lithography [95] or focused ion beam milling [101] has been observed to give rise to background emission, the antenna design is based

on a plane silver film with the aim of minimizing background. In order to minimize ohmic antenna loss, the bullseye grating is designed to support two low-loss plasmonic modes: The SPP and CGD modes introduced in section 2.3 and 2.4, supported by the high-index titania bullseye grating, separated from the plane silver film by a 15 nm low-index SiO₂ spacer layer. Numerical optimization of grating parameters for a wavelength of 670 nm and a titania height of 100 nm theoretically allowed for 85% of the power emitted by a vertical dipole to be collected with a 0.9 NA objective. Simultaneously, the decay rate is enhanced by a factor of 18 relative to vacuum. For an experimental examination of the antenna, the numerically optimized antenna is fabricated by electron beam lithography. Importantly, durable antennas could be fabricated without lossy adhesion layers at the Ag-SiO₂-TiO₂ interfaces, which would have increased antenna loss. A nano diamond containing ~ 400 NV-centers is subsequently picked up from a coverslip with an AFM and placed in the center of the bullseye antenna (figure 8.4a), using the pick and place technique [46]. As analytically described in section 4.1, NV-centers close to a silver interface efficiently decay by excitation of SPP propagating along the interface, illustrated experimentally in figure 8.4b. The SPP subsequently scatter on the periodic TiO₂ bullseye grating, resulting in directional antenna emission (figure 8.4c). The presence of decay rate enhancement was experimentally observed as a narrowband (quality factor ~ 18) resonant peak in the fluorescence spectrum at 675 nm, following the spectral shape of the modelled decay rate enhancement. The on-resonance emission is demonstrated to be highly directional by Fourier microscopy, revealing peak emission at an angle of 5° wrt. the plane normal, based on a center cut of the Fourier image. The emission pattern being in excellent agreement with numerical modelling of the designed antenna. The polarization of the emission is demonstrated to be radially polarized, imposed by symmetry considerations. Finally, the antenna was confirmed to be stable under operation at saturation laser powers, confirmed by retracing the same saturation curve upon increasing and decreasing the laser power.

The above work was conducted during a 5 month visit to Purdue University, in collaboration with members from the research groups of Prof. Vladimir Shalaev and Prof. Alexandra Boltasseva.

8.5 FABRICATION OF BRAGG MIRRORS FOR PLASMONIC CAVITIES

Beyond the main focus of this PhD on studying nano antennas for enhancement of nonclassical light emission, further work has been dedicated to supporting the complementary work of coworkers on realizing an on-chip photon source. Efficient coupling of emitter radiation to an on-chip waveguide mode may be achieved by placing the emitter in a cavity, which leaks into the waveguide. Such a Fabry-perot or standing wave cavity is commonly achieved by truncating a waveguide system with two semitransparent mirrors. A large quality factor is achievable for such systems, as scattering losses are typically small [102]. An efficient mirror for such cavities is the Bragg mirror, consisting of a refractive index periodically varying along the waveguide [103, 104]. The section widths of large and small refractive index are carefully defined, such that constructive interference is achieved in reflection and destructive interference in transmission. This section reviews the efforts in this PhD to fabricate Bragg mirrors by electron beam lithography, on two waveguide systems, a V-groove [105] or a film coupled silver nanowire. The mirror fabrication on V-grooves partially constitutes the authors contribution to the publication in appendix E.

8.5.1 V-GROOVE

We initially describe the fabrication of a PMMA Bragg mirror on a V-groove. The Bragg mirror functions by achieving constructive interference in reflection from a set of periodic dielectric ridges. Constructive interference in reflection is maximized by setting the dielectric ridge width to a quarter wavelength of the waveguide mode in the dielectric material. However, due to limitations in fabrication resolution, $3/4$ -wavelength ridges of PMMA are fabricated in this work, that is, air(w_{air}) and PMMA widths(w_{PMMA}) are set to¹:

$$w_{air} = \frac{3\lambda_0}{4n_{air}} = 525 \text{ nm}, \quad (8.2)$$

$$w_{PMMA} = \frac{3\lambda_0}{4n_{PMMA}} = 350 \text{ nm}. \quad (8.3)$$

Where $\lambda_0 = 700 \text{ nm}$ is the target wavelength of the Bragg mirror, with $n_{air} = 1$, $n_{PMMA} = 1.5$ being the refractive index for air and PMMA. Figure 8.5a illustrates a trial fabrication of a PMMA Bragg mirror on a V-Groove. The optimized fabrication appears in Figure 8.5b, having dimensions within $\pm 10 \text{ nm}$ of the design. Angled view of the groove indicates that the PMMA reach the bottom of the groove (figure 8.5c). For a confirmation of a functional Bragg mirror, the V-groove transmission was measured by illuminating the input mirror with a super continuum laser, polarized perpendicular to the groove (figure 8.5d, e). The transmission spectrum is obtained by selecting transmitted light, apparent in figure 8.5e, with a pinhole, and spectrally resolving the light using a fiber-coupled spectrometer. Normalizing the transmission spectrum with that of a V-groove without Bragg mirror should reveal a stop-band in transmission (not shown). Unfortunately, no stop-band was observed in the present work and so the

¹The effective index of the channel plasmon polariton mode propagating along the V-groove is ~ 1 at air interface, and so plasmon mode wavelength is reasonably approximated by λ_0/n

work does not appear in the final publication. The non-functional Bragg mirror is speculated to arise from the electron beam depth of focus being much smaller than the V-groove depth, causing varying ridge width down through the groove. The V-groove fabrication is in this sense difficult to characterize, as vertical variations down through the groove is not easily accessible with standard characterization techniques.

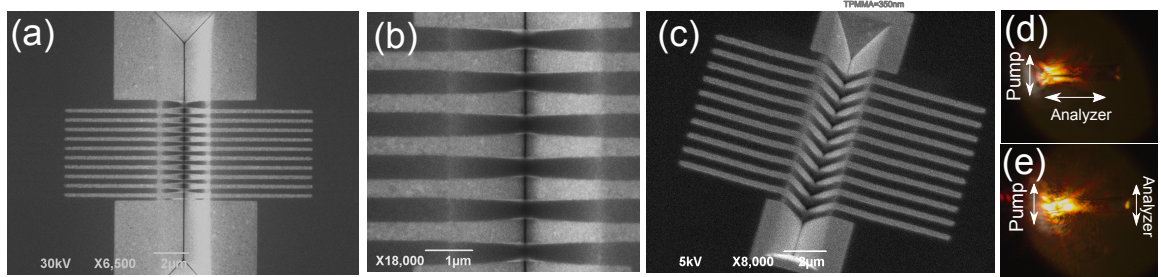


Figure 8.5: (a) Example of PMMA Bragg grating fabricated on V-groove. (b) Optimized fabrication of Bragg mirror for reflection at $\lambda_0=700$ nm (c) 35° angled view of fabrication in b, indicating that the PMMA reach the bottom of the groove. Transmission measurement of the V-groove appearing in b,c using a super continuum laser, polarized perpendicular to the groove for analyzer (d) along or (e) perpendicular to the groove.

8.5.2 FILM COUPLED NANO WIRE

Another promising plasmonic cavity has been proposed [106] in the form of a silver nano wire separated from a silver film by a structured dielectric spacer layer. For dielectric spacer, we use the electron beam resist hydrogen silsesquioxane (HSQ) (XR-1541-002, Dow Corning), diluted 1:3 with MIBK in-house, for a target spacer thickness of 20 nm. The corresponding effective index ($N_{eff}^{air} = 1.57$; $N_{eff}^{HSQ} = 2.03$) of the mode propagating along the wire-film gap is obtained at the target vacuum wavelength of 700 nm from finite element modelling, and Bragg mirror dimensions were fabricated for $1/4$ or $3/4$ the wavelength. As the silver wires spincoated on the sample are randomly oriented, a procedure was developed for alignment of the exposure pattern to a randomly oriented and positioned nano wire. Initially, gold alignment marks is introduced on the silver film by electron beam lithography, followed by spincoating of HSQ ~ 20 nm and then silver nano wires. A MATLAB script was programmed to obtain the silver wire coordinates wrt. to alignment marks, taking a dark-field image as input (figure 8.6a). A coordinate system is defined by selecting the lower left alignment mark as origin, with a mouse click. Selecting the point P2 defines the x-axis and scales the coordinate system to the real physical dimension by the known separation of origin and P2, here being $90 \mu m$. The script then plots the estimated positions of the top alignment marks P3 and P4, for confirmation of good alignment. Finally, by user selection of the nano wire end points, P5 and P6, the coordinates of the Bragg mirror exposure pattern is calculated wrt. the alignment marks and written to a txt file for import to the electron beam lithography software. Figure 8.6b gives the dark-field image of the final fabrication, after alignment of electron beam write-field to the alignment marks, exposure and development in Tetramethylammonium hydroxide 25% for 4 min followed by 2 min in Mili-Q water. Corresponding electron microscopy images are given in figure 8.6c, d. Measuring the system transmission wrt. a direct reflection on the silver film, as described in sec-

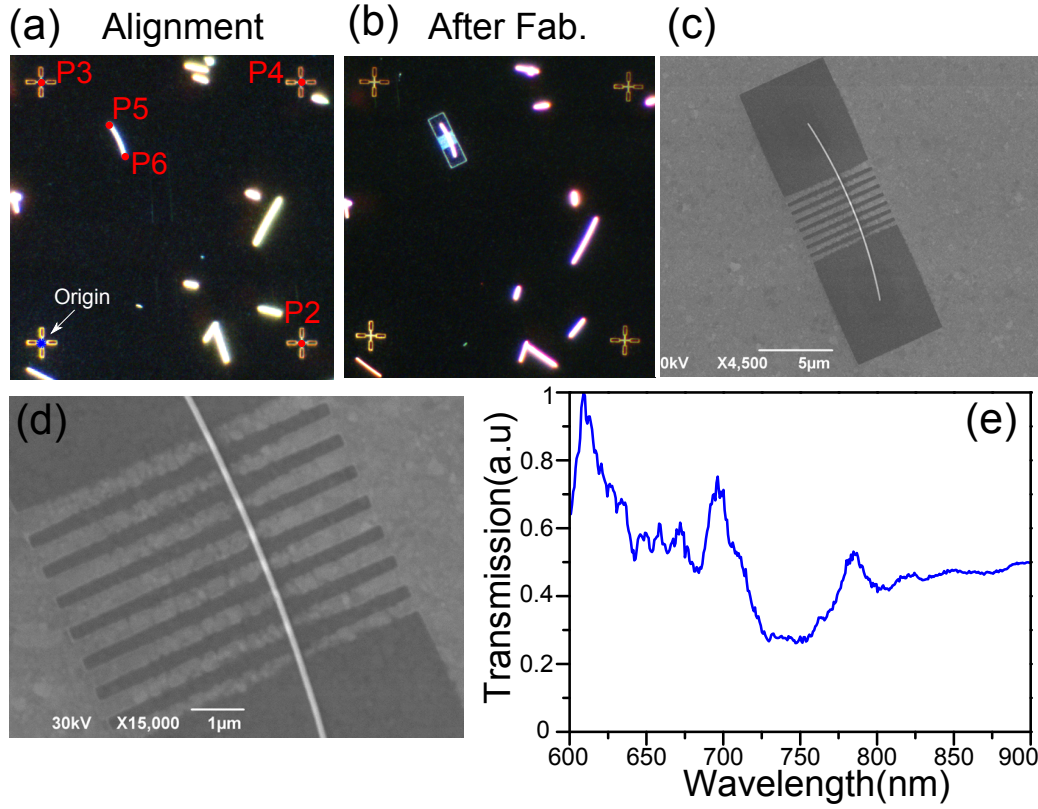


Figure 8.6: Fabrication of Bragg mirror for film coupled silver nano wire. (a) Procedure for alignment of fabrication pattern to randomly oriented nano wire. (b) Dark field image after fabrication. (c) Comparative electron micrograph and a (d) zoom in on Bragg mirror. Transmission spectrum of another nanowire indicating the presence of a stopband.

tion 8.5.1, indicates the presence of a stop-band, observed for one $1/4$ -wavelength Bragg mirror (figure 8.6e). The red shifted position of the stop-band wrt. the design wavelength of 700 nm may be a result of the gap being 15 nm (measured with AFM), rather than design of 20 nm.

9

Conclusion and outlook

The primary aim of this PhD study has been the investigation of plasmonic nano antennas for improving the spontaneous emission properties of quantum emitters, for the generation of nonclassical light. In this context, we studied the mechanism by which photoluminescence from gold is enhanced when structured to the shape of a nano patch antenna. The study demonstrated resonantly enhanced photoluminescence at the GSPR, polarized along the particle axis of resonant charge oscillation. Demonstrations of a tunable photoluminescence spectrum with the orientation of pump polarization solidified our analytical model, stating the enhancement of gold photoluminescence, relative to a plane gold film, scales with the spatial overlap between the radiating GSP mode and the pump field intensity in the metal. The model provides intuitive insight into the origin of plasmonically enhanced photoluminescence from gold. While resonant enhancement of background emission from gold is problematic for the purity of nonclassical light generation, further studies of the enhancement as a function of the GSPR spectral position and excitation wavelength are desirable. Such studies might better define a parameter space in which gold nano antennas are viable, when coupled to a quantum emitter of an appropriate emission wavelength. From a fundamental point of view, plasmonically enhanced photoluminescence from metal is an interesting study, as the largest contribution arises right at the metal side of a the dielectric-metal interface. In this sense, the study of plasmonically enhanced metal photoluminescence may contribute to the science of interfaces or expand our understanding of optics occurring in very small metal-dielectric-metal gaps.

With the ambition of minimizing background emission and unnecessary ohmic loss, antennas for enhancement of nonclassical light emission were realized using monocrystalline silver nanoparticles, plane silver films and structured high-index dielectrics, separated from metallic interfaces by low-index dielectrics as the building blocks. The experimentally demonstrated antennas yielded improvements to the desirable photon source parameters of photon purity, photon rate, efficiency and photon polariza-

tion. Further, it is encouraging to observe that the demonstrated antennas indeed can be operated at saturation laser power without apparent antenna damage, which is a prerequisite for achieving a high photon rate by taking advantage of decay rate enhancement. Monocrystalline silver cube antennas assembled with an AFM were demonstrated to be a viable approach for high-purity photon sources, as a $g^{(2)}(0) = 0.08$ was demonstrated from a cube dimer antenna. While silver corrosion may degrade the photon purity over time, a potential solution may be to operate the antenna in a vacuum- or nitrogen-purged environment. The experimentally detected photon rate of 850 kcps is encouraging as further improvements are feasible. Employing smaller nanodiamonds may allow for reduction of the dimer gap size, thereby significantly increasing the decay rate of the quantum emitter, while also red shifting the GSPR closer to the emission wavelength. Further, the efficiency of photon collection may potentially be improved by modifying the far-field emission pattern using a parabolic mirror or radiation leakage into a high-index substrate. In this sense, the large antenna efficiency of the dimer antenna is a good starting point for achieving an overall high-efficiency photon source.

Alternatively, we proposed a hybrid plasmonic bullseye antenna based on a plane silver film and a lithographically structured TiO_2 bullseye grating. The proposed design aimed at improving the efficiency by which NV-center radiation may be collected by an objective or optical fiber, while implementing a scalable fabrication design, potentially limiting background emission. The proposed design featured a narrow band decay rate enhancement, a feature experimentally observed as a resonant peak in the NV-center emission spectrum. A highly directive radially polarized emission pattern, expected from the numerical design was replicated in experiment based on backfocal imaging. The experimental observations of directive emission and a resonantly modulated emission spectrum are promising as it so far validates the main features of the proposed design. Further studies are however required on a single emitter level, to quantify the efficiency by which photons can be collected. In order to take further advantage of the narrow band decay rate enhancement, a quantum emitter featuring narrow band emission should be implemented into the antenna. The silicon vacancy center with a zero phonon line at 738 nm may in this case be a good candidate, as beyond being a narrow band emitter, the antenna loss can be expected to decrease toward longer wavelengths. For fully scalable photon source fabrication, a scalable approach is required to position single emitters in the bullseye. In this regard, electro-static emitter positioning using thin dielectric pads is a quite interesting prospect [47]. Further improvements to the antenna performance may be achieved by using a monocrystalline silver film, in a future fabrication. Implementation of the above described antenna improvements, in combination with the continuous discovery and improvement of quantum emitters, can be expected to lead to brighter and more efficient photon sources in the future.



GOLD PHOTOLUMINESCENCE
WAVELENGTH AND POLARIZATION ENGINEERING

ACS Photonics 2, 432-438, (2015)

Gold Photoluminescence Wavelength and Polarization Engineering

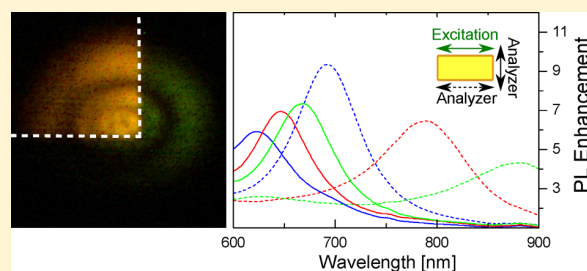
Sebastian K. H. Andersen, Anders Pors, and Sergey I. Bozhevolnyi*

Department of Technology and Innovation, University of Southern Denmark, Niels Bohrs Allé 1, DK-5230 Odense M, Denmark

Supporting Information

ABSTRACT: We demonstrate engineering of the spectral content and polarization of photoluminescence (PL) from arrayed gold nanoparticles atop a subwavelength-thin dielectric spacer and optically thick gold film, a configuration that supports gap-surface plasmon resonances (GSPRs). Choice of shapes and dimensions of gold nanoparticles influences the GSPR wavelength and polarization characteristics, thereby allowing us to enhance and spectrally mold the plasmon-assisted PL while simultaneously controlling its polarization. In order to understand the underlying physics behind the plasmon-enhanced PL, we develop a simple model that faithfully reproduces all features observed in our experiments showing also good quantitative agreement for the PL enhancement.

KEYWORDS: metal photoluminescence, plasmonics, gold nanostructures, polarization, gap surface plasmons



Photoluminescence (PL) from gold was first brought to attention in 1969 by Mooradian,¹ who observed broadband unpolarized emission from a plane gold film, which was also independent of the pump light polarization. PL from gold has conventionally been attributed to a three-step process consisting of photoexcitation of electron–hole pairs by excitation of d-band valence electrons to the s–p conduction band, relaxation of electron–hole pairs, and finally, photon emission by electron–hole recombination.² The radiative recombination of electrons and holes from a plane gold film was reported to be an extremely inefficient process with an estimated quantum yield of $\eta_0 \sim 10^{-10}$. Experimental observations of PL enhancement from rough gold surfaces was later theoretically treated by Boyd et al.³ By approximating surface roughness as a random collection of noninteracting hemispheroids, PL enhancement was assigned to the excitation of localized surface plasmons (LSPs), which resulted in improvement of both excitation and emission efficiency by enhancing the local electric field at the respective wavelengths. The electric field enhancement picture, presented by Boyd et al., has been widely adopted for the description of PL from nanoparticles for both linear^{4,5} and nonlinear excitation.^{6,7} Experimental evidence of the plasmon-enhanced PL has been demonstrated with single gold nanoparticles, for which the PL spectra were strongly modulated by a pronounced peak at the wavelength of the LSP.^{8,9} Very large enhancements in PL quantum yield (up to 10^6) have been reported when conducting ensemble measurements of gold nanorods in solutions¹⁰ and tuning the transverse and longitudinal LSPs to the excitation and emission wavelength, respectively.

More recently, increased attention has been given to the mechanism of radiative recombination of electrons and holes. The radiative decay of electron–hole pairs has been suggested¹¹ to consist of a direct contribution from

recombination into photons and an indirect contribution from excitation of an LSP that subsequently decays via both absorption (ohmic loss) and radiation in the form of PL (Figure 1). The mechanism of plasmon-enhanced PL as being

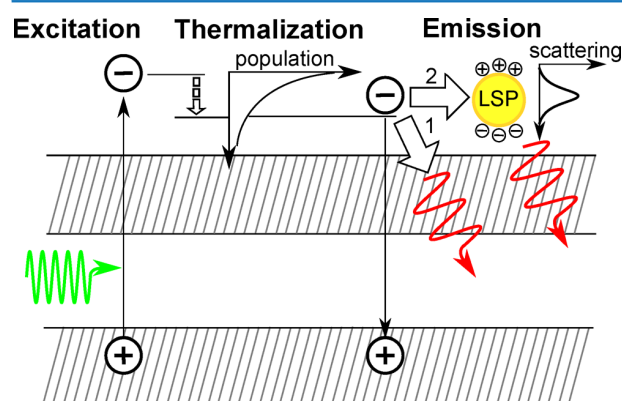


Figure 1. Sketch of the processes involved in photoluminescence from gold nanostructures.

associated with the LSP excitation is largely confirmed, since many of the LSP properties were found to be imprinted into the corresponding PL characteristics. For example, LSP wavelengths seen in scattering were found to practically coincide with the peaks in PL spectra.^{12–15} Also, the temporal delay of plasmon-enhanced PL emission with respect to its excitation is ≤ 50 fs¹⁶ and, thus, of the same order as the LSP lifetime.¹⁷ Finally, it has recently been demonstrated that

Received: December 22, 2014

Published: February 16, 2015

plasmon-enhanced PL is polarized along the resonant axis of gold nanorods^{18,19} or transverse to a silver nanowire on a dielectric spacer/gold surface.²⁰ In this regard, it is worth noting that polarization resolved PL studies of nanorods have been limited to the long-axis LSP excitation, although utilization of the transverse LSP may improve the overall control of PL polarization.

In this work, we demonstrate the PL wavelength and polarization engineering by exploiting arrayed gold nanoparticles atop a subwavelength-thin dielectric spacer and optically thick gold film, a configuration that supports gap-surface plasmon (GSP) resonances.²¹ Spectral positions of GSP resonances (GSPRs) can be straightforwardly controlled by choosing shapes and dimensions of the nanoparticles.^{22,23} Moreover, GSP-based structures in this geometry are characterized not only by large electric field enhancements at resonance, but also by ease of nanofabrication with one step of electron-beam lithography being involved.^{21,23} These properties make GSP-resonator arrays attractive for plasmon-enhanced PL wavelength and polarization engineering. Especially, the usage of arrayed rectangular shaped nanoparticles (i.e., nanobricks) allows us to illustrate the excitation dependent interplay of two nondegenerate LSPs (associated with the resonant excitation of two orthogonally propagating GSPs) and its use for the gold PL engineering. In order to understand the underlying physics responsible for spectral and polarization properties of the plasmon-enhanced PL, we develop an intuitive model incorporating the local field enhancement effects at the excitation wavelength and explicitly relating the PL occurrence to the excitation of an LSP (Figure 1), whose radiative decay generates the enhanced PL with the corresponding spectral and polarization properties. This model faithfully reproduces all PL features observed in our experiments, including the PL dependence on the excitation polarization that has recently been reported.^{20,24} Moreover, it is also found in good quantitative agreement when evaluating the PL enhancement, thus providing design guidelines for the PL wavelength and polarization engineering.

RESULTS AND DISCUSSION

Experimental Results. Let us start by considering plasmon-enhanced gold PL arising from a GSP-resonator array of circular shaped nanoparticles (i.e., nanodisks) illuminated at a wavelength of 532 nm. The GSP-resonator configuration consists of a 100 nm-thick gold film on a silicon substrate with a 20 nm thin SiO₂ dielectric spacer layer and a 50 nm top gold layer of nanodisks, defined by electron beam lithography, in a 50 × 50 μm² array with a 300 nm period (Figure 2a). The structure features Fabry–Perot like resonances,²⁵ originating from propagating GSP modes that for certain wavelengths (or disk sizes) form standing wave LSPs due to efficient reflection at disk boundaries. Here, we only consider the fundamental GSPR, which is (within the metamaterial community) also known as the magnetic resonance,²⁶ whose LSP wavelength can be simply controlled by varying the diameter of the disks. In fact, we vary the LSP wavelength from ~600–780 nm by varying the average nanodisk diameter from ~70–150 nm, as evident from correlating scanning electron microscopy (SEM) images and dark-field scattering spectra (Figure 2d). Note also a distinct dark-red color of a nanodisk array, observed with a dark field microscopy, originating from the strong scattering of light at the corresponding LSP wavelength (Figure 2b). The LSP

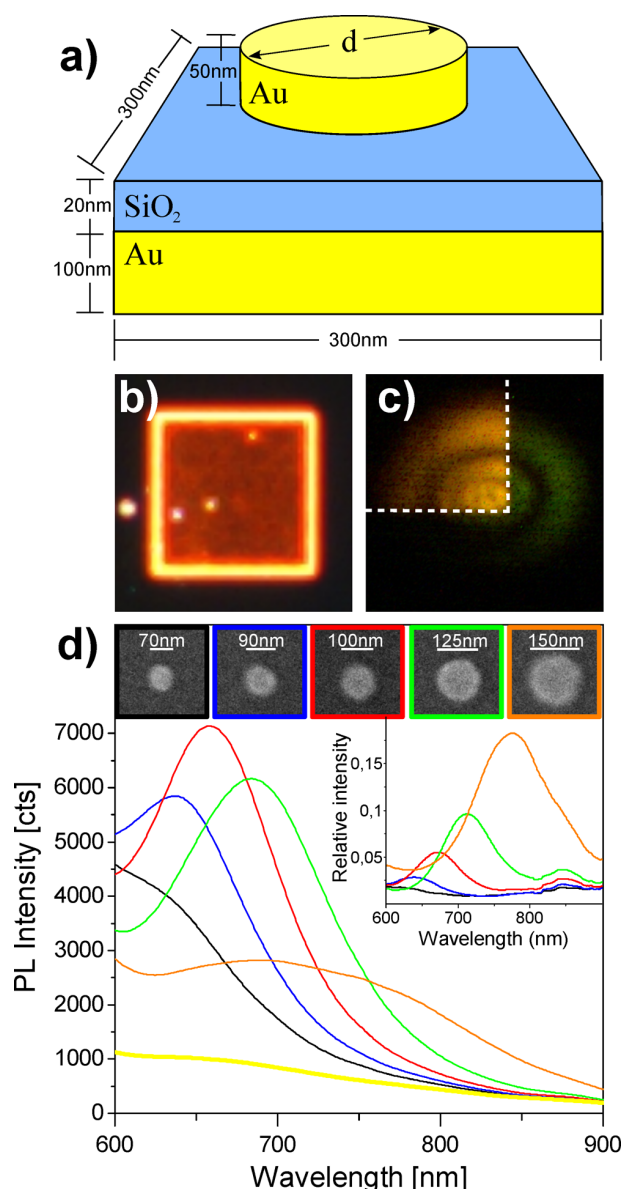


Figure 2. (a) Schematic of unit cell dimensions for nanodisk GSP-resonator array. (b) Dark-field image of 50 × 50 μm² nanodisk array with $d = 100$ nm. (c) Plasmon-enhanced PL arising from the overlap of the excitation laser spot with the nanodisk array imaged in (b; indicated by the dashed boundary), and the surrounding plane SiO₂/gold surface. (d) PL spectra of five nanodisk arrays and surrounding plane SiO₂/gold surface (thick yellow line); the corresponding scattering spectra relative to silver mirror reflection is given in inset, with SEM micrographs of the nanodisks given in top panel.

modes have apparent influence on the strength and spectral distribution of the PL signal, as illustrated by imaging the PL with the excitation laserspot only partially overlapping the nanodisk array (Figure 2c). In order to quantify the influence of GSP-resonator arrays on the PL signal, we have recorded the PL spectrum for each array (Figure 2d) using a linear polarized pulsed laser at wavelength of 532 nm, weakly focused on the sample to ensure a broad excitation covering the center portion of the array. The PL count was found linearly dependent on the excitation power, confirming that the observed PL is related to single photon absorption. The PL from the plane gold film is

seen to gradually decrease in intensity toward long wavelengths, since the population of excited charge carriers decreases for energies being further away from the excitation. Contrary, the PL spectra from the nanodisk arrays are strongly modulated, featuring higher photon counts and reaching maxima that are progressively red-shifted when increasing the disk diameter. The plasmonic origin of the observed PL enhancement is confirmed by a direct comparison of the PL and scattering spectra (Figure 2d) that reveal a close resemblance between spectral peak positions.

The decreasing PL intensity for LSP wavelengths below 650 nm, we attribute to increased nonradiative damping of the LSP from interband transitions in the gold, which is well-known to set in for wavelengths <650 nm.²⁷ Interestingly, the PL intensity also falls off at a significant rate for the LSP wavelengths red-shifted beyond 650 nm, despite the fact that the radiative damping of the LSP is increasingly dominating over the nonradiative decay channel with increasing particle size. The same effect has previously been attributed to the decreasing population of nonequilibrium charge carriers for plasmon excitation at long wavelengths.²⁴ In order to account for charge carrier population effects, we obtain the PL enhancement of the respective nanodisk arrays (Figure 3a)

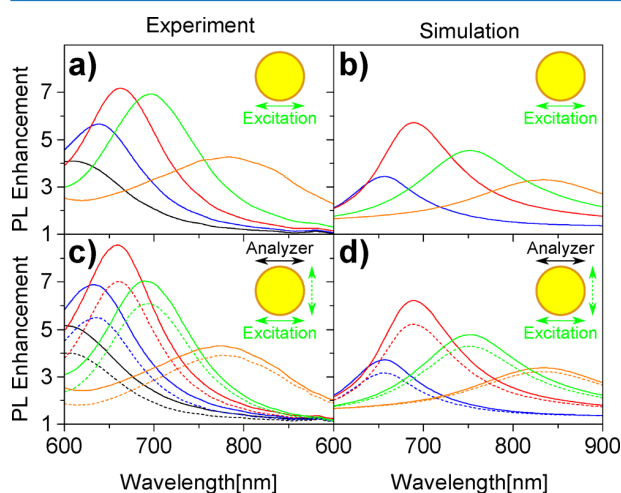


Figure 3. PL enhancement of nanodisk GSP-resonator arrays relative to plane SiO₂/gold film, with array color identifier established in Figure 2d, without analyzer (a) experiment and (b) simulation, and with analyzer for excitation polarized parallel (solid) and perpendicular (dashed) to analyzer given for (c) experiment and (d) simulation. In simulations, disk diameters are 80 (blue), 100 (red), 120 (green), and 140 nm (orange).

by normalizing the PL spectra with an identically measured PL spectrum of the plane gold film, for which the PL intensity should be directly proportional to the excited charge carrier population. It is important to note that the PL spectra arise from a large excitation spot area on the array containing both areas of weak PL (gold film) and strong PL (nanodisks). The PL enhancement therefore represents the surface average enhancement, which is very different from single nanoparticle PL enhancement for which only the nanoparticle area is considered. The PL enhancement is decreasing for LSP wavelengths >650 nm, hereby indicating a secondary effect (beyond a decreasing charge carrier population) is contributing to the decline in PL intensity. As will be clear from the

proposed theoretical model, plasmon-enhanced PL results from the spatial overlap between the absorption profile within the metal, at the excitation wavelength, and LSP mode profile. The decline in PL enhancement at long LSP wavelengths is a consequence of decreasing overlap, resulting from the gold becoming more metallic at long wavelengths, thus, lowering the fraction of LSP mode energy in the metal. Furthermore, the enhanced absorption via off-resonant LSP excitation at the pump wavelength is progressively diminished with increased LSP red-shift from excitation wavelength. Finally, we note that the PL peaks, in accordance with the LSP resonances observed in scattering, spectrally broaden with increasing particle size. The broadening of the line width results from increasing the radiative LSP damping, that rapidly increases with the particle size. In principle, one may narrow the spectral width of PL peaks by suppressing the influence of the electric dipole moment of the LSP mode.²⁸ The cost, however, is a reduced PL enhancement because of the decreased LSP quantum yield.

We now consider the polarization-dependent properties of the nanodisk arrays. By inserting an analyzer in the PL collection path, the PL polarization was checked as a function of excitation polarization (Figure 3c). Despite the fact that nanodisks possess two orthogonal degenerate LSP modes, the PL is slightly polarized along the direction of excitation, as PL intensity is consistently strongest in the parallel analyzer-excitation configuration. We would like to emphasize that the same conclusion can be reached by utilizing an orthogonally oriented analyzer [see Figure S1 in Supporting Information (SI)]. The observation can be explained by the absorption profile in the metal spatially overlapping more strongly with the copolarized LSP mode profile compared to the orthogonally polarized, thus resulting in an uneven excitation of the LSP modes. As a measure of the polarization contrast of PL, we define the quantity $\alpha = |I_{\parallel} - I_{\perp}| / (I_{\parallel} + I_{\perp})$ at the LSP wavelength, where I_{\parallel} and I_{\perp} are, respectively, the PL intensity polarized parallel and perpendicular to excitation. For the nanodisk arrays, we find a value of $\alpha \approx 0.1$ for the peak PL intensity (Figure 3c, red curve), with the quantity decreasing for longer wavelengths.

It is clear from the above discussion that nanodisk arrays allow for an enhanced and spectrally engineered PL emission, with the polarization contrast being weak due to the degeneracy of orthogonal LSP modes. As a way to control the polarization properties of plasmon-enhanced PL, we now study nanobrick GSP-resonator arrays, featuring two orthogonal nondegenerate LSPs that can be spectrally tuned by adjusting the size and aspect ratio of the nanobricks. The nanobricks were prepared with the same layer thickness and array configuration as the nanodisk arrays. Three arrays with average geometrical cross sections of nanobricks being 110×70 , 130×72 , and 150×77 nm² (Figure 4a) were investigated (Figure 4b,d). The corresponding PL spectra (Figure 4b) show two peaks resulting from the two orthogonally polarized LSP modes associated with the short and long axis, as confirmed by scattering measurements (see Figure S2 in SI). Consequently, the polarization resolved PL spectra feature individual peaks related to the correspondent LSPs, resulting thereby in strongly polarized emission at both LSP wavelengths (Figure 4d). For excitation polarized along the long axis of the nanobrick, the polarization contrast at the corresponding long wavelength LSP is as large as $\alpha \approx 0.7$ (Figure 4d, red curves), with an average value of ~ 0.6 for the three cases considered. For the short wavelength LSP, the polarization contrast is slightly lower with

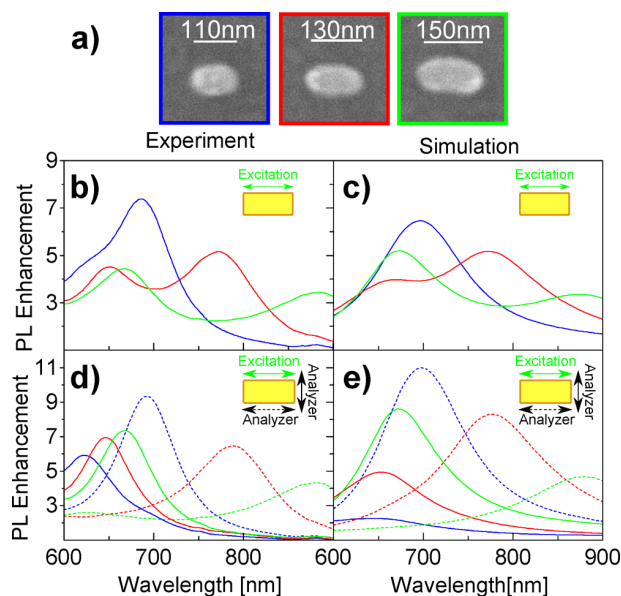


Figure 4. (a) SEM micrographs of nanobrick GSP-resonators with frame color identifier blue, red, and green. (b–e) PL enhancement of nanobrick GSP-resonator arrays relative to plane film for excitation polarized along the long axis of the brick; (b) measured and (c) calculated PL spectra for detection without analyzer; (d) experiment and (e) simulation for PL spectra detected with analyzer along the long axis of the brick (solid) and for orthogonal orientation (dashed). In simulations, the geometrical cross sections of nanobricks are 80×40 (blue), 105×55 (red), and 130×70 nm² (green).

$\alpha \approx 0.5$ for the two largest nanobrick configurations, while the latter configuration (Figure 4d; blue curves) demonstrates $\alpha \approx 0.3$. It is evident from the presented α -values that nanobrick arrays facilitate the possibility (within a desired wavelength range) to engineer the polarization of PL from being completely unpolarized to strongly polarized by choosing nanobricks of proper size and aspect ratio. In this regard, it is worth noting that the nature of PL does not allow for complete polarization contrast ($\alpha = 1$) since the omni-present PL contribution from the direct radiative decay of an electron–hole pair, although it might be small compared to the plasmonic contribution, is unpolarized. As a final comment, it should be emphasized that the total PL spectrum of nanobrick arrays can be modified by varying the angle of the excitation polarization relative to the nanobrick axes (Figure 5), which alters the relative contribution from the two nondegenerate orthogonal LSPs. Similar to the case of the nanodisk array, the largest contribution to PL from an LSP mode is achieved when the excitation polarization is aligned with the associated axis, as the absorption profile in the metal achieves the largest spatial overlap with the LSP mode profile (see insets in Figure 5). The PL dependency on excitation polarization is observed to weaken when the LSP wavelength moves away from excitation wavelength. Note that this effect has also been observed for the other two nanobrick arrays (see Figure S3 in SI).

Theoretical Discussion. As a way to better understand the underlying physics behind PL spectra from gold nanostructures, we develop a theoretical model that (despite its simplicity) is able to account for all the features observed in the above experiments. Following the discussion of related work,^{11,13,24} the generation of PL is considered as a three-step process (Figure 1) involving excitation of electron–hole pairs, thermal-

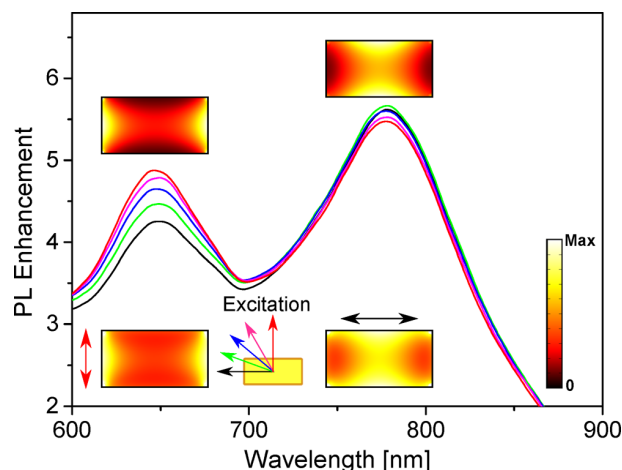


Figure 5. Measured PL enhancement spectra of nanobrick GSP-resonator array for the excitation polarization angled with respect to the long axis of the brick at 0° (black), 20° (green), 40° (blue), 60° (pink), and 90° (red), as illustrated by colored arrows in the lower part of the figure. Insets show simulations of the field intensity distribution ($|E|^2$) in the gold nanobrick at the LSP resonances (upper panels) and at the excitation wavelength for polarization along the two main axes (lower panels).

ization (giving rise to broad distribution of electron energies), and relaxation either via direct radiative recombination or indirectly by excitation of an LSP that may subsequently decay radiatively as PL or nonradiatively (ohmic loss). As a starting point, we assume the three processes to be independent, meaning that, for a plane gold film, in which the plasmonic relaxation path is not an option, we may write the position-dependent PL intensity as

$$I_{\text{PL}}^{\text{film}}(\omega_{\text{ex}}, \omega, \mathbf{r}) = U(\omega_{\text{ex}}, \mathbf{r})f(\omega_{\text{ex}}, \omega)\eta_0 \quad (1)$$

where ω is the angular frequency, ω_{ex} is the excitation frequency, \mathbf{r} is the coordinate vector, $U = 1/2\omega_{\text{ex}}\epsilon_0\epsilon_{\text{au}}''(\omega_{\text{ex}})|\mathbf{E}(\omega_{\text{ex}}, \mathbf{r})|^2$ is the Ohmic heating density that represents the rate of excitation, $\epsilon_0 = 8.854 \times 10^{-12}$ F/m is the vacuum permittivity, ϵ_{au}'' is the imaginary part of the relative gold permittivity, $\mathbf{E}(\omega_{\text{ex}}, \mathbf{r})$ is the local electric field, f represents the probability density distribution of excited electron–hole pairs, and $\eta_0 \sim 10^{-10}$ is the quantum yield. Note that f has the property that $\int_0^{\omega_{\text{ex}}} f(\omega_{\text{ex}}, \omega) d\omega = 1$, which ensures that the total PL intensity (obtained by integrating eq 1 over volume and frequency) divided by the total power dissipated in the metal at the excitation frequency equals η_0 , as originally defined by Mooradian.¹ If we now consider a metallic nanostructure, there is a probability $P(\omega, \mathbf{r})$ for relaxation of excited electron–hole pairs by excitation of an LSP, which leads to the position-dependent PL intensity

$$\begin{aligned} I_{\text{PL}}^{\text{ns}}(\omega_{\text{ex}}, \omega, \mathbf{r}) &= U(\omega_{\text{ex}}, \mathbf{r})f(\omega_{\text{ex}}, \omega)[\eta_0(1 - P(\omega, \mathbf{r})) \\ &\quad + P(\omega, \mathbf{r})\eta_{\text{lsp}}] \\ &\approx U(\omega_{\text{ex}}, \mathbf{r})f(\omega_{\text{ex}}, \omega)[\eta_0 + P(\omega, \mathbf{r})\eta_{\text{lsp}}] \end{aligned} \quad (2)$$

where the validity of the last equality owes to $\eta_{\text{lsp}} \gg \eta_0$, since the quantum yield η_{lsp} of the LSP is determined by the ratio of scattering to extinction cross section at resonance and, hence, typically $\eta_{\text{lsp}} > 0.1$ for particles larger than a few tenths of

nanometers.¹¹ In order to proceed, we note that the probability of an excited electron–hole pair at position \mathbf{r} to relax via LSP excitation is proportional to the local density of states of the LSP mode at that position.²⁹ Here, we approximate the probability of LSP excitation by the local field intensity enhancement at resonance, that is,

$$P(\omega, \mathbf{r}) = \beta \frac{|\mathbf{E}(\omega_{\text{LSP}}, \mathbf{r})|^2}{E_0^2} N(\omega) \quad (3)$$

where β is a proportionality factor and \mathbf{E} is the electric field in the metal of the LSP mode, which we find by numerical means (using the commercial finite element software Comsol Multiphysics) by plane wave excitation with amplitude E_0 at resonance frequency ω_{LSP} . The fact that probability of LSP excitation $P(\omega, \mathbf{r})$ should decrease for frequencies that deviate from the resonance LSP frequency is accounted for by the function $N(\omega)$, which has the property that $N(\omega_{\text{LSP}}) = 1$ and decreases toward zero away from resonance. In this work, we extract $N(\omega)$ from calculation of the absorption spectrum of GSP-resonator arrays, but N could also be approximated with a Lorentzian function whose center frequency and line width equals the resonance frequency and line width of the GSPR, respectively.

We can now setup a simple expression for the enhancement factor (EF) of PL intensity by the ratio of eqs 1 and 2 integrated over the respective metal volumes, while taking into account all LSPs (denoted by integer i) found in the system, that is,

$$\text{EF}(\omega_{\text{ex}}, \omega) = \frac{Q_{\text{ns}}}{Q_{\text{film}}} \left[1 + \frac{1}{\eta_0} \sum_i \beta^{(i)} \eta_{\text{LSP}}^{(i)} S^{(i)} N^{(i)} \right] \quad (4)$$

where $Q_j(\omega_{\text{ex}}) = \int_{\text{metal}} U(\omega_{\text{ex}}, \mathbf{r}) dV$ is the power absorbed in the metal (subscript j = ns or film), and S is defined as

$$S(\omega_{\text{ex}}, \omega_{\text{LSP}}) = \frac{1}{E_0^2 Q_{\text{ns}}} \int_{\text{ns}} U(\omega_{\text{ex}}, \mathbf{r}) |\mathbf{E}(\omega_{\text{LSP}}, \mathbf{r})|^2 dV \quad (5)$$

and characterizes the spatial overlap between the absorption distribution at excitation frequency and the mode intensity at the LSP frequency. The different field distributions are exemplified in insets of Figure 5, hereby visually underlining that (for a given LSP mode) the spatial overlap S depends on the excitation polarization. Note that the factor in front of the square bracket in eq 4 accounts for the increased absorption at excitation frequency due to an increased amount of metal in GSP-resonator arrays relative to the metal film or due to any resonance effects at the excitation frequency, while the first term inside the square brackets represents PL from direct radiative decay of excited electron–hole pairs. The sum inside the square brackets, on the other hand, describes the plasmonic contribution to PL, with the integer i representing all different LSPs that can be excited. For example, in considering detection of the total PL from GSP-resonator arrays we must take into account the two orthogonal LSPs whose contribution to the PL spectrum depends on the excitation polarization (i.e., S depends on excitation polarization via U). In the different case of an analyzer in front of the detector (see, e.g., Figure 4e), we calculate the PL response by properly weighting the contribution from the two LSP modes, with the modes of orthogonal (with respect to the analyzer axis) polarization being completely suppressed. It is interesting to note that the plasmonic part in eq 4 resembles recently derived formulas⁴

that have been used to accurately account for experimental observations. As a final comment, it ought to be mentioned that the direct applicability of eq 4 rests on the knowledge of the product $\beta^{(i)} \eta_{\text{LSP}}^{(i)}$ in which $\eta_{\text{LSP}}^{(i)}$, as previously stated, can be estimated from the associated optical cross sections. No such simple estimation of $\beta^{(i)}$ exists (to the best of our knowledge), but it can be used as a fit parameter to experimental PL spectra. Alternatively, as adopted in this work, we can rely on studies of PL from spheres¹¹ and nanorods,¹⁹ which conclude that the PL quantum yield related to plasmonic resonances is to a large degree independent of size and shape due to the counteracting processes of decreasing probability of electron–hole pair relaxation via LSP excitation and increasing radiative decay of the LSP when the size of the nanostructure increases. As such, we can to a first approximation assume $\beta^{(i)} \eta_{\text{LSP}}^{(i)}$ constant, with a value of 6×10^{-11} used throughout this work.

Having developed a simple expression for the plasmon-assisted PL enhancement (eq 4), we apply the formalism to the nanodisk and brick arrays studied in this work (Figures 3b,d and 4c,e). Note that the dimensions of the nanoparticles used in calculations were chosen to demonstrate the plasmon-induced influence on PL when the LSP is scanned through the wavelength range ~ 600 – 900 nm. As such, the dimensions of the simulated GSP-resonator arrays were adjusted wrt the fabricated arrays in order to match resonance wavelength. In fact, since the shapes of fabricated nanodisks and nanobricks were not ideal (Figures 2d and 4a), their dimensions are not well-defined. Additionally, the thickness and refractive index of the evaporated silica spacer layer are difficult to control.²¹ Overall, the modeled PL enhancement is in good agreement with experimental values and reflects the observed spectral tendencies. For nanodisk arrays, it is clear that the model predicts a maximum PL enhancement for LSP wavelengths near 680 nm (Figure 3b), with an associated maximum polarization contrast of $\alpha \sim 0.1$ (Figure 3d). This is in line with experiments, though calculations predict a faster decrease in PL intensity for LSP wavelengths below ~ 680 nm; a fact that we relate to the additional damping included in calculations, hereby leading to too strong contribution from interband transitions. Importantly, it should be stressed that in calculations the plasmonic contribution to the PL intensity lies solely in the parameter S (eq 5), meaning that large plasmon-enhanced PL can be reached by strong field enhancement at the excitation and LSP wavelengths together with a significant spatial overlap of the corresponding fields. Finally, let us consider calculations of PL from nanobrick arrays. In agreement with experimental results, the total PL enhancement features two peaks when the two orthogonal LSPs are spectrally separated (Figure 4c), while detection of PL with analyzer along either of the two nanobrick axes confirms the possibility of strongly polarized PL (Figure 4e). Neglecting the smallest array of nanobricks due to a strongly damped short-axis LSP, the remaining two configurations (Figure 4e, red and green curves) show average polarization contrast of $\alpha \sim 0.5$ at the long and short LSP wavelength, respectively.

In the above presented work, the engineering of metal PL has been demonstrated within the spectral range 600–900 nm, which is not an arbitrary chosen wavelength interval but ultimately related to interband transitions of gold, thereby determining the availability of electrons and holes to recombine at a particular wavelength. Furthermore, the strong plasmon-induced modulation of PL relies on gold being a relative good conductor in the considered wavelength range. Therefore, the

engineering of metal PL in a different spectral range requires the usage of another plasmonic metal with a suitable absorption band. For example, silver with strong absorption at ~ 400 nm is a potential option for transferring PL engineering to the blue and green spectral range.³⁰

CONCLUSION

In summary, we have demonstrated the flexibility of the GSP-resonator configuration for engineering the spectral and polarization content of gold PL by defining, in a single electron-beam lithography step, the dimensions of arrayed gold nanoparticles atop a subwavelength-thin dielectric spacer on an optically thick gold layer. The configuration features LSP modes that are excited by relaxation of excited charge carriers in gold and resulting in PL enhancement (at the geometrically defined LSP wavelength) via the LSP radiative decay. Broad wavelength tunability of PL enhancement was demonstrated, for which limiting factors were identified to be interband damping of LSP mode (short wavelengths) and diminished LSP excitation resulting from decreasing mode confinement in metal (long wavelengths). The PL was found to be either weakly or strongly polarized depending on whether nanoparticles exhibited degenerate (nanodisk) or nondegenerate (nanobrick) orthogonal LSP modes. Additionally, we have shown how the relative contributions of the two orthogonal LSP modes are influenced by the polarization of the pump light. In order to understand the underlying physics behind plasmon-enhanced PL, we have developed a simple model that takes into account the two relaxation paths of excited electron-hole pairs in metallic nanostructures, while relating local field enhancement effects at the excitation wavelength to enhanced PL emission at the LSP wavelength through the spatial overlap of absorption and LSP intensity profiles. The model faithfully reproduces all the PL features observed in experiment, including the dependence on excitation polarization and the strongly polarized nature of PL from nanobrick arrays with good quantitative agreement on PL enhancement values. We believe that the presented systematic study clearly demonstrates the potential of PL engineering by utilizing plasmonic resonances, with the developed theoretical model allowing one to properly choose system parameters, thereby providing guidelines for the wavelength and polarization engineering of PL. The results obtained might, in our opinion, also find implications in engineering of two-photon luminescence⁷ and cathodeluminescence.³¹

METHODS

Fabrication. Samples were prepared on a diced silicon substrate by e-beam evaporation of 100 nm gold (Au) and RF-sputtering of 20 nm silicon dioxide (SiO_2) with intermediate 3 nm layers of titanium (Ti), added for adhesive purposes. The sample were then spin-coated with PMMA 2A 950k to ~ 100 nm thickness and prebaked for 90 s at 180 °C. Arrays of 300 nm period disks or bricks were then defined by electron beam lithography (JSM-6400LV JEOL), developed in methyl isobutyl (MIBK)/isopropyl alcohol (IPA) 1:3 (30 s) with subsequent IPA stopper (30 s) and blow-dried with nitrogen. Finally, 3 nm Ti/50 nm Au was deposited by thermal evaporation, and lift-off was done by leaving sample in acetone overnight (~ 10 h). The sample was removed from the acetone bath under constant rinse of IPA and subsequently blow-dried with nitrogen. Disk

and brick arrays were prepared under two separate fabrication cycles.

PL Measurement. PL spectra of the prepared GSP-resonator arrays were obtained on a PL spectroscopy setup constructed on a IX73 microscope (Olympus). The arrays were excited by a linearly polarized, pulsed laser (LDH-P-FA-530L Pico Quant) at 532 nm wavelength and 40 MHz repetition rate, resulting in 1.2 mW average power incident on sample. A half-waveplate were inserted in excitation path for rotating excitation polarization. Excitation and back collection of PL were done through a $\times 100$ IR objective (NA 0.95), defocused to ensure broad excitation of the center portion of the array. The defocused spot was continuously reproduced by defocusing on the plane gold film to achieve the same spot image observed on CCD (wrt image markers). PL was separated from excitation by a dichroic mirror and subsequent LP filter (band edge 550 nm) and fiber coupled to a grating spectrometer (QE65000 Ocean Optics). For measurements of fluorescence polarization, an analyzer was fitted in front of the fiber coupler.

Scattering Measurement. Scattering spectra were obtained using a dark-field spectroscopy setup on a BX51 microscope (Olympus). The arrays were illuminated by a halogen lamp at highly oblique angles $\sim 70^\circ$, while scattered light, was collected in the range $0\text{--}64^\circ$ by a $\times 100$ (NA 0.9) objective. The collection of scattered light was restricted to a 32 μm spot (centered on array) by a pinhole in the objective image plane and fiber coupled to a grating spectrometer (QE65000 Ocean Optics). For measurements of polarization of scattered light, an analyzer was inserted in front of the pinhole. Scattering spectra were obtained relative to a reflection measurement of a silver mirror.

Simulations. All modeling results are performed using the commercially available finite-element software Comsol Multiphysics, version 4.3b. In the calculations, we only model a single unit cell of the two-dimensional GSP-resonator arrays, applying periodic boundary conditions on the vertical sides of the cell. The lower boundary of the simulation domain, representing the truncation of the optically thick gold substrate, behaves as a perfect electric conductor, while the air domain above the GSP-resonator array is truncated using a port boundary. The same port boundary is also used for excitation of plane waves that propagate normal to the gold surface. Throughout this paper, we use a unit cell period of 300 nm, a dielectric spacer thickness of 20 nm, and nanostructures of height 50 nm. The spacer is assumed to be silicon dioxide with a constant permittivity of 2.1, while the permittivity of gold is described by interpolated experimental values.²⁷ The imaginary part of the gold permittivity is increased by four times as a way of modeling the increased electron relaxation rate due to surface scattering and grained boundaries, and the presence of 3 nm thin Ti adhesion layers.^{32,33}

ASSOCIATED CONTENT

Supporting Information

Comparative PL spectra of disk arrays for excitation co- and cross-polarized to either horizontal or vertical analyzer (S1); scattering and PL spectral comparison for analyzer probing polarization along short or long axis of brick arrays (S2); PL spectra of brick arrays for excitation polarized along short or long axis (S3). This material is available free of charge via the Internet at <http://pubs.acs.org>.

■ AUTHOR INFORMATION

Corresponding Author

*E-mail: seib@iti.sdu.dk.

Notes

The authors declare no competing financial interest.

■ ACKNOWLEDGMENTS

We acknowledge financial support for this work from the Danish Council for Independent Research (the FNU Project, Contract No. 12-124690) and the European Research Council, Grant 341054 (PLAQNAP).

■ REFERENCES

- (1) Mooradian, A. Photoluminescence of metals. *Phys. Rev. Lett.* **1969**, *22*, 185–187.
- (2) Apell, P.; Monreal, R.; Lundqvist, S. Photoluminescence of noble metals. *Phys. Scr.* **1988**, *38*, 174–179.
- (3) Boyd, G. T.; Yu, Z. H.; Shen, Y. R. Photoinduced luminescence from the noble metals and its enhancement on roughened surfaces. *Phys. Rev. B* **1986**, *33*, 7923–7936.
- (4) Lumdee, C.; Yun, B.; Kik, P. G. Gap-plasmon enhanced gold nanoparticle photoluminescence. *ACS Photonics* **2014**, *1*, 1224–1230.
- (5) Lee, J.; Govorov, A. O.; Dulka, J.; Kotov, N. A. Bioconjugates of CdTe nanowires and Au nanoparticles: Plasmon-exciton interactions, luminescence enhancement, and collective effects. *Nano Lett.* **2004**, *4*, 2323–2330.
- (6) Bouhelier, A.; Beversluis, M. R.; Novotny, L. Characterization of nanoplasmonic structures by locally excited photoluminescence. *Appl. Phys. Lett.* **2003**, *83*, 5041–5043.
- (7) Beermann, J.; Novikov, S. M.; Søndergaard, T.; Boltasseva, A.; Bozhevolnyi, S. I. Two-photon mapping of localized field enhancements in thin nanostrip antennas. *Opt. Express* **2008**, *16*, 17302–17309.
- (8) Bouhelier, A.; Bachelot, R.; Lerondel, G.; Kostchev, S.; Royer, P.; Wiederrecht, G. P. Surface plasmon characteristics of tunable photoluminescence in single gold nanorods. *Phys. Rev. Lett.* **2005**, *95*, 267405.
- (9) Beversluis, M.; Bouhelier, A.; Novotny, L. Continuum generation from single gold nanostructures through near-field mediated intraband transitions. *Phys. Rev. B* **2003**, *68*, 115433.
- (10) Mohamed, M. B.; Volkov, V.; Link, S.; El-Sayed, M. A. The “lightning” gold nanorods: Fluorescence enhancement of over a million compared to the gold metal. *Chem. Phys. Lett.* **2000**, *317*, 517–523.
- (11) Dulkeith, E.; Niedereichholz, T.; Klar, T. A.; Feldmann, J.; von Plessen, G.; Gittins, D. I.; Mayya, K. S.; Caruso, F. Plasmon emission in photoexcited gold nanoparticles. *Phys. Rev. B* **2004**, *70*, 205424.
- (12) Shahbazy, T. V. Theory of plasmon-enhanced metal photoluminescence. *Nano Lett.* **2013**, *13*, 194–198.
- (13) Walsh, G. F.; Negro, L. D. Engineering plasmon-enhanced Au light emission with planar arrays of nanoparticles. *Nano Lett.* **2013**, *13*, 786–792.
- (14) Steiner, M.; Debus, C.; Failla, A. V.; Meixner, A. J. Plasmon-enhanced emission in gold nanoparticle aggregates. *J. Phys. Chem. C* **2008**, *112*, 3103–3108.
- (15) Fang, Y.; Chang, W.-S.; Willingham, B.; Swanglap, P.; Dominguez-Medina, S.; Link, S. Plasmon emission quantum yield of single gold nanorods as a function of aspect ratio. *ACS Nano* **2012**, *6*, 7177–7184.
- (16) Varnavski, O. P.; Mohamed, M. B.; El-Sayed, M. A.; Goodson, T. Relative enhancement of ultrafast emission in gold nanorods. *J. Phys. Chem. B* **2003**, *107*, 3101–3104.
- (17) Sönnichsen, C.; Franzl, T.; Wilk, T.; von Plessen, G.; Feldmann, J.; Wilson, O.; Mulvaney, P. Drastic reduction of plasmon damping in gold nanorods. *Phys. Rev. Lett.* **2002**, *88*, 077402.
- (18) Tcherniak, A.; Dominguez-Medina, S.; Chang, W.-S.; Swanglap, P.; Slaughter, L. S.; Landes, C. F.; Link, S. One-photon plasmon luminescence and its application to correlation spectroscopy as a probe for rotational and translational dynamics of gold nanorods. *J. Phys. Chem. C* **2011**, *115*, 15938–15049.
- (19) Yorulmaz, M.; Khatua, S.; Zijlstra, P.; Gaiduk, A.; Orrit, M. Luminescence quantum yield of single gold nanorods. *Nano Lett.* **2012**, *12*, 4385–4391.
- (20) Hu, H.; Akimov, Y. A.; Duan, H.; Li, X.; Liao, M.; Tan, R. L. S.; Wu, L.; Chen, H.; Fan, H.; Bai, P.; Lee, P. S.; Yang, J. K. W.; Shen, Z. X. Photoluminescence via gap plasmons between single silver nanowires and a thin gold film. *Nanoscale* **2013**, *5*, 12086–12091.
- (21) Nielsen, M. G.; Pors, A.; Albrechtsen, O.; Bozhevolnyi, S. I. Efficient absorption of visible radiation by gap plasmon resonators. *Opt. Express* **2012**, *20*, 13311–13319.
- (22) Pors, A.; Bozhevolnyi, S. I. Efficient and broadband quarter-wave plates by gap-plasmon resonators. *Opt. Express* **2013**, *21*, 2942–2952.
- (23) Roberts, A. S.; Pors, A.; Albrechtsen, O.; Bozhevolnyi, S. I. Subwavelength plasmonic color printing protected for ambient use. *Nano Lett.* **2014**, *14*, 783–787.
- (24) Hu, H.; Duan, H.; Yang, J. K.; Shen, Z. X. Plasmon-modulated photoluminescence of individual gold nanostructures. *ACS Nano* **2012**, *6*, 10147–10155.
- (25) Bozhevolnyi, S. I.; Søndergaard, T. General properties of slow-plasmon resonant nanostructures: Nano-antennas and resonators. *Opt. Express* **2007**, *15*, 10869–10877.
- (26) Yuan, H.-K.; Chettiar, U. K.; Cai, W.; Kildishev, A. V.; Boltasseva, A.; Drachev, V. P.; Shalae, V. M. A negative permeability material at red light. *Opt. Express* **2007**, *15*, 1076–1083.
- (27) Johnson, P. B.; Christy, R. W. Optical constants of the noble metals. *Phys. Rev. B* **1972**, *6*, 4370–4379.
- (28) Pors, A.; Willatzen, M.; Albrechtsen, O.; Bozhevolnyi, S. I. From plasmonic nanoantennas to split-ring resonators: Tuning scattering strength. *J. Opt. Soc. Am. B* **2010**, *27*, 1680–1687.
- (29) Viarbitskaya, S.; Teulle, A.; Marty, R.; Sharma, J.; Girard, C.; Arbouet, A.; Dujardin, E. Tailoring and imaging the plasmonic local density of states in crystalline nanoprisms. *Nat. Mater.* **2013**, *12*, 426–432.
- (30) Alqudami, A.; Annapoorni, S. Fluorescence from metallic silver and iron nanoparticles prepared by exploding wire technique. *Plasmonics* **2007**, *2*, 5–13.
- (31) García de Abajo, F. J. Optical excitations in electron microscopy. *Rev. Mod. Phys.* **2010**, *82*, 209–275.
- (32) Chen, K.-P.; Drachev, V. P.; Borneman, J. D.; Kildishev, A. V.; Shalae, V. M. Drude relaxation rate in grained gold nanoantennas. *Nano Lett.* **2010**, *10*, 916–922.
- (33) Pors, A.; Nielsen, M. G.; Bozhevolnyi, S. I. Broadband plasmonic half-wave plates in reflection. *Opt. Lett.* **2013**, *38*, 513–515.

Supporting information for:

Gold Photoluminescence Wavelength and

Polarization Engineering

Sebastian K. H. Andersen, Anders Pors, and Sergey I. Bozhevolnyi*

*Department of Technology and Innovation, University of Southern Denmark, Niels Bohrs
Allé 1, DK-5230 Odense M, Denmark*

E-mail: seib@iti.sdu.dk

*To whom correspondence should be addressed

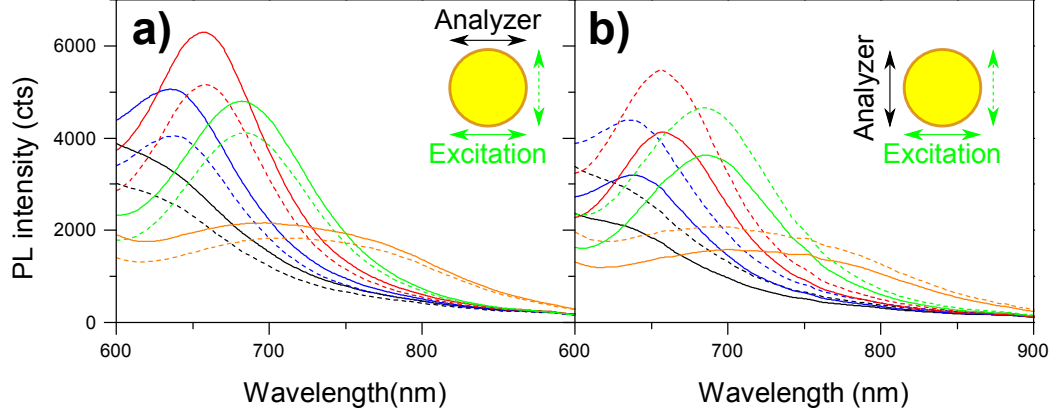


Figure S1: PL spectra from arrays of nanodisk GSP-resonators of diameter 70 nm (black), 90 nm (blue), 100 nm (red), 125 nm (green) and 150 nm (orange) for (a) horizontal and (b) vertical analyzer. Solid curves illustrate spectra for horizontal excitation polarization and dashed curves for vertical. For either orientation of analyzer, the co-polarized excitation-detection gives the strongest signal, illustrating that PL is slightly polarized along the excitation axis. We attribute the discrepancy in intensity between (a) and (b) to the non-perfect repositioning of the fiber in the fibercoupler after reorienting the analyzer.

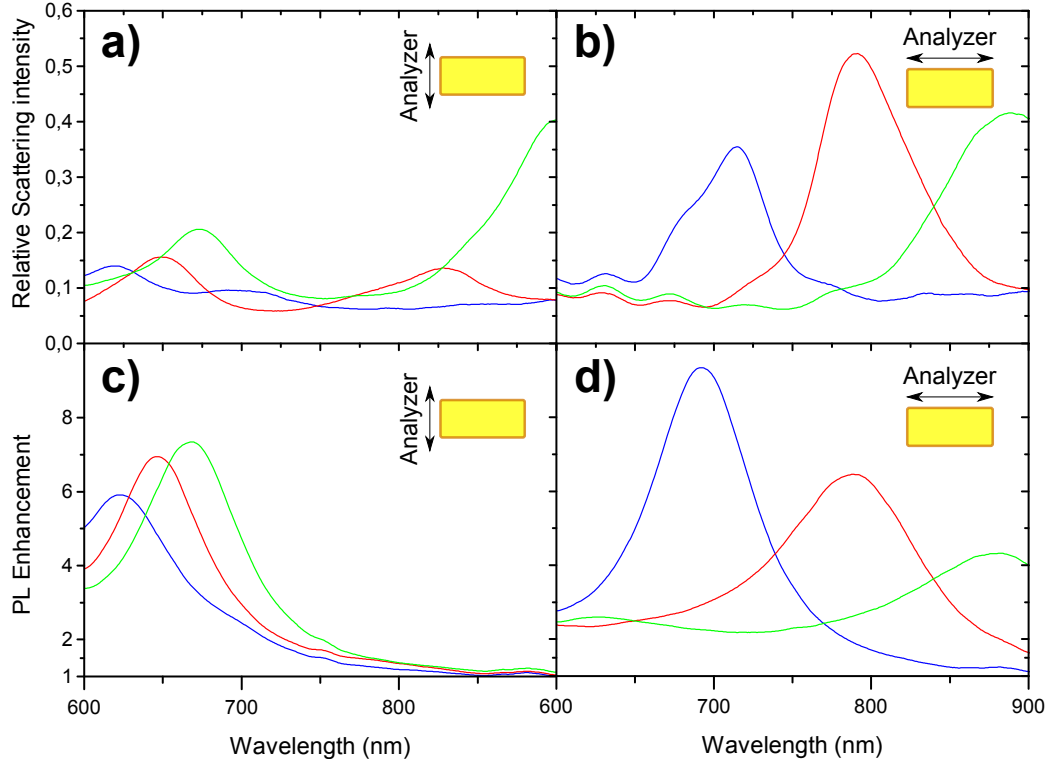


Figure S2: Scattering spectra for arrays of nanobrick GSP-resonators of average geometrical cross sections $100 \times 70 \text{ nm}^2$ (blue), $130 \times 72 \text{ nm}^2$ (red), and $150 \times 77 \text{ nm}^2$ (green). Detection with analyzer along (a) short and (b) long brick axis, and corresponding PL enhancement spectra relative to gold film for analyzer along (c) short and (d) long brick axis. Excitation is polarized along long brick axis in PL measurements. The spectra show that LSP resonances observed in scattering closely coincide with enhancement peaks in PL. The scattering peaks at long wavelengths in panel a, we attribute to slight misalignment of analyzer.

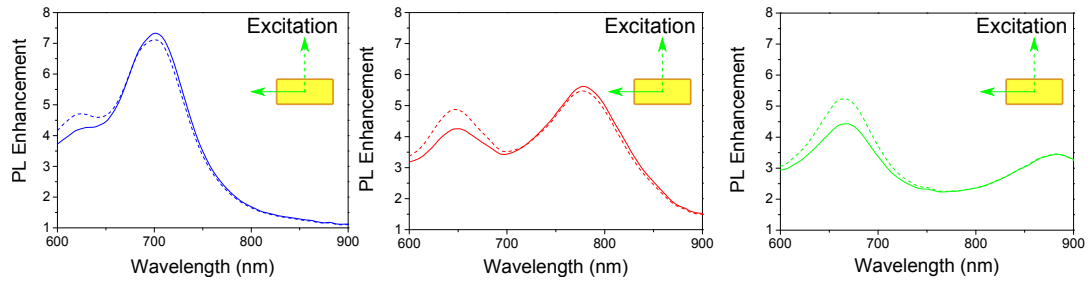


Figure S3: PL enhancement spectra for arrays of nanobrick GSP-resonators relative to gold film [average geometrical cross sections $100 \times 70 \text{ nm}^2$ (blue), $130 \times 72 \text{ nm}^2$ (red) and $150 \times 77 \text{ nm}^2$ (green)] for excitation polarized along long- (solid) and short brick axis (dashed). It is seen that the strongest LSP contribution to PL occurs when excitation polarization is aligned along the corresponding axis.

B

COUPLING OF NITROGEN-VACANCY CENTERS IN A NANODIAMOND TO A SILVER NANOCUBE

Optical Materials Express 6, 3394-3406, (2016)

Coupling of nitrogen-vacancy centers in a nanodiamond to a silver nanocube

SEBASTAIN K. H. ANDERSEN,* SHAILESH KUMAR, AND SERGEY I. BOZHEVOLNYI

Centre for Nano Optics, University of Southern Denmark, Campusvej 55, DK-5230 Odense M, Denmark

*sekh@iti.sdu.dk

Abstract: Spontaneous emission (SE) of nitrogen-vacancy centers (NV-centers), which are contained in a single nanodiamond (ND), placed near a silver nanocube, is investigated both experimentally and theoretically. The ND-cube system is assembled with an atomic force microscope, allowing us to directly compare its SE properties to that of the isolated ND. It is demonstrated that the cube coupled NV-centers exhibit strongly polarized SE. For optimal pump laser polarization, the rate of photons is enhanced by a factor of 4.1, with the excited state lifetime being reduced by a factor of 4.1. The enhancement of photon rate is a consequence of local field enhancement of the pump laser, while the SE polarization and lifetime reduction results from coupling of NV-centers to the localized surface plasmon mode of the nanocube. The experimental observations are in qualitative agreement with the model of SE from randomly oriented electric dipoles, allowing us to reveal the underlying physics of the investigated configuration.

© 2016 Optical Society of America

OCIS codes: (270.0270) Quantum optics; (260.3910) Metal optics; (160.2540) Fluorescent and luminescent materials; (230.6080) Sources.

References and links

1. B. Lounis and M. Orrit, "Single-photon sources," *Rep. Prog. Phys.* **68**, 1129 (2005).
2. I. A. Walmsley, "Quantum optics: Science and technology in a new light," *Science* **348**, 525–530 (2015).
3. J. G. Rarity, P. C. M. Owens, and P. R. Tapster, "Quantum Random-number Generation and Key Sharing," *J. Mod. Opt.* **41**, 2435–2444 (1994).
4. A. Beveratos, R. Brouri, T. Gacoin, A. Villing, J. Poizat, and P. Grangier, "Single Photon Quantum Cryptography," *Phys. Rev. Lett.* **89**, 187901 (2002).
5. M. Pelton, "Modified spontaneous emission in nanophotonic structures," *Nat. Photon.* **9**, 427–435 (2015).
6. E. M. Purcell, "Spontaneous emission probabilities at radio frequencies," *Phys. Rev.* **69**, 681 (1946).
7. A. Kinkhabwala, Z. Yu, Y. Avlasevich, K. Mullen, and W. E. Moerner, "Large single-molecule fluorescence enhancements produced by a bowtie nanoantenna," *Nat. Photon.* **3**, 654–657 (2009).
8. V. I. Kukushkin, I. M. Mukhametzhano, I. V. Kukushkin, V. D. Kulakovskii, I. V. Sedova, S. V. Sorokin, A. A. Toropov, S. V. Ivanov, and A. S. Sobolev, "Control of semiconductor quantum dot emission intensity and polarization by metal nanoantennas," *Phys. Rev. B* **90**, 235313 (2014).
9. A. Huck, S. Kumar, A. Shako, and U. L. Andersen, "Controlled Coupling of a Single Nitrogen-Vacancy Center to a Silver Nanowire," *Phys. Rev. Lett.* **106**, 096801 (2011).
10. E. Bermudez-Urena, C. Gonzalez-Ballester, M. Geiselmann, R. Marty, I. P. Radko, T. Holmgaard, Y. Alavverdyan, E. Moreno, F. J. Garcia-Vidal, S. I. Bozhevolnyi, and R. Quidant, "Coupling of individual quantum emitters to channel plasmons," *Nat. Commun.* **6**, 7883 (2015).
11. A. G. Curto, G. Volpe, T. H. Taminiau, M. P. Kreuzer, R. Quidant, and N. F. van Hulst, "Unidirectional Emission of a Quantum Dot Coupled to a Nanoantenna," *Science* **329**, 930–933 (2010).
12. G. M. Akselrod, C. Argyropoulos, T. B. Hoang, C. Cirac  n, C. Fang, J. Huang, D. R. Smith, and M. H. Mikkelsen, "Probing the mechanisms of large Purcell enhancement in plasmonic nanoantennas," *Nat. Photon.* **8**, 835–840 (2014).
13. S. J. P. Kress, F. V. Antolinez, P. Richner, S. V. Jayanti, D. K. Kim, F. Prins, A. Riedinger, M. P. C. Fischer, S. Meyer, K. M. McPeak, D. Poulikakos, and D. J. Norris, "Wedge Waveguides and Resonators for Quantum Plasmonics," *Nano Lett.* **15**, 6267–6275 (2015).
14. J. Gerard and B. Gayral, "Strong Purcell effect for InAs quantum boxes in three-dimensional solid-state microcavities," *J. Lightwave Technol.* **17**, 2089–2095 (1999).
15. F. Wang and Y. R. Shen, "General Properties of Local Plasmons in Metal Nanostructures," *Phys. Rev. Lett.* **97**, 206806 (2006).
16. K. Chen, V. P. Drachev, J. D. Borneman, A. V. Kildishev, and V. M. Shalaev, "Drude Relaxation Rate in Grained Gold Nanoantennas," *Nano Lett.* **10**, 916–922 (2010).

17. V. P. Drachev, U. K. Chettiar, A. V. Kildishev, H. Yuan, W. Cai, and V. M. Shalaev, "The Ag dielectric function in plasmonic metamaterials," *Opt. Express* **16**, 1186–1195 (2008).
18. M. Bosman, L. Zhang, H. Duan, S. F. Tan, C. A. Nijhuis, C. Qiu, and J. K. W. Yang, "Encapsulated Annealing: Enhancing the Plasmon Quality Factor in Lithographically Defined Nanostructures," *Sci. Rep.* **4**, 5537 (2014).
19. N. P. de Leon and B. J. Shields and C. L. Yu, D. E. Englund, A. V. Akimov, M. D. Lukin, and H. Park, "Tailoring Light-Matter Interaction with a Nanoscale Plasmon Resonator," *Phys. Rev. Lett.* **108**, 226803 (2012).
20. T. B. Hoang, G. M. Akselrod, and M. H. Mikkelsen, "Ultrafast Room-Temperature Single Photon Emission from Quantum Dots Coupled to Plasmonic Nanocavities," *Nano Lett.* **16**, 270–275 (2015).
21. S. K. H. Andersen, A. Pors, and S. I. Bozhevolnyi, "Gold Photoluminescence Wavelength and Polarization Engineering," *ACS Photonics* **2**, 432–438 (2015).
22. Y. Alaverdyan, N. Vamivakas, J. Barnes, C. Leboutteiller, J. Hare, and M. Atatüre, "Spectral tunability of a plasmonic antenna with a dielectric nanocrystal," *Opt. Express* **19**, 18175–18181 (2011).
23. P. Anger, P. Bharadwaj, and L. Novotny, "Enhancement and Quenching of Single-Molecule Fluorescence," *Phys. Rev. Lett.* **96**, 113002 (2006).
24. K. H. Drexhage, "Influence of a dielectric interface on fluorescence decay time," *JOL* **1-2**, 693–701 (1970).
25. G. W. Ford and W. H. Weber, "Electromagnetic interactions of molecules with metal surfaces," *Phys. Rep.* **113**, 195–287 (1984).
26. A. Pors and S. I. Bozhevolnyi, "Quantum Emitters near Layered Plasmonic Nanostructures: Decay Rate Contributions," *ACS Photonics* **2**, 228–236 (2015).
27. S. Schietinger, M. Barth, T. Aichele, and O. Benson, "Plasmon-Enhanced Single Photon Emission from a Nanoassembled Metal-Diamond Hybrid Structure at Room Temperature," *Nano Lett.* **9**, 1694–1698 (2009).
28. M. Geiselmann, R. Marty, J. Renger, F. J. G. de Abajo, and R. Quidant, "Deterministic Optical-Near-Field-Assisted Positioning of Nitrogen-Vacancy Centers," *Nano Lett.* **14**, 1520–1525 (2014).
29. A. W. Schell, G. Kewes, T. Hanke, A. Leitenstorfer, R. Bratschitsch, O. Benson, and T. Aichele, "Single defect centers in diamond nanocrystals as quantum probes for plasmonic nanostructures," *Opt. Express* **19**, 7914–7920 (2011).
30. T. T. Tran, J. Fang, H. Zhang, P. Rath, K. Bray, R. G. Sandstrom, O. Shimon, M. Toth, and I. Aharonovich, "Facile Self-Assembly of Quantum Plasmonic Circuit Components," *Adv. Mater.* **27**, 4048–4053 (2015).
31. A. Gruber, A. Dräbenstedt, C. Tietz, L. Fleury, J. Wrachtrup, and C. von Borczyskowski, "Scanning Confocal Optical Microscopy and Magnetic Resonance on Single Defect Centers," *Science* **276**, 2012–2014 (1997).
32. F. A. Inam, M. D. W. Grogan, M. Rollings, T. Gaebel, J. M. Say, C. Bradac, T. A. Birks, W. J. Wadsworth, S. Castelletto, J. R. Rabeau, and M. J. Steel, "Emission and Nonradiative Decay of Nanodiamond NV Centers in a Low Refractive Index Environment," *ACS Nano* **7**, 3833–3843 (2013).
33. A. Mohtashami and A. F. Koenderink, "Suitability of nanodiamond nitrogen-vacancy centers for spontaneous emission control experiments," *New J. Phys.* **15**, 043017 (2013).
34. S. Zhang, K. Bao, N. J. Halas, H. Xu, and P. Nordlander, "Substrate-Induced Fano Resonances of a Plasmonic Nanocube: A Route to Increased-Sensitivity Localized Surface Plasmon Resonance Sensors Revealed," *Nano Lett.* **11**, 1657–1663 (2011).
35. J. M. Taylor, P. Cappellaro, L. Childress, L. Jiang, D. Budker, P. R. Hemmer, A. Yacoby, R. Walsworth, and M. D. Lukin, "High-sensitivity diamond magnetometer with nanoscale resolution," *Nat. Phys.* **4**, 810–816 (2008).
36. T. Wolf, P. Neumann, K. Nakamura, H. Sumiya, T. Ohshima, J. Isoya, and J. Wrachtrup, "Subpicotesla Diamond Magnetometry," *Phys. Rev. X* **5**, 041001 (2015).
37. M. W. Doherty, J. Michl, F. Dolde, I. Jakobi, P. Neumann, N. B. Manson, and J. Wrachtrup, "Measuring the defect structure orientation of a single NV-centre in diamond," *New J. Phys.* **16**, 063067 (2014).
38. K. C. Fu, C. Santori, P. E. Barclay, L. J. Rogers, N. B. Manson, and R. G. Beausoleil, "Observation of the Dynamic Jahn-Teller Effect in the Excited States of Nitrogen-Vacancy Centers in Diamond," *Phys. Rev. Lett.* **103**, 256404 (2009).
39. L. Novotny and B. Hecht, *Principles of Nano-Optics* (Cambridge University, 2006).
40. P. B. Johnson and R. W. Christy, "Optical Constants of the Noble Metals," *Phys. Rev. B* **6**, 4370–4379 (1972).
41. I. H. Malitson, "Interspecimen Comparison of the Refractive Index of Fused Silica," *J. Opt. Soc. Am.* **55**, 1205–1209 (1965).
42. C. Ropp, Z. Cummins, S. Nah, J. T. Fourkas, B. Shapiro, and E. Waks, "Nanoscale probing of image-dipole interactions in a metallic nanostructure," *Nat. Commun.* **6**, 6558 (2015).

1. Introduction

Efficient single photon source [1] is an enabling technology for quantum technological schemes, exploiting the quantum nature of light [2–4]. The realization of such a device requires controlling the spontaneous emission (SE) of a bright photostable quantum emitter [5]. Based on the pioneering work of Purcell [6], efforts towards this goal typically consist of coupling the quantum emitter, such as a molecule, quantum dot or diamond color center to engineered electromagnetic modes e.g. resonator- or waveguide mode [7–10]. The coupling of emitters to a resonator

mode has previously been demonstrated to allow for modification of the excited state lifetime, spectral distribution and spatial SE pattern [11–13]. The potential coupling rate is optimized by maximizing the quality factor to mode volume ratio of the resonant mode [14]. Generally, the resonator design is optimized by two approaches: a low-loss all dielectric approach with approximately diffraction limited mode volume or resonant metal nanostructures supporting strongly confined plasmonic modes with quality factors limited by the intrinsic losses in metal [15]. In the pursuit of limiting the influence of extrinsic loss factors such as grain boundaries, surface roughness and lattice defects [16–18] of the metal, recent works have demonstrated the potential of implementing atomically smooth chemically synthesized monocrystalline metal nanoparticles in resonator configurations [19, 20]. Silver is typically the metal of choice for such configurations, given the low loss and absence of background metal fluorescence (for 532nm pump), which problematically mimic enhancement effects observed for quantum emitters [21, 22]. The probability of a quantum emitter decaying to the resonator mode, free radiation or non-radiative loss, respectively, is strongly dependent on the emitter position and the orientation of its dipole moment [23–26]. The well-controlled coupling of emitters to metal nanoparticles requiring accurate emitter positioning and orientation is therefore a strong focus in current plasmonic research [27–30]. Excellent results have previously been achieved by coupling either molecules or quantum dots to silver nanocubes [12, 20], however, these demonstrations suffer from photobleaching of the emitter, thus limiting long-term use. A promising emitter to remedy this issue is the nitrogen-vacancy center (NV-center) in diamond, given its photostable SE at room temperature [31]. However, quantifying the influence of resonator effects on the SE properties of NV-centers contained inside a single nanodiamond (ND) is challenging, with conventional use of reference samples, due to the large ND-to-ND spread in lifetime and brightness [32, 33].

In this work, we directly quantify the changed SE properties of NV-centers in close proximity to a monocrystalline silver nanocube, relative to a dielectric environment, by deterministic assembly of a single ND-cube system using an atomic force microscope (AFM). The system yields a background-free response for which the localized surface plasmon (LSP) mode of the cube is well confined near the substrate, given the strong substrate-particle interaction for this specific particle geometry [34]. In order to probe the range of NV-center responses, given the strong dependence on position and dipole orientation, we initially consider the case of a ND containing multiple emitters (~ 15), coupled to a silver nanocube. The system exhibits strongly polarized SE, with an enhanced photon rate, strongly dependent on the pump polarization, reaching a lifetime reduction of a factor 4.1 (and corresponding photon rate enhancement of 4.1) under optimal pump polarization. The experimental results are in qualitative agreement with modelling, which allows us to identify governing parameters for the overall experimental observations. Finally we demonstrate the consistency of our results for a ND-cube system containing few emitters (1-2). The results provide a foundation for the optimization of SE properties of more complex cube-based photon sources and may find applications within nanometer scale magnetometry based on single or NV-center ensembles, for which optical read-out of the ground spin state is essential [35, 36].

2. Experiment, results and discussion

The sample was prepared by introducing gold reference marks on a low fluorescence fused silica substrate (SPI supplies) by standard electron beam lithography. The marks allowed for easy identification of a specific ND, in both AFM and fluorescence scan maps. A following 10min RCA1 cleaning step removed residual organic material and promoted surface hydrophilicity for the subsequent spincoating of ND's (Adamas Nanotechnology) with mean size/number of NV-centers of 40 nm/ ~ 15 suspended in water. Successively, a water suspension of chemically synthesized silver nanocubes (nanoComposix), Fig. 1(b), of mean size 100 nm, encapsulated in a polyvinylpyrrolidone (PVP) layer ≤ 5 nm, was spincoated onto the sample. The SE of

NV-centers in diamond, situated on a low fluorescence fused silica substrate, were excited by a 532 nm linearly polarized pulsed laser (LDH-P-FA-530L - Picoquant) with pulse width/period of ~ 50 ps/400 ns, Fig. 1(a). A half-wave plate situated in the excitation light path controls the polarization of the pump light, which is focused onto the sample by a $\times 100$ (NA 0.90) objective. The fluorescence, collected by the objective, was filtered by a dichroic mirror (cut-off 550 nm), passed through an analyzer and detected either by a grating spectrometer (SR303i - Andor), equipped with an electron multiplying CCD (IXon Ultra - Andor), or a single photon sensitive photo avalanche diode (APD) (τ -SPAD - Picoquant) connected to a pulse-to-photon arrival timing box (PicoHarp 300 - Picoquant). We apply this setup to characterize the spectral and temporal response for various configurations of pump polarization and analyzer. For direct comparison of the spectral power, all measurements were done at an average laser power of $10 \mu\text{W}$, using the same acquisition time of 10 min.

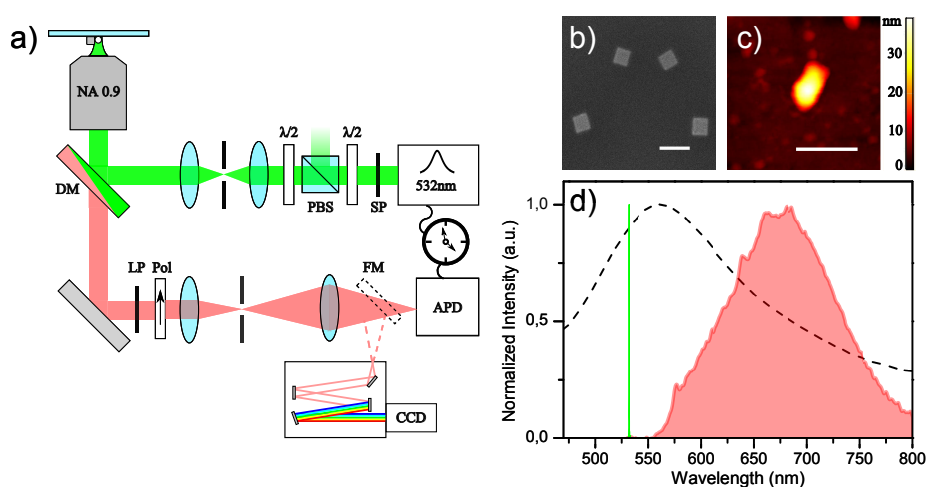


Fig. 1. Schematic of experimental setup for characterization of NV-center SE (a). SP, short pass; LP, long pass filter; PBS, polarizing beam splitter; $\lambda/2$, half-wave plate; DM, dichroic mirror; Pol, analyzer; FM, flip mirror. Experimental constituents, scale bar 200 nm, micrograph of silver cubes (b) and AFM scan of ND (c). Spectral properties of individual elements (d) scattering spectra of silver cubes on quartz glass, relative to white paper (dashed), fluorescence spectrum of ND (red) and excitation laser line (green).

The measurements were completed within 72 hours of spincoating the silver cubes, during which time we observed no fluorescence of the cubes, as cubes located with AFM did not show up in our fluorescence scan maps. Scanning the sample with an AFM, we locate a single ND, Fig. 1(c). The diamond emits the characteristic fluorescence spectrum of an NV-center, identified by the zero phonon line peaks for the neutral (575 nm) and negative (637 nm) charge states respectively, Fig. 1(d). Correspondingly, the resonance of the silver nanocube is measured to ~ 560 nm, based on the scattering spectrum of numerous nanocubes distributed on a glass substrate. Enhancement effects can thus be expected at both the excitation and SE wavelength for the assembled ND-cube system. We place the 30 nm ND, near the center of a cube facet, by only manipulating the 110 nm cube with the AFM, Fig. 2(a). It is worth pointing out that by this approach the ND (and hence NV-center dipole orientation) was unmoved throughout the experiment. For reliable comparison of polarization dependent measurements, cf. the appendix. For reference purposes, we introduce a cartesian coordinate system, with the x -, y -axes parallel with the substrate and the x -axis aligned with the ND-cube axis, normal to the cube facet.

Initially, we do not consider the dependence of SE polarization, by omitting the analyzer in

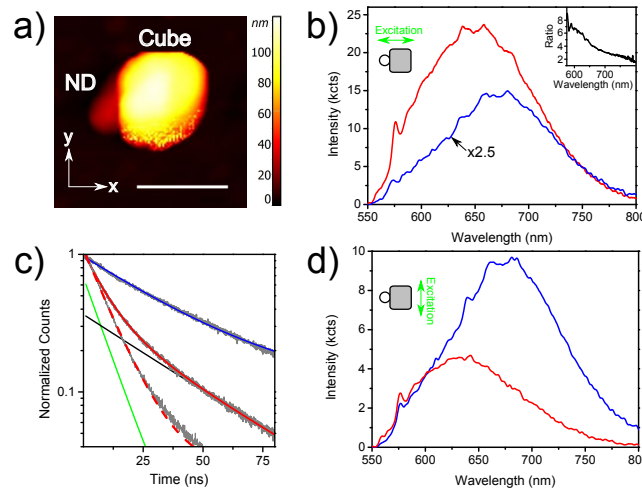


Fig. 2. AFM scan of assembled ND-cube system, scale bar 200 nm (a). The x -, y -vectors define the reference coordinate axis. Measurements of isolated ND (blue) and ND-cube system (red). Exponential fits of lifetime decay data (c) for x - (solid) and y -polarized pump (dashed). Green and black curve give respectively fast and slow exponential of bi-exponential decay for ND-cube system under x -polarized pump (solid red). Decay curve of isolated ND under y -pump overlays that for x -pump and is omitted for clarity. Corresponding SE spectra for excitation polarized along x (b) and y (d). Inset give the ND-cube to ND spectral ratio.

the detection light path. For x -polarized pump light, Fig. 2(b), the photon rate or fluorescent power (obtained by integration of fluorescence spectrum) of the ND-cube system is enhanced by a factor of 4.1 relative to the isolated ND. The spectral power is increasingly enhanced towards the cube resonance, as NV-centers couple to the LSP-cube mode, effectively increasing decay probability of near-resonance dipole transitions. The excited state lifetime is reduced by a factor of 4.1, evident as the lifetime decay curve goes from single exponential (isolated ND) with a fitted lifetime of 36.1 ns to double exponential (ND-cube) with a fast lifetime component of 8.9 ns, Fig. 2(c). For y -polarized pump light, the lifetime reduction is 3.2, Fig. 2(c), while the total fluorescent power is decreased with an enhancement factor of 0.5, Fig. 2(d).

In the following, we consider the polarization dependent properties of NV-center SE. Inserting an analyzer in the detection light path, we measure spectral and temporal SE properties for x - and y -orientations of analyzer and pump light, Fig. 3. In the case of an x -oriented analyzer we recover similar spectrum and decay curves observed for the ND-cube system in the absence of analyzer for x -pump light, Fig. 3(a), with slight differences observed in the spectrum for y -pump light, Fig. 3(c). The similarity is a result of the SE being mainly polarized along the x -axis, as respectively 86 % (x -pump light) and 93 % (y -pump light) of the detected power is x -polarized. In contrast, the SE of the isolated ND is preferentially co-polarized with the excitation, as respectively 78 % (x -pump light) and 43 % (y -pump light) of the emitted photons are x -polarized. The polarization of NV-center emission in the presence of the cube, result from excitation of the plasmonic cube mode during NV-center relaxation. The cube mode is a dipole-like mode [34], consisting of charge density oscillations along the ND-cube axis. The energy funnelled from the NV-center into the cube is either ohmically dissipated or scattered to free space in dipolar fashion, polarized along the dipole axis of the cube mode (ND-cube axis). The result is experimentally observed as the apparent polarization of NV-center emission, for NV-centers efficiently coupling to the cube. The efficiency of NV-to-cube energy transfer increases with the NV-center dipole projection on the electric field of the cube mode, oriented perpendicular to the cube surface. For NV-center

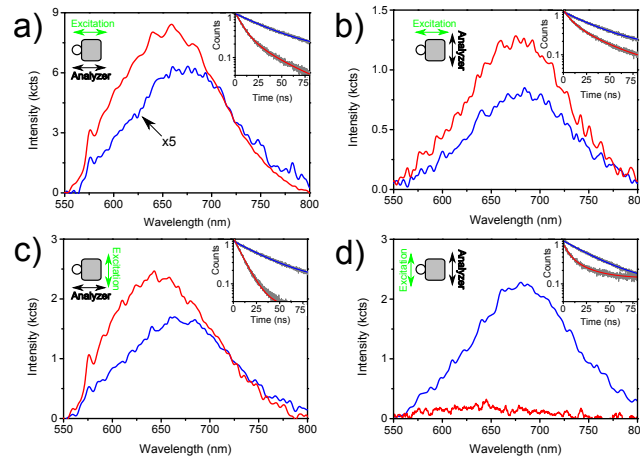


Fig. 3. Polarized SE spectra of isolated ND(blue) and ND-cube system(red). Excitation polarized along x and analyzer orientation, x (a) or y (b). Excitation polarized along y and analyzer orientation x (c) or y (d). Insets give corresponding measurements of lifetime decay curves.

dipoles oriented along this axis, the increased rate at which the NV-center may dissipate energy, given coupling to the cube, is observed as a decrease in lifetime. We note the reduced lifetime and spectral modulations observed for x -oriented analyzer, demonstrate the strongly x -polarized SE result from NV-centers coupling to the LSP mode of the cube. For y -oriented analyzer and x -polarized excitation, Fig. 3(b), the signal can predominately be attributed to NV-centers not coupling to the cube mode, as 78 % of the photons contribute to an exponential decay with a near unchanged lifetime of 35 ns, in agreement with the unmodulated SE spectrum. Finally, for y -polarized pump light, Fig. 3(d), the signal was reduced to an inadequate level for resolving spectral features. The correspondingly weak lifetime decay curve, only slightly above the background of the APD dark count, is included for completeness.

With the purpose of identifying the underlying factors responsible for experimental observations, we numerically model the SE of NV-centers in close proximity to a silver nanocube situated on a glass substrate. As the SE response of an emitter is strongly dependent on dipole orientation, it is initially worth noting the physical dipole configuration of the NV-center. The NV-center consists of a substitutional nitrogen-vacancy pair situated along the $\langle 111 \rangle$ crystal axis in diamond [37]. 4 orientations of the N-V axis are thus possible within the diamond lattice. The excitation and SE of the negatively charged NV-center is facilitated by 2 orthogonal dipole axes, corresponding to the double degenerate excited electronic states, with the dipole axes lying in the plane perpendicular to the N-V axis. At room temperature the population of the excited electronic states completely mix, allowing spontaneous decay by either dipole axes [38]. The modelling of SE from multiple NV-centers, distributed throughout the ND, with different dipole orientation is clearly a complex challenge. In the following we, therefore, limit ourselves to a simplified model by approximating the NV-center as a randomly oriented dipole. Considering the relatively omnidirectional response of the negatively charged NV-center, given the 2-dipole configuration, we consider such an approximation quite reasonable. The most likely response of the ND, is obtained by averaging the modelled dipole response over the ND. Though only qualitative agreement of experiment and model should be expected, the model captures the governing physics of the experiment.

We proceed by a detailed description of the model. The excited NV-center is modelled as an electric dipole, harmonically oscillating at the SE frequency, with the associated point source

current density \mathbf{j}_p , for which unit vector $\hat{\mathbf{n}}_p$ defines the axis of charge oscillation or dipole axis. Assuming unity intrinsic quantum yield, we note the time-averaged power P^{rad} radiated from the volume enclosing the cube and point source is given by the energy dissipation of currents included in the volume [39]. Splitting current terms into the point source driving term and sink terms for the polarization currents induced in the cube, we write:

$$P^{tot} = P^{rad} + P^{nr} \quad (1)$$

where P^{nr} is the power dissipated in the cube by ohmic heating, while the total power dissipated by the point source is given by $P^{tot} = -\frac{1}{2}\text{Re}\{\mathbf{j}_p^* \cdot \mathbf{E}(\mathbf{r}_0)\}$. \mathbf{E} being the electric field, generated by the point source, at the source origin \mathbf{r}_0 . Assuming the Cartesian dipole components are not coupled, that is, the generated electric field is parallel with the dipole axis at \mathbf{r}_0 , for an x -, y - or z -oriented dipole, respectively. The power dissipated by the randomly oriented dipole is written as a weighted superposition of contributions from Cartesian dipole components i.e. $P^{tot} = \sum_{x,y,z} g_i P_i^{tot}$. The weighting factors are found to be $g_{||} = 0.6$ for the dipole component parallel with pump polarization and $g_{\perp} = 0.2$ for the orthogonal dipole components, imposed by the photo-selective dipole excitation of the pump light, on the assumption of parallel absorption and emission dipole axis cf. the appendix. In order to model enhancement effects of the fluorescent photon rate, we note the measured lifetime of the isolated ND (36.1 ns) is much longer than the laser pulse duration (~ 50 ps) and significantly shorter than the pulse period (400 ns). The NV-centers, therefore, decay before the next laser pulse. We thus write the detected photon rate (R), in the non-saturated form, limited by the excitation rate.

$$R = \gamma_{ex} \Phi \eta \quad (2)$$

The excitation rate is given by $\gamma_{ex} \propto |\hat{\mathbf{n}}_p \cdot \mathbf{E}^{ext}(\mathbf{r}_0)|^2$, where \mathbf{E}^{ext} is the electric field generated by an external source (eg. laser) at the excitation frequency. While $\Phi = P^{rad}/P^{tot}$ is the quantum yield and $\eta = P^{obj}/P^{rad}$ the collection efficiency of the objective for the power P^{obj} radiated to the objective. For simplicity, we model the NV-centers distributed within the 30 nm tall ND, by simulating the dipole response for an emission wavelength of 637 nm, over a 30 nm \times 30 nm area in the xz plane, centred near the facet of a 110 nm cube. Enhancement factors for each point is obtained relative to the response of the dipole above the glass substrate, with reference parameters subscripted by 0. Finally, the enhancement factors most likely to be observed in experiment, are obtained by averaging over the simulated dipole map. The best agreement of experiment and model is found for a 16 nm separation of cube and ND simulation area. Such a separation is quite realistic and the subsequent modelled values are thus simulated under this condition.

Having established the general model, we proceed to identify the parameters responsible for experimental observations by numerical full-wave 3D simulations (using the commercial finite element software Comsol Multiphysics). Material parameters for the 110 nm silver cube with side/corner rounding radius of 7 nm and the fused quartz glass substrate were obtained from tabulated data [40, 41]. Considering the photon rate, Eq. 2, we find virtually unchanged values for the quantum yield and collection efficiency, with average values for the ND-cube system of $\Phi = 0.98, 0.97$ and $\eta = 0.22, 0.20$ for x -, y -polarized pump respectively and $\Phi_0 = 1, \eta_0 = 0.17$ for the reference. The enhancement of photon rate, is therefore attributed to an increased excitation rate, resulting from local enhancement of the incident laser field. For x -polarized pump, the field is strongly enhanced at the ND, given the excitation of the LSP mode of the cube (polarized with the pump), well-confined near the substrate, Fig. 4(a). In contrast the excitation field is suppressed under y -polarized illumination, Fig. 4(b), resulting in respectively enhancement and

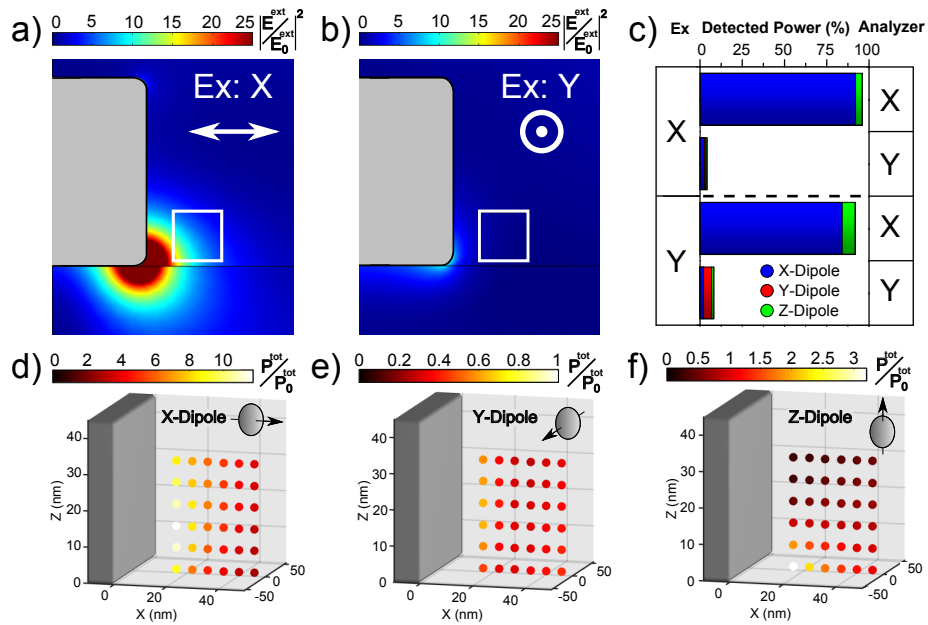


Fig. 4. Simulation of norm squared excitation field generated at by plane wave (wavelength: 532 nm) at normal incidence on silver cube, polarized along x (a) and y (b), relative to field in absence of silver cube. White square indicate the simulated ND area. Contributions of dipole components to average power radiated to objective for randomly oriented dipole (c). Power dissipation of dipole radiating at emission wavelength 637 nm, relative to dipole in absence of cube, for dipole moment orientation x (d), y (e) and z (f), mapped over the ND simulation area.

suppression of the photon rate, in good agreement with experimental observations. Concerning physical effects related to the emission wavelength (eg. radiative decay rate and polarization of fluorescence), we initially consider the power dissipated by x -, y - and z -oriented dipoles in the ND simulation area, Figs. 4(d)-4(f). The power dissipated by an x -oriented dipole is significantly enhanced in close proximity to the cube, as the dipole orientation is well-aligned with the electric field of the LSP mode, while the z -dipole show modest enhancement near the rounded cube corner, the y -dipole is suppressed, presumably due to an anti-phase image dipole induced in the cube facet, limiting dipole radiation by destructive interference [42]. Consequently the reduced lifetime, mainly result from the randomly oriented dipole's projection on the x -axis. The model agrees qualitatively with experiment as a significant decrease in lifetime was observed for x -oriented analyzer, Fig. 3(a) and 3(c), while the lifetime was mainly unchanged for y -aligned analyzer, Fig. 3(b). Finally, we decompose the power radiated into the objective in terms of x - and y -polarization and consider the contributions of the various dipole components to the overall power radiated by the randomized dipole, Fig. 4(c). In order to account for the spatially dependent dipole excitation efficiency, we apply a weighted average for the ND simulation area, using $|E^{ext}|^2$ as weighting function. The power radiated to the objective, is dominated by the efficient power dissipation of the x -dipole component, resulting in strongly x -polarized SE for both x - and y -polarized pump light, in agreement with experimental observations.

We conclude the numeric study by comparing the trend of modelled and experimental enhancement factors, Table 1. Note the modelled value for lifetime reduction, given by (P^{tot}/P_0^{tot}) , is obtained by a weighted average over the ND simulation area, using the excitation field as weighting function. Generally the simple model of a randomly orientated dipole emitting at a

Table 1. Experimental (red) and modelled (blue) values of photon rate enhancement and lifetime reduction.

Photon rate enhancement				Lifetime reduction
Analyzer Excitation	X	Y	\div	\div
X	6.3	1.5	4.1	4.1
	11.6	1.9	8.5	4.2
Y	1.4	0.08	0.5	3.2
	1.8	0.06	0.6	2.0

● Experiment

● Model

single wavelength, follow the trend of experimental values for lifetime reduction and photon rate enhancement, when averaged over the ND. The photon rate enhancement factors observed in experiment, may therefore be interpreted by two polarization dependent factors, enhancement of excitation field and polarized SE resulting from NV-centers coupling to the LSP mode of the cube. For x-oriented analyzer and pump polarization, the excitation field is enhanced at the ND and the analyzer is aligned with the strongly x-polarized SE, resulting in the largest enhancement factor. Rotating either pump or analyzer to y-orientation, either the excitation field is suppressed or the analyzer probe the weak y-polarized SE, resulting in modest enhancement factors for crossed analyzer and pump. In the case of both analyzer and pump parallel with the y-axis, both factors contribute to a strongly suppressed signal. Beyond the simplified model, we qualitatively comment on expected effects not captured by the model. We note the intrinsic quantum efficiency of an NV-center in a ND is in fact not unity [33]. Enhancement of quantum yield by an increase in the radiative decay, in the presence of the cube, may therefore be a contributing factor to the enhancement of photon rate observed experimentally. On the other hand, neglecting the high refractive index of the diamond in the model, is expected to result in an overestimation of the excitation rate and hence photon rate enhancement, as the plasmonic field is typically "pushed" from the dielectric to the metal side, when increasing the refractive index of the dielectric. Neither effect is however expected to change the polarization dependent tendencies modelled in Table 1.

Lastly, we demonstrate the consistency of our experimental observations by reproducing the ND-cube coupled system for a ND containing few NV-centers. For the few emitter experiment, the setup, Fig. 1(a), was upgraded with a continuous wave 532 nm laser (CL532-100 - Crystal Laser), introduced in the excitation light path by a flip mirror. Excitation and collection was facilitated by a $\times 100$ (NA 1.4) oil immersion objective, while a 50:50 beamsplitter, inserted in the collection light path, passes collected photons to a secondary APD (τ -SPAD - Picoquant), for second order correlation measurements. The second order correlation function ($g^{(2)}(\tau)$) is obtained as an event histogram by accumulating the time delay (τ) for events of a photon arriving on one APD and starting a timer and the arrival of a photon on the other APD stopping the timer. As single quantum emitters may only emit one photon at the time, the zero delay value follow $g^{(2)}(0) = 1 - 1/n$, n being the number of emitters contributing to the signal, assuming no background. The number of NV-centers contained in the 20nm ND, Fig. 5(a), is determined to be 1 or 2, evident as the $g^{(2)}(0)$ -value drops to ~ 0.5 , without applying any background correction, Fig. 5(b). The absence of background fluorescence from the silver cube is evident as the $g^{(2)}(0)$ -value for the assembled ND-cube system is nearly unchanged from the isolated ND. The lifetime decay curve, Fig. 5(c), is fitted for a bi-exponential decay. We attribute the fast exponential to background, fitted to respectively 4.9ns and 4.1ns for the isolated ND and assembled ND-cube system. The slow exponential, resulting from NV-center emission, drop from 27.9ns for the isolated ND to 11.6ns, after system assembly, giving a lifetime reduction factor of 2.4. The assembly of the ND-cube system, Fig. 5(d), result in the characteristic spectral

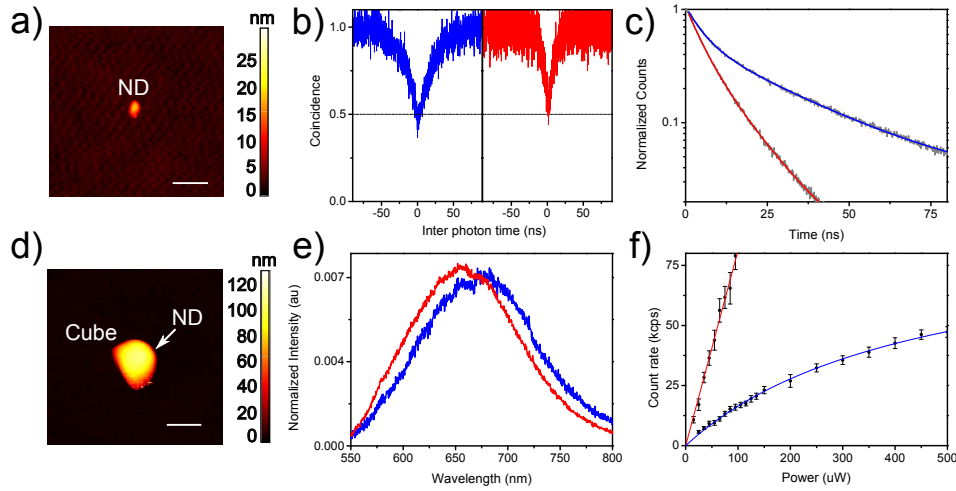


Fig. 5. Few NV-center emission from isolated ND (blue) and assembled ND-cube system (red). AFM scans (a),(d) give the respective configurations, scalebar 200nm. 2. order correlation measurement (b) no background correction applied. Lifetime decay curves fitted to bi-exponentials (c). SE spectra normalized to a spectral area of 1 (e). Saturation model for 2-level system(line) fitted to measured photon count rate (points) as function of laser power (f), errorbar correspond to one standard deviation.

change favouring near cube resonance emission, Fig. 5(e). Measuring the count rate on a single APD as a function of pump power, for pump polarization optimized for maximal count rate, we collect saturation curves for either configuration, Fig. 5(f). The curves are fitted to a saturation model for a 2-level system of the form $R = R_{\infty}P/(P + P_s)$, R being the detected count rate, P the laser pump power, P_s the saturation pump power and R_{∞} the maximum detectable count rate at infinite pump power. The curves are bounded between a linear non-saturated regime at small laser power, for which the photon rate is limited by the excitation rate of the emitter. In the saturated regime for large laser power, the photon rate is limited by the rate at which the emitter can emit photons into the objective, given the finite lifetime of the excited state. Considering the linear slope for the non-saturated regime, we find the photon rate increases by a factor 4.1 after introducing the cube, in good agreement with the previous experiment. The count rate, for the isolated ND at infinite pump power, is fitted to $R_{\infty} = 90$ kcps, while the saturation curve for the ND-cube system appear to increase beyond this level. The increase of R_{∞} after introducing the cube, suggest the corresponding reduction of lifetime result from an increase in radiative decay rate, given coupling to the cube, rather than quenching.

3. Conclusion

In summary, we have studied the SE properties of NV-centers in close proximity to a silver nanocube relative to a homogeneous environment, by deterministic assembly of a single ND-cube system using an AFM. The SE from the assembled system is strongly polarized along the x -axis, intersecting the ND and cube, while the rate of emitted photons strongly depend on the polarization of the pump laser. For optimal pump, the photon rate is enhanced by a factor of 4.1, while the excited state lifetime is reduced by a factor of 4.1. Separating fluorescence spectrum and lifetime decay curves into x - and y -polarization; the strongly x -polarized SE is attributed to NV-centers coupling to the LSP mode of the cube, while a weak y -polarized signal is attributed to uncoupled NV-centers. The physics observed in experiment is qualitatively reproduced by modelling, the ND averaged, response of a randomly oriented electric dipole. Based on the model,

we identify the total photon rate enhancement to result from local field enhancement of the pump laser and potentially increased quantum yield, while the reduction in lifetime is a consequence of NV-centers coupling to the LSP mode of the cube. The consistency of experimental results was further demonstrated by the coupling of a ND containing few NV-centers to a silver nanocube. The results provide a foundation for incorporating NV-centers into more complex cube-based photon sources.

Appendix

Nanodiamond orientation

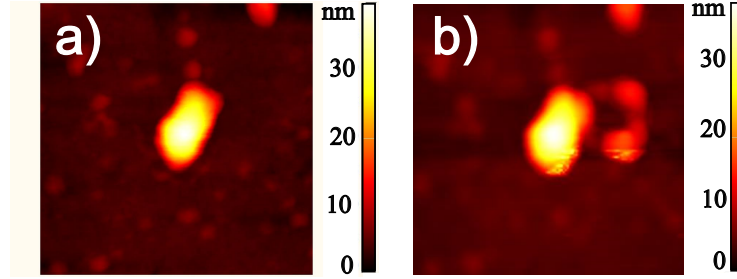


Fig. 6. AFM scan of ND as initially characterized, before moving silver cube (a) and complementary scan after, moving silver nanocube to ND, characterization and finally cube pickup with AFM (b). The ND orientation appear unchanged throughout the experiment.

Power dissipation by randomly oriented dipole

In the following we calculate the average dipole components of an excited dipole for a random absorption dipole orientation. The power dissipated by the dipole at the emission wavelength is expressed as a superposition the power dissipated by respective an x, y or z oriented dipole moment, weighted by the average dipole components of the excited dipole.

We specify the vector for the absorption dipole moment in spherical coordinates with azimuthal angle φ and inclination angle θ . The probability of finding the absorption dipole in the interval $[\theta, \theta + d\theta; \varphi, \varphi + d\varphi]$, is given by the differential surface area of a sphere, relative to the total area.

$$f(\theta)d\theta d\varphi = \frac{\sin(\theta)d\theta d\varphi}{4\pi} \quad (3)$$

We consider the electric excitation field oriented along the cartesian z-axis, and note the probability, the excitation field will excite the dipole, is proportional to the squared norm of the absorption dipole projection on the excitation field. The probability of finding the excited dipole in the interval $[\theta, \theta + d\theta; \varphi, \varphi + d\varphi]$ is thus given by:

$$f_{ex}(\theta)d\theta d\varphi = C \frac{\sin(\theta) \cos^2(\theta)d\theta d\varphi}{4\pi} \quad (4)$$

C being the normalization factor, such that $1 = \int_0^{2\pi} \int_0^\pi f_{ex} d\theta d\varphi$. Expressing the excited dipole moment in cartesian components.

$$\mathbf{p} = |p|(\hat{\mathbf{n}}_x \cos(\varphi) \sin(\theta) + \hat{\mathbf{n}}_y \sin(\varphi) \sin(\theta) + \hat{\mathbf{n}}_z \cos(\theta)) \quad (5)$$

We calculate the average norm squared components of the excited dipole.

$$\langle |p_x|^2 \rangle = \int_0^{2\pi} \int_0^\pi |p_x(\theta, \varphi)|^2 f_{ex}(\theta) d\theta d\varphi = g_x |p|^2 \quad (6)$$

$$\langle |p_y|^2 \rangle = \int_0^{2\pi} \int_0^\pi |p_y(\theta, \varphi)|^2 f_{ex}(\theta) d\theta d\varphi = g_y |p|^2 \quad (7)$$

$$\langle |p_z|^2 \rangle = \int_0^{2\pi} \int_0^\pi |p_z(\theta, \varphi)|^2 f_{ex}(\theta) d\theta d\varphi = g_z |p|^2 \quad (8)$$

Weighting factors being respectively, $g_z=0.6$ for dipole component parallel with excitation field and $g_x=g_y=0.2$ for dipole components orthogonal to excitation. Assuming the absorption dipole axis (ie. dipole axis at the excitation wavelength) is parallel with the emission dipole axis (ie. dipole axis at the emission wavelength), we express the emission dipole unit vector ($\hat{\mathbf{n}}_p$), interims of the average excited dipole orientation.

$$\hat{\mathbf{n}}_p = (\hat{\mathbf{n}}_x \sqrt{g_x} + \hat{\mathbf{n}}_y \sqrt{g_y} + \hat{\mathbf{n}}_z \sqrt{g_z}) \quad (9)$$

The power dissipated by the radiating dipole oscillating at the emission frequency, is given by the classical expression [39].

$$P^{tot} = \frac{\omega^2 |p|^2}{2c^2 \epsilon_0 \epsilon} \left(\hat{\mathbf{n}}_p \cdot \text{Im} \{ \vec{\mathbf{G}}(\mathbf{r}_0, \mathbf{r}_0, \omega) \} \cdot \hat{\mathbf{n}}_p \right) \quad (10)$$

ω being the emission frequency, c the vacuum speed of light, ϵ_0 the vacuum permittivity, ϵ the permittivity of the medium and $\vec{\mathbf{G}}$ Green's dyadic evaluated at the dipole location \mathbf{r}_0 . Assuming no coupling of the cartesian dipole components, that is the Green dyadic only contain diagonal elements, as the electric field (evaluated at \mathbf{r}_0) generated by an x, y or z -oriented dipole, is parallel with the respective dipole axis. We express the total power dissipated by the dipole, as a superposition of the power dissipation for a x, y and z oriented dipole, weighted by the corresponding weighting factor.

$$P^{tot} = \frac{\omega^2 |p|^2}{2c^2 \epsilon_0 \epsilon} \left(\sum_{i=x,y,z} g_i \hat{\mathbf{n}}_i \cdot \text{Im} \{ \vec{\mathbf{G}}(\mathbf{r}_0, \mathbf{r}_0, \omega) \} \cdot \hat{\mathbf{n}}_i \right) \quad (11)$$

Funding

European Research Council (Grant 341054 (PLAQNAP)).



ULTRABRIGHT LINEARLY POLARIZED PHOTON GENERATION
FROM A NITROGEN VACANCY CENTER IN A NANOCUBE DIMER ANTENNA

Nano Letters 17, 3889-3895, (2017)

Ultrabright Linearly Polarized Photon Generation from a Nitrogen Vacancy Center in a Nanocube Dimer Antenna

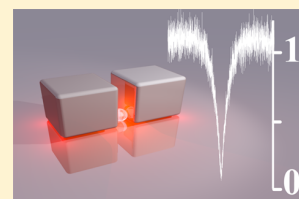
Sebastian K. H. Andersen,*¹ Shailesh Kumar, and Sergey I. Bozhevolnyi¹

Center for Nano Optics, University of Southern Denmark, Campusvej 55, DK-5230 Odense M, Denmark

S Supporting Information

ABSTRACT: We demonstrate an exceptionally bright photon source based on a single nitrogen-vacancy center (NV center) in a nanodiamond (ND) placed in the nanoscale gap between two monocrystalline silver cubes in a dimer configuration. The system is operated near saturation at a stable photon rate of 850 kcps, while we further achieve strongly polarized emission and high single photon purity, evident by the measured autocorrelation with a $g^{(2)}(0)$ value of 0.08. These photon source features are key parameters for quantum technological applications, such as secure communication based on quantum key distribution. The cube antenna is assembled with an atomic force microscope, which allows us to predetermine the dipole orientation of the NV center and optimize cube positioning accordingly, while also tracking the evolution of emission parameters from isolated ND to the one- and two-cube configuration. The experiment is well described by finite element modeling, assuming an intrinsic quantum efficiency of 0.35. We attribute the large photon rate of the assembled photon source, to increased quantum efficiency of the NV center and high antenna efficiency.

KEYWORDS: Single photon, plasmonics, Dimer antenna, silver, polarization



The single photon source is a fundamental component in the quantum technological evolution,¹ enabling secure communication based on single photon quantum key distribution,^{2,3} optical quantum computing⁴ or light-matter interfaces for quantum information storage.⁵ For practical applications, the single photon source should efficiently deliver a stable stream of indistinguishable, strongly polarized single photons at high rate and high purity, preferably under room-temperature operation. Single photon emission may be achieved by spontaneous emission from a wealth of quantum emitters (QE) such as a molecule, quantum dot, defect in diamond, boron nitride, carbon nanotubes, and so forth.⁶ However, the particular single photon emission properties are a function of both the intrinsic characteristics of the emitter and the surrounding dielectric environment. The desirable single photon source properties are hence achieved by proper choice of QE and engineering of the photonic environment, that is, by coupling the QE to an antenna,^{7–9} waveguide^{10,11} or directing the emission with a solid immersion lens. For photostable operation at room-temperature, the nitrogen-vacancy center in diamond (NV center) is an excellent emitter,¹² while the emission is poorly polarized given phonon promoted population averaging of the doublet excited state.^{13,14} Several works have previously focused on improving the efficiency and photon rate of the NV center either by top-down fabrication in bulk diamond^{15,16} or by incorporating a nanodiamond (ND) containing an NV center into a plasmonic antenna.¹⁷ Though often, engineering the photonic environment comes at the cost of reducing the purity of the source, as background fluorescence from impurities in the diamond or materials introduced during fabrication limit the single photon quantum character of the source. The degree to which background compromises the

single photon character may be measured by the dip of the autocorrelation function at time zero ($g^{(2)}(0)$), indicating the probability of detecting two photons at the same time. The measured $g^{(2)}(0)$ -value of previously demonstrated NV center based photon sources have typically been ~ 0.3 .^{16–19} Schietinger et al. assembled a dimer antenna consisting of two gold spheres around a ND containing an NV center and demonstrated photon rates up to ~ 420 kcps with $g^{(2)}(0) = 0.3$.¹⁷ Choy et al. realized an NV center in a diamond post surrounded by a silver film with grating corrugations and reported an asymptotic photon rate limit up to 704 kcps, achievable at infinite laser power with $g^{(2)}(0) \sim 0.2$.¹⁹ A record asymptotic limit of 2.7 Mcps from an NV center in a diamond membrane with an etched in grating was reported by Li et al. with $g^{(2)}(0) = 0.28$.¹⁸

In this work, we demonstrate an exceptionally pure photon source, consisting of a nanodiamond containing a single NV center situated in the gap between two monocrystalline silver nanocubes. We measure a $g^{(2)}(0)$ value of 0.08 for the total system. The configuration is stable under large pump powers, as we operate the source near saturation, at a detected photon rate of 850 kcps, similar to state of the art NV center sources based on solid immersion lenses in diamond (~ 1 Mcps)²⁰ or ZrO_2 (~ 850 kcps, stable emission).²¹ Though unlike such sources, we further demonstrate strongly linearly polarized emission from our NV center with a polarization ratio of 9, between the power detected along the major and minor axis. The system is assembled with an atomic force microscope (AFM), which allows us to directly probe the evolution of the

Received: April 6, 2017

Revised: May 2, 2017

Published: May 4, 2017

NV center emission properties from the isolated ND to the one-cube and two-cube configuration. The freedom to precharacterize our NV center before system assembly allows us to determine the orientation of the NV center dipole axes and optimize the position of our nanocubes accordingly for optimal NV-to-antenna coupling. Such optimization improves both the excitation efficiency and photon rate of the NV center, as the excitation rate is improved by a factor of 5.86, while the detected photon rate at saturation increases by a factor 6.6, relative to the isolated ND. Finite element modeling agree well with experimental observations assuming an intrinsic quantum efficiency of 0.35. The enhanced photon rate, detected from the assembled photon source, is attributed to increased quantum efficiency and high radiation efficiency of the antenna.

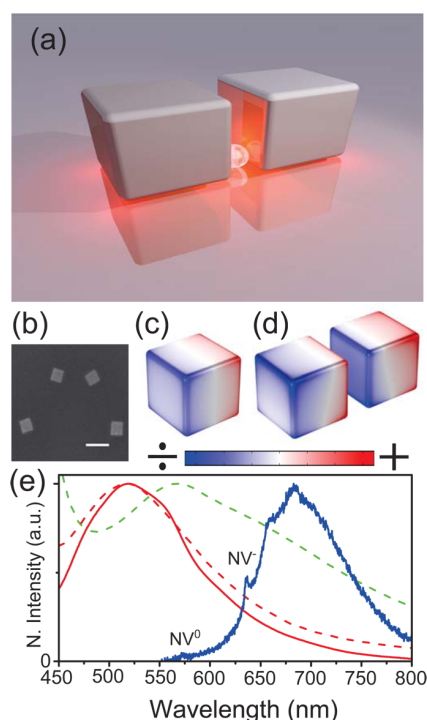


Figure 1. (a) Illustration of ND containing a single NV center situated in the gap between two silver nanocubes. The NV center emission is accelerated as it couples to the plasmonic cube mode. (b) Electron micrograph of silver cubes with scalebar of 200 nm. (c,d) Charge distribution of the dipolar mode of a single and coupled cubes. (e) Fluorescence spectrum of single NV center (blue) and measured scattering spectrum of single nanocube ~ 100 nm (red) with corresponding simulations for single (red dashed) and coupled cubes (green dashed) separated by a 35 nm gap.

Results and Discussion. Figure 1a illustrates the physics of our experiment. A single NV center in a ND decays from the excited electronic state by excitation of plasmonic charge density oscillations in a single- (Figure 1c) or 2-cube configuration (Figure 1d). The excited antenna mode subsequently decays either by ohmic loss or scattering of single photons, polarized along the axis of charge oscillation, hence imposing the radiation properties of the antenna on the NV center. Further, the photon rate of the system is increased, as the NV center spends less time in the excited state between emission events, when allowed to efficiently dissipate its energy into the antenna mode. Clearly, these desirable single photon

source features rely on achieving a large NV-to-antenna coupling rate, compared to direct photon emission or metal quenching. Optimizing the NV-to-antenna coupling rate is typically done by maximizing the quality factor to mode volume ratio of the antenna, spectrally tuned for the optical transition. The NV center should further be positioned at the point of maximum mode amplitude with the NV-dipole axis coaligned with the electric field of the antenna mode.²² The near-field interaction of two cubes hybridize the dipolar cube modes (Figure 1c) into an “antibonding” and a “bonding” mode (Figure 1d) shifted to respectively higher and lower energies (Figure 1e). The “bonding” mode is particularly well-suited for coupling to a QE, as the mode is strongly confined to the nanoscale gap,²³ whereas the superradiant damping of the in-phase cube oscillations ensures high antenna radiation efficiency.²⁴ The capacitor-like field distribution in the gap requires the cube facet to be aligned normal to the dipole axes of the NV center for optimal coupling. We realize the optimal coupling configuration by precharacterization of the NV center dipole orientation and deterministic nanoassembly of the cube dimer antenna with an AFM.

The NV center is pumped with a 532 nm linearly polarized continuous wave or pulsed laser. The pump light is focused onto the ND by an oil immersion objective (NA 1.4), situated below the quartz glass sample. Photons spontaneously emitted into the same objective are filtered by a dichroic mirror (cutoff 550 nm) and detected by two avalanche photodiodes (APD) in a Hanbury Brown-Twiss configuration, a grating spectrometer, or a charge-coupled device (CCD) camera. The pump polarization is controlled by a halfwave plate in the excitation light path, whereas an analyzer introduced in the detection path probes the polarization of emitted photons. Nanoparticle manipulation is performed by an AFM positioned above the sample (see Supporting Information (SI) for a schematic). Pumping an ~ 35 nm ND (Figure 2b), we observe single photon emission from an NV center, identified by a measured $g^{(2)}(0)$ -value of 0.14 (Figure 3c) and the zero phonon line fingerprint for the neutral (NV^0 , 575 nm) and negative charge state (NV^- , 637 nm) (Figure 1e). The NV center continuously flip-flops between the charge states by photoionization,²⁵ however photon emission is dominated by the NV^- -state, populated $\sim 75\%$ of the time. Our experiment is hence well described by considering purely the NV^- -state (see SI for cube coupled NV center spectra). Excitation and emission from the excited doublet state of NV^- -center is facilitated by two orthogonal dipole axes ($\mathbf{p}_x, \mathbf{p}_y$) lying in the plane normal to the nitrogen atom-vacancy axis²⁶ (Figure 2a). We probe the projection of $\mathbf{p}_x, \mathbf{p}_y$ on the sample plane by rotating the pump polarization while operating the NV center in the nonsaturated regime (105 μW pump power) (Figure 2e). The detected photon rate then follows $R(\varphi) = \eta q_e \gamma_{\text{ex}}(\varphi)$ with η being the collection efficiency of the objective and q_e the quantum efficiency of the emitter. The excitation rate $\gamma_{\text{ex}}(\varphi) \propto \sum_{i=x,y} |\mathbf{p}_i \cdot \mathbf{E}(\varphi)|^2$ depends on the electric field of the pump laser $\mathbf{E} = \mathbf{E}_{\text{pump}}$ at the emitter position, polarized along the sample plane at the azimuth angle φ . We fit $R(\varphi)$ for the dipole plane containing $\mathbf{p}_x, \mathbf{p}_y$ and determine the largest dipole projection on the sample plane by the pump angle φ_p^{NV} resulting in maximum photon rate (Figure 2e). φ_p^{NV} is indicated by the blue arrow with respect to the system configurations in Figure 2b–d. Two 80 nm chemically synthesized silver cubes are subsequently positioned along φ_p^{NV} in a dimer configuration for optimal NV-to-antenna coupling (Figure 2c,d). $R(\varphi)$ for the cube-coupled

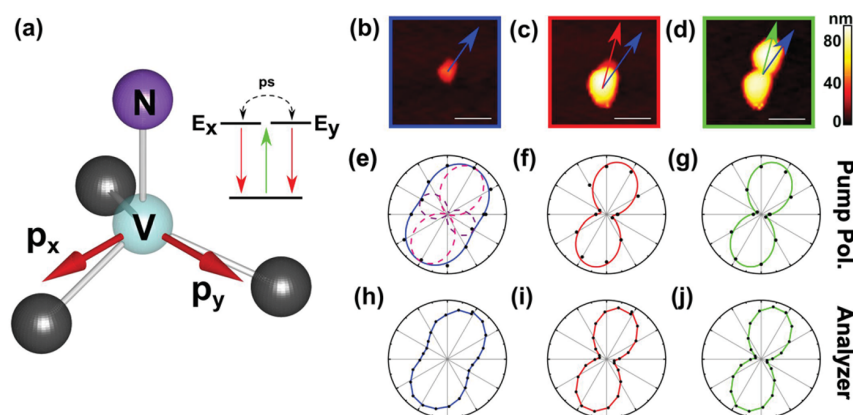


Figure 2. (a) Sketch of the NV center in diamond. The excitation rate of the NV^- charge state scales with the pump field projection on the dipole axes \mathbf{p}_x , \mathbf{p}_y . Phonon promoted population averaging of the doublet excited state E_x , E_y (inset) facilitate spontaneous emission, polarized along either dipole axis. (b–d) AFM assembly of photon source color-coded to corresponding experimental measurements for (b) isolated ND (blue), (c) single cube (red), and (d) 2-cube configuration (green) scale bar 200 nm. Blue arrow represent the orientation of largest inplane dipole moment of the NV center, while red and green arrow give the electric field orientation of the antenna mode. (e–g) Normalized photon rate versus pump polarization angle, measured (dot) and model fit (solid). Dash curves in (e) indicate potential linear contributions of \mathbf{p}_x and \mathbf{p}_y to the model. (h–j) Normalized photon rate versus analyzer angle, measured (dot) and interpolation (solid).

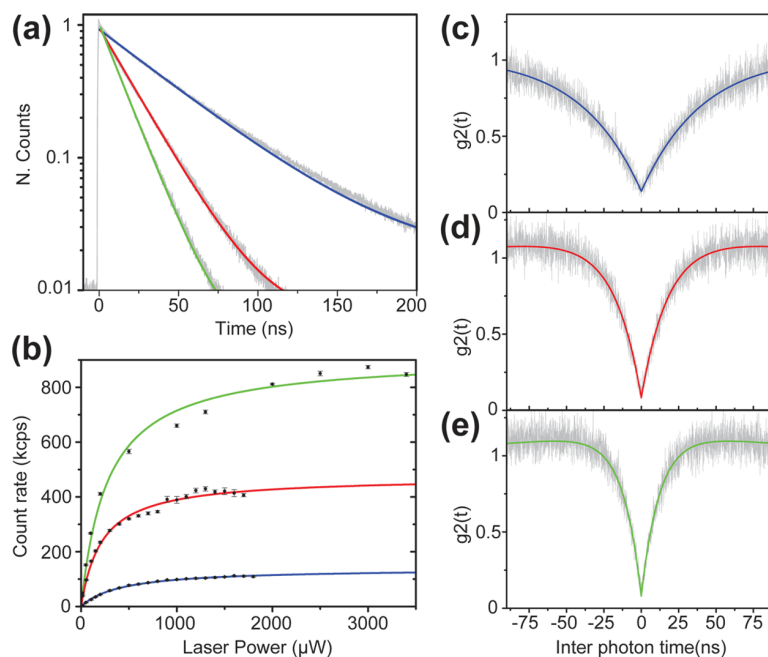


Figure 3. Color coded model fits to experimental data (gray) for isolated ND (blue), single cube (red), and 2 cubes (green). (a) Excited state decay curves, fitted to single exponentials. (b) Saturation curves, background corrected for signal from nearby plain surface and (c–e) 2. order correlation measurement (raw data).

system is well described by adding an additional term for the electric field generated by the cube(s) $\mathbf{E}_{\text{cube}} = f_e \tilde{\alpha} \mathbf{E}_{\text{pump}}$, such that $\mathbf{E} = \mathbf{E}_{\text{pump}} + \mathbf{E}_{\text{cube}}$, $f_e + 1$ is the electric field enhancement and $\tilde{\alpha}(\varphi_p^{\text{cube}})$ is the polarizability tensor of the cube, defined by the orientation of the cube dipole moment (φ_p^{cube}), which is coaligned with the electric field of the cube mode. We account for the enhancement factor $\eta q_e / \eta_0 q_{e,0}$ of 1.52 (one cube) and 2 (two cubes), relative to the isolated ND indexed 0, and fit f_e , φ_p^{cube} to experiment (Figure 2f, g) (see SI for details). For both cube configurations, we find $\varphi_p^{\text{cube}} - \varphi_p^{\text{NV}} = 15^\circ$, confirming near optimal alignment of the NV dipole axes with the electric field of the cube(s). The orientation of φ_p^{cube} with respect to cube

configurations is given by, respectively, a red or green arrow in Figure 2c,d. The enhancement of excitation rate is determined by $\gamma_{\text{ex}} / \gamma_{\text{ex},0} = R q_e \eta_0 / R_0 q_e \eta$ for which we find values of 5.1 (one cube) and 5.86 (two cubes) at pump orientation φ_p^{cube} . Having established the dipole orientation of the NV center and optimized the antenna configuration accordingly, we turn to the emission properties of the photon source. Rotating an analyzer in front of our detector, we find weakly polarized photons emitted from the isolated ND, with a polarization ratio of $r_{\text{pol}} = 2.1$, between the photon rate detected along the major and minor axis (Figure 2h). The major axis of polarization is coaligned with φ_p^{NV} , as photons are generally polarized along the dipole axis of emission, while the two dipole configuration

of the NV⁻ state result in an overall weak photon polarization. The photon emission becomes increasingly polarized throughout assembly of the cube antenna, as we find $r_{\text{pol}} = 6.9$ for a single cube and $r_{\text{pol}} = 9$ for two cubes (Figure 2i,j). We note a slight shift of the major axis of polarization toward $\varphi_{\text{p}}^{\text{cube}}$, which is in good agreement with the polarization of emission, being the result of polarized photon scattering from plasmonic charge oscillations along the antenna dipole axis. The increase of photon polarization is naturally accompanied by an increase of the excited state decay rate (γ), as the degree of photon polarization scales with the increasing rate at which the NV center decays from the excited state, by driving charge oscillations in the cube antenna. We recorded the temporal response to a sharp excitation pulse and found an enhancement of the excited state decay rate of respectively $\gamma/\gamma_0 = 2.25$ for one cube and $\gamma/\gamma_0 = 3.28$ for two cubes (Figure 3a). Unfortunately, the faster decay rate does not translate directly to an increase in photon rate, as the decay rate enhancement may partially result from metal quenching, or emission coupled to the antenna may be lost ohmically. The brightness of the source is hence determined by tracing out the saturation curve in terms of detected photon rate as a function of pump power (Figure 3b). After subtraction of background from the plain sample surface, the detected photon rate is fitted to the conventional model

$$R(P) = R_{\infty} \frac{P}{P + P_{\text{sat}}} \quad (1)$$

with P being the pump power, P_{sat} is the saturation power and R_{∞} the asymptotic photon rate limit, detected at infinite pump power. Curiously, the $R_{\infty}/R_{\infty 0}$ enhancement is significantly larger than the decay rate enhancement, as we find $R_{\infty}/R_{\infty 0} = 3.41$ for one cube and $R_{\infty}/R_{\infty 0} = 6.58$ for two cubes with $R_{\infty} = 914$ kcps. The system is stable under large pump power as we operate the source at a photon rate of 850 kcps, close to the photon rate limit. An AFM scan after ~ 10 min of operation indicates no morphological changes of the antenna. We attribute such power stability to the low ohmic heating losses of pristine monocrystalline silver, impeding thermal deformation even at large pump powers, while the strong radiative damping of the dimer mode may also be a contributing factor. Further, the large interband transition energy of silver, ~ 3.4 eV,²⁷ prevents background photoluminescence from the metal, thereby ensuring high single photon purity. The photon purity is examined by histogramming the time interval (τ) between photon detection events, yielding the second order correlation function $g^{(2)}(\tau)$. $g^{(2)}(0)$ events hence correspond to simultaneous detection of two photons, which are only possible in the presence of background as the NV center may only emit one photon at a time. The $g^{(2)}(0)$ -value is determined by fitting a three-level rate model including a background term, normalized for $\tau \rightarrow \infty$ ²⁸ (Figure 3c–e). The $g^{(2)}(0)$ value slightly improves by the addition of cubes to 0.08 from 0.14 measured for the isolated ND. The improved $g^{(2)}(0)$ value may be a result of the increased brightness of the NV center effectively improving the signal-to-background ratio.

Concluding the description of photon source emission properties, we now numerically examine the relation of the experimentally observed enhancement factors γ/γ_0 and $R_{\infty}/R_{\infty 0}$. We write the decay rate of the isolated NV center in terms of a radiative rate (γ_{r0}) and an intrinsic nonradiative rate (γ_{nr0}), such that $\gamma_0 = \gamma_{\text{r0}} + \gamma_{\text{nr0}}$ with a corresponding intrinsic quantum efficiency $q_{\text{e0}} = \gamma_{\text{r0}}/\gamma_0$. Introducing a silver cube accelerates the

radiative decay rate as additional decay channels, such as the plasmonic cube mode or metal quenching, are available for emission, whereas γ_{nr0} is unaffected by the environment. The changed radiative decay is written $\gamma_{\text{r}} = \Gamma\gamma_{\text{r0}}$ such that the decay rate for the one or two cube configuration is given by $\gamma = \Gamma\gamma_{\text{r0}} + \gamma_{\text{nr0}}$. The decay rate enhancement in this case takes the form

$$\frac{\gamma}{\gamma_0} = \Gamma q_{\text{e0}} + (1 - q_{\text{e0}}) \quad (2)$$

The photon rate limit is given by $R_{\infty} = \eta\gamma_{\text{r}}$. We define collection efficiency as the probability of a radiative decay event, resulting in a photon being emitted into the objective. Losses due to metal quenching or ohmic dissipation of antenna excitations are thereby included in η and the photon rate enhancement can be written

$$\frac{R_{\infty}}{R_{\infty 0}} = \frac{\eta}{\eta_0} \Gamma \quad (3)$$

The NV center emission is modeled by 3D finite element simulations, as the power dissipated at 680 nm wavelength by two orthogonal electric dipoles, oriented along the experimentally determined dipole plane and positioned in the center of a 35 nm ND. The ND is modeled as a four-sided truncated pyramid. Γ is then obtained as the total power dissipated in the one or two cube configuration, relative to the ND situated on a glass substrate. Decay rate enhancement is calculated by eq 2 for various q_{e0} values (Figure 4a). We find good agreement of modeled and experimental values for realistic gap sizes 40–45 nm, for an intrinsic quantum efficiency of $q_{\text{e0}} \sim 0.35$, which is in good agreement with previous experimental studies of the ND product.²⁹ Setting $q_{\text{e0}} = 0.35$ and inserting experimental values γ/γ_0 , $R_{\infty}/R_{\infty 0}$ in eqs 2 and 3, we confirm the consistency of experiment and model by predicting η/η_0 in similar good agreement with modeling (Figure 4b (inset)), while $R_{\infty}/R_{\infty 0}$ may be directly modeled for similar gap sizes (Figure 4b). The disparity of γ/γ_0 and $R_{\infty}/R_{\infty 0}$ is thereby well explained by the nonunity intrinsic quantum efficiency of the NV center. For $q_{\text{e0}} = 0.35$ we find $\Gamma = 4.57$ for one cube and $\Gamma = 7.51$ for two cubes using eq 2. The corresponding quantum efficiency is calculated to respectively 0.71 and 0.80 by $q_{\text{e}} = \Gamma q_{\text{e0}} / (1 + q_{\text{e0}}(\Gamma - 1))$. The modeled and experimentally predicted increase of collection efficiency, going from one to two cubes (Figure 4b (inset)) is attributed to an increase of antenna efficiency as the numerical model finds respectively $\sim 63\%$ and $\sim 97\%$ of dipole emission reaching the far-field, while the fraction of far-field emission collected by the objective is nearly unchanged. The increase in antenna efficiency should be expected given the superradiative damping of the dimer mode, compared to the plasmonic mode of a single nanoparticle. The large photon enhancement is thereby a result of an increased quantum efficiency of the NV center, while an improved antenna efficiency of the dimer configuration, is a contributing factor to the enhancement over the single cube.

We conducted the experiment four times, labeled experiment A–D, A being the experiment presented up to this point (Figure 4c–f) (see SI for measurements). Consistently we find $R_{\infty}/R_{\infty 0} > \gamma/\gamma_0$ suggestive of a nonunity intrinsic quantum efficiency. The photon rate limit improved for all assembled photon sources by the addition of a second cube, with values $R_{\infty} = 671$ –1460 kcps and a consistently high photon purity of $g^{(2)}(0) = 0.08$ –0.26 for the dimer configuration (Figure 4c,d). Curiously the $g^{(2)}(0)$ value did however deteriorate for the

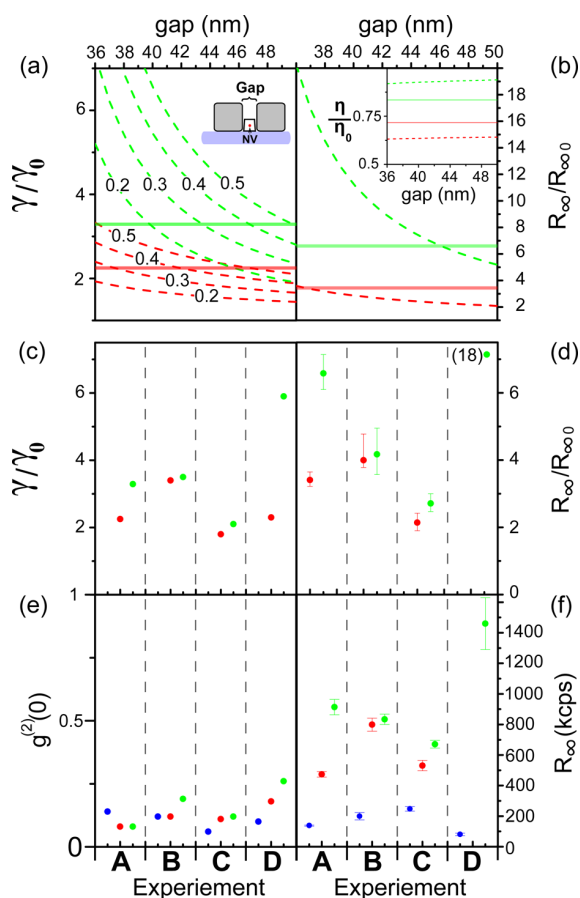


Figure 4. (a,b) Modeling of experiment A (dashed) and experimental values (solid, horizontal) for a single (red) or two cube configuration (green). (a, inset) Modeled values are given for an NV center situated in the center of a 35 nm ND for realistic gap separation of nanocubes. (a) Decay rate enhancement for intrinsic quantum efficiency $q_{e0} = 0.2$ – 0.5 labeled on the curve. (b) Enhancement of detected photon rate at saturation, inset gives the experimentally predicted ratio of collection efficiency for $q_{e0} = 0.35$ (solid) together with modeling (dashed). (c–f) Data summary of experiment A–D for isolated ND (blue), one cube (red), and two cubes (green). The single cube data point in experiment D (d,f) is absent as the saturation curve was not traced to high enough laser power for a reliable fit. Errorbars indicate the 95% confidence interval, not shown for (c) as errors ~ 0.01 .

cube coupled systems in experiment B–D, even though the photon rate went up, which suggest an increase in background as well. We speculate such an increase in background may be a result of silver corrosion giving rise to background fluorescence from the cubes. The background level is in this case expected to increase with the time the cubes spend on the sample. The main corrosion agent of silver is sulfur forming silver sulfide (Ag_2S). The corrosion rate increase with the sulfur concentration in the air, while high air humidity may also accelerate the process.³⁰ On the other hand the nanometers thin polyvinylpyrrolidone (PVP) layer encapsulating the silver cubes can be expected to limit the corrosion rate. Once the AFM tip breaks the PVP-layer at the onset of cube manipulation, the corrosion could be accelerated. The cubes spend 4–5 days on the sample, while characterization and assembly was conducted over the last continuous stretch of 16–22 h. Variations in assembly time, humidity, and sulfur air

concentration may therefore cause different $g^2(0)$ values though generally contributing to the deterioration of the $g^2(0)$ value over time. We note the quality of the $g^2(0)$ value seem to follow the enhancement of photon rate at nonsaturated laser powers of $\sim 100 \mu\text{W}$ for which the autocorrelation function was measured. The largest photon rate enhancement and improvement of $g^2(0)$ was observed in experiment A. Experiment C exhibited near unchanged photon rate and $g^2(0)$ values for the one- and two-cube configuration, while both photon rate and $g^2(0)$ value deteriorated in experiment B and D after adding a second cube. The decrease in photon rate observed in experiment B and D going from a one- to two-cube configuration, may be the result of an angled cube gap. The excitation field is hence preferentially confined to the small gap side, while the nanodiamond is located at the large gap side. Enhancement factors for a single cube are $\gamma/\gamma_0 = 1.8$ – 3.4 , $R_\infty/R_{\infty 0} = 2.1$ – 4.0 , whereas the spread is more significant for two cubes $\gamma/\gamma_0 = 2.1$ – 5.9 , $R_\infty/R_{\infty 0} = 2.7$ – 18.0 . The larger spread is expected, given the strong dependence on cube separation, which is limited to the size of the ND, varying between experiments ~ 30 – 35 nm. Asymmetry of cube configurations, varying dipole orientation, and position of NV center in the ND should further contribute to the spread in experimental results.

Conclusion and Outlook. In summary, we have presented a remarkably pure photon source, with a $g^{(2)}(0)$ value of 0.08, based on an NV center contained in a ~ 35 nm ND, placed in the gap between two monocrystalline silver nanocubes. The low ohmic heating losses of pristine monocrystalline silver allowed for stable operation under large laser powers at a detected photon rate of 850 kcps near the saturation limit of 914 kcps. We demonstrated how AFM assembly of the photon source allowed for near optimal alignment of nanocubes for the maximum inplane dipole moment of the NV center, while further tracking the photon polarization properties, from weak polarization for the bare ND to strong linear polarization for the assembled system. The experimental findings is consistent with modeling of an NV center with an intrinsic quantum efficiency of ~ 0.35 . The presented results are quite encouraging as significant improvements is within reach, by going for smaller gap sizes by employing smaller NDs down to 5 nm in size for stable NV center emission³¹ or 1.6 nm for the silicon vacancy center.³² A scalable approach to realizing the photon source is also conceivable with molecular self-assembly as controlled assembly of face–face or edge–edge cube dimer configurations have already been realized.³³ The edge–edge configuration appearing to be a promising configuration for further acceleration of the spontaneous decay rate.³⁴

Methods. Sample Preparation. An 0.18 mm thick fused quartz glass slide (SPI supplies) was cleaned by an RCA1 cleaning step. Five milliliters of Mili-Q and 1 mL of 28–30% $\text{NH}_4\text{OH}(\text{aq})$ solution heated to 65 °C were removed from heating plate and 1 mL of 30% $\text{H}_2\text{O}_2(\text{aq})$ and slide glass added for 10 min, followed by a two-step submersion in Mili-Q baths of 5 min each. The cleaning step removed organic residue and promoted surface hydrophilicity for subsequent spin-coating of a ND solution < 50 nm (Microdiamant), 100 nm of mean width silver cubes (nanoComposix) coated in a < 5 nm of polyvinylpyrrolidone (PVP) layer, and finally $\sim 10 \mu\text{m}$ long silver wires synthesized in-house. The macroscopic silver wires were used as reference markers during experiment.

Experimental characterization. The sample was mounted on a piezo scan stage, which allowed for identification of single

NV centers by confocal mapping of fluorescence using a 532 nm linear polarized continuous or pulsed laser with pulse width/period 50 ps/400 ns. See SI for procedure of identifying nanodiamonds containing single NV centers. The pump light was focused by a 1.4 NA oil immersion objective, used for excitation and collection of photon, while a halfwave plate controlled the pump polarization. The laser light was filtered from fluorescent photons by dichroic mirrors (SEMROCK) (cutoff 550 nm) before being detected by a CCD camera (Hamamatsu-Orca-Flash4LT), an EMCCD (Andor, iXon Ultra888) connected to a grating spectrometer (Andor, Shamrock 500i), or two APDs (Picoquant, τ -SPAD) in a Hanbury Brown-Twiss configuration. Photon rate as a function of pump polarization or power was obtained by the time average of 2 s time traces accumulated from both APDs. Decay rate curve and $g^{(2)}(\tau)$ was obtained by histogramming the time interval from respectively a laser sync pulse or APD detection event to a detection event on the other APD, using an electronic timing box (Picoquant, PicoHarp 300) in a start-stop configuration. The polarization of emission was probed by the accumulated CCD image count (4 s int) for various analyzer orientations. All experiments were completed within 5 days of spin-coating nanocubes.

Dark-Field Spectrum. The dark-field spectrum of a single silver cube was obtained in transmission mode, illumination through the glass slide with a 1.2 NA DF oil condenser lens, and collecting light above the sample with a 50 \times NA 0.75 objective. A 400 μ m pinhole positioned in image plane in front of a fiber coupled spectrometer allowed for selection of a single cube. The background signal obtained in the absence of a sample was subtracted from cube- and reference spectrum, using the diffuse scattering from the glass substrate as reference resulting in the cube scattering spectrum.

Finite Element Modeling. The 3D finite element modeling was conducted in the commercially available Comsol Multiphysics 5.1. The parameter Γ is modeled classically using the relation $\Gamma = \gamma_r/\gamma_{r0} = P^{NV}/P_0^{NV}$ with P^{NV} being the total power dissipated by two orthogonal classical electric dipoles, lying in the dipole plane experimentally determined by the model fit in Figure 2e with regards to the antenna axis φ_p^{cube} . Simulation performed at emission wavelength 680 nm was found to be independent of the dipoles orientation in the plane. Index 0 refers to the reference system of dipoles situated in the center of a 35 nm tall, 4-sided truncated pyramid shaped, diamond on a semi-infinite glass substrate, bordered from above by an air hemisphere. The modeled domain is bounded by a perfectly match layer. An 8 nm corner/side rounding radius were used for the 80 nm cubes introduced symmetrically around the diamond. Material parameters were based on interpolation of tabulated data.^{35–37} The collection efficiency was modeled as $\eta = P_{\text{obj}}^{NV}/P^{NV}$ with P_{obj}^{NV} being the power integrated over a spherical surface in the glass substrate, corresponding to the solid collection angle of the experimental 1.4 NA objective.

■ ASSOCIATED CONTENT

■ Supporting Information

The Supporting Information is available free of charge on the ACS Publications website at DOI: 10.1021/acs.nanolett.7b01436.

Section S1: Schematic of experimental setup. Section S2: Fluorescence spectra of respectively isolated ND, 1 cube and 2 cube configuration for experiment A. Section S3:

Detailed explanation of the model, fitted to photon rate as a function of pump polarization angle for isolated ND and cube coupled configurations. Section S4: Experimental data plots for experiment B-D. Section S5: Procedure for AFM alignment and identification of ND's containing single NV centers (PDF)

■ AUTHOR INFORMATION

Corresponding Author

*E-mail: sekh@mci.sdu.dk.

ORCID

Sebastian K. H. Andersen: 0000-0003-4566-6036

Sergey I. Bozhevolnyi: 0000-0002-0393-4859

Notes

The authors declare no competing financial interest.

■ ACKNOWLEDGMENTS

The authors gratefully acknowledge the financial support of the European Research Council (Grant 341054 (PLAQNAP)).

■ ABBREVIATIONS

NV center	nitrogen vacancy center
ND	nanodiamond
QE	quantum emitter
AFM	atomic force microscope
APD	avalanche photodiode
PVP	polyvinylpyrrolidone

■ REFERENCES

- (1) O'Brien, J. L.; Furusawa, A.; Vuckovic, J. *Nat. Photonics* **2009**, *3*, 687–695.
- (2) Bennet, C. H.; Bassard, G. Quantum cryptography: Public key distribution and coin tossing, *Theoretical Computer Science*; Vol 560, Part 1, 4 December 2014, pp 7–11. DOI: 10.1016/j.tcs.2014.05.025, (<http://www.sciencedirect.com/science/article/pii/S0304397514004241>).
- (3) Beveratos, A.; Brouri, R.; Gacoin, T.; Villing, A.; Poizat, J.-P.; Grangier, P. *Phys. Rev. Lett.* **2002**, *89*, 187901.
- (4) Knill, E.; Laflamme, R.; Milburn, G. J. *Nature* **2001**, *409*, 46–52.
- (5) Dutt, M. V. G.; Childress, L.; Jiang, L.; Togan, E.; Maze, J.; Jelezko, F.; Zibrov, A. S.; Hemmer, P. R.; Lukin, M. D. *Science* **2007**, *316*, 1312–1316.
- (6) Aharonovich, I.; Englund, D.; Toth, M. *Nat. Photonics* **2016**, *10*, 631–641.
- (7) Ringler, M.; Schwemer, A.; Wunderlich, M.; Nichtl, A.; Kürzinger, K.; Klar, T. A.; Feldmann, J. *Phys. Rev. Lett.* **2008**, *100*, 203002.
- (8) Taminiau, T. H.; Stefani, F. D.; Segerink, F. B.; van Hulst, N. F. *Nat. Photonics* **2008**, *2*, 234–237.
- (9) Curto, A. G.; Volpe, G.; Taminiau, T. H.; Kreuzer, M. P.; Quidant, R.; van Hulst, N. F. *Science* **2010**, *329*, 930–933.
- (10) Bermúdez-Ureña, E.; Gonzalez-Ballester, C.; Gieslmann, M.; Marty, R.; Radko, I.; Holmgaard, T.; Alaverdyan, Y.; Moreno, E.; J. Garcia-Vidal, F.; I. Bozhevolnyi, S.; Quidant, R. *Nat. Commun.* **2015**, *6*, 7883.
- (11) Kolesov, R.; Grotz, B.; Balasubramanian, G.; Stohr, R. J.; Nicolet, A. A. L.; Hemmer, P. R.; Jelezko, F.; Wrachtrup, J. *Nat. Phys.* **2009**, *5*, 470.
- (12) Kurtsiefer, C.; Mayer, S.; Zarda, P.; Weinfurter, H. *Phys. Rev. Lett.* **2000**, *85*, 290–293.
- (13) Rogers, L. J.; McMurtrie, R. L.; Sellars, M. J.; Manson, N. B. *New J. Phys.* **2009**, *11*, 063007.
- (14) Ulbricht, R.; Dong, S.; Chang, I.-Y.; Mariserla, B. M. K.; Dani, K. M.; Hyeon-Deuk, K.; Loh, Z.-H. *Nat. Commun.* **2016**, *7*, 13510.

- (15) Babinec, T. M.; Hausmann, B. J. M.; Khan, M.; Zhang, Y.; Zhang, Y.; Maze, J. R.; Hemmer, P. R.; Loncar, M. *Nat. Nanotechnol.* **2010**, *5*, 195–199.
- (16) Choy, J. T.; Hausmann, B. J. M.; Babinec, T. M.; Bulu, I.; Khan, M.; Maletinsky, P.; Yacoby, A.; Loncar, M. *Nat. Photonics* **2011**, *5*, 738–743.
- (17) Schietinger, S.; Barth, M.; Aichele, T.; Benson, O. *Nano Lett.* **2009**, *9*, 1694–1698.
- (18) Li, L.; Chen, E. H.; Zheng, J.; Mouradian, S. L.; Dolde, F.; Schröder, T.; Karaveli, S.; Markham, M. L.; Twitchen, D. J.; Englund, D. *Nano Lett.* **2015**, *15*, 1493–1497.
- (19) Choy, J. T.; Bulu, I.; Hausmann, B. J.; Janitz, E.; Huang, I.-C.; Loncar, M. *Appl. Phys. Lett.* **2013**, *103*, 161101.
- (20) Jamali, M.; Gerhardt, I.; Rezai, M.; Frenner, K.; Fedder, H.; Wrachtrup, J. *Rev. Sci. Instrum.* **2014**, *85*, 123703.
- (21) Schröder, T.; Gädeke, F.; Banholzer, M. J.; Benson, O. *New J. Phys.* **2011**, *13*, 055017.
- (22) Gerard, J.-M.; Gayral, B. *J. Lightwave Technol.* **1999**, *17*, 2089.
- (23) Huang, J.-S.; Kern, J.; Geisler, P.; Weinmann, P.; Kamp, M.; Forchel, A.; Biagioni, P.; Hecht, B. *Nano Lett.* **2010**, *10*, 2105–2110.
- (24) Alù, A.; Engheta, N. *Phys. Rev. B: Condens. Matter Mater. Phys.* **2008**, *78*, 195111.
- (25) Aslam, N.; Waldherr, G.; Neumann, P.; Jelezko, F.; Wrachtrup, J. *New J. Phys.* **2013**, *15*, 013064.
- (26) Doherty, M. W.; Michl, J.; Dolde, F.; Jakobi, I.; Neumann, P.; Manson, N. B.; Wrachtrup, J. *New J. Phys.* **2014**, *16*, 063067.
- (27) Christensen, N. *Phys. Status Solidi B* **1972**, *54*, 551.
- (28) Novotny, L.; Hecht, B. *Principles of Nano-Optics*; Cambridge University Press, 2006.
- (29) Mohtashami, A.; Koenderink, A. F. *New J. Phys.* **2013**, *15*, 043017.
- (30) Graedel, T. E. *J. Electrochem. Soc.* **1992**, *139*, 1963–1970.
- (31) Bradac, C.; Gaebel, T.; Naidoo, N.; Sellars, M. J.; Twamley, J.; Brown, L. J.; Barnard, A. S.; Plakhotnik, T.; Zvyagin, A. V.; Rabeau, J. R. *Nat. Nanotechnol.* **2010**, *5*, 345–349.
- (32) Vlasov, I. I.; et al. *Nat. Nanotechnol.* **2013**, *9*, 54–58.
- (33) Gurunatha, K. L.; Marvi, S.; Arya, G.; Tao, A. R. *Nano Lett.* **2015**, *15*, 7377–7382.
- (34) Bahari, B.; Tellez-Limon, R.; Kante, B. *J. Appl. Phys.* **2016**, *120*, 093106.
- (35) Johnson, P. B.; Christy, R. W. *Phys. Rev. B* **1972**, *6*, 4370–4379.
- (36) Zaitsev, A. M. *Optical properties of diamond - a data hand book*; Springer, 2001.
- (37) Malitson, I. H. *J. Opt. Soc. Am.* **1965**, *55*, 1205–1209.

Supporting information for:

Ultrabright Linearly Polarized Photon Generation

from a Nitrogen Vacancy Center in a Nanocube

Dimer Antenna

Sebastian K. H. Andersen,* Shailesh Kumar, and Sergey I. Bozhevolnyi

*Center for nano optics, University of Southern Denmark, Campusvej 55, DK-5230 Odense
M, Denmark*

E-mail: sekh@mci.sdu.dk

1 S1: Experimental setup

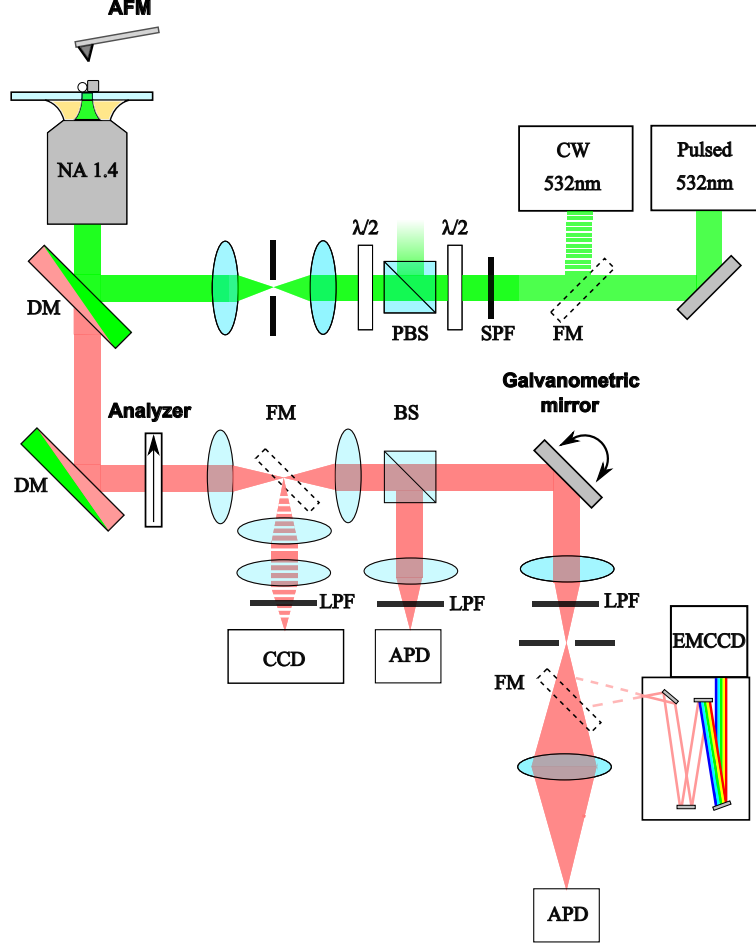


Figure S1: Experimental setup for characterization of NV-center emission properties. A fused quartz slide glass with spincoated silver cubes and ND's containing NV-centers, is illuminated from a 532 nm continuous wave (CW) or pulsed laser, through an oil immersion objective (NA 1.4). An AFM situated above the sample is applied for particle manipulation. The spontaneously emitted photons collected by the objective is filtered from laser light by dichroic mirrors (DM) and a long pass filter (LPF) and detected either by a CCD camera, two APD's or spectrally dispersed on an EMCCD, by a grating spectrometer. The laser polarization is controlled by a half-wave plate ($\lambda/2$), while the polarization of photon can be probed by introducing an analyzer in the detection light path. FM: Flip mirror, SPF: Short pass filter, PBS: Polarizing beam splitter.

2 S2: NV-center fluorescence spectra experiment A

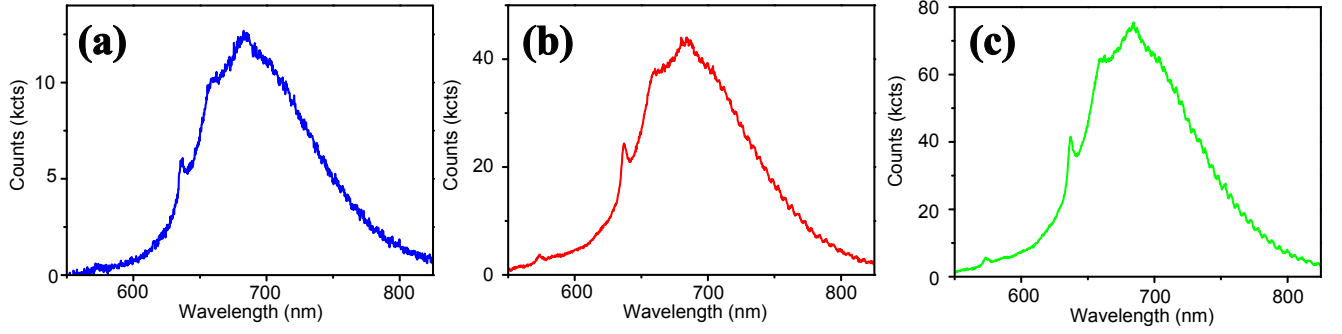


Figure S2: Fluorescence spectra from single NV-center as obtained from experiment A in configurations (a) Isolated ND, (b) single cube and (c) two cube configuration.

3 S3: Photon rate as function of pump polarization

In the non-saturated regime the detected photon rate follow $R(\varphi) = \eta q_e \gamma_{ex}(\varphi)$. η being the collection efficiency of the objective and q_e the quantum efficiency of the NV-center. The excitation rate (γ_{ex}) is proportional to $\gamma_{ex}(\varphi) \propto \sum_{i=x,y} |\mathbf{p}_i \cdot \mathbf{E}(\varphi)|^2$. $\mathbf{p}_x, \mathbf{p}_y$ being the two orthogonal dipole axes of the NV-center, lying in the plane normal to the vector \mathbf{v}_{NV} defining the axis connecting the vacancy and nitrogen atom of the NV-center. \mathbf{E} is the electric field vector at the emitter location, which for the bare nanodiamond is given by the laser field $\mathbf{E} = \mathbf{E}_{pump}$ oriented along the sample plane.

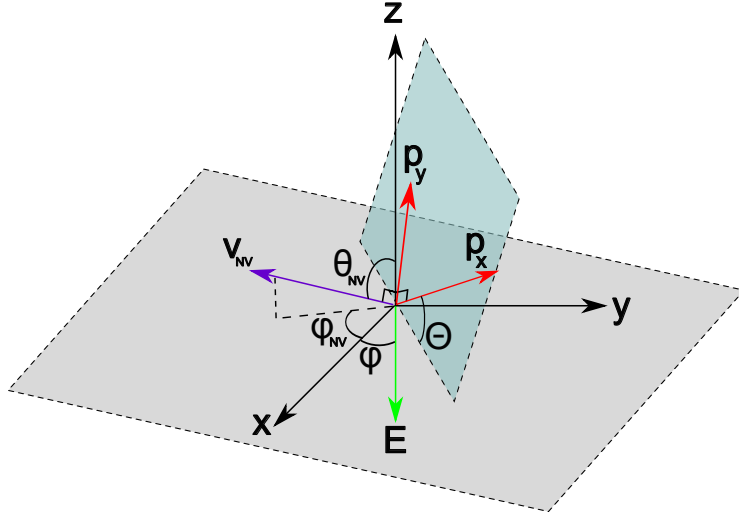


Figure S3: Cartesian coordinate frame indicating NV-center dipole plane (blue) containing dipole axes (red), defined by the purple normal vector. Green arrow indicate electric field vector lying in the sample plane (grey).

We define a cartesian coordinate system with z-axis normal to the sample plane (figure S3). The orientation of \mathbf{E}_{pump} is defined by the azimuthal angle φ . The dipole plane containing $\mathbf{p}_x, \mathbf{p}_y$ is defined by the normal vector \mathbf{v}_{NV} described by the angles $\varphi_{NV}, \theta_{NV}$, while the inplane orientation of $\mathbf{p}_x, \mathbf{p}_y$ is given by the angle Θ . Assuming $|\mathbf{p}_x| = |\mathbf{p}_y| = |\mathbf{p}|$ it can be shown that:

$$\gamma_{ex}(\varphi) \propto |\mathbf{p}|^2 |\mathbf{E}_{pump}|^2 (1 - \cos(\varphi - \varphi_{NV})^2 \sin(\theta_{NV})^2) \quad (1)$$

The measurement of $R(\varphi)$ thus contain no information of the orientation of $\mathbf{p}_x, \mathbf{p}_y$ in the dipole plane given by angle Θ . The orientation of the dipole plane can however be determined with some ambiguity as $\varphi_{NV} = \varphi_{NV} + \pi$ and $\pm\theta_{NV}$ yield equally good solutions. For practical purposes we extract $\varphi_{NV}, \theta_{NV}$ by fitting the normalized photon rate $R(\varphi)/R_{Max}^{ND} = (1 - \cos(\varphi - \varphi_{NV})^2 \sin(\theta_{NV})^2)$. R_{Max}^{ND} being the maximal photon rate.

Introducing one or two silver cubes yield a secondary electric field term arising from the incident laser field polarizing the silver cubes. For the cube geometry, the induced dipole moment (\mathbf{p}_{cube}) is expected to have a well defined orientation normal to the cube facet, defined by the azimuthal angle φ_p^{cube} (figure S4).

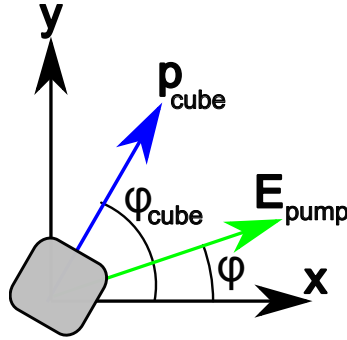


Figure S4: Sketch of cube dipole axis (\mathbf{p}_{cube}) wrt. silver cube inserted in cartesian coordinate frame.

Further the strength of the induced dipole moment is expected to vary with pump orientation as $|\mathbf{p}_{cube}| \propto \hat{\mathbf{p}}_{cube} \cdot \mathbf{E}_{pump}$. Finally we note in the near-field the electric field arising from cube polarization is coaligned with \mathbf{p}_{cube} and proportional in magnitude. The electric field (\mathbf{E}_{cube}), generated at the NV-center position is thereby assumed to have the form:

$$\mathbf{E}_{cube} = f_e \frac{\mathbf{p}_{cube} \cdot \mathbf{E}_{pump}}{|\mathbf{p}_{cube}| |\mathbf{E}_{pump}|} \begin{bmatrix} \cos(\varphi_p^{cube}) \\ \sin(\varphi_p^{cube}) \end{bmatrix} \quad (2)$$

f_e being a proportionality constant. Equation 2 may be rewritten to the form:

$$\mathbf{E}_{cube} = f_e \overset{\leftrightarrow}{\alpha} \mathbf{E}_{pump} \quad (3)$$

$$\overset{\leftrightarrow}{\alpha} = \begin{vmatrix} \cos(\varphi_p^{cube})^2 & \sin(\varphi_p^{cube}) \cos(\varphi_p^{cube}) \\ \sin(\varphi_p^{cube}) \cos(\varphi_p^{cube}) & \sin(\varphi_p^{cube})^2 \end{vmatrix} \quad (4)$$

Setting $\mathbf{E} = \mathbf{E}_{cube} + \mathbf{E}_{pump}$, the excitation rate is written:

$$\gamma_{ex} \propto \sum_{i=x,y} |\mathbf{p}_i \cdot (1 + f_e \overset{\leftrightarrow}{\alpha}) \mathbf{E}_{pump}|^2 \quad (5)$$

$\overset{\leftrightarrow}{\alpha}$ is thereby identified as the polarizability tensor of the cube, while f_e+1 is the field enhancement. For both cube configurations we fit the normalized photon rate $R(\varphi)/R_{Max}^{ND} = C \sum_{i=x,y} |\mathbf{p}_i \cdot (1 + f_e \overset{\leftrightarrow}{\alpha}) \mathbf{E}_{pump}(\varphi)|^2$ for fit parameters f_e , φ_p^{cube} , while maintaining the dipole configuration initially fitted for the bare nanodiamond. $C = \eta q_e / \eta_0 q_{e0}$ being a constant accounting for the estimated changes of collection- and quantum efficiency, relative to the NV-center in the isolated nanodiamond, indexed 0. Subsequent multiplication by R_{Max}^{ND} recovers fits for the experimental photon rates (figure S5). The presented model ignore field enhancement arising from the polarization of the orthogonal cube axis, as the field should be negligible. Further \mathbf{E}_{pump} and \mathbf{E}_{cube} are assumed to be inphase as f_e is assumed real. Phase delay included as a complex f_e , only affect 2. order terms and is not expected to affect the fitted φ_p^{cube} - value significantly.

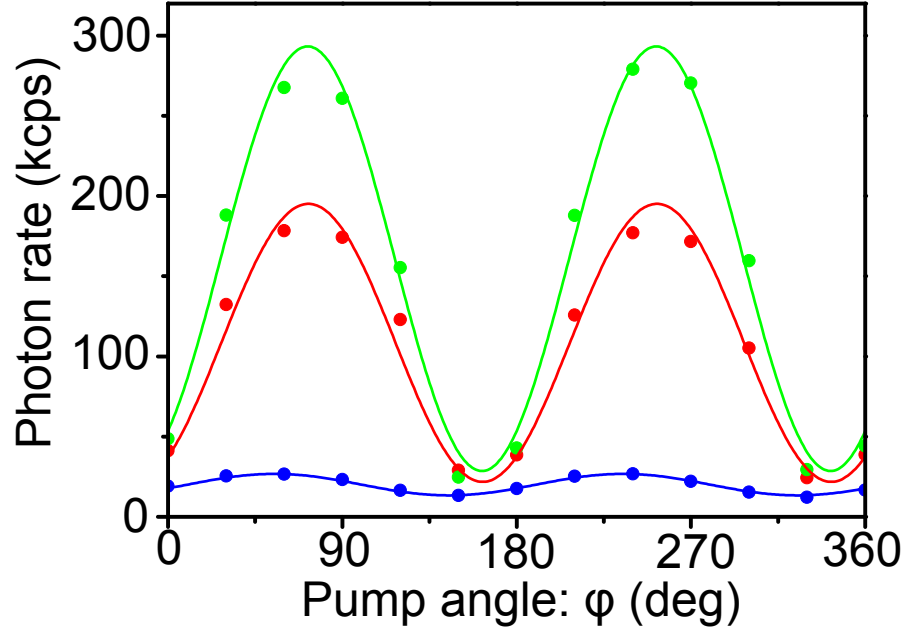


Figure S5: Photon rate as a function of pump polarization angle. Model fit (line) to experimental measurements (dot) for isolated nanodiamond(blue), single cube (red) and 2 cube configuration (green)

4 S4: Datasets for experiment B-D

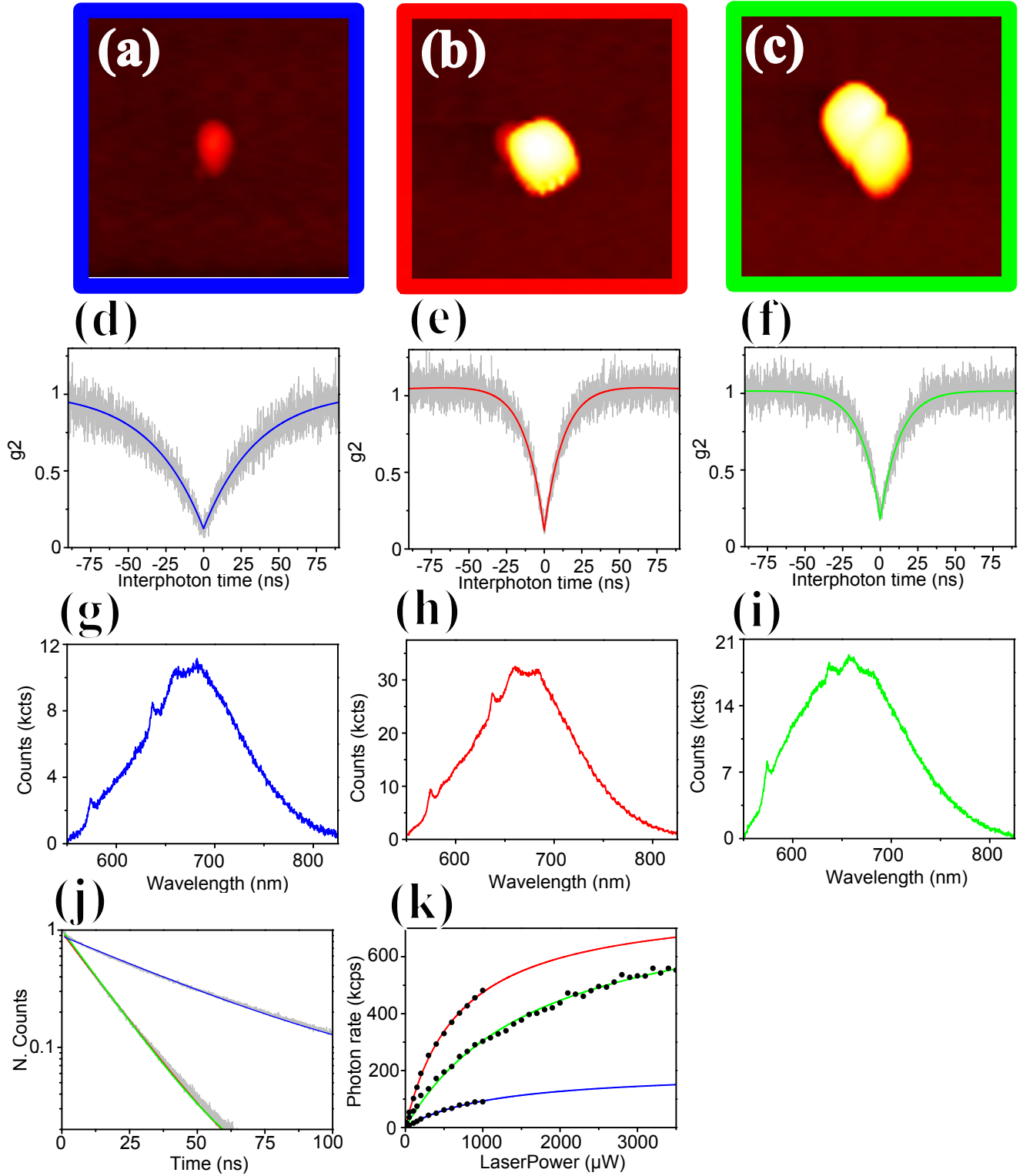


Figure S6: Experiment B. (a-c) AFM scans of photon source configurations, color coded to experimental measurements for (a) isolated ND (blue), (b) single cube (red) and (c) two cubes (green). (d-f) $g^{(2)}$ -measurement. (g-i) Fluorescence spectra. (j) Excited state decay curve and (k) saturation curve.

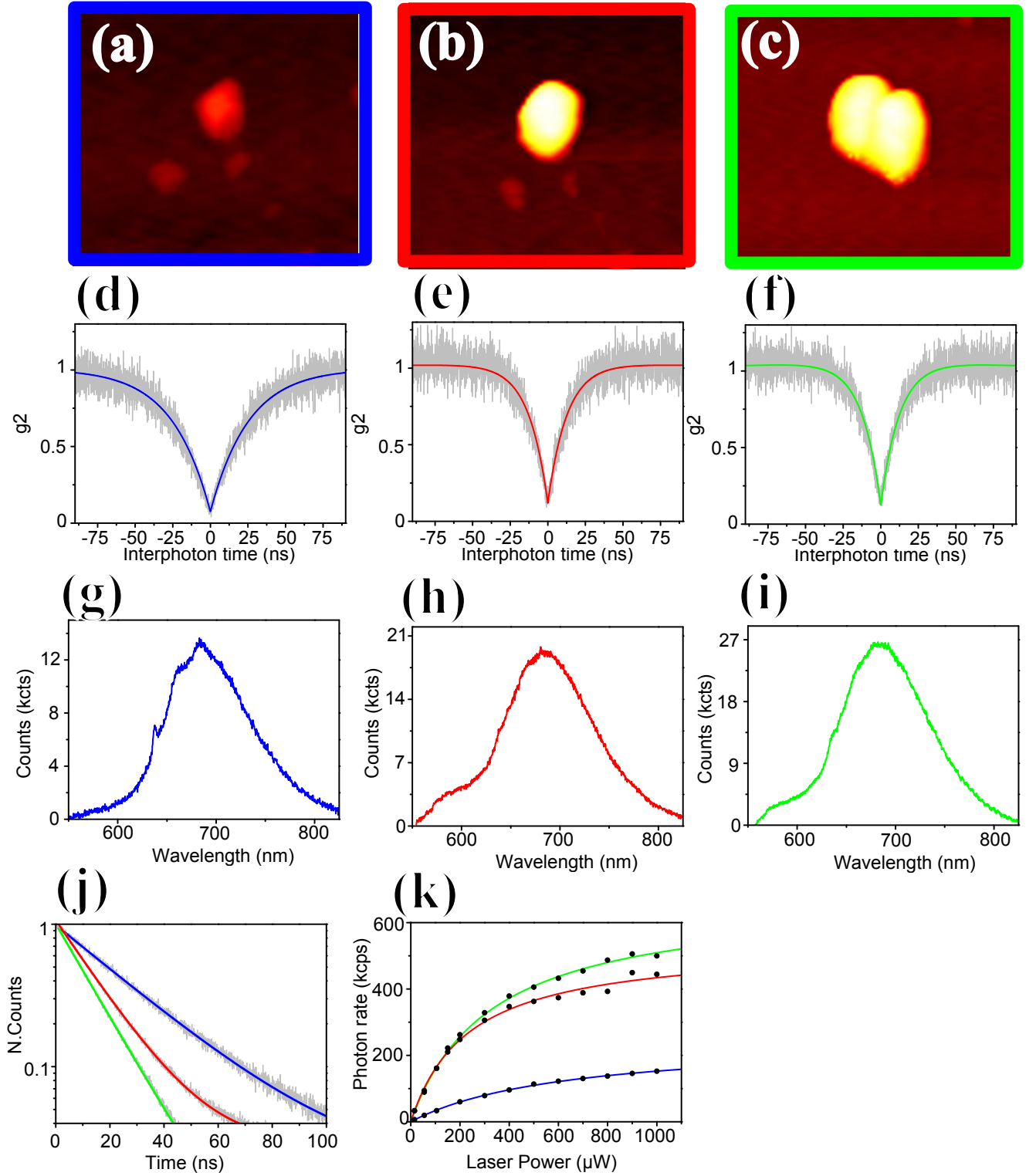


Figure S7: Experiment C. (a-c) AFM scans of photon source configurations, color coded to experimental measurements for (a) isolated ND (blue), (b) single cube (red) and (c) two cubes (green). (d-f) $g^{(2)}$ -measurement. (g-i) Fluorescence spectra. (j) Excited state decay curve and (k) saturation curve.

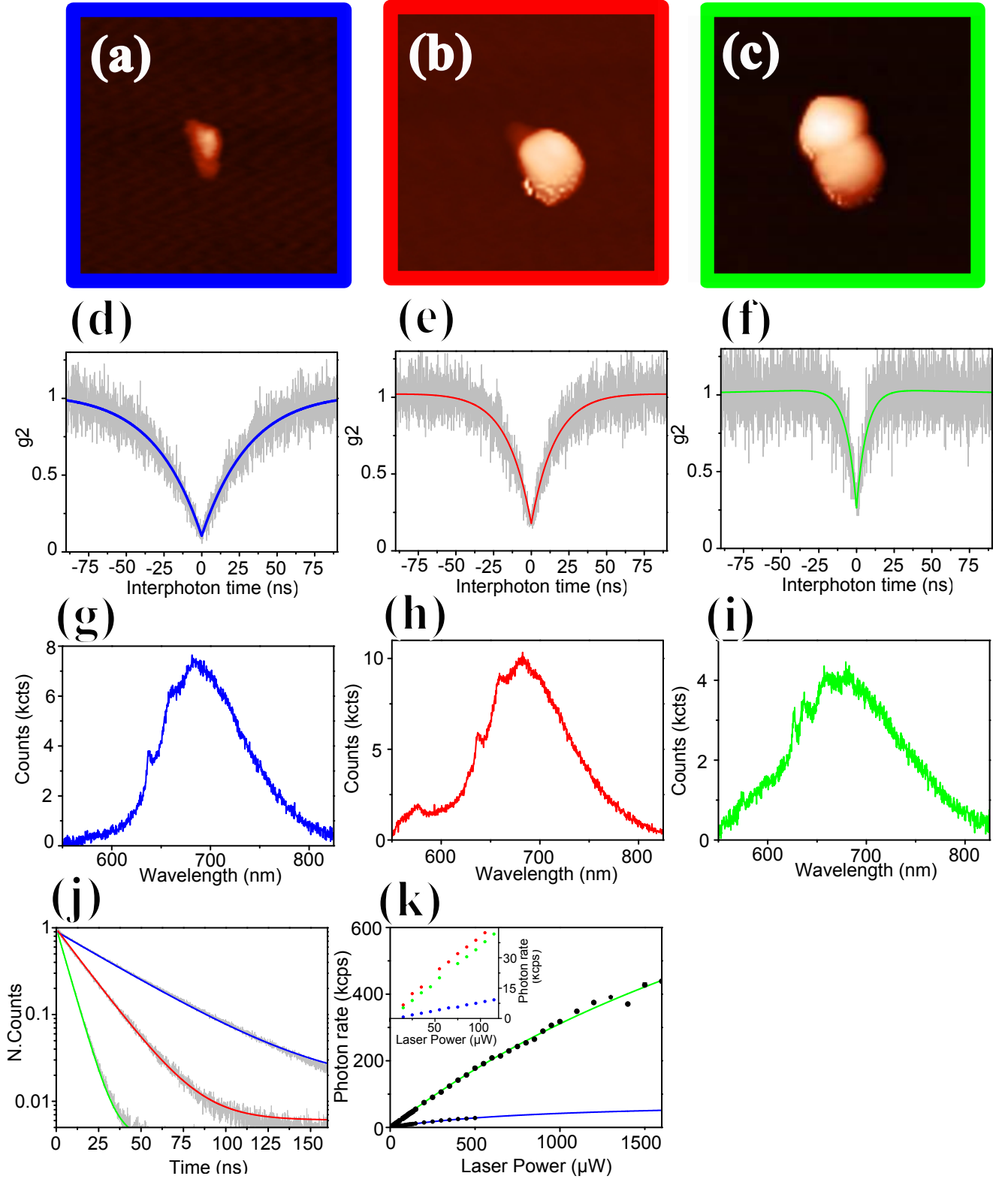


Figure S8: Experiment D. (a-c) AFM scans of photon source configurations, color coded to experimental measurements for (a) isolated ND (blue), (b) single cube (red) and (c) two cubes (green). (d-f) $g^{(2)}$ -measurement. (g-i) Fluorescence spectra. (j) Excited state decay curve and (k) saturation curve, inset give measured points for the initial linear slope.

5 S5: Procedure for AFM alignment and identification of nanodiamonds containing single NV-centers

The AFM assembly of a cube dimer antenna incorporating a ND containing a single NV-center, initially require the identification of a ND containing a single NV-center. As the AFM scan may only resolve the individual ND's, but not which ND contain an NV-center, a confocal fluorescence scan is required to identify the NV-center. The issue being a confocal scan does not resolve the individual ND's. In order to identify the specific ND that contain an NV-center, AFM scan and confocal map of the same sample region must therefore be compared. In this section we describe our procedure of aligning the AFM tip for the laser beam, allowing for AFM scan and confocal mapping of the same sample region. We then describe how the specific ND containing an NV-center may be identified.

1) Rough alignment Rough alignment of the AFM tip for the laser spot is performed by visually inspecting a mirror angled at 45° above the AFM cantilever. The mirror is conventionally used for bright light illumination of the sample below the cantilever and inspection of the sample region with a CCD camera, however here we use it for alignment. The piezo stage and AFM is positioned on a micrometer screw stage, which allow us to translate the sample and AFM wrt. the laser spot. For a misaligned laser spot and AFM tip, broadly distributed laser light is observed in the mirror, from the laser positioned below the cantilever. Aligning the AFM with the micrometer screw stage, the shadow of the cantilever can be observed in the mirror, meaning cantilever is closely aligned for the laser beam. For our case this is within $100\ \mu\text{m}$, which is the scan limit of our AFM. Please note visual inspection of laser light can be dangerous and should be done at low laser power to avoid eye damage.

2) Fine alignment Fine alignment is performed by scanning the sample with the AFM. For this purpose we spin coated $\sim 10\mu\text{m}$ long and $\sim 200\text{nm}$ high silver nanowires on the sample, as reference marks. A comparison of the AFM scan, showing wires and a bright field image, showing wires and laser spot, was enough to accurately align both laser spot and AFM for the same reference point on the sample.

3) Identification of nanodiamond In order to identify the nanodiamond on the AFM scan, that contain a single NV-center, we use the silver wire as a reference marker. Transferring the relative x, y coordinates of the tip of the silver wire and the NV-center, from the confocal map to the AFM scan, an approximate location of the nanodiamond can be determined. It is at that point just a matter of pushing potential nanodiamonds around with the AFM tip, and observe the movement on the confocal scan map to determine which nanodiamond that contain a single NV-center. Figure S9 show confocal map and AFM scan used in experiment C, to determine the nanodiamond containing a single NV-center.

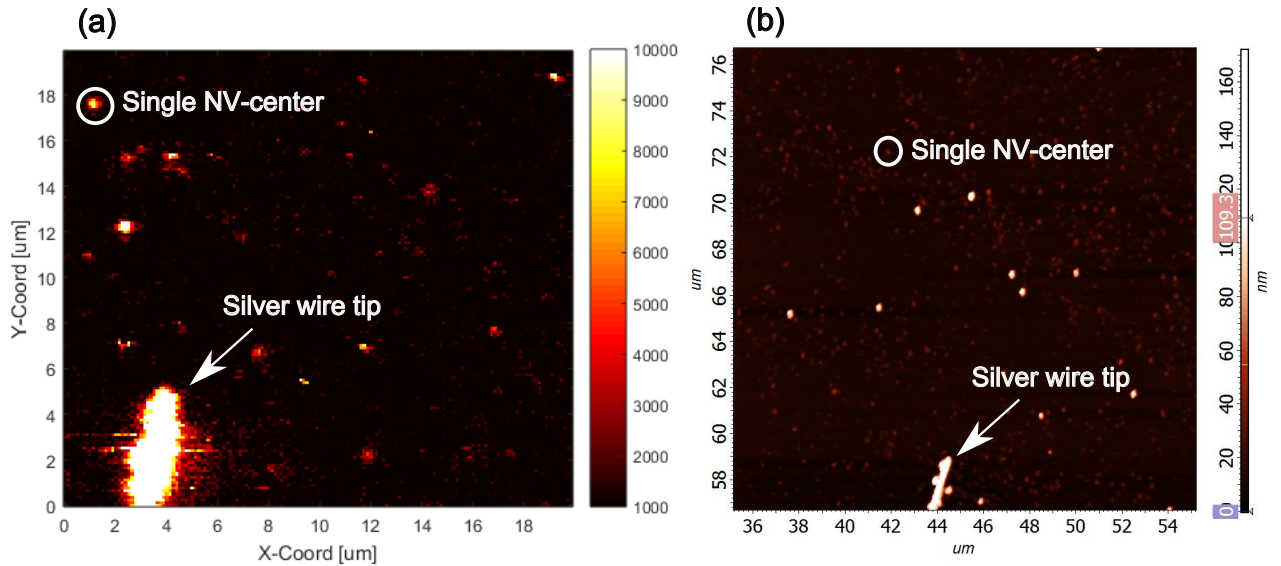


Figure S9: Corresponding (a) confocal map and (b) AFM scan used in used in experiment C, to relate identified NV-center in confocal map to specific ND in AFM scan.

D

HYBRID PLASMONIC BULLSEYE ANTENNAS
FOR EFFICIENT PHOTON COLLECTION

ACS Photonics - Accepted for publication

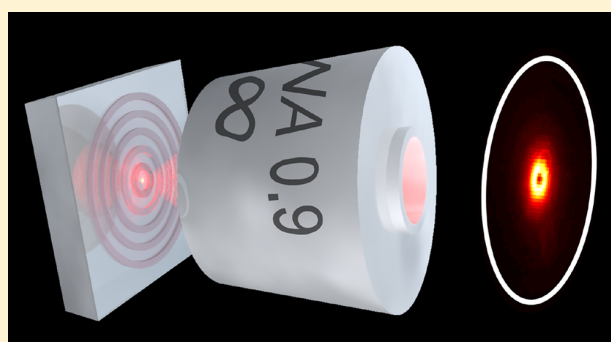
Hybrid Plasmonic Bullseye Antennas for Efficient Photon Collection

Sebastian K. H. Andersen,^{*,†} Simeon Bogdanov,[‡] Oksana Makarova,[‡] Yi Xuan,[‡] Mikhail Y. Shalaginov,[‡] Alexandra Boltasseva,[‡] Sergey I. Bozhevolnyi,[†] and Vladimir M. Shalaev[‡][†]Center for Nano Optics, University of Southern Denmark, DK-5230 Odense M, Denmark[‡]School of Electrical and Computer Engineering, Purdue Quantum Center, Purdue University, West Lafayette, Indiana 47907, United States

Supporting Information

ABSTRACT: We propose highly efficient hybrid plasmonic bullseye antennas for collecting photon emission from nm-sized quantum emitters. In our approach, the emitter radiation is coupled to surface plasmon polaritons that are consequently converted into highly directional out-of-plane emission. The proposed configuration consists of a high-index titania bullseye grating separated from a planar silver film by a thin low-index silica spacer layer. Such hybrid systems are theoretically capable of directing 85% of the dipole emission into a 0.9 NA objective, while featuring a spectrally narrow-band tunable decay rate enhancement of close to 20 at the design wavelength. Hybrid antenna structures were fabricated by standard electron-beam lithography without the use of lossy adhesion layers that might be detrimental to antenna performance. The fabricated antennas remained undamaged at saturation laser powers exhibiting stable operation. For experimental characterization of the antenna properties, a fluorescent nanodiamond containing multiple nitrogen vacancy centers (NV-center) was deterministically placed in the bullseye center, using an atomic force microscope. Probing the NV-center fluorescence we demonstrate resonantly enhanced, highly directional emission at the design wavelength of 670 nm, whose characteristics are in excellent agreement with our numerical simulations.

KEYWORDS: plasmonics, collection efficiency, nitrogen-vacancy center, quantum emitter, fluorescence



Efficient collection of photons from single quantum emitters (QE) is a key requirement for many quantum technological applications,¹ utilizing on-demand photon generation, optical spin read-out,^{2,3} or coalescence of indistinguishable photons.^{4,5} The efficiency by which photons can be collected is, however, often compromised by the nonunity quantum yield and relatively omnidirectional emission pattern of typical QEs, whether it is a molecule, quantum dot, or solid state defect.⁶ Fortunately, both aspects can be improved upon by engineering the photonic environment. Quantum yield may be increased by accelerating the radiative spontaneous decay rate, relative to intrinsic nonradiative decay, via the Purcell effect.⁷ Directional emission is typically achieved by two approaches:⁸ either a geometrical- or a mode-coupling approach. The geometrical approach relies on redirecting far-field emission by reflection or refraction on appropriately shaped surfaces, such as a parabolic mirror⁹ or solid immersion lens.¹⁰ Alternatively, the mode-coupling approach is based on near-field coupling QE emission to an antenna or waveguide mode. The emission pattern then conforms to that of the antenna,¹¹ while for detection with an objective, plane film waveguide modes may be redirected to free space by leakage into high index substrates¹² or scattering on periodic gratings.^{13,14} For highly directional emission, the circular symmetric bullseye grating is particularly attractive as

tight beaming of photons is achievable by appropriate grating design. Bullseye gratings have been utilized for photon collection from QEs in dielectric membranes^{13,14} or situated near a grating imprinted in a metal film. Here we consider the metallic counterpart. Metallic bullseye designs currently fall in two categories. The first category consists of an aperture in a metal film, encircled by a bullseye grating.^{15–17} This so-called bullseye aperture configuration features both large decay rate enhancement and highly directional emission from QEs situated in the aperture, however the antenna efficiency suffers from large ohmic losses. Single photon emission from such a configuration was demonstrated by Choy et al., considering a nitrogen-vacancy center (NV-center) in a diamond/silver-aperture.¹⁷ The design theoretically allowed for a decay rate enhancement of ~25 (relative to bulk diamond) and collection of ~17% of dipole emission with a 0.6 NA objective. Photon collection being compromised by reflections from the diamond/air interface appearing before the objective, and high losses of plasmon modes supported by diamond/silver interface. More recently, a second design, consisting of a quantum dot situated in a dielectric film above a silver film

Received: October 11, 2017

Published: January 7, 2018

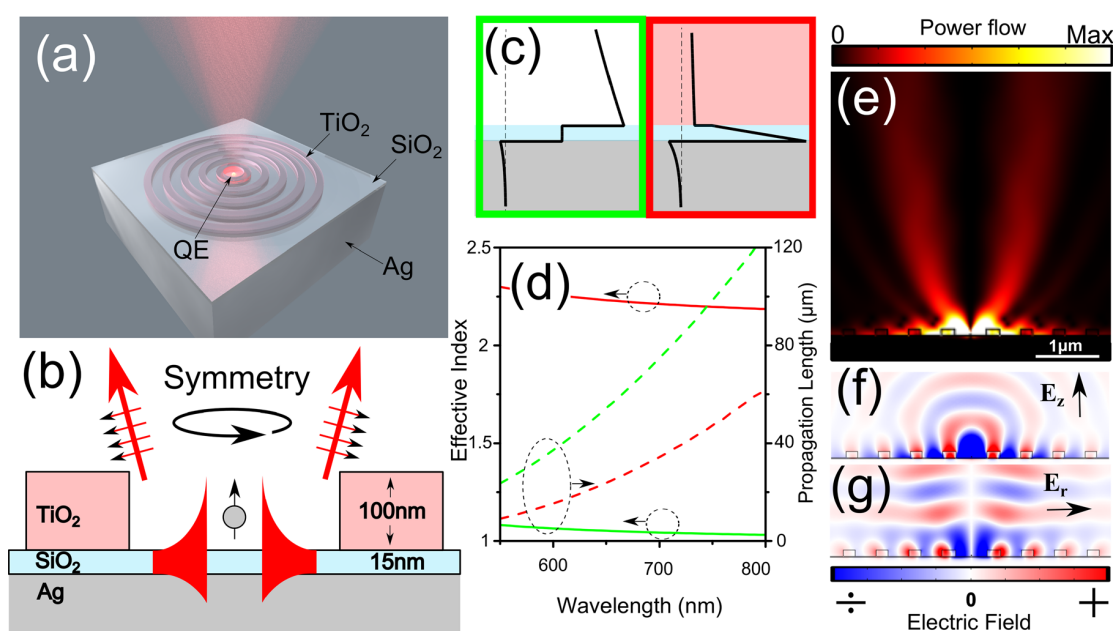


Figure 1. (a) Concept image of bullseye structure. Spontaneous emission from a centered quantum emitter is efficiently directed into the collection optics, as SPP-coupled emission scatters on the periodic ridges. (b) Profile view of the rotationally symmetric structure, emission is numerically modeled for a vertical dipole aligned with the symmetry axis. (c) Analytical out-of-plane electric field distribution for SPP modes supported by semi-infinite air (green) or TiO_2 (red) top layer on a 15 nm SiO_2 spacer, and semi-infinite bottom Ag layer. (d) Corresponding effective index (solid) and propagation length (dashed). (e) On resonance power density flow of optimized antenna with corresponding (f) out-of-plane and (g) radial electric field distributions.

bullseye grating, has been explored by Livneh et al., as a way to circumvent metal losses.^{18,19} Exceptionally directional beaming of single photons has been demonstrated by this design, allowing for $\sim 37\%$ of dipole emission to be collected with a 0.65 NA objective, while no decay rate enhancement was reported. The combination of appreciable decay rate enhancement and low-loss directive photon generation thus appears elusive from previous metal bullseye designs, while both are desirable to boost quantum yield and collection efficiency, respectively. Further, a common characteristic of these previous bullseye designs is the corrugation of the metal film. However, recently such structuring of silver films has been observed to be problematic for single photon applications, as corrugating silver films, either by focused ion beam milling or standard electron beam lithography, result in a significant background, detrimental for single photon applications.^{18,20} Antenna designs compatible with fabrication techniques which yield low background emission levels are therefore highly desirable for quantum photonics. Though novel fabrication techniques may improve background levels from corrugated silver,²¹ antenna designs based on planar silver films is an appealing approach, as background is significantly reduced compared to a corrugated surface.¹⁸ Further planar film designs are readily compatible with high-quality monocrystalline silver film fabrication techniques.²² While a variety of plasmonic antenna designs based on patterned metal films and/or metal nanoparticles has been realized, the planar silver film antenna employing a dielectric bullseye grating has not been explored.

In this study, we propose a hybrid plasmonic bullseye antenna design based on a planar silver film, employing a high-index, 100 nm-thick, dielectric, titania (TiO_2) bullseye grating, situated on a low-index, 15 nm-thin spacer layer, made of silica (SiO_2). The configuration combines low antenna loss and

highly directional emission with a moderate decay rate enhancement. Theoretically, 85% of the QE emission may be collected by a 0.9 NA objective lens, while the photon emission rate is accelerated by a decay rate enhancement of 18 (relative to vacuum), at the design wavelength of 670 nm. The design inherently ensures environmental protection of silver, by consequence of the protective silica layer, while the particular choice of materials allows for fabrication without compromising antenna performance by the use of lossy adhesion layers and stable operation at a laser power of 2.5 mW corresponding to saturation of NV-center fluorescence. For experimental demonstration of the design, a nanodiamond (ND) containing a large number of NV-centers was deterministically placed in the center of the bullseye, using an atomic force microscope. Spectrally resolving NV-center emission, a resonant enhancement peak (quality factor ~ 18) is observed at the design wavelength. The on-resonance emission is selected with a band-pass filter and confirmed to be highly directional by back-focal plane imaging, with the overall emission pattern closely following numerical predictions. Specifically, emission takes the form of a radially polarized, donut-shaped beam, imposed by the rotational symmetry of the antenna, with peak emission radiated at an angle of $5^\circ \pm 3^\circ$ fwhm with respect to the plane normal.

RESULTS AND DISCUSSION

The general operation of our device is conceptually illustrated in Figure 1a,b. A QE, centered in the bullseye antenna in close proximity to the silver film, spontaneously decays by excitation of surface plasmon polaritons (SPP) propagating along the dielectric–metal interface. The SPP subsequently scatter directionally on the periodically spaced TiO_2 ridges, resulting in highly directional emission.

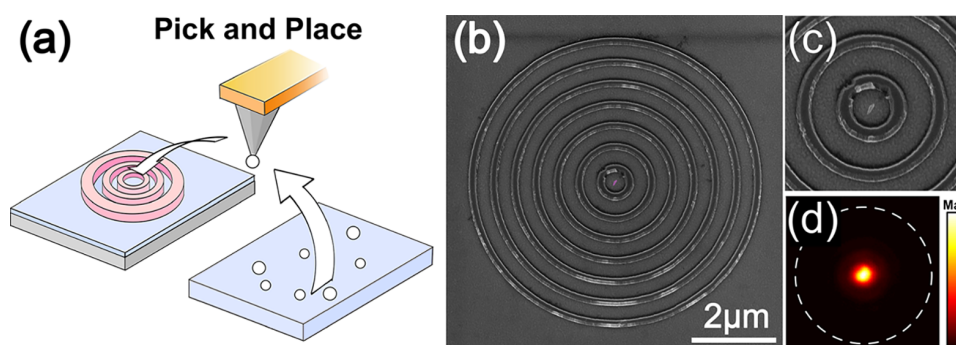


Figure 2. (a) Sketch of AFM “pick and place” technique used in transferring a ND from a coverslip to the bullseye center. (b) Electron micrograph of fabricated bullseye antenna, the transferred ND appears in false color in the center, (c) clearly apparent in the zoomed image. (d) False color CCD image of emission from the ND, dashed line indicates bullseye boundary.

The emission of a QE or electric dipole, situated in close proximity to a silver film, has been thoroughly studied²³ and analytically described.^{24,25} It is thus well-known the decay rate is accelerated when the dipole is oriented normal to the metal plane, as beyond photon radiation the dipole may release its energy by SPP emission or nonradiative metal quenching. SPP emission being the dominating decay channel for dipole-metal separations slightly larger than ~ 10 nm, ensured here by placing the emitter on top of a thin SiO₂ layer. On the other hand, when the dipole is oriented along the plane, emission is suppressed, as the dipole induces a mirrored antiphase charge distribution in the silver film (see [Support Information \(SI\)](#)). In the present study we thus neglect the weak in-plane dipole emission, and model QE emission solely in terms of the dominating vertical dipole ([Figure 1b](#)). Placing the dipole along the symmetry z -axis, our system reduces to a cylindrical symmetric system, for which we assume a constant azimuthal phase, as no particular phase preference can be expected. In other words, the emission field is assumed to be unchanged upon rotation about the z -axis. Clearly, in this case the radial electric field component is singular on the symmetry axis, and must therefore be zero ([Figure 1g](#)). The condition prohibits emission along the symmetry axis, as the transverse field of a plane wave, propagating along the symmetry axis, must be zero. The rotational symmetry of dipole source and antenna is thus expected to result in a radially polarized emission field, for which emission normal to the silver film is prohibited, regardless of emission wavelength.

With the symmetry constraints in place, we now seek to maximize dipole emission into the 0.9 NA objective, at the target wavelength of $\lambda_0 = 670$ nm, by introducing a dielectric grating for scattering of SPP coupled emission. In order to maximize antenna efficiency, we seek to minimize SPP propagation loss by employing a high-index TiO₂ grating ($n = 2.2$ index, measured with ellipsometry see [SI](#)), separated from the silver film by a thin low-index SiO₂ spacer layer ($n = 1.45$ index). The SPP mode of the high index-low index spacer - on conductor configuration²⁶ is receiving increasing interest as a possible approach for low-loss plasmonics.^{27,28} Analytical solutions for the SPP mode supported by the 3-layer structure ([Figure 1c,d](#)) reveal large modulation of the effective index from $N_{\text{eff}}^{\text{air}} = 1.05$ (air-SiO₂-Ag) to $N_{\text{eff}}^{\text{TiO}_2} = 2.25$ (TiO₂-SiO₂-Ag), with propagation lengths of, respectively, $L_p^{\text{air}} = 63$ μm and $L_p^{\text{TiO}_2} = 28$ μm , far exceeding lateral antenna dimensions. SPP coupled emission is thus prone to either scatter on the TiO₂ grating or reflect back to the emitter, while propagation losses

are minimal. For fabrication purposes, we set titania and silica film thicknesses to 100 and 15 nm, respectively, and numerically optimize in-plane grating parameters for collecting the maximal amount of power from a dipole, positioned 15 nm above the SiO₂ film, using a 0.9 NA objective (see [SI](#) for optimization procedure). While the vertical dipole position is set to a typical height, expected experimentally, the optimized antenna performance is weakly dependent on the actual position (see [SI](#)). For the optimized antenna, the inner TiO₂ ridge (inner radius 250 nm, TiO₂ width 212 nm) forms a standing wave cavity ([Figure 1f](#)), accelerating dipole emission by a decay rate enhancement of 18 (relative to vacuum). Simultaneously, the periodic TiO₂ grating (period 520 nm, duty cycle 0.36), directionally scatters SPP coupled emission, such that 85% of the power emitted by the dipole is collected by the objective. While on-resonance SPP emission is scattered at an angle near normal to silver plane ([Figure 1e,g](#)), the scattering angle generally seems to follow the grating equation (see [SI](#) for comparison). The geometrical optimization of TiO₂ height is a trade-off between decay rate enhancement and collection efficiency. Collection efficiency defined as the fraction of the total dipole power, collected by the objective, while decay rate enhancement is the factor by which the total dipole emission power increases in the bullseye environment, relative to vacuum. Indeed, a significant increase in decay rate enhancement is possible by increasing the TiO₂ thickness (see [SI](#) for modeling) at the cost of collection efficiency, as the SPP perform an increasing number of lossy round trips in the cavity before scattering to free space. For practical fabrication purposes, the low aspect ratio design of 100 nm TiO₂ was preferred, while the 15 nm SiO₂ film thickness was set to ensure a homogeneous coverage of the silver film, for environmental protection of the silver.

The bullseye antenna sample was fabricated on a Si substrate by e-beam evaporation of 10 nm Ti, 3 nm Ge, followed by a 200 nm Ag film, and topped by a 15 nm SiO₂ layer, without breaking the vacuum. The Ge layer act as a wetting layer, reducing roughness of the consecutively deposited Ag film.²⁹ The 100 nm TiO₂ bullseye grating was subsequently formed by standard electron beam lithography and e-beam evaporation ([Figure 2b](#)). Importantly, device performance was not degraded by the use of any lossy adhesion layers at the Ag-SiO₂-TiO₂ interfaces, while remaining mechanically robust to sonication, applied during lift-off. A ND (length ~ 140 nm, height ~ 35 nm) containing a large number of NV-centers was subsequently picked up from a coverslip and placed in the center of the

bullseye antenna, using an atomic force microscope (AFM; Figure 2a). The AFM “pick and place” technique³⁰ allows for precise centering of the ND, as confirmed by electron microscopy (Figure 2d). Pumping the ND with a 532 nm continuous-wave laser, we image the NV-center fluorescence onto a CCD camera, using a 0.9 NA $\times 100$ objective and fluorescence filtering from a dichroic mirror (cutoff 550 nm) and long pass filter (cutoff 550 nm; see SI for thorough method description). NV-center emission is observed as a spot, tightly confined to the center of the antenna (Figure 2c). While fluorescence is weakly observed throughout the whole antenna (see SI for log-scale image), the fast drop-off in fluorescence intensity indicate efficient scattering of SPP emission on the TiO₂ ridges. Correspondingly, antennas without a ND appear dark, when mapping fluorescence by laser-scanning confocal microscopy (see SI for comparison). In order to observe the wavelength dependent decay rate enhancement, expected from numerical modeling (Figure 3a), the NV-center emission was

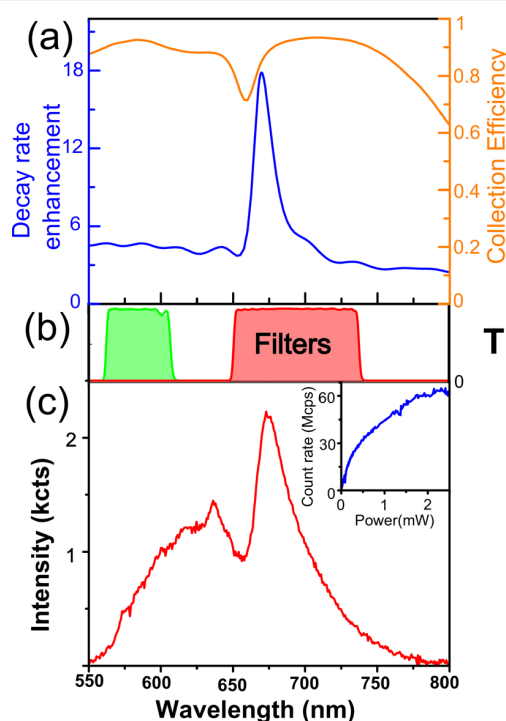


Figure 3. (a) Modeled decay rate enhancement (blue) and collection efficiency (orange) for fabricated bullseye design. (b) Transmission of bandpass filters used for detecting off-resonance (560–610 nm; green) and on-resonance (650–740 nm; red) emission, respectively. (c) Emission spectrum from ND centered in bullseye. Inset shows the background corrected saturation curve, demonstrating stable antenna operation up to saturation laser power.

spectrally resolved on a grating spectrometer (Figure 3c). The zero phonon lines (ZPL) for the neutral (575 nm) and negative (637 nm) charge states confirm the NV-center as the origin of fluorescence, while the overall spectrum is dominated by a resonant enhancement peak at 675 nm, in reasonable agreement with the spectral position and shape of the modeled decay rate enhancement. The experimental quality factor of ~ 18 (estimated from spectrum) is broader than the modeled resonance ~ 41 (estimated from decay rate enhancement curve), presumably due to fabrication imperfections. Collection

efficiency is not expected to significantly affect the spectrum, as modeling finds overall high broadband collections efficiency (Figure 3a), stemming from emission into SPP and grating scattering of SPP into objective both being broadband effects.

For efficient photon generation, it is typically desired to maximize photon rate from the QE, by pumping the QE to saturation. We confirmed that our device is stable under such conditions by increasing laser power to the 2.5 mW limit of our equipment. Simultaneously monitoring the photon rate detected by a avalanche photo diode, we smoothly transition to stable operation at saturation (Figure 3c, inset). Subsequently, reducing laser power, we retrace the saturation curve, thereby confirming no antenna alterations. The planar film bullseye antenna is generally expected to exhibit a higher laser damage threshold, than structured film configurations, as nanostructuring of metals suffer from melting point depression.³¹ Having confirmed stable operation at saturation laser power and the presence of resonantly enhanced emission, we proceed by examining the off- and on-resonance emission pattern, selected with bandpass filter in the wavelength range 560–610 nm and 650–740 nm (Figure 3b). Introducing a bertrand lens in infinity space, we resolve the emission pattern by imaging the back-focal plane (BFP) of the objective onto the CCD camera (Figure 4a). This lens configuration is particularly well suited for Fourier microscopy.³² Filtering for resonant emission reveals a highly directional radiation pattern in the characteristic donut-shaped pattern, imposed by the antenna symmetry (Figure 4d). Introducing an analyzer in the optical path, the radiation is confirmed to be radially polarized (Figure 4e,f). This is apparent as emission is spatially extinguished along the axis normal to the analyzer axis for a random analyzer orientation. For a comparison with the numerical design, we extracted the angular radiation pattern from a single pixel slice of the BFP-image, finding the experiment generally replicates numerical expectations. On resonance, the peak emission is detected at an angle of $5^\circ \pm 3^\circ$ fwhm wrt. the plane normal, in good agreement with the designed emission angle of $6^\circ \pm 4^\circ$ fwhm, modeled for the resonance wavelength of 670 nm (Figure 4g). Probing off-resonant emission, we find the peak emission increasing to an angle of $14^\circ \pm 8^\circ$ fwhm (Figure 4k), while the symmetry conditioned, radially polarized donut shaped beam pattern is conserved (Figure 4h–j). Off-resonance emission is in line with the modeled emission for a wavelength of 610 nm having peak emission at an angle of $16^\circ \pm 5^\circ$. Off-resonance emission is modeled at the wavelength of 610 nm, as experimentally, the maximum spectral power transmitted by the band-pass filter is found at this wavelength (Figure 3c). The directional emission is in stark contrast to the nondirectional emission observed from the same type of ND in the absence of a bullseye antenna (Figure 4b,c). The agreement of the experimental case considering an ensemble of relatively randomly oriented dipole emitters and the numerical model of a vertical dipole, result from the selective radiative enhancement/suppression of emitters with a predominately vertical/horizontal dipole moment, given efficient coupling to SPP or destructive interference. The fluorescence signal dominated by vertical dipoles, thereby mimic the numerical model considering only a vertical dipole. Indeed the particularly broad decay rate distribution, observed for the ND placed in the antenna, does indicate an enhancement/suppression of decay rates (see SI). The antenna performance on a single emitter level is therefore expected to strongly depend on the dipole orientation.

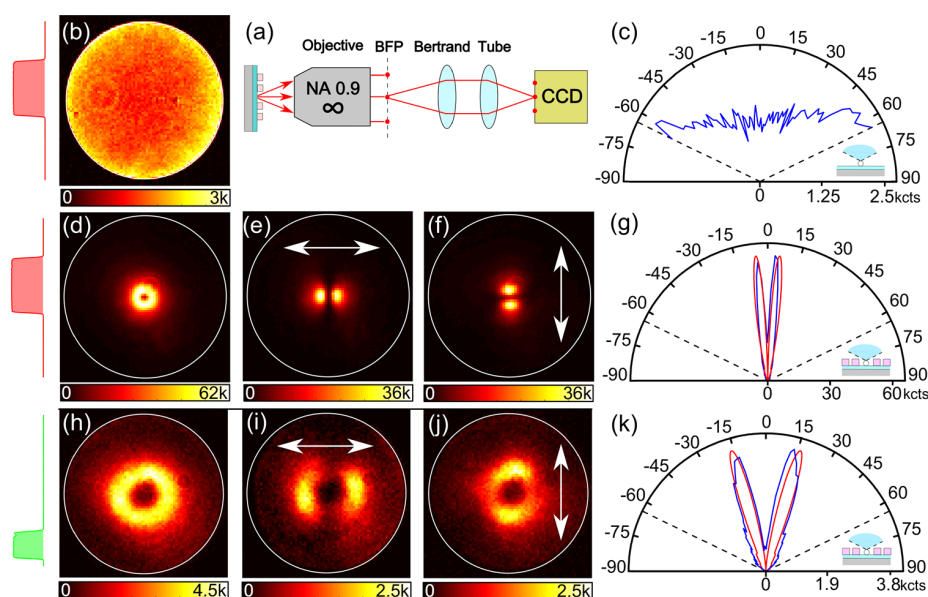


Figure 4. (a) Schematic of experimental setup for back-focal plane (BFP) imaging. (b) Reference BFP-image from ND, without antenna, on the plane SiO_2/Ag sample and (c) corresponding emission pattern, filtered for on-resonance emission. The detection limit of the 0.9 numerical aperture of the objective is indicated by respectively a white circle or black dashed lines. BFP-images filtered for (d–f) on- and (h–j) off-resonance emission from ND in bullseye, imaged with (e, i) horizontal or (f, j) vertical analyzer. Experimental (blue) and modeled (red) emission patterns for (g) on-resonance, model wavelength 670 nm and (k) off-resonance regime, model wavelength 610 nm. BFP images are obtained at 28 μW laser power and 10 s integration time, while colorbars give the camera counts.

The relatively narrowband decay rate enhancement and directive emission, demonstrated for this design, may be of interest for indistinguishable photon experiments, as the selective enhancement and efficient collection of ZPL photons from solid state emitters is desirable. The simple fabrication allows for easy tuning of the antenna resonance to the ZPL of new promising QEs such as the silicon- or germanium vacancy centers.^{33,34} However, for scalable single photon source fabrication, large-scale QE positioning techniques need to be explored. Potential approaches may be lithographic patterning³⁵ or electro-static pad positioning.³⁶ Further, the highly directional emission pattern should lend itself to optical fiber coupling. Theoretically, 23% and 74% of dipole emission (wavelength 670 nm) fall within the numerical aperture of respectively a single- (NA 0.12) or multimode fiber (NA 0.4). It is in this context worth noting that the radially polarized emission pattern, inherent to the bullseye antenna, may be converted to the fundamental mode of an optical fiber with high fidelity.³⁷ Directive emission is further advantageous for NV ensemble-based sensing applications, relying on optical read-out of the NV-center spin state, where strong decay rate enhancement should be avoided.³

CONCLUSION

In summary, we have proposed a high-efficiency hybrid plasmonic bullseye antenna design, consisting of a high-index titania grating, separated from a planar silver film by a thin low-index silica spacer layer. The architecture is motivated by previous issues with background emission resulting from nanostructuring of silver films. Our design combines low antenna loss, directional emission and moderate decay rate enhancement, leading to a theoretical collection efficiency of 85% for a 0.9 NA objective and acceleration of the emission rate by a decay rate enhancement of 18, at the design wavelength of 670 nm. The design is experimentally realized by

standard electron beam lithography, followed by deterministic placement of a fluorescent ND in the bullseye, using the AFM “pick and place” technique. The particular material design allows for fabrication without lossy adhesion layers compromising device performance, and stable operation of the antenna at laser powers large enough for saturated pumping of the NV-centers contained in the ND. Decay rate enhancement is experimentally observed as a resonant peak in the NV-center emission spectrum at 675 nm (quality factor ~ 18). The resonantly filtered fluorescence is demonstrated to be highly directional by back-focal plane imaging, with peak emission at an angle of 5° with respect to plane normal. Specifically, the emission pattern takes the form of a donut-shaped, radially polarized beam as imposed by the antenna symmetry, regardless of emission wavelength. Experimental observations closely mimic the numerical design, thereby validating the proposed design. However, further experiments must be conducted using single emitters in order to experimentally quantify collection efficiency of the antenna. The demonstrated design is significant for quantum technological development, as light-matter interfaces ensuring efficient photon collection from single QEs are highly desirable for quantum optical applications.

ASSOCIATED CONTENT

Supporting Information

The Supporting Information is available free of charge on the ACS Publications website at DOI: 10.1021/acsphotonics.7b01194.

- S1: Schematic of experimental setup. S2: Analytical model of electric dipole above silver film. S3: Ellipsometry measurement of TiO_2 refractive index. S4: Numerical optimization procedure of bullseye antenna. S5: Antenna performance as function vertical dipole

position S6: Comparison of bullseye emission angle with grating equation. S7: Optimized antenna design for different TiO₂ heights. S8: Antenna fluorescence image in log scale S9: Confocal scan of bullseye antenna with and without ND. S10: Lifetime distribution measurements (PDF).

AUTHOR INFORMATION

Corresponding Author

*E-mail: sekh@mci.sdu.dk.

ORCID

Sebastian K. H. Andersen: 0000-0003-4566-6036

Sergey I. Bozhevolnyi: 0000-0002-0393-4859

Notes

The authors declare no competing financial interest.

ACKNOWLEDGMENTS

The authors gratefully acknowledge the financial support of the European Research Council (Grant 341054 (PLAQNAP)), Georgia St. (Grant 106806), MRSEC (Grant 105675), ONR-DURIP (Grant No. N00014-16-1-2767), AFOSR-MURI (Grant No. FA9550-14-1-0389), and DOE (Grant DE-SC0017717).

ABBREVIATIONS

QE	quantum emitter
TiO ₂	titania
SiO ₂	silica
SI	Supporting Information
NV-center	nitrogen vacancy center
ND	nanodiamond
BFP	back focal plane
AFM	atomic force microscope
ZPL	zero phonon line
SPP	surface plasmon polariton

REFERENCES

- O'Brien, J. L.; Furusawa, A.; Vuckovic, J. Photonic quantum technologies. *Nat. Photonics* **2009**, *3*, 687–695.
- Steiner, M.; Neumann, P.; Beck, J.; Jelezko, F.; Wrachtrup, J. Universal enhancement of the optical readout fidelity of single electron spins at nitrogen-vacancy centers in diamond. *Phys. Rev. B: Condens. Matter Mater. Phys.* **2010**, *81*, 035205.
- Bogdanov, S.; Shalaginov, M. Y.; Akimov, A.; Lagutchev, A. S.; Kapitanova, P.; Liu, J.; Woods, D.; Ferrera, M.; Belov, P.; Irudayaraj, J.; Boltasseva, A.; Shalae, V. M. Electron spin contrast of Purcell-enhanced nitrogen-vacancy ensembles in nanodiamonds. *Phys. Rev. B: Condens. Matter Mater. Phys.* **2017**, *96*, 035146.
- Bernien, H.; Childress, L.; Robledo, L.; Markham, M.; Twitchen, D.; Hanson, R. Two-Photon Quantum Interference from Separate Nitrogen Vacancy Centers in Diamond. *Phys. Rev. Lett.* **2012**, *108*, 043604.
- Sipahigil, A.; Jahnke, K. D.; Rogers, L. J.; Teraji, T.; Isoya, J.; Zibrov, A. S.; Jelezko, F.; Lukin, M. D. Indistinguishable Photons from Separated Silicon-Vacancy Centers in Diamond. *Phys. Rev. Lett.* **2014**, *113*, 113602.
- Aharonovich, I.; Englund, D.; Toth, M. Solid-state single-photon emitters. *Nat. Photonics* **2016**, *10*, 631–641.
- Kinkhabwala, A.; Yu, Z.; Fan, S.; Avlasevich, Y.; Mullen, K.; E, M. Large single-molecule fluorescence enhancements produced by a bowtie nanoantenna. *Nat. Photonics* **2009**, *3*, 654–657.
- Barnes, W.; Björk, G.; Gérard, J.; Jonsson, P.; Wasey, J.; Worthing, P.; Zwiller, V. Solid-state single photon sources: light collection strategies. *Eur. Phys. J. D* **2002**, *18*, 197–210.
- Schell, A. W.; Neumer, T.; Shi, Q.; Kaschke, J.; Fischer, J.; Wegener, M.; Benson, O. Laser-written parabolic micro-antennas for efficient photon collection. *Appl. Phys. Lett.* **2014**, *105*, 231117.
- Jamali, M.; Gerhardt, I.; Rezai, M.; Frenner, K.; Fedder, H.; Wrachtrup, J. Microscopic diamond solid-immersion-lenses fabricated around single defect centers by focused ion beam milling. *Rev. Sci. Instrum.* **2014**, *85*, 123703.
- Curto, A. G.; Volpe, G.; Taminiau, T. H.; Kreuzer, M. P.; Quidant, R.; van Hulst, N. F. Unidirectional Emission of a Quantum Dot Coupled to a Nanoantenna. *Science* **2010**, *329*, 930–933.
- Lee, K. G.; Chen, X. W.; Eghlidi, H.; Kukura, P.; Lettow, R.; Renn, A.; Sandoghdar, V.; Gotzinger, S. A planar dielectric antenna for directional single-photon emission and near-unity collection efficiency. *Nat. Photonics* **2011**, *5*, 166–169.
- Li, L.; Chen, E. H.; Zheng, J.; Mouradian, S. L.; Dolde, F.; Schröder, T.; Karaveli, S.; Markham, M. L.; Twitchen, D. J.; Englund, D. Efficient Photon Collection from a Nitrogen Vacancy Center in a Circular Bullseye Grating. *Nano Lett.* **2015**, *15*, 1493–1497.
- Davanço, M.; Rakher, M. T.; Schuh, D.; Badolato, A.; Srinivasan, K. A circular dielectric grating for vertical extraction of single quantum dot emission. *Appl. Phys. Lett.* **2011**, *99*, 041102.
- Aouani, H.; Mahboub, O.; Bonod, N.; Devaux, E.; Popov, E.; Rigneault, H.; Ebbesen, T. W.; Wenger, J. Bright Unidirectional Fluorescence Emission of Molecules in a Nanoaperture with Plasmonic Corrugations. *Nano Lett.* **2011**, *11*, 637–644.
- Jun, Y. C.; Huang, K. C.; Brongersma, M. L. Plasmonic beaming and active control over fluorescent emission. *Nat. Commun.* **2011**, *2*, 1–6.
- Choy, J. T.; Bulu, I.; Hausmann, B. J. M.; Janitz, E.; Huang, I.-C.; Loncar, M. Spontaneous emission and collection efficiency enhancement of single emitters in diamond via plasmonic cavities and gratings. *Appl. Phys. Lett.* **2013**, *103*, 161101.
- Livneh, N.; Harats, M. G.; Istrati, D.; Eisenberg, H. S.; Rapaport, R. Highly Directional Room-Temperature Single Photon Device. *Nano Lett.* **2016**, *16*, 2527–2532.
- Livneh, N.; Harats, M. G.; Yochelis, S.; Paltiel, Y.; Rapaport, R. Efficient Collection of Light from Colloidal Quantum Dots with a Hybrid Metal Dielectric Nanoantenna. *ACS Photonics* **2015**, *2*, 1669–1674.
- Kumar, S.; Lu, Y.-W.; Huck, A.; Andersen, U. L. Propagation of plasmons in designed single crystalline silver nanostructures. *Opt. Express* **2012**, *20*, 24614–24622.
- Nagpal, P.; Lindquist, N. C.; Oh, S.-H.; Norris, D. J. Ultrasmooth Patterned Metals for Plasmonics and Metamaterials. *Science* **2009**, *325*, 594–597.
- Park, J. H.; Ambwani, P.; Manno, M.; Lindquist, N. C.; Nagpal, P.; Oh, S.-H.; Leighton, C.; Norris, D. J. Single-Crystalline Silver Films for Plasmonics. *Adv. Mater.* **2012**, *24*, 3988–3992.
- Drexhage, K. Influence of a dielectric interface on fluorescence decay time. *J. Lumin.* **1970**, *1*, 693–701.
- Ford, G.; Weber, W. Electromagnetic interactions of molecules with metal surfaces. *Phys. Rep.* **1984**, *113*, 195–287.
- Chance, R. R.; Proc, A.; Silbey, R. Molecular fluorescence and energy transfer near interfaces. *Adv. Chem. Phys.* **1978**, *37*, 1–34.
- Avrutsky, I.; Soref, R.; Buchwald, W. Sub-wavelength plasmonic modes in a conductor-gap-dielectric system with a nanoscale gap. *Opt. Express* **2010**, *18*, 348–363.
- Cui, S.; Zhang, X.; Liu, T.-I.; Lee, J.; Bracher, D.; Ohno, K.; Awschalom, D.; Hu, E. L. Hybrid Plasmonic Photonic Crystal Cavity for Enhancing Emission from near-Surface Nitrogen Vacancy Centers in Diamond. *ACS Photonics* **2015**, *2*, 465–469.
- Yang, Y.; Miller, O. D.; Christensen, T.; Joannopoulos, J. D.; Soljačić, M. Low-Loss Plasmonic Dielectric Nanoresonators. *Nano Lett.* **2017**, *17*, 3238–3245.
- Chen, W.; Thoreson, M. D.; Ishii, S.; Kildishev, A. V.; Shalae, V. M. Ultra-thin ultra-smooth and low-loss silver films on a germanium wetting layer. *Opt. Express* **2010**, *18*, 5124–5134.
- Schell, A. W.; Kewes, G.; Schröder, T.; Wolters, J.; Aichele, T.; Benson, O. A scanning probe-based pick-and-place procedure for

assembly of integrated quantum optical hybrid devices. *Rev. Sci. Instrum.* **2011**, *82*, 073709.

(31) Jiang, Q.; Zhang, S.; Zhao, M. Size-dependent melting point of noble metals. *Mater. Chem. Phys.* **2003**, *82*, 225–227.

(32) Kurvits, J. A.; Jiang, M.; Zia, R. Comparative analysis of imaging configurations and objectives for Fourier microscopy. *J. Opt. Soc. Am. A* **2015**, *32*, 2082–2092.

(33) Neu, E.; Steinmetz, D.; Riedrich-Möller, J.; Gsell, S.; Fischer, M.; Schreck, M.; Becher, C. Single photon emission from silicon-vacancy colour centres in chemical vapour deposition nano-diamonds on iridium. *New J. Phys.* **2011**, *13*, 025012.

(34) Iwasaki, T.; et al. Germanium-Vacancy Single Color Centers in Diamond. *Sci. Rep.* **2015**, *5*, 12882.

(35) Manfrinato, V. R.; Wanger, D. D.; Strasfeld, D. B.; Han, H.-S.; Marsili, F.; Arrieta, J. P.; Mentzel, T. S.; Bawendi, M. G.; Berggren, K. K. Controlled placement of colloidal quantum dots in sub-15 nm clusters. *Nanotechnology* **2013**, *24*, 125302.

(36) Jiang, M.; Kurvits, J. A.; Lu, Y.; Nurmikko, A. V.; Zia, R. Reusable Inorganic Templates for Electrostatic Self-Assembly of Individual Quantum Dots, Nanodiamonds, and Lanthanide-Doped Nanoparticles. *Nano Lett.* **2015**, *15*, 5010–5016.

(37) Ramachandran, S.; Kristensen, P.; Yan, M. F. Generation and propagation of radially polarized beams in optical fibers. *Opt. Lett.* **2009**, *34*, 2525–2527.

Supporting information for:

Hybrid Plasmonic Bullseye Antennas for Efficient Photon Collection

Sebastian K. H. Andersen,^{*,†} Simeon Bogdanov,[‡] Oksana Makarova,[‡] Yi Xuan,[‡]
Mikhail Y. Shalaginov,[‡] Alexandra Boltasseva,[‡] Sergey I. Bozhevolnyi,[†] and
Vladimir M. Shalaev[‡]

[†]*Center for Nano Optics, University of Southern Denmark, DK-5230 Odense M, Denmark*

[‡]*School of Electrical and Computer Engineering, Purdue Quantum Center, Purdue
University, West Lafayette, Indiana 47907, USA*

E-mail: sekh@mci.sdu.dk

Sample Preparation

The bullseye antenna was fabricated by successive electron-beam evaporation of 10 nm Ti, 3 nm Ge, 200 nm Ag topped by 15 nm SiO₂ on a Si wafer, at a deposition rate of ~ 1 Å/s and 10^{-6} mbar chamber pressure, without breaking the vacuum. The Ge layer act as a wetting layer, reducing roughness of the consecutively deposited Ag film.^{S1} PMMA 4A was subsequently spincoated at 4000 rpm on the sample, and prebaked at 180 C° for 3 min before patterning by a 100kV electron beam lithography system (Leica VB6). After development (1:3 MIBK-to-IPA for 1 min followed by 1 min rinse in IPA), a 100 nm TiO₂ layer was deposited by electron-beam evaporation at ~ 1 Å/s and 10^{-6} mbar pressure. Lift-off in acetone at 60 C° for 5 h was partially successful, as subsequently 5 min of sonication in acetone was

required to remove PMMA between the TiO_2 ridges to reveal the bullseye. In preparation of ND placement, 100 nm ND's containing ~ 400 NV-centers (Adamas technology) was spin-coated on a coverslip, previously cleaned in piraniha etch (Nanostrip x2 - KMG electronic chemicals). To ease the transfer, the bullseye sample was coated with a ~ 2 nm thick layer of positively charged poly-allylamine hydrochloride (PAH) layer. ND pick-up was performed by a force curve sequence, with the AFM cantilever situated above the ND. Successful pick-up was confirmed by a subsequent non-contact scan. Exchanging samples, a force curve was performed in the center of the bullseye, followed by an AFM scan to confirm the placement of the ND.

Numerical Modelling

Numerical modelling was performed in the commercially available Comsol Multiphysics 5.1. The full 3-D field of the axial symmetric system is numerically modelled by solving a 2-D slice, on the assumption of a constant azimuthal phase. The limited computational requirements of 2-D modelling, allowed us to model the full bullseye antenna, in a domain of radius $22\mu\text{m}$, bounded from the top by a perfectly matched layer and below by the silver film. Material parameters for silver were obtained for tabulated data,^{S2} while TiO_2 data was measured by ellipsometry (see figure S4) and a refractive index of 1.45 was set for SiO_2 . The emission field was generated by an electric dipole source positioned on the symmetry axis, 15 nm above the SiO_2 film. The decay rate enhancement was obtained as the total power dissipated by the dipole in the bullseye environment, relative to that of free space. Collection efficiency was obtained as the power integrated over a 0.9 NA collection surface, relative to the total power dissipated by the dipole. The radiation pattern was obtained by plotting the normal component of the Poynting vector over a circular arc in the 2-D plane, centered on the dipole. A large arc radius of $20\mu\text{m}$ was necessary in order to reach a convergent solution of the emission pattern. Knowing the radius of the circular path and the arc length with respect to zero degree out of plane, the angle of emission for a particular point could easily

be calculated.

Experiment

The ND was excited with a 532 nm continuous wave laser, focused onto the sample by a 0.9 NA x100 objective which was mounted on a piezo-stage for fine positioning of laser spot. Fluorescence collected by the same objective was filtered by a 550 nm dichroic mirror (DMLP550L- Thorlabs) and 550 nm long pass filter (FEL0550- Thorlabs), before being directed to a spectrometer (QE65000 - Ocean Optics) or avalanche photodiode (SPCM-AQRH - Excelitas) in a confocal detection configuration using a $50\mu\text{m}$ pinhole. Alternatively fluorescence was detected by a charge coupled camera (414Ex - Atik Cameras) imaging sample plane (using a 20 mm tube lens) or back-focal plane (600 mm bertrand- and 75 mm tube lens) onto the camera. off- or on-resonance emission was selected by filters of respectively 560-610 nm and 650-740 nm transmission bands, while an analyzer (LPVISC050-MP2 - Thorlabs) was introduced to probe polarization. Back-focal plane images from bullseye antenna, was background corrected for a corresponding image from an empty antenna. Saturation curve measurement was performed with a ND2 filter positioned in front of the avalanche photodiode, the presented count rate was corrected for transmission of ND2 filter and the pinhole. The experimental setup is given in figure S1.

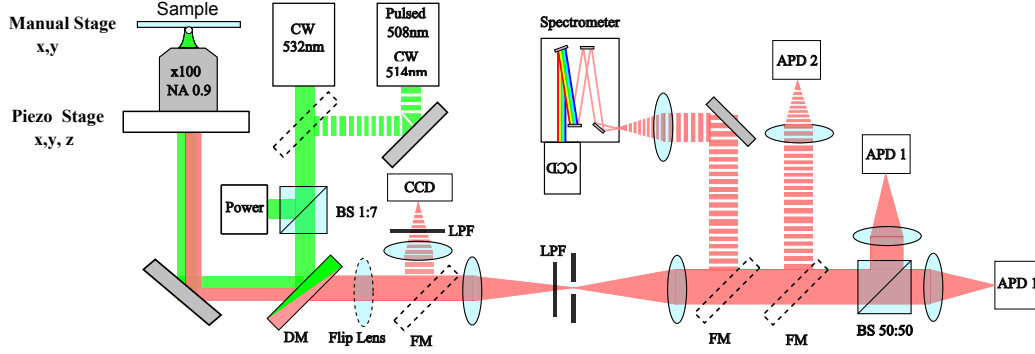


Figure S1: Schematic of experimental setup applied for characterization of emission properties of ND in bullseye antenna. DM: Dichroic mirror, FM: Flip mirror, APD: avalanche photodiode, CCD: charge coupled device, BS: Beamsplitter. The 532nm CW pump laser was used for excitation of NV-centers, through the NA 0.9 x100 Objective. Fluorescence collected by the same objective, was imaged onto the CCD camera, spectrally resolved on the spectrometer or detected by APD2 for saturation curve measurement. For back-focal plane imaging, a flip lens was introduced before the CCD.

Dipole above plane silver film

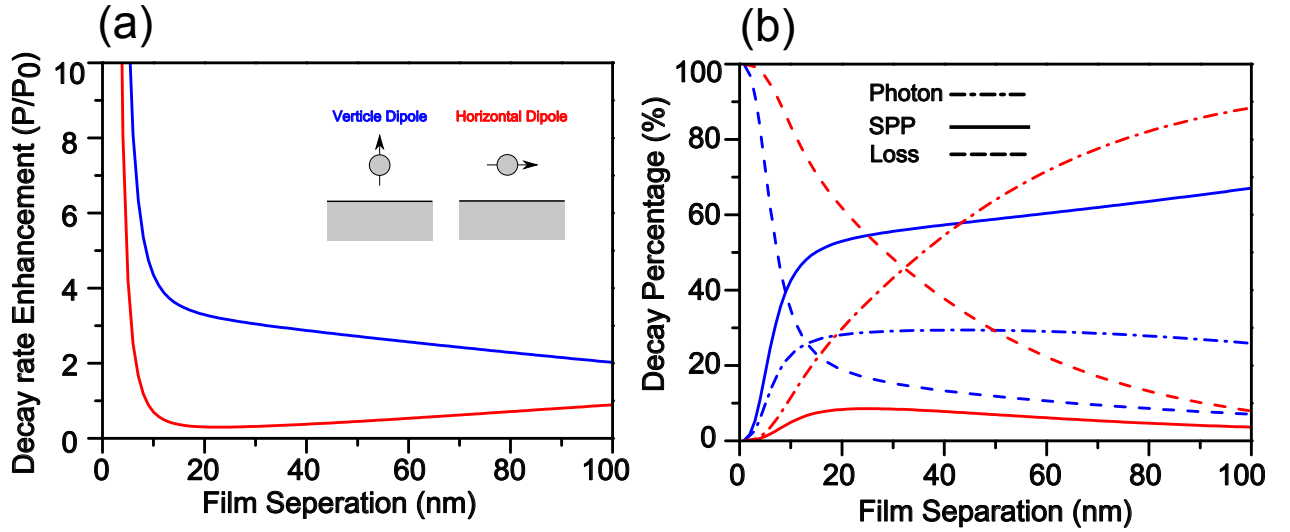


Figure S2: Analytical model for dipole emission above an infinite silver film, emitting at a wavelength of 670 nm. For dipole oriented vertical (blue) or horizontal (red). (a) Power dissipated by dipole relative to vacuum. The emission is suppressed for a horizontal dipole in close proximity (~ 30 nm) to the silver film (b) Relative decay rates into photons (dash-dot), SPP (solid) and quenching (dashed). The vertical dipole couples efficiently to SPP. Modelling is reproduced based on the analytical model developed in reference.^{S3}

Ellipsometry Measurement of TiO₂ film

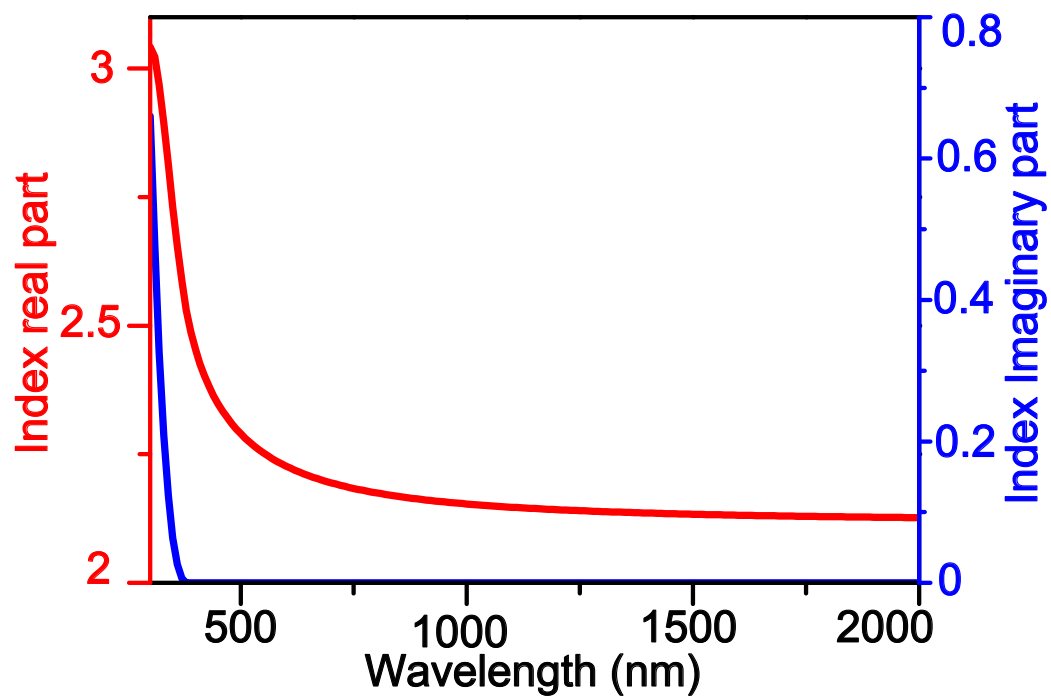


Figure S3: Ellipsometry measurement of 100 nm TiO₂ film deposited by e-beam evaporation on Si substrate. The measurement is applied for numerical modelling of TiO₂ film.

Numerical Optimization Procedure

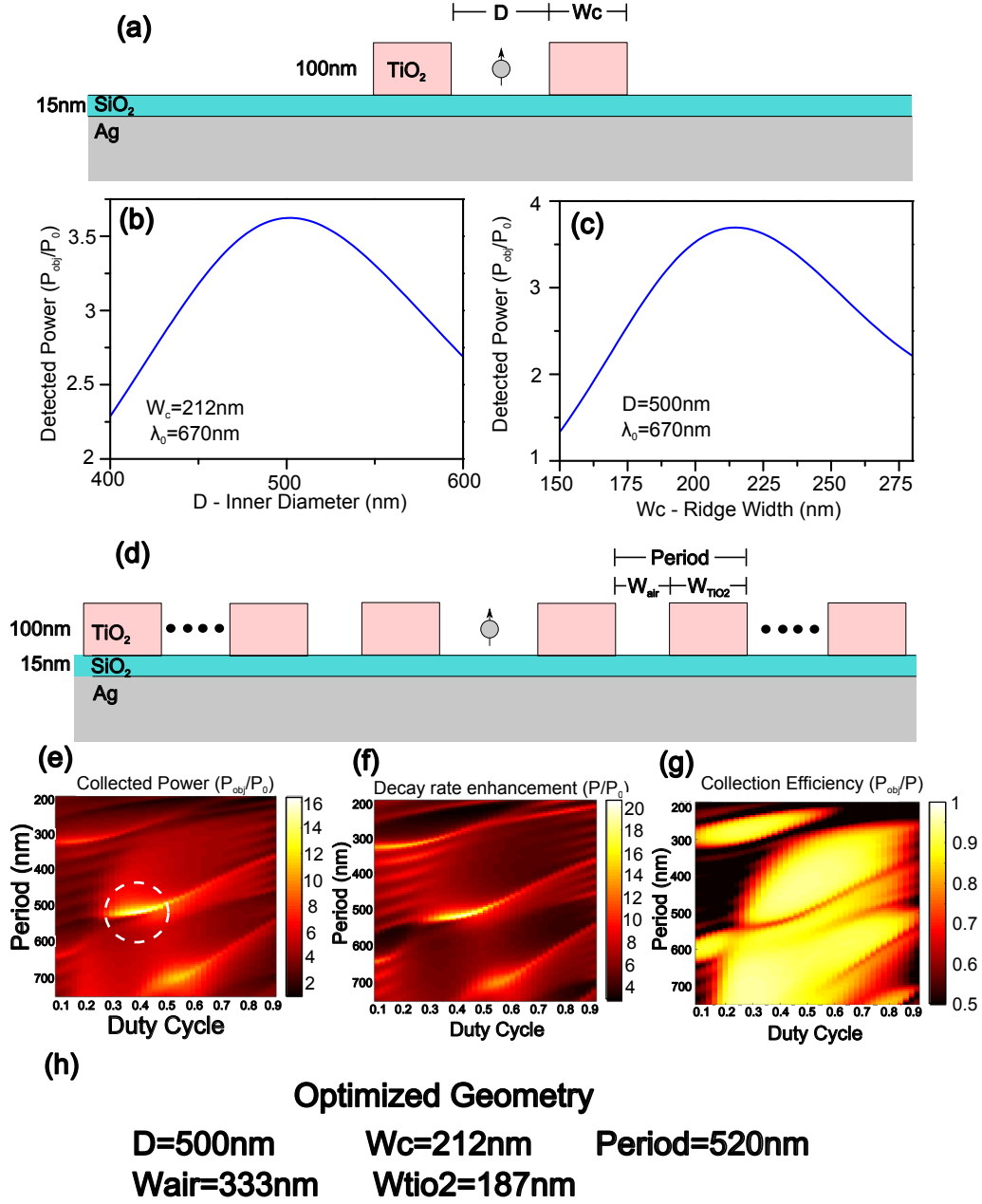


Figure S4: Numerical optimization procedure for bullseye antenna targeted for emission wavelength 670 nm (a) A single TiO_2 ridge is initially optimized for maximum dipole power radiated to the objective. (b,c) The parameters of inner diameter (D) and TiO_2 ridge width (W_c) is iteratively optimized until a self-consistent maxima is reached. (d) The 7 ridge grating, geometrically described by period and duty cycle, is then added. (e) Mapping the dipole power collected by the objective as a function of period and duty cycle the optimal grating configuration is determined. (f,g) The corresponding maps of decay rate enhancement and collection efficiency is included to illustrate their invers relationship. (h) List of optimized parameters.

Antenna performance vs dipole height

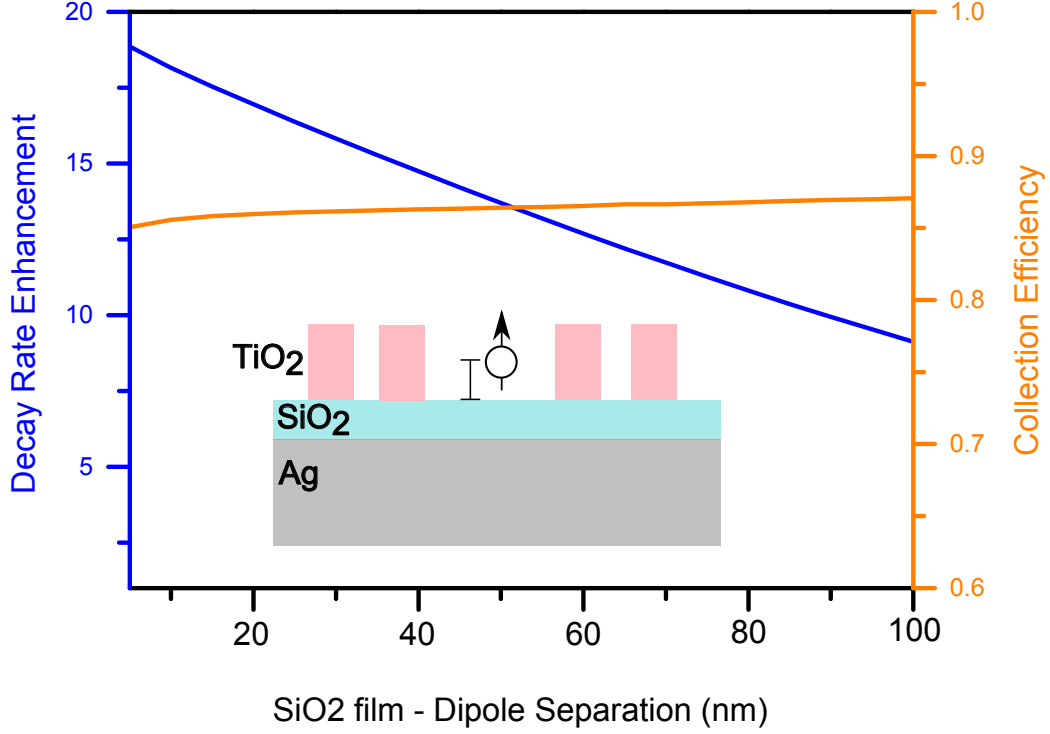


Figure S5: Decay rate enhancement (blue) and collection efficiency (orange) as function of dipole height, above the SiO₂ film. The dipole response is modelled for a verticle dipole, emitted at a wavelength of 670 nm positioned on the symmetry axis of the bullseye antenna optimized in figure S4.

Comparision of emission pattern with grating equation

In the following, the numerically modelled emission pattern is compared with the grating equation (eq 1), describing the condition for coupling propagating surface plasmon polaritons to free space radiation.

$$k_{spp} = k_{\sigma} \pm nG \quad n = \pm 1, 2, 3, 4... \quad (1)$$

$G = \frac{2\pi}{\Lambda}$ being the grating vector with period Λ , $k_{\sigma} = k_0 \sin(\theta)$ being the in-plane wavevector of free radiation propagating along emission angle θ and $k_{spp} = k_0 N_{eff}^G$ SPP wavevector.

For the dielectric grating we describe N_{eff}^G , weighted by grating fill factor.

$$N_{eff}^G = \chi N_{eff}^{TiO_2} + (1 - \chi) N_{eff}^{Air} \quad (2)$$

$N_{eff}^{TiO_2} = 2.25$ being the SPP effective index for the TiO_2 - SiO_2 -Ag layer structure and $N_{eff}^{Air}=1.05$ for the Air_2 - SiO_2 -Ag profile, modelled by the 3-layer dispersion relation for the design wavelength of 670 nm and $\chi = 0.36$ the grating duty cycle for the optimized bullseye design. The numerically modelled bullseye emission generally follow the trends of the grating equation (Figure S4).

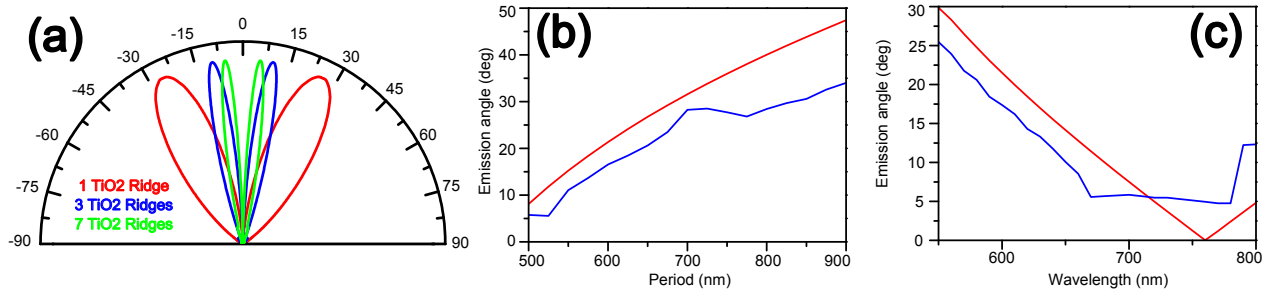


Figure S6: Emission pattern modelled for the optimized bullseye design at the target wavelength $\lambda_0 = 670$ nm. (a) Emission pattern as function of number of TiO_2 ridges, the emission pattern becomes increasingly directional with increasing number of ridges. Numerically modelled angle of maximum emitted power for optimized bullseye design (blue) and comparison with emission angle calculated with grating equation (red). (b) as a function of grating period or (c) vacuum wavelength.

Optimization for different TiO₂ heights

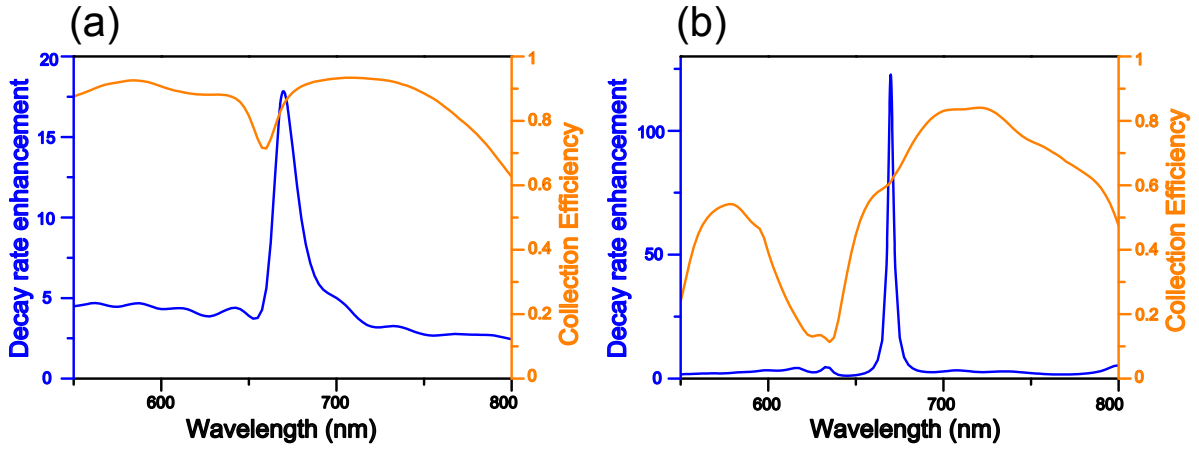


Figure S7: Modelled decay rate enhancement (blue) and collection efficiency (Orange) for (a) design optimized in figure S4 at a TiO₂ height of 100 nm and SiO₂ thickness of 15 nm. (b) Alternative design optimized for TiO₂ height of 260 nm and 15 nm SiO₂ thickness. Increasing TiO₂ height increase SPP reflectivity of the TiO₂ ridges, leading to a larger cavity Q-factor and increased decay rate enhancement, at the cost of collection efficiency as the SPP perform an increasing number of lossy, standing wave, round trips before scattering to free space.

Fluorescence image of bullseye antenna in log scale

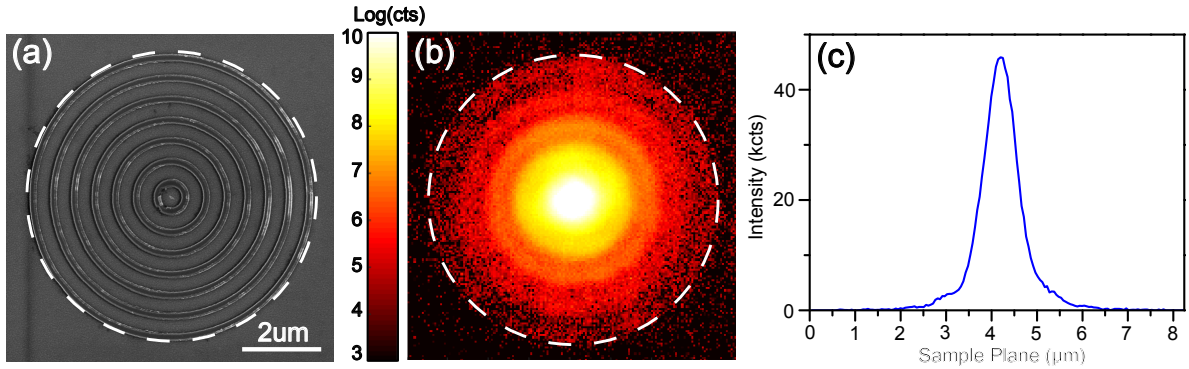


Figure S8: (a) Scanning electron micrograph of bullseye antenna containing single nanodiamond. (b) Corresponding fluorescence image in log scale, dashed line indicate boundary of bullseye antenna, measured with 550 nm long pass filter. The linear scale version of the image appearing in the article figure 2d. (c) Intensity profile through center of image in b.

Confocal scans of bullseye antennas

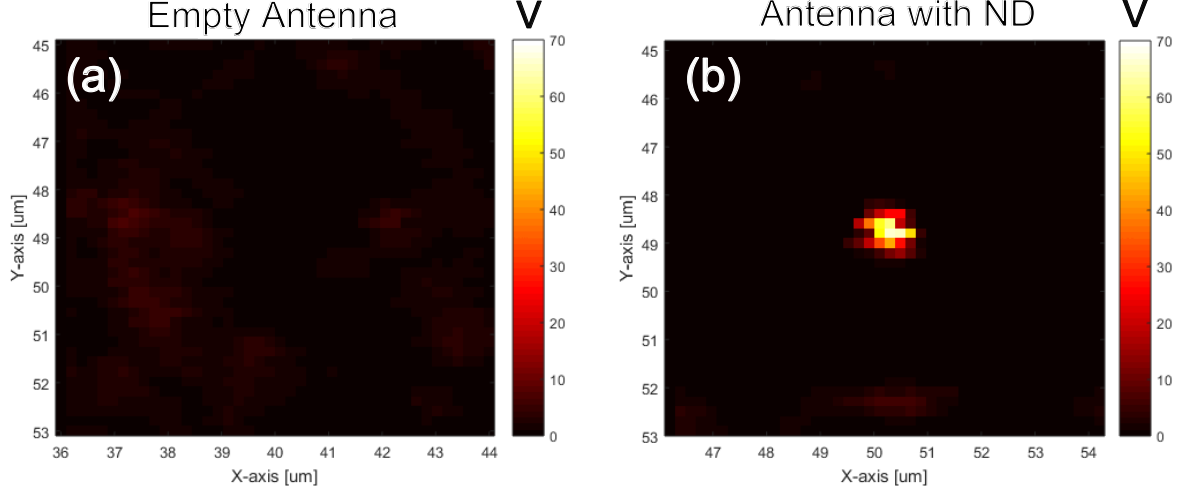


Figure S9: Confocal scan of (a) empty bullseye antenna and (b) bullseye antenna containing a fluorescent ND. Scanned with 532 nm pump laser at $100\mu W$. Scale bar is identical for both images.

Lifetime distribution of NV-centers in nano diamonds

Lifetime decay curves ($I(t)$) are measured by a 1MHz pulsed excitation at a wavelength of 508 nm. For the nano diamond in the bullseye antenna or same type of nano diamond on a glass coverslip. As the nano diamonds contain on average 400 NV-centers, the lifetime decay curve consist of distribution of single exponential decays for the individual NV-centers. The lifetime distribution is extracted by fitting a stretched exponential to the decay curve (figure S10a).

$$I(t) = e^{(t/\tau_0)^\beta} = \int_0^\infty P(s, \beta) e^{-st/\tau_0} ds \quad ; \quad s = \tau_0/\tau \quad (3)$$

β and τ_0 being the fitting parameters and P being the probability of finding an NV-center with a lifetime τ . Following the work of Johnnton,^{S4} P is given by.

$$P(s, \beta) = \int_0^\infty e^{-u^\beta \cos(\pi\beta/2)} \cos(su - u^\beta \sin(\pi\beta/2)) du \quad (4)$$

Figure S10b, give the lifetime probability distribution for the nanodiamond in the antenna and distributions from nanodiamonds on glass. While significant variations in lifetime distributions is observed between individual nano diamonds on glass, the broadest lifetime distribution is observed for nano diamond in the antenna.

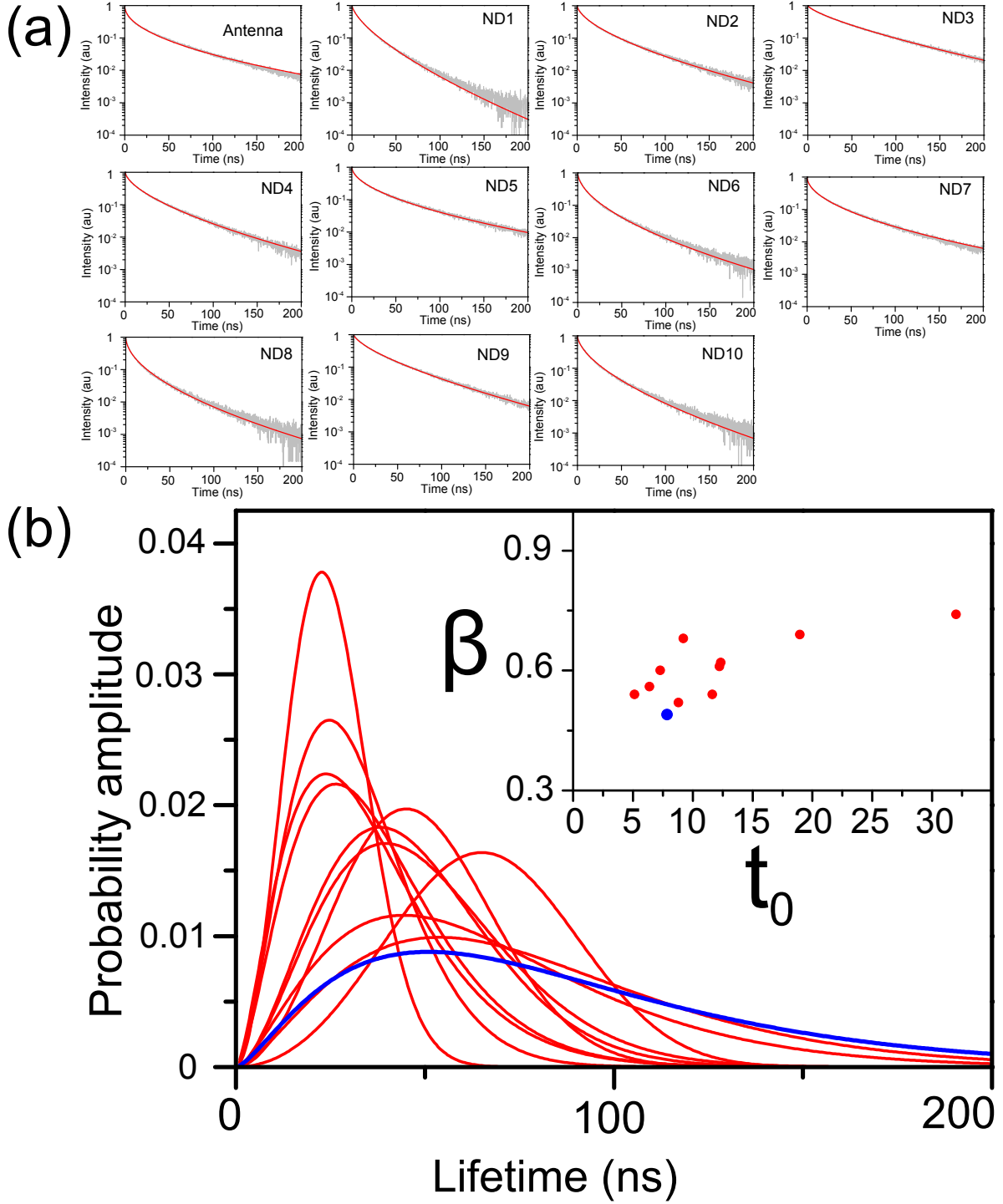


Figure S10: (a) Lifetime measurements of ND in antenna, and 10 nanodiamonds of the same type spincoated on a glass coverslip, ND1 to ND10. Experimental data (grey) and stretched exponential fit (red). (b) Lifetime distributions extracted from stretched exponential fits, for nanodiamond in antenna (blue) and nanodiamonds on glass. Inset gives corresponding β - and t_0 -value of stretched exponential fits.

References

- (S1) Chen, W.; Thoreson, M. D.; Ishii, S.; Kildishev, A. V.; Shalaev, V. M. *Opt. Express* **2010**, *18*, 5124–5134.
- (S2) Johnson, P. B.; Christy, R. W. *Phys. Rev. B* **1972**, *6*, 4370–4379.
- (S3) Ford, G.; Weber, W. *Physics Reports* **1984**, *113*, 195 – 287.
- (S4) Johnston, D. C. *Phys. Rev. B* **2006**, *74*, 184430.

E

EXCITATION OF SURFACE PLASMON POLARITONS MODES WITH
MULTIPLE NITROGEN VACANCY CENTERS IN SINGLE NANODIAMONDS

Journal of Optics 18, 024002, (2016)

Excitation of surface plasmon polariton modes with multiple nitrogen vacancy centers in single nanodiamonds

Shailesh Kumar^{1,4}, Jens L Lausen^{1,4}, Cesar E Garcia-Ortiz²,
Sebastian K H Andersen¹, Alexander S Roberts¹, Ilya P Radko¹,
Cameron L C Smith³, Anders Kristensen³ and Sergey I Bozhevolnyi¹

¹ Centre for Nano Optics, University of Southern Denmark, DK-5230 Odense M, Denmark

² CONACYT Research Fellow—CICESE, Unidad Monterrey, Alianza Centro 504, PIIT Apodaca, Nuevo Leon, 66629, Mexico

³ Department of Micro- and Nanotechnology, Technical University of Denmark, DK-2800 Kgs. Lyngby, Denmark

E-mail: shku@iti.sdu.dk

Received 15 September 2015, revised 4 November 2015

Accepted for publication 11 November 2015

Published 21 December 2015



Abstract

Nitrogen-vacancy (NV) centers in diamonds are interesting due to their remarkable characteristics that are well suited to applications in quantum-information processing and magnetic field sensing, as well as representing stable fluorescent sources. Multiple NV centers in nanodiamonds (NDs) are especially useful as biological fluorophores due to their chemical neutrality, brightness and room-temperature photostability. Furthermore, NDs containing multiple NV centers also have potential in high-precision magnetic field and temperature sensing. Coupling NV centers to propagating surface plasmon polariton (SPP) modes gives a base for lab-on-a-chip sensing devices, allows enhanced fluorescence emission and collection which can further enhance the precision of NV-based sensors. Here, we investigate coupling of multiple NV centers in individual NDs to the SPP modes supported by silver surfaces protected by thin dielectric layers and by gold V-grooves (VGs) produced via the self-terminated silicon etching. In the first case, we concentrate on monitoring differences in fluorescence spectra obtained from a source ND, which is illuminated by a pump laser, and from a scattering ND illuminated only by the fluorescence-excited SPP radiation. In the second case, we observe changes in the average NV lifetime when the same ND is characterized outside and inside a VG. Fluorescence emission from the VG terminations is also observed, which confirms the NV coupling to the VG-supported SPP modes.

Keywords: NV center, nanodiamond, surface plasmon polariton, channel plasmon polariton, V-groove, quantum plasmonics

(Some figures may appear in colour only in the online journal)

1. Introduction

Nitrogen-vacancy (NV) centers in diamonds have attracted much attention as a possible candidate for solid-state quantum bits (qubits) [1, 2]. Their ground-state electron-spin coherence time is sufficiently longer than the time it takes to perform a

qubit operation in such qubits. The electronic qubit state can be initialized and read out optically and, importantly, even at room temperatures [3–6]. The fluorescence from NV centers is stable, and a single NV center is a stable source of single photons [7]. NV centers are also a promising candidate for a high-precision magnetic field, electric field and temperature sensors [8–14]. It is argued that high densities of NV centers are needed for achieving the best performance of NV centers

⁴ These authors contributed equally to this work.

in magnetic field sensors. Multiple NV centers in nanodiamonds (NDs) can provide high sensitivity (depending on number of NV centers in the ND) as well as high resolution (determined by the size of the ND) for the magnetic field sensors [11, 12]. In addition, NDs with multiple NV centers are also useful as a stable fluorophore in biological applications due to their chemical neutrality and brightness [15]. In general, the applications potentially enabled by NV centers stand to benefit from the enhancement of the fluorescence rate as well as the efficient collection of the fluorescence from the NV centers. There are several methods that have been proposed and investigated in this direction, such as coupling NV centers to diamond pillars [16], dielectric waveguides [17], dielectric cavities [18–20], plasmonic nanostructures [21, 22] and plasmonic waveguides [23–28].

Waveguide configurations supporting the SPP propagation, i.e., plasmonic waveguides, exhibit (at least, in some cases) a unique feature of guiding SPP modes with extreme confinement, far beyond the diffraction limit [29]. This opens a way to realize a very efficient coupling of emitters to these SPP guided modes [30–32]. Channel plasmon polariton (CPP) modes supported by VGs cut into metal are especially suited for efficient coupling to emitters due to their strong confinement and relatively long propagation lengths [28, 33, 34]. The so-called β -factor, defined as the probability of a spontaneous decay of an emitter leading to excitation of the plasmonic waveguide mode, is not only high for CPP modes but also distributed more uniformly in space (within a VG), compared to other plasmonic waveguides such as cylindrical and wedge waveguides [33]. VGs have been proposed for realization of long-distance resonant energy transfer and super-radiance effects [33] as well as long-distance entanglement of two quantum emitters [34]. In addition, a wide range of devices, including plasmonic circuit components and nanofocussing elements formed by VGs, have also been demonstrated [35–37]. With nano-mirrors fabricated at the VG terminations, the efficient in- and out-coupling of far-field propagating radiation and CPP modes is demonstrated to be feasible [38, 39].

In this work, we investigate the possibility of exploiting multiple NV centers in individual NDs for coupling to the surface plasmon polariton (SPP) modes supported by silver surfaces (protected by thin dielectric layers) and by gold V-grooves (VGs) produced via the self-terminated silicon etching. This article is organized as follows: We first consider, in section 2.1, the coupling of multiple NV centers in NDs to the SPP modes supported by a silver–dielectric interface. The SPPs propagating along the interface are scattered by another ND. We conduct measurements of the fluorescence spectra obtained from a source ND, which is illuminated by a pump laser, and from a scattering ND illuminated only by the fluorescence-excited SPP radiation. The normalized fluorescence spectrum (by the source spectrum) measured from the scattering ND shows short-wavelength attenuation, which we explain by using an analytic expression based on the point-dipole approximation. Next, in section 2.2, we consider the coupling of multiple NV centers in an ND to the CPP mode supported by a gold VG, which is fabricated

using UV lithography and self-terminated silicon etching [39]. The investigated ND is pushed from the gold–air interface outside the VG to inside the VG using an atomic force microscope (AFM) [22, 24–28]. Fluorescence lifetimes are measured before and after movement of the ND, revealing a noticeable change in the average lifetime that we associate with the NV–CPP coupling. Emission from the VG termination mirrors, when the ND is excited, further confirms this coupling. We terminate our paper with section 3, in which we summarize the results obtained and offer our conclusions.

2. Experiments and results

The experiments are performed using NDs with an average diameter of 100 nm and containing ~ 400 NV centers each (Adamas Nanotechnologies). To characterize our systems, we use a scanning confocal microscope. A 532 nm linearly polarized pulsed laser with pulsewidth of ~ 50 ps and a repetition rate varying between 2.5 and 80 MHz is used as the excitation source for NV centers in NDs. The laser beam is focused with a $100\times$ objective (NA 0.9) onto the sample to a spot size of ~ 500 nm. The same objective is used for collection of the fluorescence signal. A long pass filter at 550 nm filters out the signal from the excitation source. The fluorescence is either temporally resolved with an avalanche photo diode (APD) and counting electronics, or spectrally resolved with an electron-multiplying charge-coupled device (EMCCD) camera mounted on a spectrometer. A schematic of the set-up is presented in figure 1(a).

2.1. Coupling of NV centers in an ND to SPPs at a silver–dielectric interface

The sample for studying the excitation of SPPs propagating along a silver–dielectric interface is prepared by thermal evaporation of an optically thick 150 nm silver film on a silicon wafer. Subsequently, a 20 nm amorphous SiO_2 film is sputtered on top of the silver film while it remains in vacuum in order to minimize its reaction with atmospheric sulphur and oxygen. NDs are deposited on the sample using a technique that has been described in [40]. Briefly, spin coating of PMMA (Poly(methyl methacrylate)), electron-beam lithography and development is used to fabricate an array of holes in PMMA. A suspension of NDs in water is then applied, is left to dry out under ambient conditions, thereafter a lift-off is used to remove the PMMA and obtain an array of NDs on the sample surface. The process ensures that the NDs are placed periodically at a controllable distance. The experiments are performed for two different distances between NDs: 7 and 9 μm .

The excitation polarization is changed between polarization parallel to the straight line connecting the source and the scattering ND (referred to as p polarization) and that perpendicular to the line (referred to as s polarization), as indicated in figure 1(c). Likewise, the signal from the NDs is analyzed in these two different orientations (p and s) and also

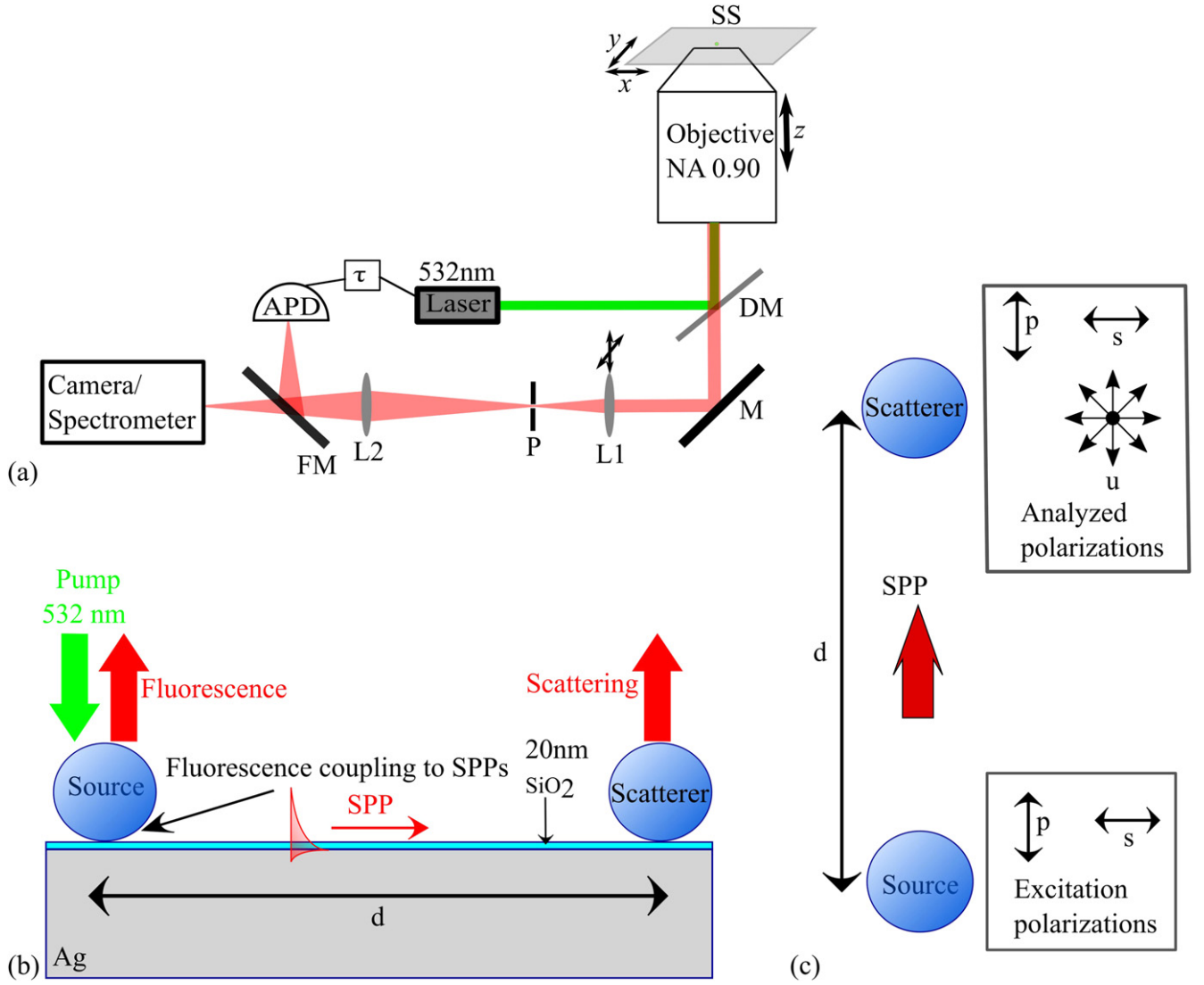


Figure 1. (a) Schematic of our experimental set-up. SS: sample stage, DM: dichroic mirror, M: mirror, L1 and L2: lenses, P: pinhole, FM: flip mirror, APD: avalanche photodiode, and τ denotes the timing electronics. The arrows indicate the possibility of moving the corresponding components. (b) side view and (c) top view of the experimental set-up for the NDs on a silver/glass surface. A pump laser excites NV centers in the source ND, where some of the fluorescence couples to the SPP mode and the scatterer ND scatters the SPPs to the far field. The source ND is excited by polarizations parallel to the line joining the source and the scatterer NDs (p) and perpendicular to the line (s). The signal is analyzed in these two polarization directions as well as unpolarized (u).

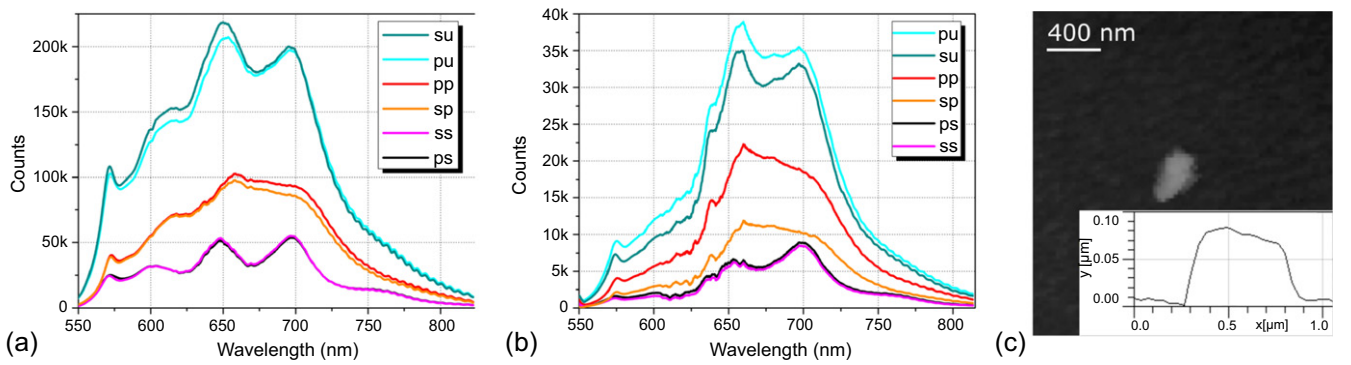


Figure 2. Typical spectra measured at the source (a) and scatterer (b) ND with different combinations of excitation and analyzed polarizations. In the graphs, the first letter denotes excitation polarization, whereas the second letter denotes analyzed polarization. (c) Shape of a single ND imaged with an AFM. The inset shows a cross-section of the ND.

in the absence of analyzer (u), which is also indicated in figure 1(c).

When an ND is excited, its fluorescence couples to SPPs at the silver–dielectric interface, propagates along the interface and is scattered by a separate ND. In figures 2(a) and (b), we present the source and the scattering spectra collected from the NDs, which are separated by 7 μm . Different configurations of polarization orientations for excitation radiation and analyzed signal are indicated in the insets in the respective figures. No significant difference in the strengths of signals collected from the source ND for the two orthogonal excitation polarizations is observed, a feature that can be explained by a high number and arbitrary orientation of NV centers inside the ND. The spectrum is found to depend only on the analyzed polarization, which we attribute to an irregular shape and relatively large size of the source ND (figure 2(c)) resulting in complicated Mie scattering spectra. For other source scatterer ND combinations, we have observed fluorescence dependence on excitation polarization (data not shown).

The signal from the scatterer ND is found dependent on the excitation polarization (figure 2(b)). The unpolarized collected signal for the s-polarized excitation (su) is lower compared to the unpolarized collected signal for the p-polarized excitation (pu). The same is observed when an analyzer is present: excitation by the p-polarized light consistently gives higher signals from the scatterer ND (the difference is small for the s-analyzed orientation). The dipoles excited by p polarization couple preferentially to the SPP propagating in the direction along the electric field of excitation [40]. A signal is still observed for the s polarization excitation, because many of the excited NV dipoles have a nonzero projection on the line connecting the source and scatterer NDs and can therefore couple to the SPPs propagating in that direction. In general, the relative strength of ND-excited SPP radiation depends on the distribution of dipoles inside the source ND [41]. Note that, similarly to the source ND spectra, the shape of the scatterer ND spectra is determined by the analyzed polarization (figure 2(b)), a feature that can again be related to the ND shape and size influence on the scattering spectra.

The signal strength collected from the scatterer ND is, in general, significantly lower compared to that collected from the source ND. Comparing the overall (over the whole spectrum) photon counts from the scatterer ND with that from the source ND, we found that their ratio varies substantially from one pair of NDs to another. It cannot be explained merely by variations in ND separation due to imperfect fabrication. The largest ratio observed is 1:2850 and the lowest is 1:4 (data not shown), where these two different pairs of NDs have the same separation of 7 μm . The decrease in signal strength when changing the detection from the source to scatterer ND is therefore not only related to the SPP propagation loss (as conjectured previously [40]) but also to the excitation polarization state, SPP coupling and scattering efficiencies, ND shape, and NV dipole-to-interface distance. We note that the ratio of scattered intensities pp:ps and sp:ss should, in principle, be the same (as observed for a distance

24 μm between source and scatterer [40]). When the distance is smaller (7 and 9 μm), a small background due to the direct illumination of scatterer (by pump or fluorescence, which affect the ps and ss spectra the most) changes these ratios.

We use two different analytical models to fit the ratio of spectra measured from the source and the scatterer NDs. In the first model suggested previously [40], it is assumed that the ratio of spectra can be expressed as follows:

$$\frac{P_{\text{scat}}(\lambda)}{P_{\text{source}}(\lambda)} = f(\lambda) \exp[-d/L_{\text{spp}}(\lambda)] \text{ with} \\ f(\lambda) = \frac{\eta_{\text{spp}}(\lambda)\sigma_{\text{sc}}}{2\pi\eta_{\text{rad}}(\lambda)da_s}, \quad (1)$$

where d is the distance between the NDs, $L_{\text{spp}}(\lambda)$ is the SPP propagation length for a given wavelength λ , $\eta_{\text{spp}}(\lambda)$ is the photon to SPP coupling efficiency for the source ND, σ_{sc} is the scattering cross-section of the scatterer ND, $\eta_{\text{rad}}(\lambda)$ is the photon emission efficiency of the source ND, and a_s is the in-plane angular dependence of the SPP intensity. In this rather simple model, the term $f(\lambda)$ is assumed to be wavelength-independent, i.e., taken as a constant, which is the fitting parameter for the model. Since $f(\lambda)$ is used as a multiplication factor, all spectra are normalized to their own maximum. In the second model, we have attempted to develop a more accurate and yet analytic description by using the expression for the SPP contribution to Green's dyadic constructed for evaluating SPP-mediated interaction between small particles located close to a metal surface [42]. When applied to our configuration, one arrives at the following expression:

$$G_{\text{spp}}^{\text{zz}}(d, \lambda) = \frac{k_{\text{spp}}}{2\sqrt{\epsilon}} \sqrt{\frac{2}{\pi k_{\text{spp}} d}} e^{-2r\sqrt{k_{\text{ND}}^2 - k_0^2}} e^{-(d/L_{\text{spp}}(\lambda))}, \quad (2)$$

where k_{spp} is the magnitude of the wave vector for the SPP at the silver–dielectric interface, k_{ND} is the magnitude of the wave vector at the silver–diamond interface, r is an average radius of NDs, ϵ is the dielectric constant of silver, $L_{\text{spp}}(\lambda)$ is the SPP propagation length at the silver–dielectric interface, and d is the distance between the two NDs. The first exponential term accounts for the SPP excitation (by a dipole source, such as an NV center) and out-coupling (by a dipole scatterer) to free propagating radiation, and the second exponential term describes the SPP propagation loss. The square root term describes the angular divergence of the propagating SPP. Using the expression for Green dyadic above (source and scatterer dipole are assumed to have z-orientation), we write the ratio of detected intensities as $P_{\text{scat}}(\lambda)/P_{\text{source}}(\lambda) = \alpha |G_{\text{spp}}^{\text{zz}}(\lambda, d)|^2$, where α is a fitting parameter constant for the second model (together with the ND radius r). The value of k_{spp} in equation (2) for a three-layer structure (air/glass/silver), and k_{ND} for a diamond–silver interface (the air above and the glass beneath the ND are neglected) are obtained analytically. The normalized scattering spectra for 7 and 9 μm of separation between NDs (figure 3) appear shifted to longer wavelengths relative to the fluorescence spectra measured from the source NDs. The SPP attenuation is larger for shorter wavelengths, which contributes to the spectral shape of the scattered spectrum. The

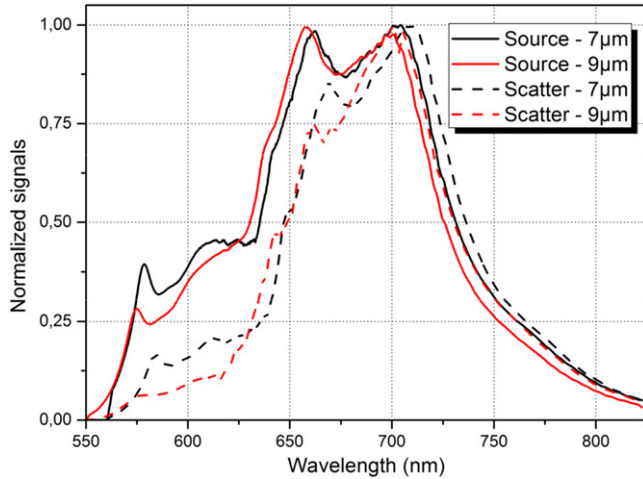


Figure 3. Source and scatterer spectra, shown for two different distances (7 and 9 μm) between the NDs. All signals are normalized to their own maximum value.

coupling efficiency of fluorescence to SPPs and angular divergence of the SPP beam depend on the wavelength, both of which also influence the shape of the scattered spectrum. This is readily seen in figure 4, where the extended model provides better fitting. The best fit for the extended model has the coefficient of determination (R^2) of 0.90 and 0.97 for the distances of 7 and 9 μm , respectively. The ND radii obtained from fits, $r = 36.38 \text{ nm}$ for the distance of 7 μm and $r = 45.44 \text{ nm}$ for the distance of 9 μm , correspond well with the NDs that are actually deposited (an average diameter of 100 nm).

2.2. Coupling of NV centers in a ND to CPP modes in a VG

The VGs used in these experiments are fabricated with the same procedure as described in [39] which consists of UV lithography, crystallographic etching of silicon and a thermally grown silicon dioxide (SiO_2) layer on the silicon to modify the V-shape geometry. Initially, a 200 nm SiO_2 layer

on the silicon substrate is patterned by both UV lithography and reactive-ion etching to define the perimeter of the VG devices. It is necessary that the patterning of the SiO_2 layer is well-aligned with the crystal $\langle 100 \rangle$ planes of the silicon substrate. The VGs and termination mirrors are formed by anisotropic wet etching of the exposed silicon in a potassium hydroxide (KOH) bath at 80 $^\circ\text{C}$. The KOH etch yields smooth $\langle 111 \rangle$ VG sidewalls and termination mirrors with a fixed inclination of 55 $^\circ$ from the surface plane. The nature of the crystallographic etching yields excellent mirror formation at the ends of the VG perimeter. Tailoring of the V-shape geometry is performed by thermal wet oxidation of the silicon VGs (1150 $^\circ\text{C}$ for 9 h, resulting in a 2320 nm SiO_2 layer at flat sections of the substrate) which sharpens the interior angle of the groove in order to support a CPP mode. The metal is deposited by electron-beam evaporation: first a 5 nm layer of chromium to promote adhesion before a 70 nm layer of gold. The gold layer is chosen to be sufficiently thick to eliminate interaction of air–interface plasmons with the underlying SiO_2 layer and also to minimize self-aggregation.

To couple NDs to the VGs, a water suspension containing NDs is spin coated on the sample with VGs. For this experiment, the concentration of NDs in water is adjusted so that the density of NDs on the surface after spin-coating is less than 1 per $10 \times 10 \mu\text{m}^2$. An AFM image of a VG together with an NDs is presented in figure 5(a). As can be observed from the figure, the depth of the VG structure is more than 2 μm . Figures 5(b) and (c) show images of the areas containing the NDs, which are also indicated in 5(a). A confocal raster scan image of the area with the ND presented in figure 5(d), shows that the fluorescence from the ND on the flat gold–air interface at an excitation of 100 μW is ~ 700 kcounts/s. Confocal scan images taken at an excitation power of 100 μW and two orthogonal polarizations show (figures 5(e)–(f)) that fluorescence from the VG is higher in case of excitation polarization across the VG (s polarization in figure 5(e)) due to the contribution from gap plasmons [43]. In figure 5(f), termination mirror A can be seen to fluoresce

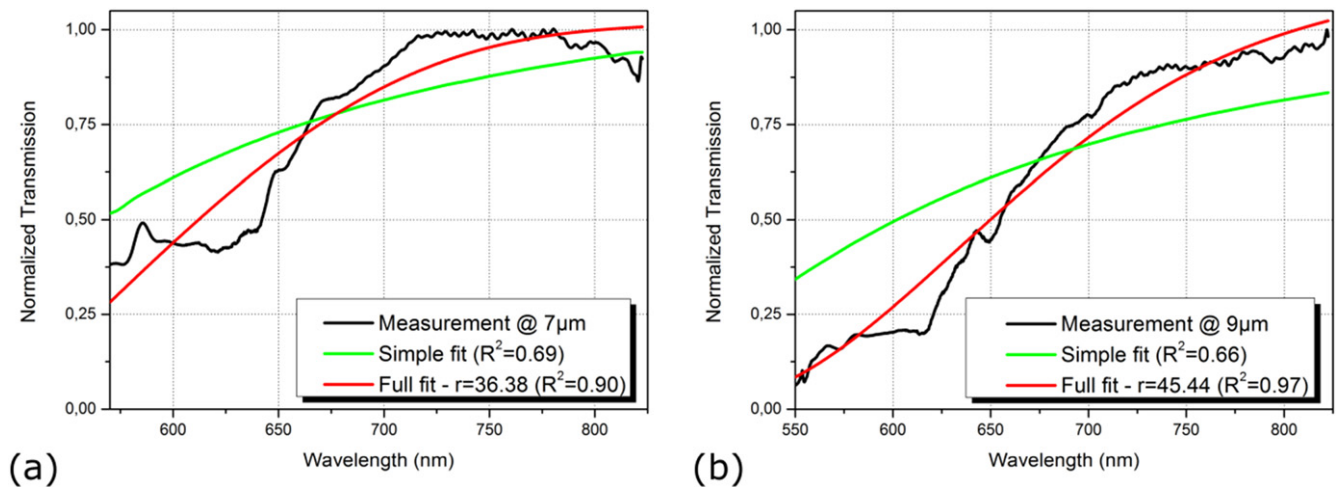


Figure 4. (a) and (b) shows model fits of the normalized source and scatterer spectra ratios obtained for distances between source and scatterer of 7 μm and 9 μm , respectively. The fits with the simple model, as well as the full model containing terms for divergence and coupling of fluorescence to SPP are shown. The fits for the full model are shown in the legends of the graphs with a fit R^2 coefficient.

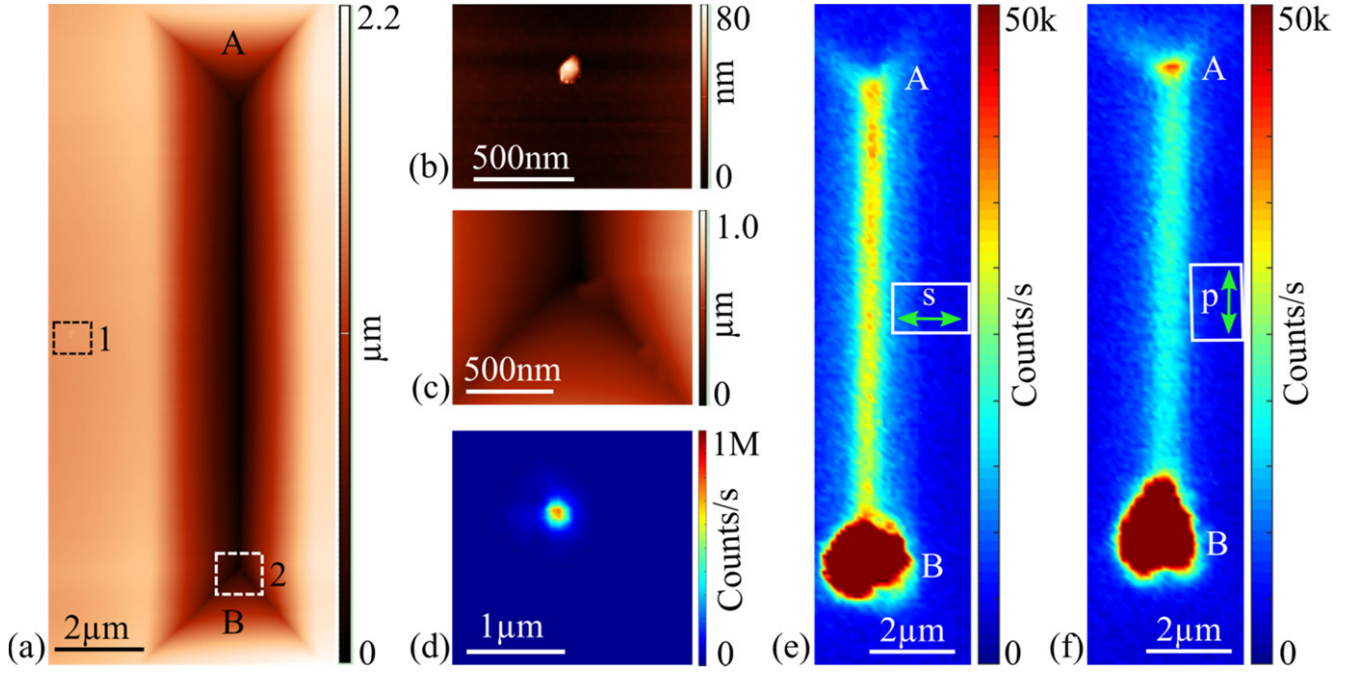


Figure 5. (a) Atomic-force microscope image of a VG structure. The rectangles with dotted lines indicates the areas containing NDs. (b) and (c) zoomed-in images of the areas 1 and 2, respectively, indicated in (a). (d) confocal-microscope fluorescence scan of the area containing the ND presented in (b). (e) and (f) confocal-microscope fluorescence scans of the VG presented in (a) with the excitation polarization indicated in the inset of respective figures. In (a), (e) and (f), A and B indicate the two VG termination mirrors.

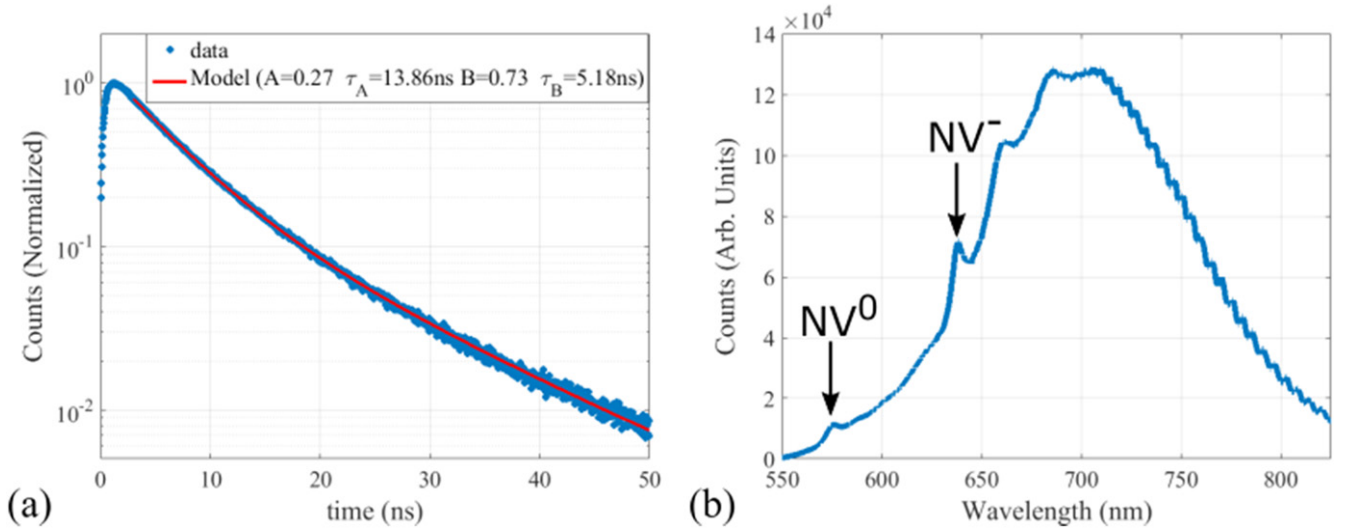


Figure 6. (a) Lifetime measurement data and a two-exponential fit for the fluorescence from the ND presented in figure 5(d). (b) emission spectrum of the ND shown in figure 5(d).

more than it does in figure 5(e), this is due to the structure of the termination mirror which allows the penetration of p-polarized excitation light and the fluorescence is enhanced due to the presence of three corners of the V-groove termination. The termination mirror B of the VG fluoresces more due to the presence of NDs in the region, which can be seen in figure 5(c).

The ND shown in figure 5(b) is further characterized by measuring its lifetime and fluorescence spectrum. The measured lifetime curve as well as a two-exponential fit ($A\exp(-t/\tau_A) + B\exp(-t/\tau_B) + \text{constant}$, where A and B are

amplitudes, t is time, τ_A and τ_B are decay lifetimes) is presented in figure 6(a). We note that NV-centers in NDs are known to have a distribution in decay lifetimes [23]. Our NDs have ~400 NV centers and each of the NV centers may have different lifetimes. Here, we have fitted the experimental data with minimum number of exponential decay rates possible. A single decay rate does not fit the data well, and a two exponential decay curve fits the data quite well ($0.9 < R^2 < 1.1$). The first 2 ns of the decay curve are not included in the fit to exclude gold fluorescence [44]. The two lifetimes obtained from the fit are $\tau_A = 13.86$ ns and $\tau_B = 5.18$ ns. These

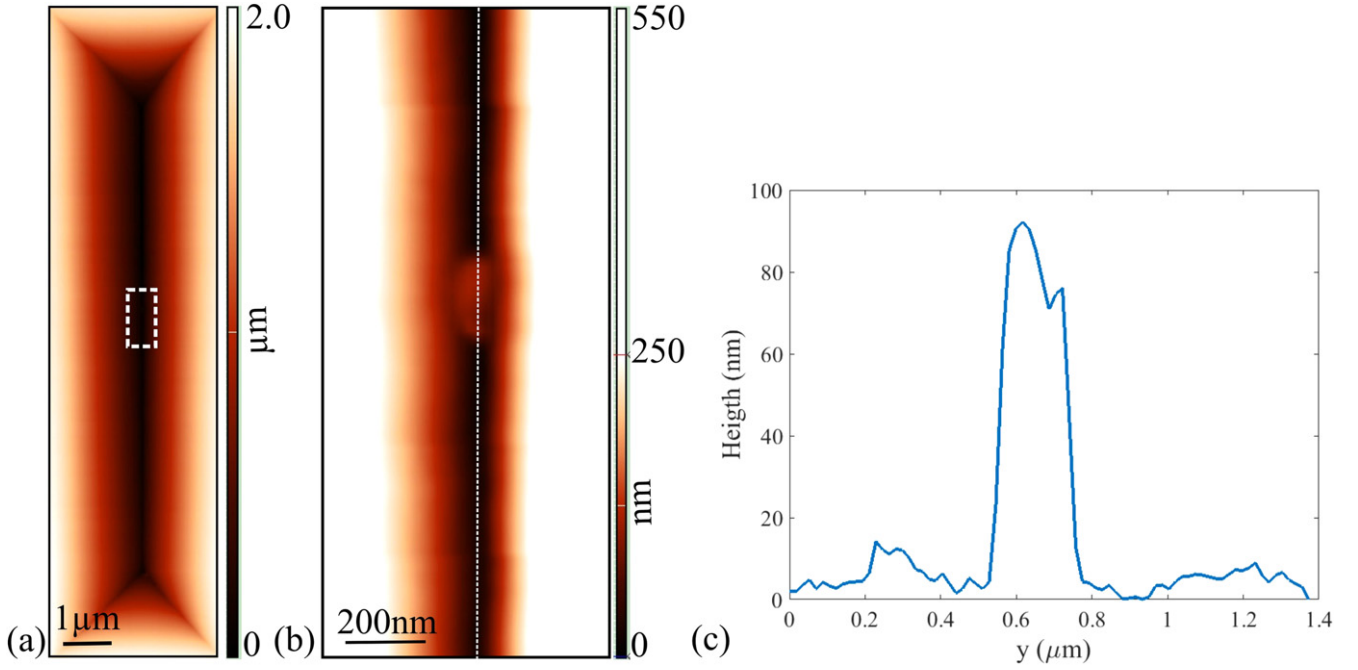


Figure 7. (a) AFM image of the VG after the ND is moved inside. The white rectangle indicates the area containing the ND. (b) zoomed-in image of the ND inside the VG. (c) The cross-section along the dotted white line in figure (b).

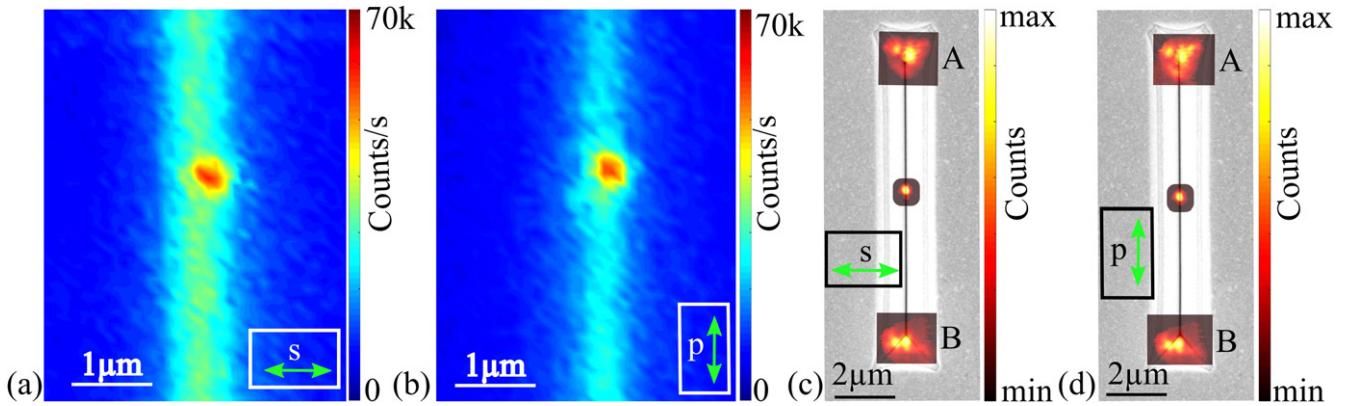


Figure 8. (a), (b) Confocal microscopy scan images of the ND located inside the V-groove with the excitation polarization indicated in the insets. (c) and (d) fluorescence images combined with SEM images indicating the emission from the far ends of the VG. The excitation spot is positioned at the ND and the excitation polarization is indicated in the insets. The three spots in both images were recorded separately. A and B indicate the two VG termination mirrors.

lifetimes are shortened when compared to those obtained when the NDs from the same suspension are spin-coated on a fused silica substrate. In the latter case, we obtained $\tau_A = 34.51$ ns and $\tau_B = 7.77$ ns (averaged over 10 NDs). The difference in lifetimes can be attributed to the excitation of SPPs on the gold–air interface by the NV centers. The fluorescence spectrum of the ND clearly shows (figure 6(b)) the characteristic zero phonon lines of NV^0 (575 nm) as well as NV^- (637 nm) centers.

After characterization of the VG as well as the ND, the ND is moved into the VG using a procedure that has been used previously [22, 24–28]. An AFM image of the VG containing the ND can be seen in figure 7(a). Figure 7(b) shows a zoomed-in image of the ND within the VG, and it can be inferred that the ND is close to the bottom of the VG.

The cross-section along the dotted line in figure 7(b) is presented in figure 7(c). The height of the ND inside the VG is around 90 nm, which is similar to the height observed outside of the VG for the ND.

Figures 8(a) and (b) present the confocal fluorescence image of the area of the VG containing the ND. The excitation laser power is, again, 100 μW. One can observe a significant decrease in the fluorescence counts obtained from the ND inside the VG when compared to the ND on gold–air interface. This could be due to the reduced intensity of the excitation laser inside the ND. In figures 8(c) and (d), the fluorescence images are overlapped with a SEM image of the VG. The fluorescence images are recorded while focusing the excitation laser on the ND, and the fluorescence images in the middle and those at the VG ends are recorded independently

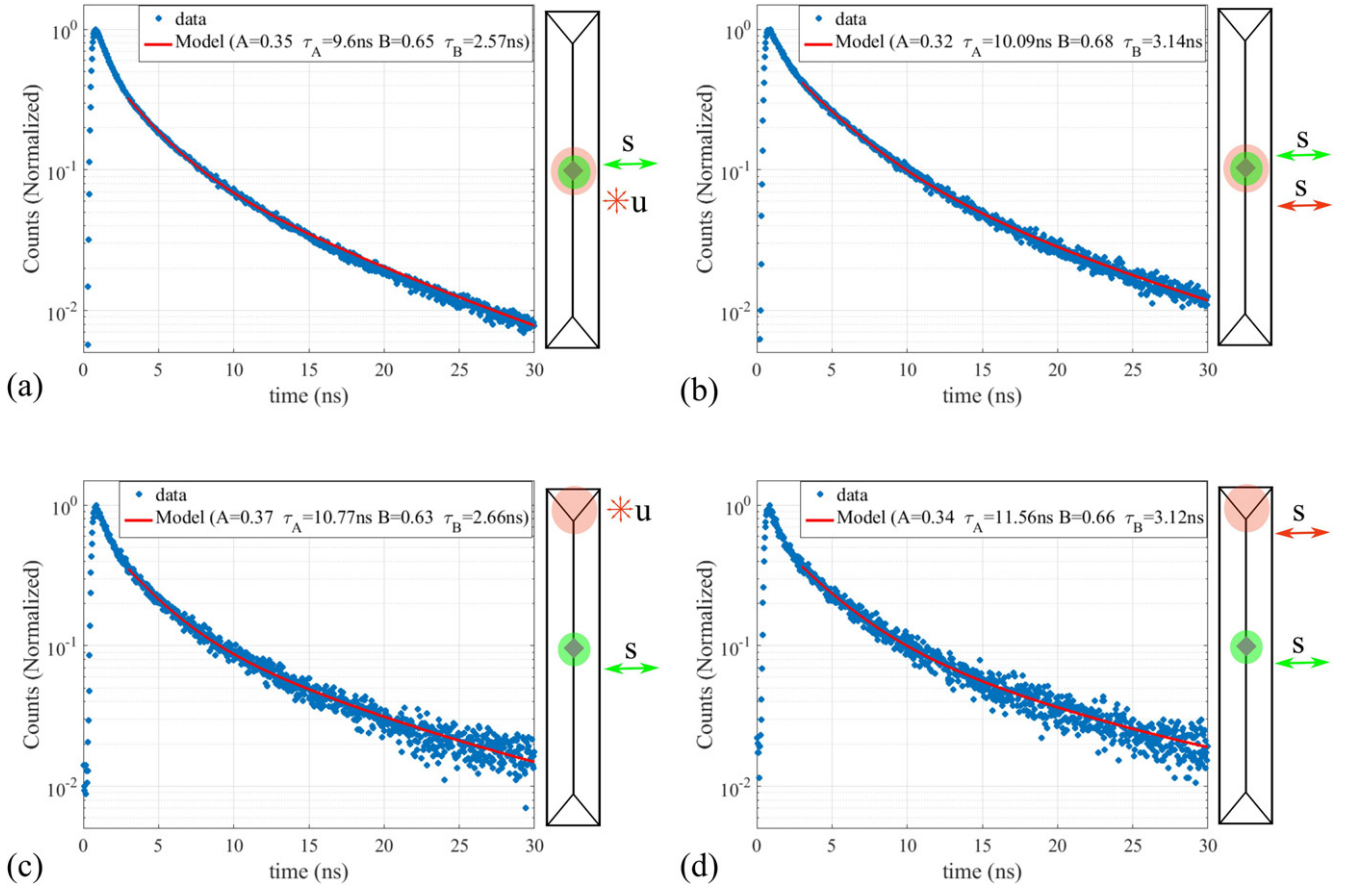


Figure 9. Lifetime measurement data and a two-exponential fit for the fluorescence collected from the ND inside the VG. In sketches next to the graphs, green and red disks represent the excitation and detection spots, respectively, whereas the arrows represent the excitation (green) and analyzed signal polarization (red).

to optimize the signal. The acquisition time for the fluorescence images in the middle is 1 s, whereas for the images at the VG termination mirrors is 60 s. The images suggest that the fluorescence from the ND couples to CPPs supported by the VG, which propagate along the VG and are out-coupled to free space from the termination mirrors of the VG. This sequence is observed for both excitation polarizations, as shown in figures 8(c) and (d). The difference in the far-field images of the two termination mirrors is attributed to the presence of NDs near the VG termination mirror B (figure 5(c)). The emission pattern for both excitation polarizations is the same due to excitation of the CPP modes in both cases.

The ND-VG system is further characterized by measuring the lifetime for different polarizations at the site of the ND, as well as at the VG termination mirrors. Figures 9 and 10 present the lifetimes of the coupled system when the excitation polarization is across the VG (s polarization) and along its axis (p polarization), respectively. In figure 9, it can be observed that the values of lifetimes obtained at the site of the emitter as well as those at VG termination mirror A are very close. This suggests that the NV centers being probed with s polarization are the same, regardless of whether the fluorescent signal is probed at the end of the waveguide or at the site of the ND itself. Under these circumstances, NV

centers with a non-zero projection of dipole moment along the excitation polarization are excited and coupled to the CPP mode of the VG. Previous studies of plasmonic modes in VGs indicate a more uniform distribution of the beta-factor across the profile when compared to cylindrical or wedge waveguides [33], which supports the assumption of a relatively uniform coupling of all the NV centers that are excited with s polarization. Furthermore, the fluorescence lifetime observed for the ND in this case is smaller than the fluorescence lifetime observed for the ND when it lied on the gold surface. The decrease for τ_A is by a factor of 1.32, and τ_B by a factor of 1.81. This is comparable to the lifetime change by a factor of ~ 2.44 observed when a single NV center in an ND lying on a gold surface is moved to inside a VG, in [28]. In figure 10, when the excitation polarization is along the VG axis, one can again observe that the values of lifetimes obtained at the end of the waveguide are very close to those at the site of the ND. However, if we compare the lifetimes obtained for the two orthogonal excitation polarizations, the lifetime in case of p-polarized excitation is longer than for s-polarized excitation. This can be attributed to the NV centers with dipoles across the VG axis, which couple more efficiently to the CPP mode of the VG. If we compare the fluorescence lifetimes of the ND when it is lying on the flat gold surface and when it is lying

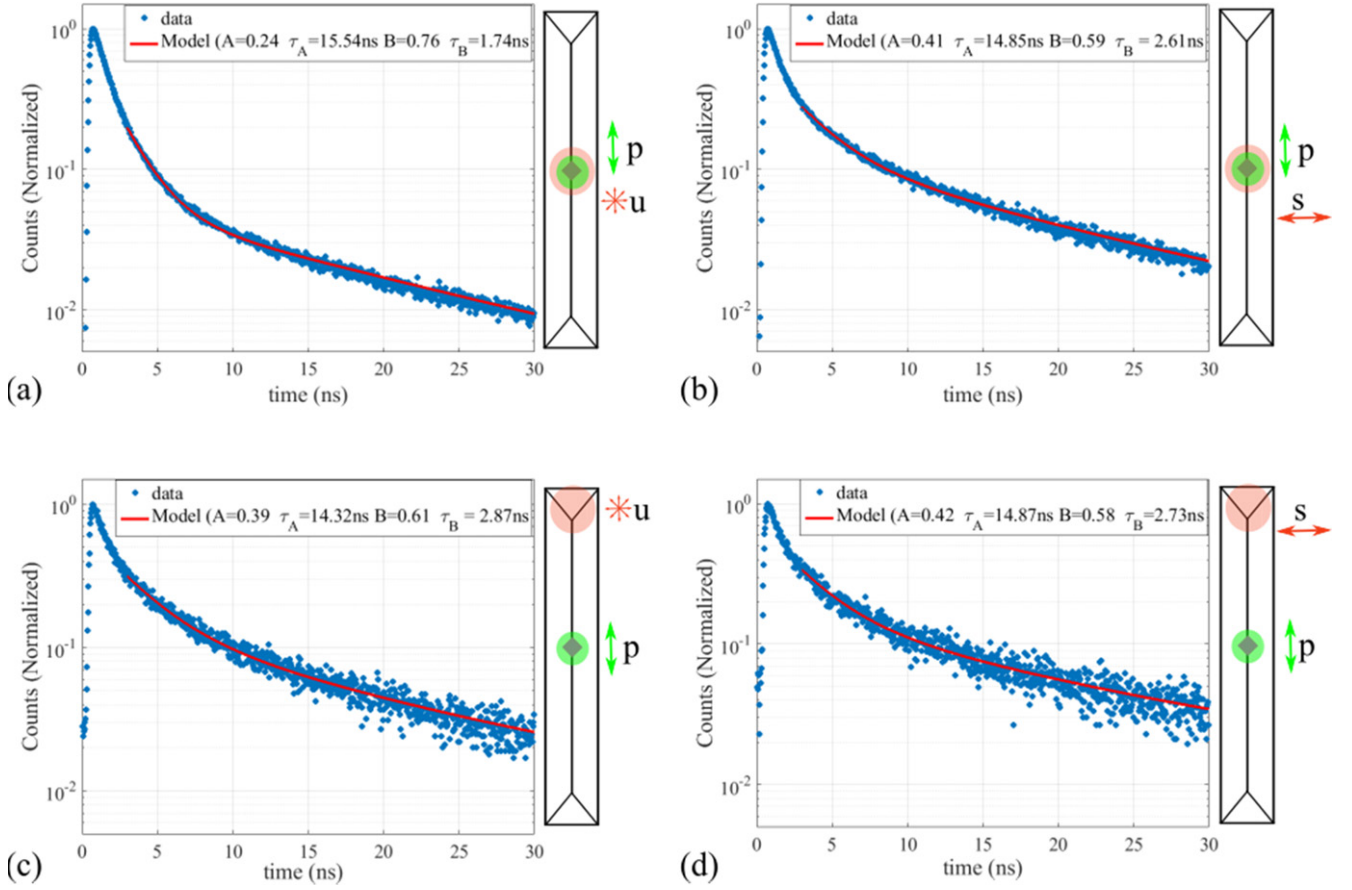


Figure 10. Lifetime measurement data and a two-exponential fit for the fluorescence collected from the ND inside the VG. In sketches next to the graphs, green and red disks represent the excitation and detection spots, respectively, whereas the arrows represent the excitation (green) and analyzed signal polarization (red).

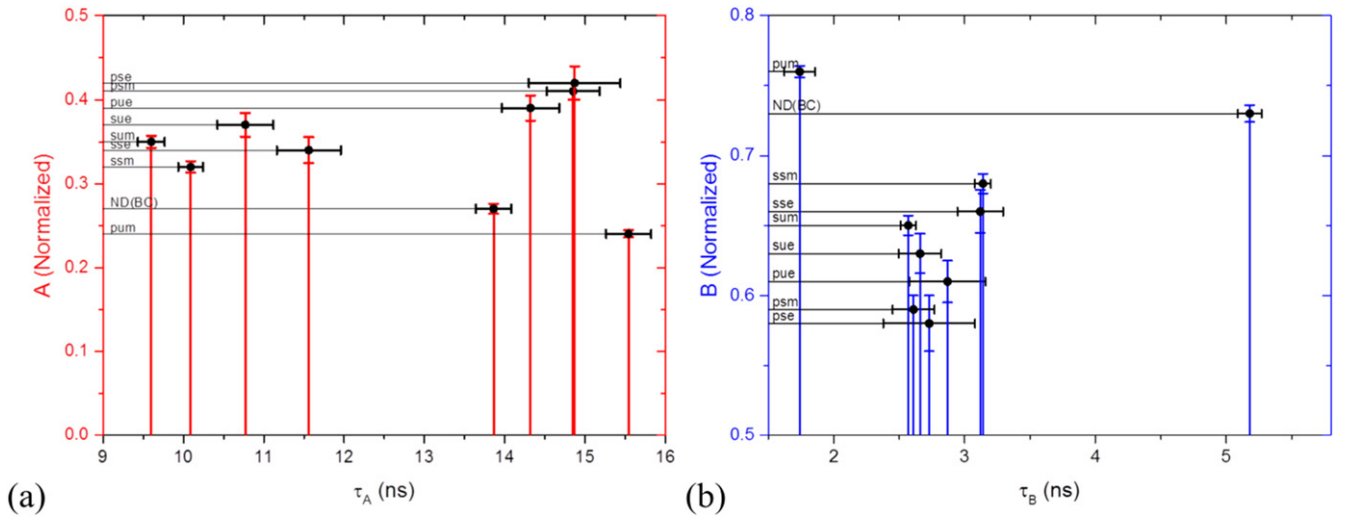


Figure 11. (a) and (b) summarize the lifetimes and amplitudes observed in figures 6(a), 9 and 10. ND(BC) denotes the nanodiamond before coupling to V-groove (figure 6(a)). In all the other symbols, the first letter denotes excitation polarization (s or p), the second letter denotes the analyzed polarization (s, p or u) and the third letter demotes the position of detection (middle (m) or end A (e)).

inside the VG and excited with p-polarized laser, the increase for τ_A is by a factor of 1.07, whereas for τ_B there is a decrease by a factor of 2.08. The slight increase of τ_A can be interpreted as a suppression of emission from dipoles aligned along the VG axis when compared to the ND lying

on a flat gold surface. In figure 11, we summarize all the lifetimes and amplitudes observed for the ND before and after its coupling to the V-groove. The errorbars represents uncertainty in the fitted parameters, that is, the lifetimes and amplitudes.

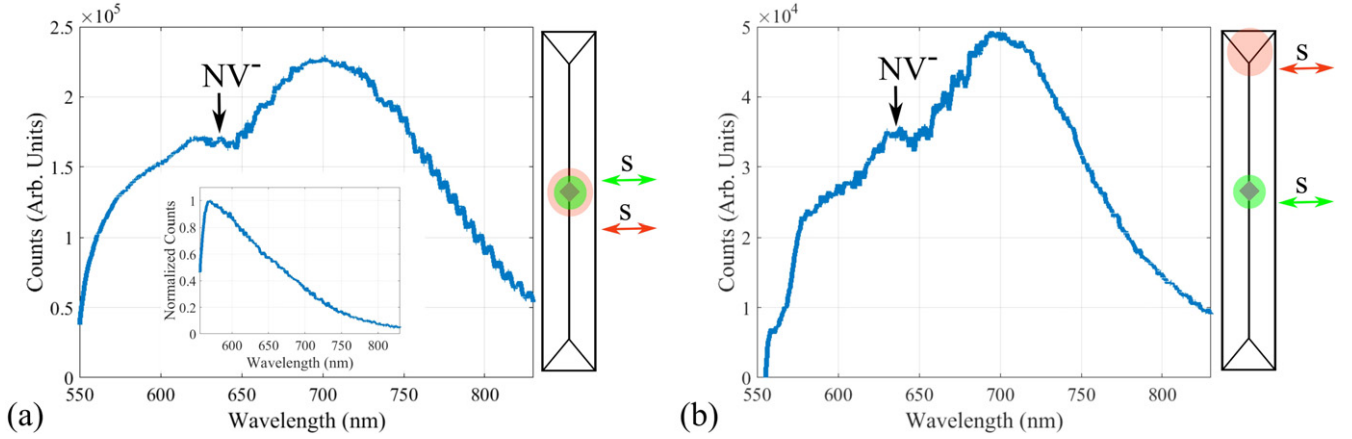


Figure 12. (a) and (b) Spectra taken at the site of the ND and at one of the VG ends, respectively. The excitation and detection polarizations are across the VG (i.e. s-polarized). The inset in (a) shows the fluorescence spectrum measured from a gold film.

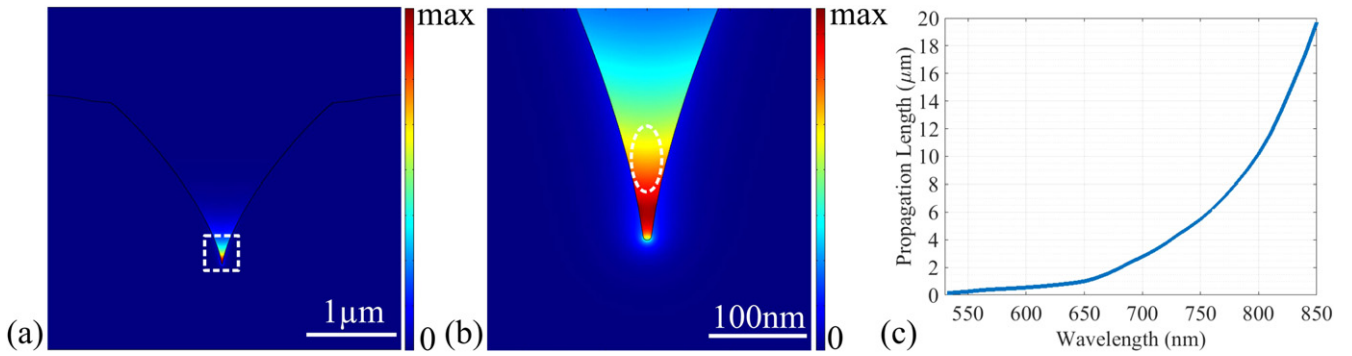


Figure 13. (a) Simulated CPP mode in a V-groove. The dotted rectangle shows the area which is zoomed-in and shown in (b). The oval shape in (b) indicates a possible position for the ND. (c) The CPP propagation distance as a function of wavelength is presented.

In figure 12, we present two fluorescence spectra of the same ND inside the VG, one of which is collected at the site of the ND, whereas the other is out-coupled from the termination mirror A of the VG. In the former case (figure 12(a)), the ND fluorescence spectrum is in superposition with fluorescence from gold, the spectrum of which is presented in the inset. In the latter case (figure 11(b)), the contribution from gold fluorescence is negligible, since it does not couple efficiently to the CPP mode [28]. The zero phonon line of NV^- centers can be observed in the spectrum that is measured at the end of the VG, which supports the argument above. The wavelength-dependent propagation loss of the CPP mode in the VG provides an additional source of modification of the observed spectra.

We simulated the CPP mode that is supported by these VGs using finite-element method (COMSOL Multiphysics). The cross-section is obtained by a numerical process simulation in ATHENA, as has been described in [39]. The dielectric constant of gold is taken from [45]. In figure 13(a), we present the distribution of the electric field of the CPP mode, calculated at a vacuum wavelength of 700 nm. The zoomed-in image in figure 13(b) shows the distribution of electric field along with the possible position for the ND inside the VG. From the dependence of the CPP propagation length on the wavelength (figure 1(c)), the suppression of shorter

wavelength is expected and is in support of the spectrum observed at the VG end.

3. Summary

We have presented the coupling of NDs containing multiple NV centers to SPPs on a silver–dielectric interface and to CPPs supported by a gold VG. The coupling to SPPs is observed by emission from other NDs that are used for scattering the SPPs to the far field. The spectrum of scattered fluorescence is fitted to a model which suggests that the dependence on propagation losses as well as the height of the NDs, both of the source as well as the scatterer must be accounted for. We have also presented the results of coupling of an ND to the CPP mode of a VG. The coupling is demonstrated by the observation of fluorescence from the VG termination mirror while the ND pushed into the VG middle is excited. A lifetime change, when moving the ND from outside to inside the VG, is also observed for the ND fluorescence, which further confirmed the coupling. The change in spectrum with respect to the ND is explained as the change caused by the propagation loss plus the inefficient coupling of gold fluorescence to the CPP mode. The reported experiments demonstrate a way of incorporating NDs containing multiple

NV-centers into plasmonic circuits as well as reveal various factors influencing the formation of fluorescence-excited SPP spectra.

Acknowledgments

The authors gratefully acknowledge the financial support from the European Research Council, Grant No. 341054 (PLAQNAP). CLCS. acknowledges financial support from the Danish Council for Independent Research (FTP Grant No. 12-126601).

References

- [1] Ladd T D, Jelezko F, Laflamme R, Nakamura Y, Monroe C and O'Brien J L 2010 Quantum computers *Nature* **464** 45–53
- [2] Doherty M W, Manson N B, Delaney P, Jelezko F, Wrachtrup J and Hollenberg L C L 2013 The nitrogen-vacancy colour centre in diamond *Phys. Rep.* **528** 1–45
- [3] Balasubramanian G *et al* 2009 Ultralong spin coherence time in isotropically engineered diamond *Nat. Mater.* **8** 383
- [4] Jelezko F, Gaebel T, Popa I, Gruber A and Wrachtrup J 2004 Observation of Coherent oscillations in a single electron spin *Phys. Rev. Lett.* **92** 076401
- [5] Gaebel T *et al* 2006 Room-temperature coherent coupling of single spins in diamond *Nat. Phys.* **2** 408
- [6] Hanson R, Mendoza F M, Epstein R J and Awschalom D D 2006 Polarization and readout of coupled single spins in diamond *Phys. Rev. Lett.* **97** 087601
- [7] Kurtseifer C, Mayer S, Zarda P and Weinfurter H 2000 Stable solid-state source of single photons *Phys. Rev. Lett.* **85** 290–3
- [8] Maletinsky P, Hong S, Grinolds M S, Hausmann B, Lukin M D, Walsworth R L, Loncar M and Yacoby A 2012 A robust scanning diamond sensor for nanoscale imaging with single nitrogen-vacancy centres *Nat. Nanotechnol.* **7** 320
- [9] Balasubramanian G *et al* 2008 Nanoscale imaging magnetometry with diamond spins under ambient conditions *Nature* **455** 648–51
- [10] Maze J R *et al* 2008 Nanoscale magnetic sensing with an individual electronic spin in diamond *Nature* **455** 644–7
- [11] Taylor J M, Cappellaro P, Childress L, Jiang L, Budker D, Hemmer P R, Yacoby A, Walsworth R and Lukin M D 2008 High-sensitivity diamond magnetometer with nanoscale resolution *Nat. Phys.* **4** 810–6
- [12] Wolf T, Neumann P, Nakamura K, Sumiya H, Ohshima T, Isoya J and Wrachtrup J A 2015 Subpicotesla diamond magnetometer *Phys. Rev. X* **5** 041001
- [13] Dolde F *et al* 2011 Electric-field sensing using single diamond spins *Nat. Phys.* **7** 459–63
- [14] Kucsko G, Maurer P C, Yao N Y, Kubo M, Noh H J, Lo P K, Park H and Lukin M D 2013 Nanometre-scale thermometry in a living cell *Nature* **500** 54–8
- [15] Mochalin V N, Shenderova O, Ho D and Gogotsi Y 2012 The properties and applications of nanodiamonds *Nat. Nanotechnol.* **7** 11–23
- [16] Babinec T M, Hausmann B J M, Khan M, Zhang Y, Maze J R, Hemmer P R and Loncar M 2010 A diamond nanowire single-photon source *Nat. Nanotechnol.* **5** 195
- [17] Schröder T, Fujiwara M, Noda T, Zhao H-Q, Benson O and Takeuchi S 2012 A nanodiamond-tapered fiber system with high single-mode coupling efficiency *Opt. Express* **20** 10490–7
- [18] Faraon A, Barclay P E, Santori C, Fu K-M C and Beausoleil R G 2011 Resonant enhancement of the zero-phonon emission from a colour centre in a diamond cavity *Nat. Photonics* **5** 301
- [19] Faraon A, Santori C, Huang Z, Acosta V M and Beausoleil R G 2012 Coupling of nitrogen-vacancy centers to photonic crystal cavities in monocrystalline diamond *Phys. Rev. Lett.* **109** 033604
- [20] Wolters J, Schell A W, Kewes G, Nüsse N, Schoengen M, Döschner H, Hannappel T, Öhel B L, Barth M and Benson O 2010 Enhancement of the zero phonon line emission from a single nitrogen vacancy center in a nanodiamond via coupling to a photonic crystal cavity *Appl. Phys. Lett.* **97** 141108
- [21] Choy J, Hausmann B, Babinec T, Bulu I, Khan M, Maletinsky P, Yacoby A and Loncar M 2011 Enhanced single-photon emission from a diamond–silver aperture *Nat. Photonics* **5** 738–43
- [22] Schietinger S, Barth M, Aichele T and Benson O 2009 Plasmon-enhanced single photon emission from a nano-assembled metal-diamond hybrid structure at room-temperature *Nano Lett.* **9** 1694–8
- [23] Kolesov R, Grotz B, Balasubramanian G, Stöhr R J, Nicolet A A L, Hemmer P R, Jelezko F and Wrachtrup J 2009 Wave–particle duality of single surface plasmon polaritons *Nat. Phys.* **5** 470
- [24] Huck A, Kumar S, Shakoar A and Andersen U L 2011 Controlled coupling of a single nitrogen-vacancy center to a silver nanowire *Phys. Rev. Lett.* **106** 096801
- [25] Kumar S, Huck A and Andersen U L 2013 Efficient coupling of a single diamond color center to propagating plasmonic gap modes *Nano Lett.* **13** 221
- [26] Kumar S, Huck A, Chen Y and Andersen U L 2013 Coupling of a single quantum emitter to end-to-end aligned silver nanowires *Appl. Phys. Lett.* **102** 103106
- [27] Kumar S, Huck A, Lu Y-W and Andersen U L 2013 Coupling of single quantum emitters to plasmons propagating on mechanically etched wires *Opt. Lett.* **38** 3838–41
- [28] Bermúdez-Ureña E *et al* 2015 Coupling of individual quantum emitters to channel plasmons *Nat. Commun.* **6** 7883
- [29] Gramotnev D K and Bozhevolnyi S I 2010 Plasmonics beyond the diffraction limit *Nat. Photonics* **4** 83–91
- [30] Chang D E, Sørensen A S, Hemmer P R and Lukin M D 2006 Quantum optics with surface plasmons *Phys. Rev. Lett.* **97** 053002
- [31] Chang D E, Sørensen A S, Hemmer P R and Lukin M D 2007 Strong coupling of single emitters to surface plasmons *Phys. Rev. B* **76** 035420
- [32] Akimov A V, Mukherjee A, Yu C L, Chang D E, Zibrov A S, Hemmer P R, Park H and Lukin M D 2007 Generation of single optical plasmons in metallic nanowires coupled to quantum dots *Nature* **450** 402
- [33] Martín-Cano D, Martín-Moreno L, García-Vidal F J and Moreno E 2010 Resonance energy transfer and superradiance mediated by plasmonic nanowaveguides *Nano Lett.* **10** 3129–34
- [34] Gonzalez-Tudela A, Martín-Cano D, Moreno E, Martín-Moreno L, Tejedor C and García-Vidal F J 2011 Entanglement of two qubits mediated by one-dimensional plasmonic waveguides *Phys. Rev. Lett.* **106** 020501
- [35] Bozhevolnyi S I, Volkov V S, Devaux E, Laluet J-Y and Ebbesen T W 2006 Channel plasmon subwavelength waveguide components including interferometers and ring resonators *Nature* **440** 508–11

List of Publications

Articles in peer-reviewed journals

1. **Sebastian K.H. Andersen**, Anders Pors and Sergey I. Bozhevolnyi
Gold Photoluminescence Wavelength and Polarization Engineering
ACS Photonics 2, 432-438, 2015
2. Anders Pors, **Sebastian K.H. Andersen** and Sergey I. Bozhevolnyi
Unidirectional scattering by nanoparticles near substrates: generalized Kerker conditions
Opt. Express 23, 28808-28828, 2015
3. Shailesh Kumar, Jens L. Lausen, Cesar E. Garcia-Ortiz, **Sebastian K. H. Andersen**, Alexander S. Roberts, Cameron L. C. Smith, Anders Kristensen and Sergey I. Bozhevolnyi.
Excitation of surface plasmon polariton modes with multiple nitrogen vacancy centers in single nanodiamonds J. Opt. 18, 024002, 2016
4. **Sebastian K.H. Andersen**, Shailesh Kumar and Sergey I. Bozhevolnyi
Coupling of nitrogen-vacancy centers in a nanodiamond to a silver nanocube
Opt. Mater. Express 6, 3394-3406, 2016
5. **Sebastian K.H. Andersen**, Shailesh Kumar and Sergey I. Bozhevolnyi
Ultrabright Linearly Polarized Photon Generation from a Nitrogen Vacancy Center in a Nanocube Dimer Antenna
Nano lett. 17, 3889-3895, 2017
6. **Sebastian K.H. Andersen**, Simeon Bogdanov, Oksana Makarova, Yi Xuan, Mikhail Y. Shalaginov, Alexandra Boltasseva, Sergey I. Bozhevolnyi and Vladimir M. Shalaev
Hybrid Plasmonic Bullseye Antennas for Efficient Photon Collection
ACS Photonics DOI: 10.1021/acsp Photonics.7b01194

Conference Proceedings

1. Poster presentation titled: Gold Photoluminescence: Wavelength and Polarization Engineering
Quantum Plasmonics Conference, March 2015, Benasque (Spain)
2. Talk titled: Spontaneous Emission Properties of Nitrogen-vacancy Color Centers Coupled to a
to a Silver Nanocube
Bremen Workshop on Light Scattering, March 2016, Bremen (Germany)

3. Poster presentation titled: Coupling of Nitrogen-vacancy Centers to a Silver Nano Cube
NANOMETA, January 2017, Seefeld (Austria)

Authorship agreement

This authorship agreement concerns the published research work conducted by PhD student Sebastian K. H. Andersen, Anders Pors and Sergey I. Bozhevolnyi.

The research work includes the following article:

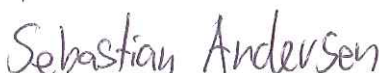
ACS Photonics 2(3), 432-438, (2015)

Gold Photoluminescence Wavelength and Polarization Engineering

In accordance with the criteria put forward at the Vancouver Convention for authorship (www.icmje.org), the undersigned Sebastian K. H. Andersen confirms he as first author is responsible for

- A substantial contribution to the intellectual content.
- Fabrication of all samples.
- Experimental characterization and data treatment.
- Preparation of all figures and wrote initial draft, except section on analytical model.
- Revision of manuscript for publication.

Similarly, the undersigned Anders Pors and Sergey I. Bozhevolnyi confirms that they as co-authors have contributed quantitatively and qualitatively to the conception and design, the critical revision for important intellectual content, the interpretation of experimental evidence, and the final approval of the versions to be published. As senior researcher, Sergey I. Bozhevolnyi stands as guarantor and takes public responsibility for the integrity of the research work as a whole, from inception to published articles.



First author, Sebastian K. H. Andersen



Co-author, Anders Pors



Co-author, Sergey I. Bozhevolnyi

Authorship agreement

This authorship agreement concerns the published research work conducted by PhD student Sebastian K. H. Andersen, Shailesh Kumar and Sergey I. Bozhevolnyi.

The research work includes the following article:

Optical Materials Express 6(11), 3394-3406, (2016)

Coupling of nitrogen-vacancy centers in a nanodiamond to a silver nanocube

In accordance with the criteria put forward at the Vancouver Convention for authorship (www.icmje.org), the undersigned Sebastian K. H. Andersen confirms he as first author is responsible for

- A substantial contribution to the intellectual content.
- Preparation of samples.
- Conducting experiment and data treatment.
- Performing numerical modelling.
- Preparation of all figures and wrote initial draft.
- Revision of manuscript for publication.

Similarly, the undersigned Shailesh Kumar and Sergey I. Bozhevolnyi confirms that they as co-authors have contributed quantitatively and qualitatively to the conception and design, the critical revision for important intellectual content, the interpretation of experimental evidence, and the final approval of the versions to be published. As senior researcher, Sergey I. Bozhevolnyi stands as guarantor and takes public responsibility for the integrity of the research work as a whole, from inception to published articles.



First author, Sebastian K. H. Andersen



Co-author, Shailesh Kumar



Co-author, Sergey I. Bozhevolnyi

Authorship agreement

This authorship agreement concerns the published research work conducted by PhD student Sebastian K. H. Andersen, Shailesh Kumar and Sergey I. Bozhevolnyi.

The research work includes the following article:

Nano Letters 17(6), 3889-3895, (2017)

Ultrabright Linearly Polarized Photon Generation from a Nitrogen Vacancy Center in a Nanocube Dimer Antenna

In accordance with the criteria put forward at the Vancouver Convention for authorship (www.icmje.org), the undersigned Sebastian K. H. Andersen confirms he as first author is responsible for

- A substantial contribution to the intellectual content.
- Preparation of samples.
- Conducting experiment and data treatment.
- Development of analytical description for excitation of cube coupled emitter.
- Performing numerical modelling.
- Preparation of all figures and wrote initial draft.
- Revision of manuscript for publication.

Similarly, the undersigned Shailesh Kumar and Sergey I. Bozhevolnyi confirms that they as co-authors have contributed quantitatively and qualitatively to the conception and design, the critical revision for important intellectual content, the interpretation of experimental evidence, and the final approval of the versions to be published. As senior researcher, Sergey I. Bozhevolnyi stands as guarantor and takes public responsibility for the integrity of the research work as a whole, from inception to published articles.



First author, Sebastian K. H. Andersen



Co-author, Shailesh Kumar



Co-author, Sergey I. Bozhevolnyi

Authorship agreement

This authorship agreement concerns the published research work conducted by Anders Pors, PhD student Sebastian K. H. Andersen and Sergey I. Bozhevolnyi.

The research work includes the following article:

Optics Express 23(22), 28808-28828, (2015)

Unidirectional scattering by nanoparticles near substrates: generalized Kerker conditions

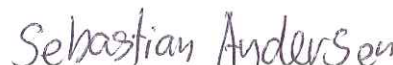
In accordance with the criteria put forward at the Vancouver Convention for authorship (www.icmje.org), the undersigned Sebastian K. H. Andersen confirms he as co-author is responsible for

- Fabrication of sample
- Conducting experiment and treatment of experimental data.
- Critical revision of manuscript.

Similarly, the undersigned Shailesh Kumar and Sergey I. Bozhevolnyi confirms that they as co-authors have contributed quantitatively and qualitatively to the conception and design, the critical revision for important intellectual content, the interpretation of experimental evidence, and the final approval of the versions to be published. As senior researcher, Sergey I. Bozhevolnyi stands as guarantor and takes public responsibility for the integrity of the research work as a whole, from inception to published articles.



First author, Anders Pors



Co-author, Sebastian K. H. Andersen



Co-author, Sergey I. Bozhevolnyi

Authorship agreement

This authorship agreement concerns the published research work conducted by Shailesh Kumar, Jens L. Lausen, Cesar E. Garcia-Ortiz, PhD student Sebastian K. H. Andersen, Alexander S. Roberts, Cameron L. C. Smith, Anders Kristensen and Sergey I. Bozhevolnyi.

The research work includes the following article:

Journal of Optics 18(2), 024002, (2016)

Excitation of surface plasmon polariton modes with multiple nitrogen vacancy centers in single nanodiamonds

In accordance with the criteria put forward at the Vancouver Convention for authorship (www.icmje.org), the undersigned Sebastian K. H. Andersen confirms he as co-author is responsible for

- Lithographic positioning of nanodiamonds in V-groove.
- Fabrication of Bragg grating in V-groove.
- Critical revision of manuscript.

Similarly, the undersigned Shailesh Kumar, Jens L. Lausen, Cesar E. Garcia-Ortiz, Alexander S. Roberts, Cameron L. C. Smith, Anders Kristensen and Sergey I. Bozhevolnyi confirms that they as co-authors have contributed quantitatively and qualitatively to the conception and design, the critical revision for important intellectual content, the interpretation of experimental evidence, and the final approval of the versions to be published. As senior researcher, Sergey I. Bozhevolnyi stands as guarantor and takes public responsibility for the integrity of the research work as a whole, from inception to published articles.



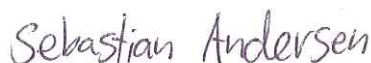
First author, Shailesh Kumar



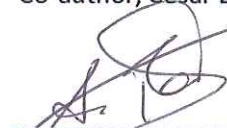
Co-author, Jens L. Lausen



Co-author, Cesar E. Garcia-Ortiz



Co-author, Sebastian K.H. Andersen



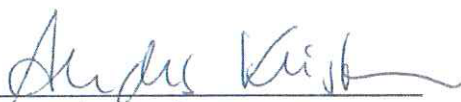
Co-author, Alexander S. Roberts



Co-author, Ilya P. Radko



Co-author, Cameron L. C. Smith



Co-author, Anders Kristensen



Co-author, Sergey I. Bozhevolnyi

Authorship agreement

This authorship agreement concerns the published research work conducted by Sebastian K.H. Andersen, Simeon Bogdanov, Oksana Makarova, Yi Xuan, Mikhail Y. Shalaginov, Alexandra Boltasseva, Sergey I. Bozhevolnyi and Vladimir M. Shalaev.

The research work includes the following article:

ACS Photonics DOI: 10.1021/acsphotonics.7b01194
Hybrid Plasmonic Bullseye Antennas for Efficient Photon Collection

In accordance with the criteria put forward at the Vancouver Convention for authorship (www.icmje.org), the undersigned Sebastian K. H. Andersen confirms he as first-author is responsible for

- Development of Idea.
- Numerical modelling.
- Implementation of backfocal imaging in experimental setup.
- Partial contribution to conducting the experiment.
- Preparation of figures and wrote initial draft.
- Revision of manuscript for publication.

Similarly, the undersigned Simeon Bogdanov, Oksana Makarova, Yi Xuan, Mikhail Y. Shalaginov, Alexandra Boltasseva, Sergey I. Bozhevolnyi and Vladimir M. Shalaev confirms that they as co-authors have contributed quantitatively and qualitatively to the conception and design, the critical revision for important intellectual content, the interpretation of experimental evidence, and the final approval of the versions to be published. As senior researcher, Sergey I. Bozhevolnyi stands as guarantor and takes public responsibility for the integrity of the research work as a whole, from inception to published articles.



First author, Sebastian K. H. Andersen



Co-author, Simeon Bogdanov



Co-author, Oksana Makarova



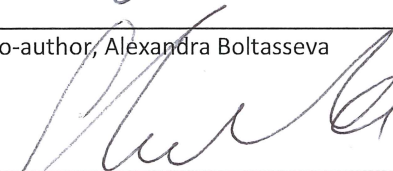
Co-author, Yi Xuan



Co-author, Alexandra Boltasseva



Co-author, Sergey I. Bozhevolnyi



Co-author, Vladimir M. Shalaev

References

- [1] P. W. Shor. Algorithms for quantum computation: Discrete logarithms and factoring. In *Proceedings of the 35th Annual Symposium on Foundations of Computer Science, SFCS '94*, pages 124–134, Washington, DC, USA, 1994. IEEE Computer Society.
- [2] Lov K. Grover. A fast quantum mechanical algorithm for database search. In *Proceedings of the Twenty-eighth Annual ACM Symposium on Theory of Computing, STOC '96*, pages 212–219, New York, NY, USA, 1996. ACM.
- [3] E. Knill, R. Laflamme, and G. J. Milburn. A scheme for efficient quantum computation with linear optics. *Nature*, 409(6816).
- [4] The LIGO Scientific Collaboration. A gravitational wave observatory operating beyond the quantum shot-noise limit. *Nat Phys*, 7(12).
- [5] J. M. Taylor, P. Cappellaro, L. Childress, L. Jiang, D. Budker, P. R. Hemmer, A. Yacoby, R. Walsworth, and M. D. Lukin. High-sensitivity diamond magnetometer with nanoscale resolution. *Nat Phys*, 4:810–816, 2008.
- [6] Alexios Beveratos, Rosa Brouri, Thierry Gacoin, André Villing, Jean-Philippe Poizat, and Philippe Grangier. Single photon quantum cryptography. *Phys. Rev. Lett.*, 89:187901, Oct 2002.
- [7] Charles H. Bennett and Gilles Brassard. Quantum cryptography: Public key distribution and coin tossing. *Theoretical Computer Science*, 560(Part 1):7 – 11, 2014. Theoretical Aspects of Quantum Cryptography – celebrating 30 years of BB84.
- [8] M. Bourennane, F. Gibson, A. Karlsson, A. Hening, P. Jonsson, T. Tsegaye, D. Ljunggren, and E. Sundberg. Experiments on long wavelength (1550nm) “plug and play” quantum cryptography systems. *Opt. Express*, 4(10):383–387, May 1999.
- [9] C. K. Hong and L. Mandel. Experimental realization of a localized one-photon state. *Phys. Rev. Lett.*, 56:58–60, Jan 1986.
- [10] Frank Diedrich and Herbert Walther. Nonclassical radiation of a single stored ion. *Phys. Rev. Lett.*, 58:203–206, Jan 1987.
- [11] Quantum emission from hexagonal boron nitride monolayers. Tran, toan trong and bray, kerem and ford, michael j. and toth, milos and aharonovich, igor. *Nat Nano*, 11:37–41, 2016.

- [12] Xuedan Ma, Nicolai F. Hartmann, Baldwin Jon K. S., Stephen K. Doorn, and Han Htoon. Room-temperature single-photon generation from solitary dopants of carbon nanotubes. *Nat Nano*, 10:671–675, August 2015.
- [13] Igor Aharonovich, Dirk Englund, and Milos Toth. *Nat Photon*, 10:631–641, October 2016.
- [14] E. M. Purcell. Spontaneous emission probabilities at radio frequencies. *Phys. Rev.*, 69:681, 1946.
- [15] Matthew Pelton. Modified spontaneous emission in nanophotonic structures. *Nat Photon*, 9:427–435, July 2015.
- [16] N. Somaschi, V. Giesz, L. De Santis, J. C. Loredó, M. P. Almeida, G. Hornecker, S. L. Portalupi, T. Grange, C. Antón, J. Demory, C. Gómez, I. Sagnes, N. D. Lanzillotti-Kimura, A. Lemaître, A. Auffeves, A. G. White, L. Lanco, and P. Senellart. Near-optimal single-photon sources in the solid state. *Nat Photon*, 10:340–345, 2016.
- [17] Sergey I. Bozhevolnyi and Jacob B. Khurgin. Fundamental limitations in spontaneous emission rate of single-photon sources. *Optica*, 3(12):1418–1421, Dec 2016.
- [18] Thang B. Hoang, Gleb M. Akselrod, and Maiken H. Mikkelsen. Ultrafast room-temperature single photon emission from quantum dots coupled to plasmonic nanocavities. *Nano Letters*, 16(1):270–275, 2016.
- [19] Igor Aharonovich, Dirk Englund, and Milos Toth. Solid-state single-photon emitters. *Nature Photonics*, 10:631–641, 9 2016.
- [20] Stefan A. Maier. *Plasmonics: Fundamentals and Applications*. Springer, 233 Spring Street, NY 10013, USA, 2007.
- [21] Jacob B. Khurgin. How to deal with the loss in plasmonics and metamaterials. *Nature Nanotechnology*, 10:2–6, 1 2015.
- [22] P. B. Johnson and R. W. Christy. Optical constants of the noble metals. *Phys. Rev. B*, 6:4370–4379, Dec 1972.
- [23] Ivan Avrutsky, Richard Soref, and Walter Buchwald. Sub-wavelength plasmonic modes in a conductor-gap-dielectric system with a nanoscale gap. *Opt. Express*, 18(1):348–363, Jan 2010.
- [24] Sergey I. Bozhevolnyi and Thomas Søndergaard. General properties of slow-plasmon resonant nanostructures: nano-antennas and resonators. *Opt. Express*, 15(17):10869–10877, Aug 2007.
- [25] J. J. Mock, M. Barbic, D. R. Smith, D. A. Schultz, and S. Schultz. Shape effects in plasmon resonance of individual colloidal silver nanoparticles. *The Journal of Chemical Physics*, 116(15):6755–6759, 2002.
- [26] Paolo Biagioni, Jer-Shing Huang, and Bert Hecht. Nanoantennas for visible and infrared radiation. *Reports on Progress in Physics*, 75(2):024402, 2012.

- [27] Jorge Zuloaga and Peter Nordlander. On the energy shift between near-field and far-field peak intensities in localized plasmon systems. *Nano Letters*, 11(3):1280–1283, 2011.
- [28] John D. Jackson. *Classical Electrodynamics*. John Wiley and Sons, 1962.
- [29] Feng Wang and Y. Ron Shen. General properties of local plasmons in metal nanostructures. *Phys. Rev. Lett.*, 97:206806, Nov 2006.
- [30] Rodney Loudon. *The Quantum Theory of Light*. Oxford University Press, Great Clarendon Street, Oxford Ox2 6DP, 2000.
- [31] Mark Fox. *Quantum Optics An Introduction*. Oxford University Press, Great Clarendon Street, Oxford Ox2 6DP, 2006.
- [32] G Colas des Francs, J Barthes, A Bouhelier, J C Weeber, A Dereux, A Cuche, and C Girard. Plasmonic purcell factor and coupling efficiency to surface plasmons. implications for addressing and controlling optical nanosources. *Journal of Optics*, 18(9):094005, 2016.
- [33] Lukas Novotny and Bert Hecht. *Principles of Nano-Optics*. Cambridge University Press, University Printing House, Cambridge CB2 8B2, United Kingdom, 2012.
- [34] K.H. Drexhage. Influence of a dielectric interface on fluorescence decay time. *Journal of Luminescence*, 1-2:693 – 701, 1970.
- [35] R. R. Chance, A. Prock, and R. Silbey. *Molecular Fluorescence and Energy Transfer Near Interfaces*, pages 1–65. John Wiley and Sons, Inc., 2007.
- [36] G.W. Ford and W.H. Weber. Electromagnetic interactions of molecules with metal surfaces. *Physics Reports*, 113(4):195 – 287, 1984.
- [37] Pascal Anger, Palash Bharadwaj, and Lukas Novotny. Enhancement and quenching of single-molecule fluorescence. *Phys. Rev. Lett.*, 96:113002, Mar 2006.
- [38] Guillermo P. Acuna, Martina Bucher, Ingo H. Stein, Christian Steinhauer, Anton Kuzyk, Phil Holzmeister, Robert Schreiber, Alexander Moroz, Fernando D. Stefani, Tim Liedl, Friedrich C. Simmel, and Philip Tinnefeld. Distance dependence of single-fluorophore quenching by gold nanoparticles studied on dna origami. *ACS Nano*, 6(4):3189–3195, 2012. PMID: 22439823.
- [39] Sergey I. Bozhevolnyi and Jacob B. Khurgin. The case for quantum plasmonics. *Nature Photonics*, 11:398–400, June 2017.
- [40] Alberto G. Curto, Giorgio Volpe, Tim H. Taminiau, Mark P. Kreuzer, Romain Quidant, and Niek F. van Hulst. Unidirectional emission of a quantum dot coupled to a nanoantenna. *Science*, 329(5994):930–933, 2010.
- [41] Young Chu Jun, Kevin C.Y. Huang, and Mark L. Brongersma. Plasmonic beaming and active control over fluorescent emission. *Nature Communications*, 2:283–289, 2011.

- [42] Nitzan Livneh, Moshe G. Harats, Daniel Istrati, Hagai S. Eisenberg, and Ronen Rapaport. Highly directional room-temperature single photon device. *Nano Letters*, 16(4):2527–2532, 2016. PMID: 26963878.
- [43] C. Sauvan, J. P. Hugonin, I. S. Maksymov, and P. Lalanne. Theory of the spontaneous optical emission of nanosize photonic and plasmon resonators. *Phys. Rev. Lett.*, 110:237401, Jun 2013.
- [44] Mohsen Kamandar Dezfouli, Christos Tserkezis, N. Asger Mortensen, and Stephen Hughes. Nonlocal quasinormal modes for arbitrarily shaped three-dimensional plasmonic resonators. *Optica*, 4(12):1503–1509, Dec 2017.
- [45] Michael Geiselmann, Renaud Marty, Jan Renger, F. Javier García de Abajo, and Romain Quidant. Deterministic optical-near-field-assisted positioning of nitrogen-vacancy centers. *Nano Letters*, 14(3):1520–1525, 2014.
- [46] Andreas W. Schell, Günter Kewes, Tim Schröder, Janik Wolters, Thomas Aichele, and Oliver Benson. A scanning probe-based pick-and-place procedure for assembly of integrated quantum optical hybrid devices. *Review of Scientific Instruments*, 82(7):073709, 2011.
- [47] Mingming Jiang, Jonathan A. Kurvits, Yao Lu, Arto V. Nurmikko, and Rashid Zia. Reusable inorganic templates for electrostatic self-assembly of individual quantum dots, nanodiamonds, and lanthanide-doped nanoparticles. *Nano Letters*, 15(8):5010–5016, 2015. PMID: 26215188.
- [48] Claire A. McLellan, Bryan A. Myers, Stephan Kraemer, Kenichi Ohno, David D. Awschalom, and Ania C. Bleszynski Jayich. Patterned formation of highly coherent nitrogen-vacancy centers using a focused electron irradiation technique. *Nano Letters*, 16(4):2450–2454, 2016. PMID: 27010642.
- [49] Gopalakrishnan Balasubramanian, Philipp Neumann, Daniel Twitchen, Matthew Markham, Roman Kolesov, Norikazu Mizuochi, Junichi Isoya, Jocelyn Achard, Johannes Beck, Julia Tissler, Vincent Jacques, Philip R. Hemmer, Fedor Jelezko, and Jorg Wrachtrup. Ultralong spin coherence time in isotopically engineered diamond. *Nat Mater*, 8:383–387, 2009.
- [50] Matthew E. Trusheim, Luozhou Li, Abdelghani Laraoui, Edward H. Chen, Hassaram Bakhru, Tim Schröder, Ophir Gaathon, Carlos A. Meriles, and Dirk Englund. Scalable fabrication of high purity diamond nanocrystals with long-spin-coherence nitrogen vacancy centers. *Nano Letters*, 14(1):32–36, 2014.
- [51] J Harrison, M.J Sellars, and N.B Manson. Optical spin polarisation of the n-v centre in diamond. *Journal of Luminescence*, 107(1–4):245 – 248, 2004.
- [52] F. Jelezko, T. Gaebel, I. Popa, A. Gruber, and J. Wrachtrup. Observation of coherent oscillations in a single electron spin. *Phys. Rev. Lett.*, 92:076401, Feb 2004.
- [53] M. Steiner, P. Neumann, J. Beck, F. Jelezko, and J. Wrachtrup. Universal enhancement of the optical readout fidelity of single electron spins at nitrogen-vacancy centers in diamond. *Phys. Rev. B*, 81:035205, Jan 2010.

- [54] P. Neumann, I. Jakobi, F. Dolde, C. Burk, R. Reuter, G. Waldherr, J. Honert, T. Wolf, A. Brunner, J. H. Shim, D. Suter, H. Sumiya, J. Isoya, and J. Wrachtrup. High-precision nanoscale temperature sensing using single defects in diamond. *Nano Letters*, 13(6):2738–2742, 2013.
- [55] F. Dolde, H. Fedder, M. W. Doherty, T. Nobauer, F. Rempp, G. Balasubramanian, T. Wolf, F. Reinhard, L. C. L. Hollenberg, F. Jelezko, and J. Wrachtrup. Electric-field sensing using single diamond spins. *Nat Phys*, 7:459–463, 2011.
- [56] I Aharonovich, S Castelletto, D A Simpson, C-H Su, A D Greentree, and S Prawer. Diamond-based single-photon emitters. *Reports on Progress in Physics*, 74(7):076501, 2011.
- [57] Takayuki Iwasaki, Fumitaka Ishibashi, Yoshiyuki Miyamoto, Yuki Doi, Satoshi Kobayashi, Takehide Miyazaki, Kosuke Tahara, Kay D. Jahnke, Lachlan J. Rogers, Boris Naydenov, Fedor Jelezko, Satoshi Yamasaki, Shinji Nagamachi, Toshiro Inubushi, Norikazu Mizuochi, and Mutsuko Hatano. Germanium-vacancy single color centers in diamond. *Scientific Reports*, 5:12882, 2015.
- [58] Takayuki Iwasaki, Yoshiyuki Miyamoto, Takashi Taniguchi, Petr Siyushev, Mathias H. Metsch, Fedor Jelezko, and Mutsuko Hatano. Tin-vacancy quantum emitters in diamond. *Phys. Rev. Lett.*, 119:253601, Dec 2017.
- [59] Marcus W. Doherty, Neil B. Manson, Paul Delaney, Fedor Jelezko, Jörg Wrachtrup, and Lloyd C.L. Hollenberg. The nitrogen-vacancy colour centre in diamond. *Physics Reports*, 528(1):1 – 45, 2013. The nitrogen-vacancy colour centre in diamond.
- [60] Xing-Fei He, Neil B. Manson, and Peter T. H. Fisk. Paramagnetic resonance of photoexcited n-v defects in diamond. ii. hyperfine interaction with the nucleus. *Phys. Rev. B*, 47:8816–8822, Apr 1993.
- [61] M W Doherty, N B Manson, P Delaney, and L C L Hollenberg. The negatively charged nitrogen-vacancy centre in diamond: the electronic solution. *New Journal of Physics*, 13(2):025019, 2011.
- [62] T. Gaebel, M. Domhan, C. Wittmann, I. Popa, F. Jelezko, J. Rabeau, A. Greentree, S. Prawer, E. Trajkor, P.R. Hemmer, and J. Wrachtrup. Photochromism in single nitrogen-vacancy defect in diamond. *Applied Physics B*, 82(2):243–246, 2006.
- [63] J H N Loubser and J A van Wyk. Electron spin resonance in the study of diamond. *Reports on Progress in Physics*, 41(8):1201, 1978.
- [64] V. M. Acosta, A. Jarmola, E. Bauch, and D. Budker. Optical properties of the nitrogen-vacancy singlet levels in diamond. *Phys. Rev. B*, 82:201202, Nov 2010.
- [65] A. Gupta, L. Hacquebard, and L. Childress. Efficient signal processing for time-resolved fluorescence detection of nitrogen-vacancy spins in diamond. *J. Opt. Soc. Am. B*, 33(3):B28–B34, Mar 2016.

- [66] K. Beha, A. Batalov, N. B. Manson, R. Bratschitsch, and A. Leitenstorfer. Optimum photoluminescence excitation and recharging cycle of single nitrogen-vacancy centers in ultrapure diamond. *Phys. Rev. Lett.*, 109:097404, Aug 2012.
- [67] S. Felton, A. M. Edmonds, and M. E. Newton. Electron paramagnetic resonance studies of the neutral nitrogen vacancy in diamond. *Phys. Rev. B*, 77:081201R, 2008.
- [68] P Neumann, R Kolesov, V Jacques, J Beck, J Tisler, A Batalov, L Rogers, N B Manson, G Balasubramanian, F Jelezko, and J Wrachtrup. Excited-state spectroscopy of single nv defects in diamond using optically detected magnetic resonance. *New Journal of Physics*, 11(1):013017, 2009.
- [69] R. J. Epstein, F. M. Mendoza, Y. K. Kato, and D. D. Awschalom. Anisotropic interactions of a single spin and dark-spin spectroscopy in diamond. *Nat Phys*, 1:94–98, 2005.
- [70] M W Doherty, J Michl, F Dolde, I Jakobi, P Neumann, N B Manson, and J Wrachtrup. Measuring the defect structure orientation of a single nv – centre in diamond. *New Journal of Physics*, 16(6):063067, 2014.
- [71] L J Rogers, R L McMurtrie, M J Sellars, and N B Manson. Time-averaging within the excited state of the nitrogen-vacancy centre in diamond. *New Journal of Physics*, 11(6):063007, 2009.
- [72] Kai-Mei C. Fu, Charles Santori, Paul E. Barclay, Lachlan J. Rogers, Neil B. Manson, and Raymond G. Beausoleil. Observation of the dynamic jahn-teller effect in the excited states of nitrogen-vacancy centers in diamond. *Phys. Rev. Lett.*, 103:256404, Dec 2009.
- [73] Naofumi Abe, Yasuyoshi Mitsumori, Mark Sadgrove, and Keiichi Edamatsu. Dynamically unpolarized single-photon source in diamond with intrinsic randomness. *Scientific Reports*, 7:46722, 2017.
- [74] A. Gruber, A. Dräbenstedt, C. Tietz, L. Fleury, J. Wrachtrup, and C. von Borczyskowski. Scanning confocal optical microscopy and magnetic resonance on single defect centers. *Science*, 276(5321):2012–2014, 1997.
- [75] Christian Kurtsiefer, Sonja Mayer, Patrick Zarda, and Harald Weinfurter. Stable solid-state source of single photons. *Phys. Rev. Lett.*, 85:290–293, Jul 2000.
- [76] N Aslam, G Waldherr, P Neumann, F Jelezko, and J Wrachtrup. Photo-induced ionization dynamics of the nitrogen vacancy defect in diamond investigated by single-shot charge state detection. *New Journal of Physics*, 15(1):013064, 2013.
- [77] Abbas Mohtashami and A Femius Koenderink. Suitability of nanodiamond nitrogen–vacancy centers for spontaneous emission control experiments. *New Journal of Physics*, 15(4):043017, 2013.

- [78] Faraz A. Inam, Michael D. W. Grogan, Mathew Rollings, Torsten Gaebel, Jana M. Say, Carlo Bradac, Tim A. Birks, William J. Wadsworth, Stefania Castelletto, James R. Rabeau, and Michael J. Steel. Emission and nonradiative decay of nanodiamond nv centers in a low refractive index environment. *ACS Nano*, 7(5):3833–3843, 2013.
- [79] F.A. Inam, M.J. Steel, and S. Castelletto. Effects of the hosting nano-environment modifications on nv centres fluorescence emission. *Diamond and Related Materials*, 45(Supplement C):64 – 69, 2014.
- [80] Ilya P. Radko, Mads Boll, Niels M. Israelsen, Nicole Raatz, Jan Meijer, Fedor Jelezko, Ulrik L. Andersen, and Alexander Huck. Determining the internal quantum efficiency of shallow-implanted nitrogen-vacancy defects in bulk diamond. *Opt. Express*, 24(24):27715–27725, Nov 2016.
- [81] C. Bradac, T. Gaebel, N. Naidoo, M. J. Sellars, J. Twamley, L. J. Brown, A. S. Barnard, T. Plakhotnik, A. V. Zvyagin, and J. R. Rabeau. Observation and control of blinking nitrogen-vacancy centres in discrete nanodiamonds. *Nature Nanotechnology*, 4:345–349, April 2010.
- [82] M. V. Hauf, B. Grotz, B. Naydenov, M. Dankerl, S. Pezzagna, J. Meijer, F. Jelezko, J. Wrachtrup, M. Stutzmann, F. Reinhard, and J. A. Garrido. Chemical control of the charge state of nitrogen-vacancy centers in diamond. *Phys. Rev. B*, 83:081304, Feb 2011.
- [83] Hayate Yamano, Sora Kawai, Kanami Kato, Taisuke Kageura, Masafumi Inaba, Takuma Okada, Itaru Higashimata, Moriyoshi Haruyama, Takashi Tanii, Keisuke Yamada, Shinobu Onoda, Wataru Kada, Osamu Hanaizumi, Tokuyuki Teraji, Junichi Isoya, and Hiroshi Kawarada. Charge state stabilization of shallow nitrogen vacancy centers in diamond by oxygen surface modification. 56:04CKo8, 04 2017.
- [84] R. Q. TWISS and R. HANBURY BROWN. Correlation between photons, in coherent beams of light, detected by a coincidence counting technique. *Nature*, 180:324–326, August 1957.
- [85] Dingwei Zheng. *Study and manipulation of photoluminescent NV color center in diamond*. PhD thesis, East China Normal University, China, Shanghai, Putuo Qu, Zhong Shan Bei Lu, 3663, October 2010.
- [86] T. Junno, K. Deppert, L. Montelius, and L. Samuelson. Controlled manipulation of nanoparticles with an atomic force microscope. *Applied Physics Letters*, 66(26):3627–3629, 1995.
- [87] L Theil Hansen, A Kühle, A H Sørensen, J Bohr, and P E Lindelof. A technique for positioning nanoparticles using an atomic force microscope. *Nanotechnology*, 9(4):337, 1998.
- [88] N. E. Christensen. The band structure of silver and optical interband transitions. *physica status solidi (b)*, 54(2):551–563, 1972.
- [89] T.E. Graedel. Corrosion mechanisms for silver exposed to the atmosphere. *J. Electrochem. Soc.*, 139(7):1963–1970, 1992.

- [90] Jose Luis Elechiguerra, Leticia Larios-Lopez, Cui Liu, Domingo Garcia-Gutierrez, Alejandra Camacho-Bragado, and Miguel Jose Yacamán. Corrosion at the nanoscale: the case of silver nanowires and nanoparticles. *Chemistry of Materials*, 17(24):6042–6052, 2005.
- [91] A. Mooradian. Photoluminescence of metals. *Phys. Rev. Lett.*, 22:185–187, Feb 1969.
- [92] Stefan Schietinger, Michael Barth, Thomas Aichele, and Oliver Benson. Plasmon-enhanced single photon emission from a nanoassembled metal–diamond hybrid structure at room temperature. *Nano Letters*, 9(4):1694–1698, 2009. PMID: 19301860.
- [93] Hailong Hu, Huigao Duan, Joel K. W. Yang, and Ze Xiang Shen. Plasmon-modulated photoluminescence of individual gold nanostructures. *ACS Nano*, 6(11):10147–10155, 2012. PMID: 23072661.
- [94] Jahnke K.D. Teraji T. Marseglia L. Müller C. Naydenov B. Schaufert H. Kranz C. Isoya J. McGuinness L.P. Jelezko F. Rogers, L.J. Multiple intrinsically identical single-photon emitters in the solid state. *Nature Communications*, 5(4739):1–6, 2014.
- [95] Nitzan Livneh, Moshe G. Harats, Daniel Istrati, Hagai S. Eisenberg, and Ronen Rapaport. Highly directional room-temperature single photon device. *Nano Letters*, 16(4):2527–2532, 2016. PMID: 26963878.
- [96] Jan Mertens, Marie-Elena Kleemann, Rohit Chikkaraddy, Prineha Narang, and Jeremy J. Baumberg. How light is emitted by plasmonic metals. *Nano Letters*, 17(4):2568–2574, 2017. PMID: 28267346.
- [97] Kuo-Ping Chen, Vladimir P. Drachev, Joshua D. Borneman, Alexander V. Kildishev, and Vladimir M. Shalaev. Drude relaxation rate in grained gold nanoantennas. *Nano Letters*, 10(3):916–922, 2010. PMID: 20128610.
- [98] Heykel Aouani, Jérôme Wenger, Davy Gérard, Hervé Rigneault, Eloïse Devaux, Thomas W. Ebbesen, Farhad Mahdavi, Tingjun Xu, and Steve Blair. Crucial role of the adhesion layer on the plasmonic fluorescence enhancement. *ACS Nano*, 3(7):2043–2048, 2009. PMID: 19518085.
- [99] Terefe G. Habteyes, Scott Dhuey, Erin Wood, Daniel Gargas, Stefano Cabrini, P. James Schuck, A. Paul Alivisatos, and Stephen R. Leone. Metallic adhesion layer induced plasmon damping and molecular linker as a nondamping alternative. *ACS Nano*, 6(6):5702–5709, 2012. PMID: 22646820.
- [100] Yi-Ren Chang, Hsu-Yang Lee, Kowa Chen, Chun-Chieh Chang, Dung-Sheng Tsai, Chi-Cheng Fu, Tsong-Shin Lim, Yan-Kai Tzeng, Chia-Yi Fang, Chau-Chung Han, Huan-Cheng Chang, and Wunshain Fann. Mass production and dynamic imaging of fluorescent nanodiamonds. *Nature Nanotechnology*, 3:284–288, 2008.
- [101] Shailesh Kumar, Ying-Wei Lu, Alexander Huck, and Ulrik L. Andersen. Propagation of plasmons in designed single crystalline silver nanostructures. *Opt. Express*, 20(22):24614–24622, Oct 2012.

- [102] Stephan J. P. Kress, Felipe V. Antolinez, Patrizia Richner, Sriharsha V. Jayanti, David K. Kim, Ferry Prins, Andreas Riedinger, Maximilian P. C. Fischer, Stefan Meyer, Kevin M. McPeak, Dimos Poulikakos, and David J. Norris. Wedge waveguides and resonators for quantum plasmonics. *Nano Letters*, 15(9):6267–6275, 2015. PMID: 26284499.
- [103] Nathalie P. de Leon, Brendan J. Shields, Chun L. Yu, Dirk E. Englund, Alexey V. Akimov, Mikhail D. Lukin, and Hongkun Park. Tailoring light-matter interaction with a nanoscale plasmon resonator. *Phys. Rev. Lett.*, 108:226803, May 2012.
- [104] Hamidreza Siampour, Shailesh Kumar, and Sergey I. Bozhevolnyi. Chip-integrated plasmonic cavity-enhanced single nitrogen-vacancy center emission. *Nanoscale*, 9:17902–17908, 2017.
- [105] C. L. C. Smith, N. Stenger, A. Kristensen, N. A. Mortensen, and S. I. Bozhevolnyi. Gap and channeled plasmons in tapered grooves: a review. *Nanoscale*, 7:9355–9386, 2015.
- [106] Erchan Yang, Houqiang Jiang, Yonghua Lu, Zheng Xi, Wenhai Yu, and Pei Wang. Coherent plasmon transport using a quantum dot coupled plasmonic nanocavity system. *Journal of Optics*, 17(5):055003, 2015.